Coordination chemistry of functionalised triarylimidazole-based ligands with Re(I) and U(VI)

A thesis submitted to Cardiff University for the degree
of Doctor of Philosophy in Chemistry

2014

Owen Bonello

Contents

Contents ... i

Summary ... vii

Declaration ... viii

Acknowlegements ... x

List of abbreviations and symbols ... xi

Chapter 1: Introduction ... 1

1.1 Luminescence spectroscopy ... 2

1.1.1 Quantum Numbers, Russell-Saunders coupling and term symbols ... 3

1.1.2 *J-J* coupling scheme ... 5

1.1.3 Selection Rules ... 6

1.1.4 Fluorescence ... 6

1.1.5 Phosphorescence ... 7

1.1.6 The Franck-Condon principle ... 8

1.1.7 Stokes' Shift ... 9

1.1.8 Quantum Yields (ϕ) and lifetimes (τ) ... 9

1.1.9 Luminescence Quenching ... 10

1.1.10 Collisional quenching ... 10

1.1.11 Static Quenching ... 11

1.1.12 Solvent Relaxation ... 12

1.1.13 Quenching through electron and energy transfer ... 14

1.2 Photophysical properties of cationic metallo-lumophores ... 15

1.2.1 Luminescent Properties of 3rd row transition metals ... 15

1.2.2 Iridium (III) Luminescence ... 16

1.2.3 Osmium (II) Luminescence ... 18

1.2.4 Rhenium (I) luminescence ... 19

1.2.5 Photophysical properties of the uranyl (UO_2^{2+}) ion ... 20

1.3 Organic lumophores ... 24

1.3.1 Triarylimidazole (lophine) ... 24

1.3.2 Chemosensing using the triarylimidazole motif ... 25

1.3.3 Fused imidazo[4,5-*f*]-1,10-phenanthroline complexes ... 26

1.4 Analytical techniques 29
  1.4.1 NMR spectroscopy 29
    1.4.1.1 Instrumentation and conditions 31
  1.4.2 Electronic Absorption Spectroscopy 31
    1.4.2.1 Instrumentation and conditions 32
  1.4.3 IR spectroscopy 32
    1.4.3.1 Instrumentation and conditions 34
  1.4.4 Mass spectrometry 34
    1.4.4.1 Ion sources 34
    1.4.4.2 Electron ionisation (EI) 35
    1.4.4.3 Chemical ionisation (CI) 35
    1.4.4.4 Electrospray ionisation (ESI) 35
    1.4.4.5 Fast atom bombardment 35
    1.4.4.6 Instrumentation and conditions 36
  1.4.5 Small Angle Neutron Scattering (SANS) 36
    1.4.5.1 Instrumentation and conditions 37
  1.4.6 Luminescence instrumentation and conditions 38
  1.4.7 X-ray Diffraction 38
1.5 Aims 38
1.6 References 40

Chapter 2: Synthesis and investigation of luminescent rhenium(I) complexes of substituted imidazole[4,5-*f*]-1,10-phenanthroline derivatives 44
  2.1 Introduction 45
  2.2 Properties and applications of [Re(CO)$_3$(diimine)]$^+$ complexes 45
    2.2.1 Effects of ligand substitution on the Re(CO)$_3$ core 45
    2.2.2 Biological applications of *fac*-[Re(diimine)(CO$_3$)L]$^{0/+}$ complexes 46
    2.2.3 Photoswitchable luminescence of rhenium(I) tricarbonyl diimines 48
    2.2.4 Applications of [Re(CO$_3$)(diimine)]$^+$ complexes as electroluminescent devices 50
    2.2.5 OLED (organic light emitting diode) devices 51
  2.3 Aims 53
  2.4 Results and discussion 54
    2.4.1 Isolated ligands 54
    2.4.2 Ligand synthesis 54
    2.4.3 Characterisation of the ligands 56
    2.4.4 Electronic Absorption Spectroscopy 58

2.5 Coordination chemistry of 21-28 with Re(I) 60
  2.5.1 Characterisation of the complexes 61
  2.5.2 Structural studies 63
  2.5.3 Electronic absorption spectroscopy and luminescent studies 69
2.6 Conclusions 73
2.7 Experimental 74
2.8 Supplementary data 88
2.9 References 90

Chapter 3: Synthesis and characterisation of fluorescent hydroxy and methoxy-substituted imidazole[4,5-f]-1,10-phenanthroline derivatives and their Re(I) carbonyl complexes 91

3.1 Introduction 92
3.2 1,2-dihydroxybenzene derivatives 92
3.3 Optical properties of catechol-containing molecules 93
3.4 Dihydroxy 3,4-dihydroxy-imidado[4,5-*f*][1,10]-phenanthroline complexes for pH monitoring 94
3.5 Luminescent properties of phenanthrene 95
  3.5.1 Phenanthrene-based OLEDs 95
  3.5.2 Metal complexes/sensing 95
3.6 DNA binding ability of dihydroxy 3,4-dihydroxy-imidado[4,5-*f*][1,10]-phenanthroline complexes 96
3.7 Aims 97
3.8 Results and Discussion 98
  3.8.1 List of isolated compounds 98
  3.8.2 Synthesis of the ligands 99
  3.8.3 Characterisation of the ligands 101
  3.8.4 Electronic Absorption Spectroscopy of the ligands 103
  3.8.5 Luminescent properties of the ligands 108
3.9 Coordination chemistry of 44-52 with Re (I) 112
  3.9.1 Characterisation of the complexes 112
  3.9.2 Structural Studies 115
  3.9.3 Electronic Absorption Spectroscopy of the complexes 122
  3.9.4 Luminescence studies 124
3.10 Conclusions 125
3.11 Experimental 127
3.12 References 146

Chapter 4 : Synthesis and characterisation of fluorescent R′-substituted imidazole[4,5-*f*]-1,10-phenanthroline derivatives and their Re(I) carbonyl complexes 148

4.1 Introduction 149

4.2 2,2′:6′,2″-terpyridine (terpy) 149

4.3 2,2′:6′,2″-terpyridine-rhenium coordination chemistry 150

4.4 Triphenylmethane “Trityl” as a bulky substituent 152

4.5 Conformational differences of Azobenzene 153

4.6 Aims 155

4.7 Results and Discussion 156

4.7.1 Synthesis of the ligands 157

4.7.2 Characterisation of the ligands 159

4.7.3 Electronic Absorption Spectroscopy of the ligands 161

4.7.4 Luminescence properties of the ligands 164

4.8 Coordination chemistry of the ligands with Re(I) 168

4.8.1 Characterisation of the complexes 169

4.8.2 Structural Studies 172

4.8.3 Electronic Absorption Spectroscopy of the complexes 176

4.8.4 Luminescence studies of the complexes 178

4.9 Conclusions 179

4.10 Experimental 180

4.11 References 194

Chapter 5 : Synthesis and characterisation of substituted imidazole [4,5-f]-1,10-phenanthroline derived uranyl complexes 195

5.1 Introduction 196

5.1.1 The actinide series 196

5.1.2 The f-orbitals 197

5.1.3 Electronic configuration and oxidation states of the actinides 197

5.1.4 Relativistic effects 199

5.1.5 The lanthanide and actinide contractions 200

5.2 Uranium 201

5.2.1 Background 201

5.3 The uranyl ion 201

5.3.1 Bonding in the uranyl ion 202

5.3.2 Coordination chemistry of the uranyl ion 203
    5.3.2.1 Uranyl complexes with N-donor ligands 203
    5.3.2.2 Uranyl-diimine complexes 206
    5.3.2.3 Uranyl- imidazole[4,5-*f*]-1,10-phenanthroline complexes 209
    5.3.2.4 Coordination chemistry of the uranyl ion with O-donor ligands 212
5.4 Electronic absorption spectra of the uranyl ion 213
5.5 The uranyl emission 214
  5.5.1 Uranyl-centred emission 215
  5.5.2 Ligand centred emission 216
5.6 Effects of substituents on uranyl infrared and raman spectra 217
5.7 Aims 218
5.8 Results and discussion 219
  5.8.1 Synthesis of the complexes 219
  5.8.2 Characterisation of the complexes through ^{1}H NMR spectroscopy 220
  5.8.3 Infrared studies of the complexes 223
  5.8.4 Electronic absorption spectroscopy of the complexes 225
  5.8.5 Luminescence studies of the complexes 227
5.9 Conclusion 234
5.10 Experimental 235
5.11 References 239

Chapter 6: Determining the partitioning of uranyl and trivalent lanthanide complexes in a microemulsion241
6.1 Introduction 242
6.2 Microemulsions 242
6.3 Metallosurfactants 243
6.4 The SDS 4.5T microemulsion system 245
6.5 Triarylimidazoles in microemulsions 248
6.6 Uranyl acetylacetone complexes 250
6.7 Aims 253
6.8 Results and discussion 254
6.9 Microemulsion formulation 254
6.10 Microemulsions containing only aceteylacetonate ligands (U1-U3) 255
  6.10.1 SANS data for U1-U3 255
  6.10.2 Electronic Absorption Spectra of U1-U3 258
  6.10.3 Luminescence Spectra of U1-U3 260

6.11 Microemulsions containing N-donor ligands (U4-U6) 264
  6.11.1 SANS data for U4-U6 264
  6.11.2 Electronic Absorption Spectra of U4-U6 266
  6.11.3 Luminescence Spectra of U4-U6 268
6.12 Microemulsions containing trivalent lanthanides (U7-U10) 270
  6.12.1 SANS data for U7-U10 270
6.13 Conclusions 272
6.14 References 274
6.15 Final conclusions 275

Summary

Reported in this thesis is the investigation of the luminescent and photophysical behaviour of triarylimidazole ligands, also known as “lophine” ligands. A series of Re(I) and U(VI) complexes have been isolated and characterised incorporating these ligands.

Triaryl imidazole ligands were isolated as substituted imidazole [4,5-*f*]-1,10-phenanthroline derivatives. Alterations to the substituents on this motif provided the ability to “tune” the solubility and optical properties of the ligand. Among the substituents incorporated onto the ligand system were extended chromophores, sterically bulky substituents, alkyl groups and substituents containing potential additional coordination sites. All isolated ligands and complexes were fully characterised through numerous spectroscopic techniques, including ^{1}H NMR, ^{13}C NMR, IR and electronic absorption spectroscopies, and further confirmation was obtained through high-resolution mass spectrometry. Crystal structures were obtained for a selection of the rhenium-coordinated imidazole [4,5-*f*]-1,10-phenanthroline derivatives, confirming the molecular structure in each case.

The photophysical behaviour of the rhenium-imidazole [4,5-*f*]-1,10-phenanthroline derivative complexes were investigated, often displaying extended lifetimes of emission as a result of phosphorescence emission from an excited triplet to a ground singlet state. The complexes displayed a significant bathochromic shift in comparison to their respective free ligands, which was attributed to lower energy emission as a result of a metal-to-ligand charge transfer.

Coordination of imidazole [4,5-*f*]-1,10-phenanthroline derivatives to U(VI) resulted in the formation of luminescent complexes. The luminescent properties of these complexes were investigated and owing to their short emission lifetimes were attributed to ligand-centred fluorescence. A significant bathochromic shift was observed for each of the complexes compared to their respective free ligands, which was attributed to the electron withdrawing effect of the uranyl centre.

Small angle neutron scattering (SANS) experiments were also performed on a selection of U(VI) complexes in order to determine the partitioning of uranyl complexes in a microemulsion as a potential method for uranyl detection.

DECLARATION

This work has not been submitted in substance for any other degree or award at this or any other university or place of learning, nor is being submitted concurrently in candidature for any degree or other award.

Signed ………………………………………… (candidate) Date …………………………

STATEMENT 1

This thesis is being submitted in partial fulfilment of the requirements for the degree of PhD.

Signed ………………………………………… (candidate) Date …………………………

STATEMENT 2

This thesis is the result of my own independent work/investigation, except where otherwise stated.

Other sources are acknowledged by explicit references. The views expressed are my own.

Signed ………………………………………… (candidate) Date …………………………

STATEMENT 3

I hereby give consent for my thesis, if accepted, to be available for photocopying and for inter-library loan, and for the title and summary to be made available to outside organisations.

Signed ………………………………………… (candidate) Date …………………………

STATEMENT 4: PREVIOUSLY APPROVED BAR ON ACCESS

I hereby give consent for my thesis, if accepted, to be available for photocopying and for inter-library loans **after expiry of a bar on access previously approved by the Academic Standards & Quality Committee.**

Signed ………………………………………… (candidate) Date …………………………

Acknowlegements

I would like to thank both my supervisors Dr. Ian Fallis and Dr. Simon Pope for their guidance, encouragement and great patience during the course of my PhD. Both were extremely helpful throughout the entirety of my studies, always ready to make time for my queries.

I'd also like to extend my thanks to those I have worked with during the course of my PhD, in particular Dr. Ian Morgan, Dr. Stephen Hughes and Dr. Andrew Hallett for putting up with my many questions. It was a pleasure to work with them in the lab and I have had great fun working with everyone in labs 1.124 and 2.91.

I am very grateful for the hard work of all the technical staff at Cardiff University who were always prepared to help whenever I needed it.

I would like to thank KESS (Knowledge Economy Skills Scholarship) fund and Magnox North for their financial support which was greatly appreciated.

I would also like to thank my family and in particular my parents for their encouragement and support not only during my PhD but during my entire university studies. I am proud to have submitted a PhD in Chemistry just like mam, although it didn't take me seven years to complete like hers! Also I would like to commend dad on his patience when forced to listen to us talk about chemistry at the dinner table.

Finally I would like to say a huge thank you to Rebecca Sherlock for sticking with me during my PhD. Without her constant love and support and I would never have gotten to this stage and I am truly grateful.

ESF
Llywodraeth Cymru
Welsh Government
Ewrop & Chymru: Buddsoddi yn eich dyfodol
Cronfa Gymdeithasol Ewrop
Europe & Wales: Investing in your future
European Social Fund

Magnox North

List of abbreviations and symbols

Å	Angstroms
Acac	Acetylacetone
a.u.	Arbitrary Units
Bipy	2,2′-bipyridine
BSA	Bovine Serum Albumin
BTEC	1,2,4,5-benzenetetracarboxylic acid
BuOH	Butan-1-ol
CI	Chemical Ionisation
CMC	Critical Micelle Concentration
CT	Charge Transfer
ct	Calf Thymus
CTAB	Cetyltrimethylammonium bromide
DCM	Dichloromethane
DMF	Dimethylformamide
DMSO	Dimethylsulfoxide
DNA	Deoxyribosenucleic Acid
dpe	1,2-di-(4-pyridyl)ethylene
EDA	Electron Donor-Acceptor
EI	Electron Ionisation
EL	Electroluminescence
ES	Electro-spray
FAB	Fast Atom Bombardment
Hacac	Acetylacetone
Hcy	Homocysteine

HFA	Hexafluoroacetylacetone
HMe_6A	Hexamethylacetylacetone
HMPA	Hexamethyl-phosphoric triamide
HOMO	Highest Occupied Molecular Orbital
HRMS	High-resolution mass spectrometry
HSA	Human Serum Albumin
ICT	Intramolecular Charge-Transfer
IL	Intra-ligand
IR	Infra-red
LMCT	Ligand to Metal Charge Transfer
LUMO	Lowest Unoccupied Molecular Orbital
MeOH	Methanol
m_l	Magnetic Quantum Number
m_s	Electron spin quantum number
MLCT	Metal to Ligand Charge Transfer
NAA	Naphthalene Acetic Acid
NMR	Nuclear Magnetic Resonance
ODHIP	3,4-dihydroxyl-imidazo[4,5-*f*][1,10]phenanthroline
OLED	Organic-Light Emitting Diode
OTf	Triflate
PCCP	Poly(2,6-(4,4-bis(2-ethylhexyl)-4H-cyclopenta[*def*]phenanthrene
PDA	1,10-phenanthroline-2,9-dicarboxylic acid
PET	Photo-induced Electron Transfer
PFs	Polyfluorenes
Ph	Phenyl
Phen	1,10-phenanthroline
PL	Photoluminescence

ppy	2-phenyl pyridine
py	Pyridine
py-3-mal	3-maleimidopyridine
py-3-NCS	3-isothiocyanatopyridine
QY	Quantum Yield
RET	Resonance Energy Transfer
rf	Radio Frequency
SANS	Small-Angle Neutron Scattering
SDS	Sodium Dodecyl Sulphate
^{t}Bu	Tertiary-butyl
Terpy	2,2′:6′,2″-terpyridine
THF	Tetrahyrdofuran
Trityl	Triphenylmethane
UV	Ultra-Violet

Chapter 1: Introduction

1.1 Luminescence spectroscopy

Luminescence spectroscopy is the study of electronic transitions in molecules, specifically the study of the radiative decay processes which occur in the relaxation of an excited electron to the ground state through fluorescence or phosphorescence. Transitions in which there is a change from one electronic state to another involve much higher energies than changes in vibrational and rotational energy levels. The result of this is that electronic transitions generally occur in the ultraviolet or visible regions of the spectrum.

Figure 1: Luminescent solutions. [1]

Luminescence occurs from the excitation of an electron from an ambient energy level to a higher energy level, defined as an excited state. After an electron is excited there are a number of ways that it can discard its excitation energy. The most common way is non-radiative decay, in which energy is translated into vibration, rotation and translation of the nearby molecules. Energy can also be translated into "thermal motion" of the environment, creating heat.[2] However, when these processes do not occur the exciton can lose its energy through radiative processes, namely fluorescence and phosphorescence. A radiative process is defined as a process in which a molecule discards its excitation energy as a photon. Shown in Figure 2 is a simplified Jablonski diagram, which illustrates the processes that occur leading to fluorescence.

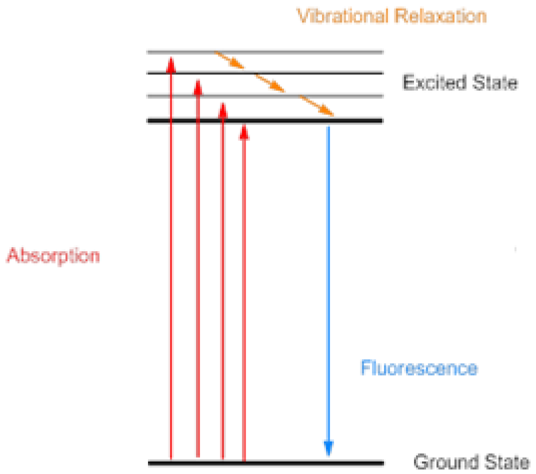

Figure 2: Jablonski diagram depicting processes that occur to allow luminescence

1.1.1 Quantum Numbers, Russell-Saunders coupling and term symbols

In order to fully understand the processes that lead to luminescence, the quantum numbers of electrons and selection rules must be taken into account. Electrons possess a set of quantum numbers, for which no electrons can possess the exact same quantum numbers as another electron (Pauli Exclusion Principle). The quantum numbers are:

n = principle quantum number

l = angular momentum

m_l = magnetic quantum number

m_s = electron spin

Every electron has an inherent spin (m_s), which can be of one of two values +1/2 or -1/2. No two electrons in the same orbital can possess the same spin as they would then possess the same quantum numbers. Spin-spin coupling gives the resultant spin quantum number for a system of electrons, S, which is calculated by adding all individual electronic spins (m_s) together. The orbit-orbit coupling is defined by L, which is the total orbital angular momentum quantum number and defines the energy state for a system of electrons. This is described alphabetically, not alphanumerically as shown in Table 1.

Total Orbital momentum	**L**
0	S
1	P
2	D
3	F
4	G
5	H

Table 1: Orbital momentum values

Multiplicity is a quantification of the amount of unpaired spin in a molecule. The multiplicity of a system of electrons can be derived from the amount of unpaired electrons the molecule possesses using Hund’s 2S+1 rule (where S = combined total of electron spins). For example, sodium has one unpaired electron. Since the spin of an electron is ± ½ we can choose one of the spins, say +1/2 to enter into the equation which gives a value of 2 corresponding to a doublet state.

Figure 3 depicts some examples of the multiplicity of electronic configurations.

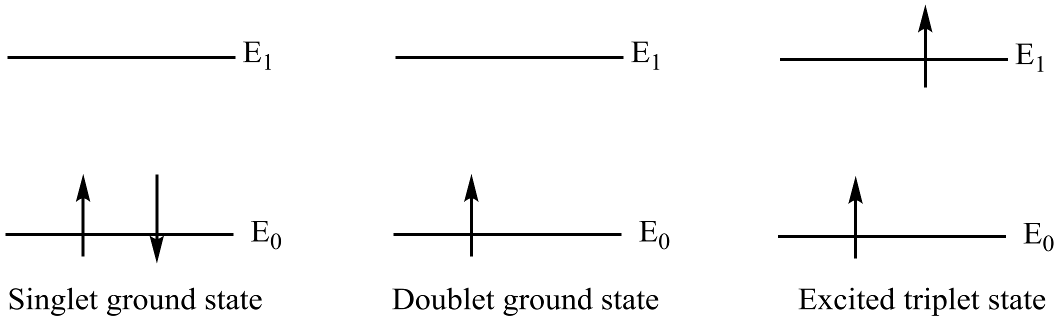

Figure 3: Electronic configurations and their multiplicity

Spin-orbit coupling is usually very weak for light elements and is as a result of coupling between the spin and orbital momenta of an electron. This is notified in the Russell-Saunders coupling scheme by the value J, which has a value of the vector of L+S.

The Russell-Saunders term symbol is an abbreviated description of the multiplicity, total orbital angular momentum and the spin-orbit coupling in an electronic system using the notation:

$$^{2S+1}L_J$$

For example the ground state term symbol for H ($1s^1$) is $^2S_{1/2}$. The spin-orbit value J is often left out of this notification as it is inconsequential in atoms of a small mass ($z < 30$).

1.1.2 *J-J* coupling scheme

If the mass of an atom exceeds $z = 30$ then the Russell-Saunders coupling model is no longer valid as it assumes that spin-spin coupling > orbit-orbit coupling > spin-orbit coupling and that spin-orbit coupling can be generally ignored. Spin-orbit coupling becomes more significant, however with atoms of increasing mass. This is due to the larger spaces between electrons and the diminishing electrostatic interactions between them in comparison with the interaction for each electron between its spin motion and its orbital motion. In this instance a new coupling scheme must be employed, i.e. *j-j* coupling.

In *j-j* coupling the individual spin and orbital momenta are coupled into individual j values, and these values are then combined to give a total value J. For instance a particle with p^2 configuration would have spin-orbital interaction from both electrons; therefore they must be calculated individually to provide angular momenta j, before being combined to give a J value. The L values for these electrons will be 1 and 0 (Table 2), while the S value for both will be ½.

L Values	1	0	-1
Electron	↑	↑	

Table 2: Possible L values for a p^2 atom

Since $j = L + S$ the values of j = 1/2 and 3/2. These values then couple together to provide J values where for example if:

$j_1 = 3/2$ and $j_2 = 3/2$ then J = 3,2,1,0.

If:

$j_1 = 1/2$ and $j_2 = 3/2$ then J = 2,1 and so on.

When discussing the energies of heavy atoms it is more accurate to refer to *j-j* coupling in this manner rather than R-S coupling. The labels of R-S coupling are still sometimes used to describe heavy atom configurations as an approximation.

1.1.3 Selection Rules

Some electronic transitions are more likely to occur than others (i.e. are subject to *selection rules*). The selection rules that apply for electronic transitions in light ($z < 30$) transition metals are:

1) $\Delta S = 0$

2) $\Delta l = \pm 1$

3) $\Delta L = 0, \pm 1$

4) $\Delta J = 0, \pm 1$ (although $J = 0 \rightarrow J = 0$ is forbidden)

The first rule is the spin rule, which stipulates that upon promotion of an electron there cannot be any overall change in spin. This means that transitions that involve a change in multiplicity (S) are disallowed so formally transition may only occur between identical multiplicities (e.g. singlet-singlet or triplet-triplet transitions). The second rule, also known as the Laporte rule, states that for a centrosymmetric environment there cannot be transition between orbitals of a similar symmetry, (*gerade* or *ungerade*). In other words, *s→s, p→p, d→d* and *f→f* transitions are forbidden. Even though both these transitions are forbidden, they can still occur through relaxation of the selection rules. This can happen through many ways, for example, spin-orbit coupling, vibronic coupling, deviations from pure centrosymmetric geometry and orbital mixing between *d* orbitals and π-donor and π-acceptor ligands so the transitions are no longer purely *d→d*. Despite these allowances, *d-d* transitions are still weak. For example the Laporte partially allowed (due to *d-p* mixing) $[CoCl_4]^{2-}$ has ε values of 50-150 $M^{-1}cm^{-1}$. Contrastingly, the Laporte allowed transitions of $[TiCl_6]^{2-}$ or MnO_4^- (charge transfer transitions) have ε values in the region of 1000-10^6 $M^{-1}cm^{-1}$.[3] The change in total quantum number, n, is not restricted in electronic transitions.

Electronic transitions in heavier atoms are more likely to undergo formally "forbidden" transition as the spin-orbit coupling will be sufficiently strong enough to bypass the Laporte rule and the spin rule.

1.1.4 Fluorescence

The diagram depicted in Figure 4 shows the processes that occur leading to fluorescence.

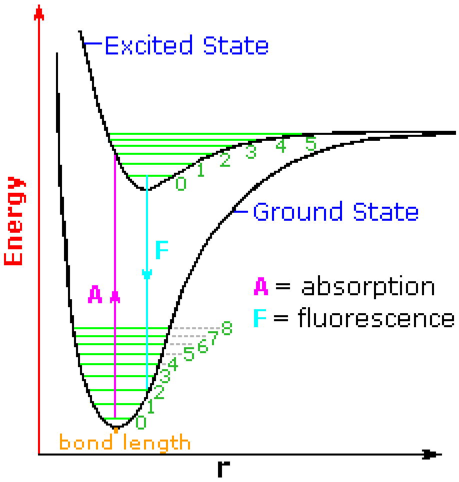

Figure 4: Energy level diagram depicting fluorescence.[4]

Firstly, the electron is promoted from a ground state (HOMO-Highest Occupied Molecular Orbital) to an excited state, retaining its spin. The electron then loses some of its energy through vibrational relaxation as it migrates to the lowest vibrational energy level of the excited state (LUMO-Lowest Unoccupied Molecular Orbital). If the solvent cannot absorb the quanta of energy that the electron has remaining (known as quenching-to be described in section 1.1.9) the electron relaxes down to the ground state with the release of energy in the form of a photon. This release of the photon is known as fluorescence, and it usually takes a very short time (nano-seconds), as it does not break any selection rules.

1.1.5 Phosphorescence

The process of phosphorescence occurs when there is an excited triplet state of a similar energy to the excited singlet state (Figure 5).

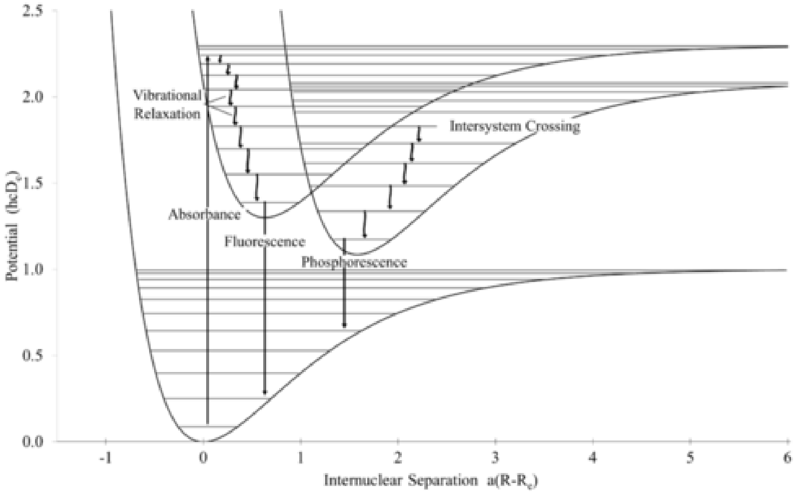

Figure 5: Energy level diagram depicting phosphorescence.[5]

At the point where the two potential energy curves intersect there is potential for inter-system crossing (ISC), where the excited electron is changed from a singlet to a triplet state (from ↑↓ to ↑↑). This is allowed to occur due to the presence of spin-orbit coupling. Heavier atoms will have a larger spin-orbit coupling and so this process is more likely to happen with third row metals. After ISC has occurred, the electron then relaxes down the vibrational energy levels of the excited triplet state to the lowest vibrational state. Once it has reached this point it is forbidden by the selection rules to relax to the singlet ground state as a change of spin state is disallowed (spin-forbidden). However, the transition is not completely forbidden due to spin-orbit coupling, and the molecule is therefore allowed to emit weakly. The result of this is a long-lived emission which can vary greatly, often to milliseconds or even seconds. Figure 6 shows a simplified Jablonski diagram comparing the differences between fluorescence and phosphorescence.

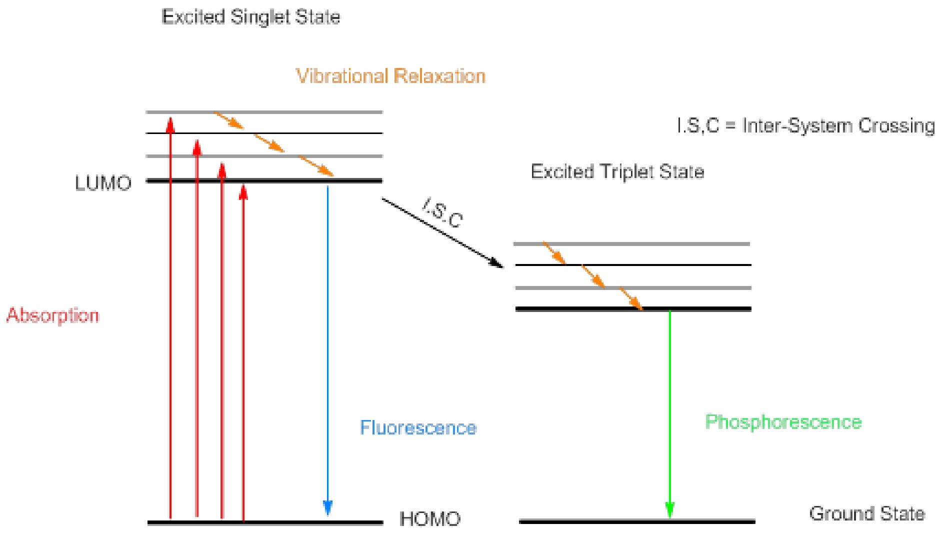

Figure 6: Simplified Jablonski diagram comparing fluorescence and phosphorescence

1.1.6 The Franck-Condon principle

The Franck-Condon principle states that the mass of a nucleus is so large compared to the mass of an electron that any movement of electrons can be considered to take place in a completely stationary framework. That is, during an electronic transition, the nuclear configuration of the molecule experiences no significant change. The result of this with respect to luminescence is that all transitions are considered to take place *vertically* on an energy level diagram (as seen in Figure 4 and Figure 5), and that the emission of a photon is as a result of a relaxation of an electron from the lowest possible excited state to the ground state energy level (although not necessarily the lowest vibrational level of that electronic level.)

1.1.7 Stokes' Shift

The wavelength emitted by a molecule during the process of luminescence is almost invariably longer than that of the initial excitation wavelength (this is only untrue for atoms in the vapour phase).[6] Put in other terms, there is a reduction in energy between the excitation of an electron and its subsequent relaxation. This phenomenon was first observed by G. G. Stokes in 1852, and is a result of both the energy lost during rapid decay to the lowest excited state energy level and the relaxation to an excited vibrational state of the electronic ground state.[7] A Stokes' shift is easily calculated by measuring the difference between the excitation maximum and emission maximum of a molecule (Figure 7).

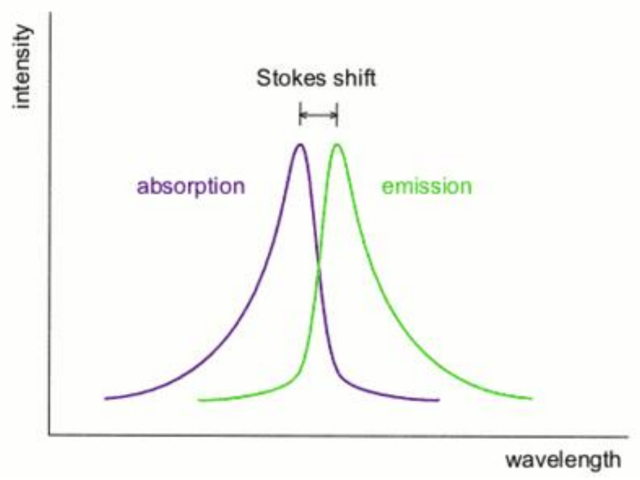

Figure 7: Stokes' shift.[8]

1.1.8 Quantum Yields (ϕ) and lifetimes (τ)

Quantum yield is defined as the ratio of the number of photons emitted to the number absorbed. If there were 100% conversion of absorbed to emitted photons then the value of the quantum yield would be unity. The quantum yield is calculated by the equation;

$$\mathrm{QY} = \frac{k_r}{k_r + k_{nr}}$$

Equation 1: Calculation of quantum yield where QY = quantum yield (ϕ), k_{r} = emissive rate of fluorophore and k_{nr} = rate of radiationless decay.

Luminescence lifetime is defined as the average amount of time that a molecule spends in the excited state. For phosphorescence, the amount of time spent in the excited state is considerably longer than that of fluorescence, and lifetimes are therefore generally long (ms to s). The lifetime of an emission (τ) can be expressed as:

$$\tau = \frac{1}{k_r + k_{nr}}$$

Equation 2: Expression for lifetime emission (τ)

The natural or intrinsic lifetime is defined as the lifetime of a lumophore in the absence of non-radiative processes and is expressed as:

$$\tau_n = \frac{1}{k_r}$$

Equation 3: Expression for natural lifetime (τ_n)

The natural lifetime can be calculated from the quantum yield and the measured lifetime, τ.

$$\tau_n = \frac{\tau}{QY}$$

Equation 4: Expression for natural lifetime (τ_n)

1.1.9 Luminescence Quenching

Quenching is the term given to any process which decreases the fluorescence intensity of any given substance, and it can take many forms such as reaction of the excited state, collisional quenching, energy transfer and complex formation.[6]

1.1.10 Collisional quenching

Collisional quenching is the process of lumophore deactivation through contact with another molecule (quencher) in solution, which can facilitate non-radiative transitions to the ground state. A wide variety of molecules can behave as quenchers, including molecular oxygen, halogens, amines and electron deficient molecules. The Stern-Volmer equation which relates the quencher concentration to the observed luminescence intensity is given by:

$$\frac{I}{I_0} = 1 + K_{sv}[Q]$$

Equation 5: Stern-Volmer equation

Where I and I_0 are the luminescence intensities in the presence and absence, respectively, of quencher, K_{SV} is the Stern-Volmer quenching constant and [Q] is the quencher concentration. In the case of purely collisional quenching the following equation also applies:

$$\frac{I_0}{I} = \frac{\tau_0}{\tau}$$

Equation 6: Relation between luminescence intensity and lifetimes

One of the most common quenchers of luminescence is molecular oxygen which readily quenches excited triplet states and forms an excited singlet oxygen.[9-11] For this reason, to get a true value of the quantum yield of a molecule, molecular oxygen must be removed from a sample (degassed) or the sample is run as a “glass” at extremely low temperatures which restricts molecular collisions.

Equation 5 and Equation 6 indicate that the lifetime of the species is dependent on the concentration of the quencher. Therefore analysing the variation of the lifetime of the species with varying quencher concentration should give an indication of the presence or absence of collisional quenchers. As collisional quenching takes place in the excited state the concentration of quencher has no impact on the absorption characteristics of the fluorescent substance.

1.1.11 Static Quenching

Lumophores can form non-emissive complexes with another molecule. If the ground state is non-fluorescent in the new complex then the molecule behaves as a quencher and the lumophore is said to be “statically quenched”. In this instance the lifetime of the emission is not affected, only the emission intensity, as the quencher will effectively remove lumophores from the solution. One example of a static quenchers is Cu(II). The dependence of the luminescence intensity upon quencher concentration is derived by consideration of the association constant for complex formation, given by:

$$K_a = \frac{[F-Q]}{[F][Q]}$$

Equation 7: Dependence of luminescence intensity upon quencher concentrations

Where K_a is the association constant, [F-Q] is the concentration of the complex and [F] is the concentration of the uncomplexed lumophore. Static quenching can be differentiated experimentally form collisional quenching by analysis of the lifetimes and absorption spectra. The lifetimes of the statically quenched lumophores will not vary from the lifetimes of the lumophore in the absence of quencher, in contrast to collisional quenchers. The absorption spectra of the statically quenched lumophores will be slightly perturbed as static quenchers affect the ground state of the lumophores, whereas the absorption spectra of lumophores is not affected by collisional quenchers.

1.1.12 Solvent Relaxation

Lumophore-solvent interactions and rotational diffusion are dynamic processes that can lead to quenching. Usually, when an electron is promoted to the excited state it possesses a larger dipole moment than in the ground state. Over the duration of the excited state lifetime, solvent reorganises around the excited state dipole and stabilises the energy level (i.e. lowers the energy of the excited state) and causes a bathochromic shift in emission (lower energy emission). Solvents of varying polarity have different effects on the stabilisation of the excited states.[6] For example, non-polar solvents such as hexane do not possess a dipole moment, and as such do not have dipoles to reorient around the excited state of the lumophore. Therefore in hexane no bathochromic shift of emission is expected. Conversely, polar solvents such as methanol will reorient around the excited state which will reduce the energy of the emission substantially which results in a larger Stokes' shift. The sensitivity of Stokes' shift to solvent polarity is the reason why luminescence is often used to determine the polarity of the environment surrounding the lumophore.

For example, protein fluorescence originates from an indole ring of the tryptophan residues. The emission wavelength of indole in cyclohexane compared to water varies from 297 nm to 347 nm respectively.[12] More recently the effect of increasing solvent polarity has been investigated for a known dye-indoline D149 (**1**) (Figure 8).[13]

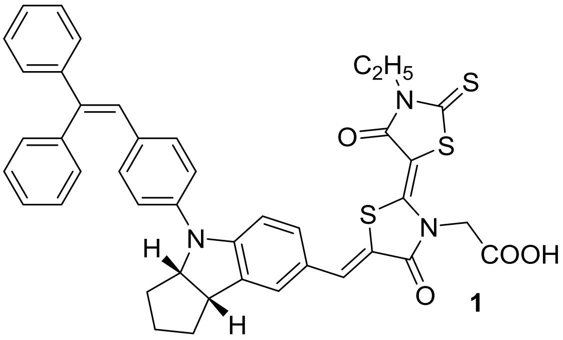

1

Figure 8: Molecular structure of indoline D149 (**1**).[13]

It was found that increasing the solvent polarity led to an increase in Stokes' shift, for example 2780 cm^{-1} for chloroform compared to 4050 cm^{-1} in acetonitrile (Figure 9). It was noted that there was little difference in the absorption spectra.

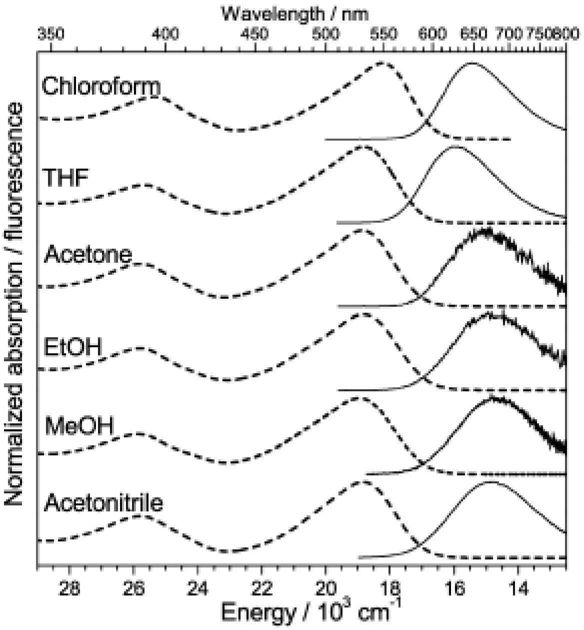

Figure 9: Electronic absorption (dashed lines) and emission spectra (unbroken lines) of **1** in various solvents.[13]

The observed Stokes' shift in the molecule indicated that the dipole moment of **1** increased upon photoexcitation, and the lower in emission energy was a result of reorganisation of the polar solvents around the excited state resulting in a stabilised energy level.

1.1.13 Quenching through electron and energy transfer

Electron or energy transfer is a quenching mechanism which results from the transfer of energy from one molecule (a donor) to another (an acceptor). Resonance energy transfer (RET) occurs when the emission spectrum of a lumophore overlaps with the absorption spectrum of another molecule, which may or may not be luminescent. If the acceptor molecule is not luminescent then the process can be considered to be a dynamic quenching process, where the excited state of the donor non-radiatively transfers energy to the acceptor. There are three mechanisms for the charge transfer from host to dopant molecules, Förster, Dexter and charge-trapping.[14] Förster transfer was first described in 1959 as a long-range (~40 – 100 Å) coulombic interaction, involving dipole-dipole coupling of the donor (D) and acceptor (A) states.[15] Due to the need for an allowed transition in the acceptor, this mechanism only transfers energy to the singlet state of the acceptor molecule.

$$D^{*} + {}^{1}A \rightarrow {}^{1}D + {}^{1}A^{*}$$

$${}^{3}D^{*} + {}^{1}A \rightarrow {}^{1}D + {}^{1}A^{*}$$

Equation 8: Förster energy transfer

Förster energy transfer from a ground-state triplet to an excited singlet state can also occur, as the slower rate of energy transfer is compensated by the long lifetime of the triplet donor electron, resulting in an overall efficient process. The extent of efficiency of RET is highly dependent on the distances between donor and acceptor and also the extent of spectral overlap, where:

$$k_t(r) = \frac{1\left({}^{R_0}/_{r}\right)^6}{\tau_D}$$

Equation 9: Efficiency of a Förster transition

Where k_T (r) is the rate of energy transfer, r is the distance between donor and acceptor, R_0 the Förster distance (at which transfer and spontaneous decay of the excited state are equally probable). As can be seen in Equation 9 the rate transfer is inversely proportional to the sixth power of the distance between the donor and acceptor, meaning small changes in distance can greatly affect the efficiency of the process.

Dexter energy transfers occur of a much shorter range (≈ 10 Å), by diffusion from donor to acceptor sites via intermolecular electron exchange.[16] Spin must be conserved in a Dexter transition, and as such only singlet-singlet or triplet-triplet transfer is allowed. (Equation 10)

$$^1D^* + {}^1A \rightarrow {}^1D + {}^1A^*$$

$$^3D^* + {}^1A \rightarrow {}^1D + {}^3A^*$$

Equation 10: Dexter energy transfer

The rate of Dexter transfer decreases with increasing donor-acceptor distance. In this instance a third energy transfer process can occur- “charge trapping”- which may compete for triplet-triplet transfer. Charge trapping occurs when a guest molecule traps the charge and generates an exciton by recombination with an opposite charge on a neighbouring molecule.[17]

1.2 Photophysical properties of cationic metallo-lumophores

1.2.1 Luminescent Properties of 3rd row transition metals

This thesis will involve the investigation of the photophysics of heavy metal complexes, and so a brief overview of the luminescent properties of 3rd row transition metals will now be given. Luminescent third row transition metals have been studied extensively over the last 30 years, and more recently particular interest has looked at the application of such complexes in the field of biological imaging and the development of organic light emitting dioides (OLEDs).[18-20] Much of this interest stems from the ability of third row transition metals to behave as “triplet harvesters”, efficiently forming excited triplet states which result in long-lived phosphorescent emission. Their ability to do so despite breaking the spin rule (as described in section 1.1.3) lies in the large spin-orbit coupling contribution found in heavier atoms. The most common third row metals in this context are Ir(III), Os(II) and Re(I), all three ions having d^6 configurations; an in depth analysis of the potential origin of phosphorescence in d^6 complexes have been undertaken by Schmehl et al.[21] The review noted that phosphorescence observed in d^6 complexes were not necessarily the result of ^{3}MLCT, but could also be a result of triplet intra-ligand ^{3}IL emission (Figure 10). The observed steady state emission arises exclusively from the lowest energy state in the triplet manifold.

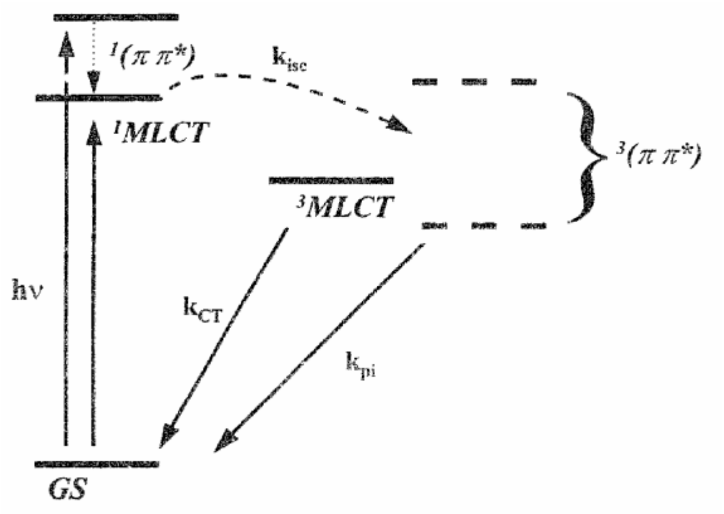

Figure 10: Jablonski diagram showing potential excited triplet energy levels.[21]

Emission resulting from a ^{3}MLCT or a ^{3}IL origin both exhibit long lifetimes (> 100 ns), however they can be differentiated as ^{3}MLCT emission is often broad and featureless with a sensitivity to solvent polarity, while ^{3}IL emission often exhibits extensive vibrational structure.

1.2.2 Iridium (III) Luminescence

Iridium (III) complexes are used extensively in biological imaging and development of OLEDs.[19,20,22] Its ground state electronic configuration is d^6 (low spin) and therefore it is in the singlet ground state. Upon excitation, an electron from the ground state can undergo MLCT to a chelating ligand, which is then transformed into the excited triplet state through inter system crossing (ISC). Loss of this excitation energy takes place through long-lived phosphorescence.

A chemosensor was reported in 2007 for homocysteine based on the iridium complex [Ir(pba)$_2$(acac)] (**2a**) where (Hpba = 4-(2-pyridyl)-benzaldehyde; acac = acetylacetone), and was compared to the non-aldehyde containing 2-phenyl pyridine (ppy) (**2b**) (Figure 11).[19]

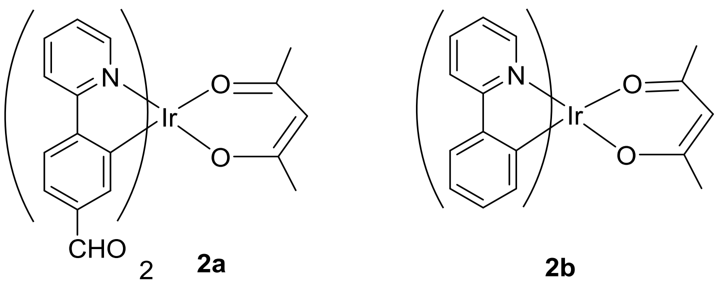

2a **2b**

Figure 11: Molecular structures of [Ir(pba)$_2$(acac)] (**2a**) (left) and [Ir(ppy)$_2$(acac)] (**2b**) (right)

The electronic absorbance spectra and luminescence spectra of the two complexes were compared (Figure 12). The electronic absorption spectrum of [Ir(pba)$_2$(acac)] exhibited high energy absorption bands at 280-350 nm with high molar absorbtivity values ($\varepsilon = 10^4\ M^{-1}cm^{-1}$) and weaker absorption bands at 355-550 nm ($\varepsilon = 10^3\ M^{-1}cm^{-1}$) which were attributed to intraligand $\pi \rightarrow \pi^*$ and the spin allowed ^{1}MLCT (dπ(Ir)-π*(pba$^-$)) transitions, respectively.

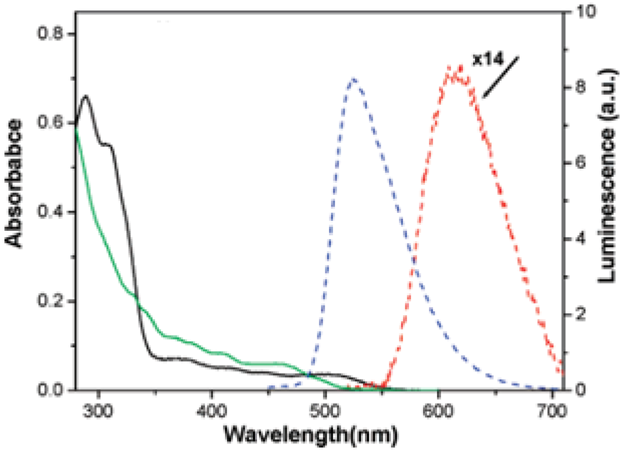

Figure 12: Electronic absorption spectra (green and black lines) and emission spectra (blue and red lines) of **2b** and **2a** respectively.[19]

The quantum yield (Φ) for [Ir(pba)$_2$(acac)] was low (~0.003) and the lifetime of the observed emission at 615 nm was measured as 106 ns, which confirmed that the emission was phosphorescence originating from the ^{3}MLCT state. Comparison of the electronic properties of [Ir(pba)$_2$(acac)] with [Ir(pba)$_2$(ppy)] indicated that the inclusion of the aldehyde reduced the quantum yield of emission (0.003 compared to 0.032), and caused a red-shift of the emission peak (λ_{em} = 615 nm compared to 525 nm). No explanation for this was provided in the literature other than it being noted that the inclusion of an electron-withdrawing aldehyde group may change the photophysical properties of the complex.

Addition of homocysteine (Hcy) to this complex resulted in a 90 nm blue-shift of emission from λ_{em} = 615 nm to 525 nm. The change in emission colour was visible to the naked eye with the originally deep red coloured [Ir(pba)$_2$(acac)] turning a light green. This proved the sensitivity of these systems to small changes that can affect the electronic properties of molecules.

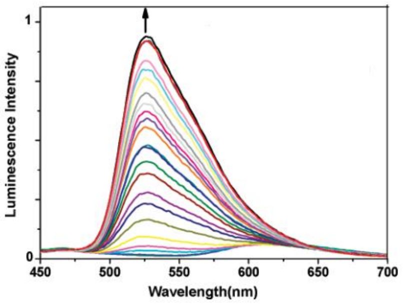

Figure 13: Emission of **2a** with increasing amounts of Hcy. [19]

1.2.3 Osmium (II) Luminescence

Osmium has enjoyed less attention in the field of light energy conservation processes.[23] Although Os(II) and Ru(II) share similar ground-state redox properties, Ru is preferable for study as it has a much longer excited state lifetimes compared to Os. This due to the fact that spin-orbit coupling is much greater in the heavier Os atom and as a result relaxations form an excited triplet state to a singlet ground state are not as forbidden as for Ru. It was reported in 1980 by Martin and Nguyen that the lifetimes of Os(II) MLCT excited states can be enhanced remarkably by replacing polypyridyl ligands with stronger π acceptors such as acetonitrile or alkylarylphosphines.[23]

Table 3 shows the emission data for a series of Os(II) complexes, incorporating bipy, phenanthroline, and mixtures with acetonitrile and alkylarylphosphines.

Complex	Complex number	λ_{max}(em) / nm	λ_{max}(abs) / nm	Emission lifetime τ / μs
$(bipy)_2Os^{2+}$	**3a**	723	640	0.02
$(bipy)_2Os(CH_3CN)_2^{2+}$	**3b**	673	555	0.07
$(bipy)_2Os(Ph_2PCH_2PPh_3)^{2+}$	**3c**	622	475	0.3
$(bipy)_2Os(Ph_2PCH{=}CHPPH_2)^{2+}$	**3d**	609	466	0.5
$(phen)_2Os^{2+}$	**3e**	690	650	0.08
$(phen)_2Os(Me_2PhP)_2^{2+}$	**3f**	661	603	0.39
$(phen)_2Os(Ph_2PCH_2PPh_3)^{2+}$	**3g**	610	500	1.13
$(phen)_2Os(Ph_2PCH{=}CHPPH_2)^{2+}$	**3h**	596	455	1.84

Table 3: Photophysical data for Os(II) complexes

The processes that lead to emission are similar to those described in section 1.2.1 (i.e. phosphorescent emission from an excited ^{3}MLCT state). The data indicated that inclusion of acetonitrile or alkylarylphosphines had two effects on the emission. Firstly the emission maxima blue shifted with the addition of stronger π-acceptors (by 100 nm in some cases), and also the lifetimes of the emission drastically increased as a result (from 0.08 μs for $[Os(phen)_3]^{2+}$ compared to 1.84 μs for $[Os(phen)_2(Ph_2\ PCH{=}CHPPh_2)]^{2+}$. This demonstrated that small chemical changes to Os(II) could result in large systemic variations in excited state energies and lifetimes.

Comparison of the emission spectrum of $[Os(phen)_3]^{2+}$ and that of its iridium analogue in the $[Ir(phen)_3]^{3+}$ show that the energy gap between the triplet excited state and singlet ground state of $[Ir(phen)_3]^{3+}$ is much larger than that of $[Os(phen)_3]^{2+}$. $[Ir(phen)_3]^{3+}$ has λ_{max}^{em} = 562 nm in 4:1 MeOH/H_2O, while $[Os(phen)_3]^{2+}$ has a λ_{max}^{em} = 690 nm. [24] Luminescence in Os(II) complexes are often weak compared to Re(I) and Ir(III) complexes as the gap between the ground state and the excited ^{3}MLCT is small. The *energy gap law* states that the k_{nr} increases with lower energy gaps resulting in weaker emission.

1.2.4 Rhenium (I) luminescence

Rhenium (I) tricarbonyl complexes have been extensively studies as typically they are good MLCT emitters, which give broad emission bands dependent on the ligands incorporated into the complex.[25] The seminal work of Wrighton and co-workers described the nature of the lowest excited state in tricarbonylchloro-1,10-phenanthrolinerhenium(I) complexes.[26] A series of *fac*-[Re(X)(CO$_3$)Cl] complexes were isolated, where X was primarily 1,10-phenanthroline or 2,2′-biquinoline derivatives. It was found that and absorbance band found in the low energy part of the electronic absorption spectra for each complex could be characterised as an Re→π^* (X) charge transfer (CT). A lower energy absorption band was observed for the 2,2′-biquinoline analogue, which was to be expected as the intraligand $\pi \rightarrow \pi^*$ energy absorption is lower for 2,2′-biquinoline, which results in a lower Re(π)→π^* absorption. Incorporation of substituents on the 1,10-phenanthroline moiety resulted in lower energy absorptions for the more electron withdrawing substituents, indicating that the X ligands were involved in the absorption, and again supporting the Re(dπ)→π^* (X) CT assignment. The relatively long emission lifetimes (10^{-6} s at 298K) of these complexes were consistent with other heavy metal complexes where spin forbidden emission occurs due to ^{3}MLCT (metal to ligand charge transfer) character, and the deactivation from a lower energy excited triplet state results in a lower energy orange-red emission.

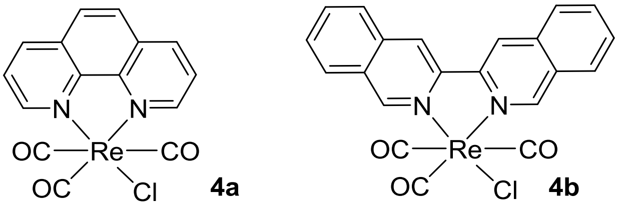

4a **4b**

Figure 14: Re(I) complexes explored by Wrighton in 1974

Re(I) is a d^6 metal and as such its *d* orbitals are split into two distinct energy levels (t_{2g} and e_g*) in the presence of ligands. The lower energy emission observed in these complexes is due to a low energy gap in between the *d* orbitals of the metal and the acceptor π* orbital of the ligand. The photophysical properties of the metal to ligand charge transfer have been studied for complexes of the type [Re(4,4′-X$_2$-bipy)(CO)$_3$Cl] (**5**) (Figure 15) where X = NH$_2$, NEt$_2$, NHCOCH$_3$, OCH$_3$, CH$_3$, H, Ph, Cl, CO$_2$,Et and NO$_2$..[27]

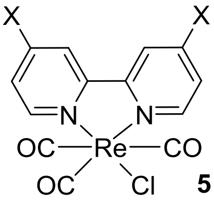

5

Figure 15: Molecular structure of [Re(4,4′-X_2-bipy)$(CO)_3$Cl]

It was observed that as the substituents X were varied from electron donating to electron withdrawing, both the maximum in the MLCT absorption band and the emission energy shift to a lower energy (Figure 16). This was attributed to the acceptor-ability of the π^* being enhanced with the increasing electron withdrawing character of X. This effect was transmitted via backbonding from the π^* orbital to the *d*(π) orbital of the meal resulting in "orbital mixing". This effect is reduced by the presence of the C-O groups, as the influence of the backbonding from the (C-O)→*d*(π) reduces $d\pi$-π^* mixing and maintains a relatively large energy gap between the *d*(π) orbitals and the bipy(π^*) orbitals . Figure 16 displays the absorption and emission profiles observed, showing decrease in emission energy with the incorporation of increasingly electron withdrawing substituents.

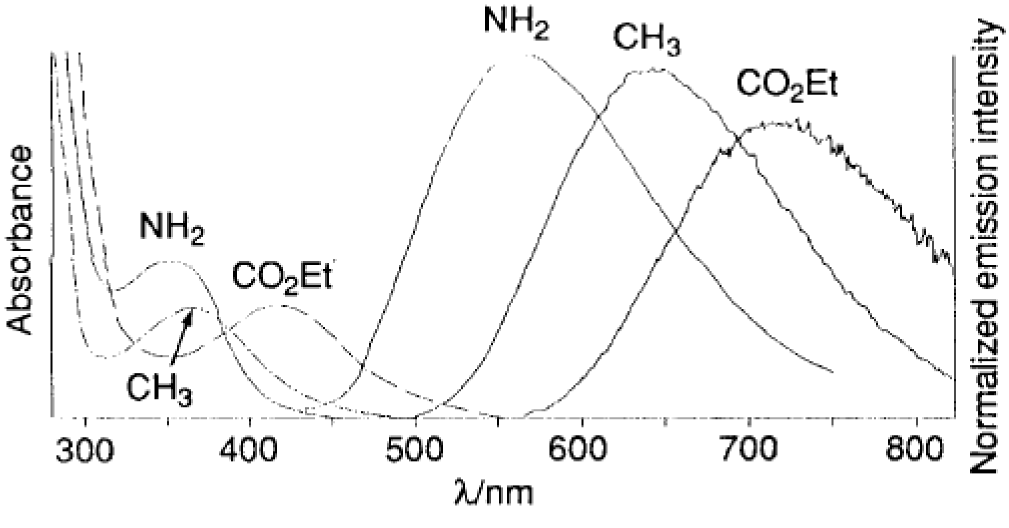

Figure 16: Effect of substituent X variation on emission of [Re(4,4′-X_2-bipy)$(CO)_3$Cl], **5.** [27]

1.2.5 Photophysical properties of the uranyl (UO_2^{2+}) ion

Typically three types of transitions are observed in the electronic absorption spectra of actinide ions in general.[28] The first are the Laporte forbidden *f-f* transitions, which produce weak bands. Laporte allowed *f→d* transitions (which result in intense bands often in the UV region) are also observed for some actinides. The third transition commonly observed in actinide elements are charge transfer bands. The ground state of the uranyl ion has a closed-shell electronic configuration, and possesses a characteristic absorption at about 400 nm which frequently gives uranyl compounds a distinctive yellow colour.[29] *f-f* and *f→d* transitions are not observed in uranyl complexes as it does not possess any *f*-electrons to promote. Uranyl complexes often display charge transfer bands from the oxygen ligand to the metal orbital (LMCT-ligand to metal charge transfer). These bands often (though not necessarily) exhibit fine structure due to progressions in symmetric O=U=O vibrations in the excited state which are well resolved. Further discussion regarding the electronic absorption spectrum of the uranyl ion is provided in chapter 5. Uranyl complexes tend to emit a bright green luminescence under UV irradiation, from the first excited state. This is used by geologists to identify the presence of uranium in ores.[30]

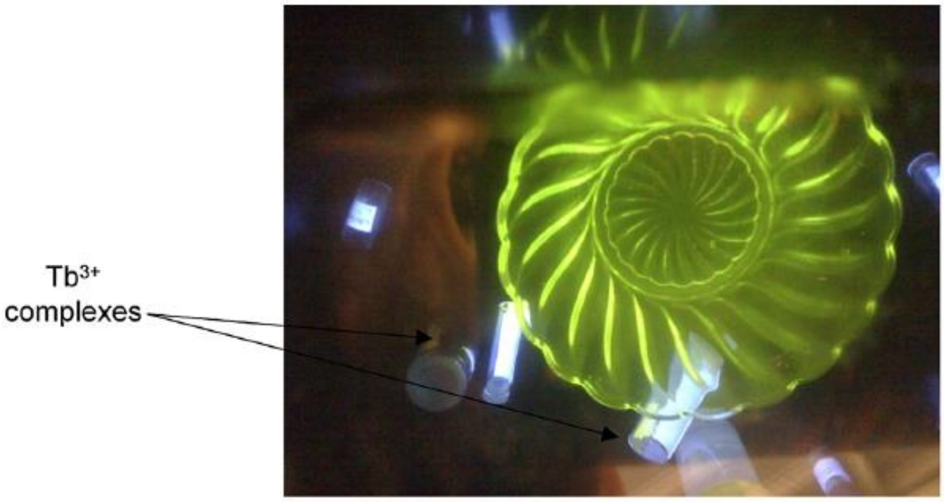

Figure 17: Uranium glass bowl under UV lamp irradiation (360 nm). Blue vials contain Tb^{3+} complexes.[31]

The investigation of photophysical properties of actinides is an area that has, in recent years, begun to attract much interest. Although the actinides, and in particular uranium play such an important role in the nuclear energy process, still relatively little is known about their emission properties and various oxidation states. Initially the photophysical properties of uranyl were investigated in 1961 by Mcglynn et al.[32,33] A review by Natrajan in 2012 has highlighted the recent advancements in this area, in particular with regards to uranyl and its coordination compounds.[31] The analysis of the uranyl ion is complicated slightly by the fact that aqueous UO_2^{2+} can form various hydroxides at different pH values, namely $[UO_2(OH)]^+$, $[UO_2(OH)]^+$, $[UO_2(OH)_3]^-$, $[UO_2(OH)_4]^{2-}$, as well as various oligomers such as $[(UO_2)_3(OH)_5]^+$, $[(UO_2)_3(OH)4]^{2+}$, $[(UO_2)_2(OH)]^{3+}$, $[(UO_2)_3(OH)_7]^-$, and $[(UO_2)_4(OH)_7]^+$.[34] The formation of these hydroxides at low (2-3.6) pH values can affect the emission spectrum of aqueous uranyl. This was observed in 1990 when the emission spectrum of aqueous uranyl was reported at varying pH values (Figure 18).[35]

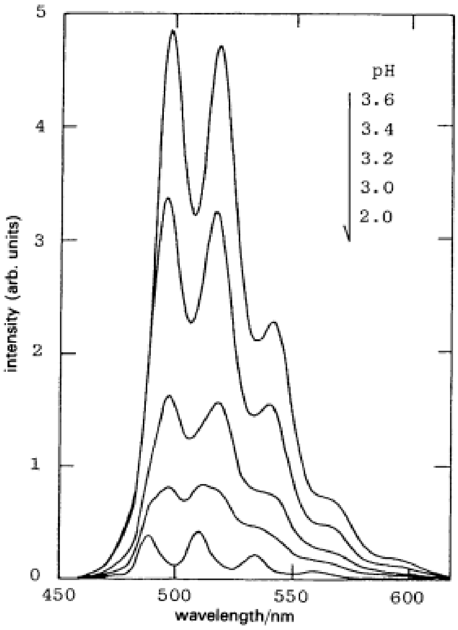

Figure 18: Emission spectra of uranyl ion in acidic perchlorate solutions as a function of pH.[35]

Figure 18 shows that at lower pH values the emission intensity was much weaker than at higher pH values. In addition there were major peak shifts to higher wavelengths at higher pH values, while no appreciable change was observed at pH < 2. This correlated to the formation of a new species at higher pH, namely $[UO_2(OH)_2]^{2+}$, while the species at pH = 2 was assumed to be aqueous uranyl. Time resolved spectra were obtained at pH = 1.9 and pH = 3.0 in order to determine if more than one species could be identified from the lifetime of the emission (Figure 19).

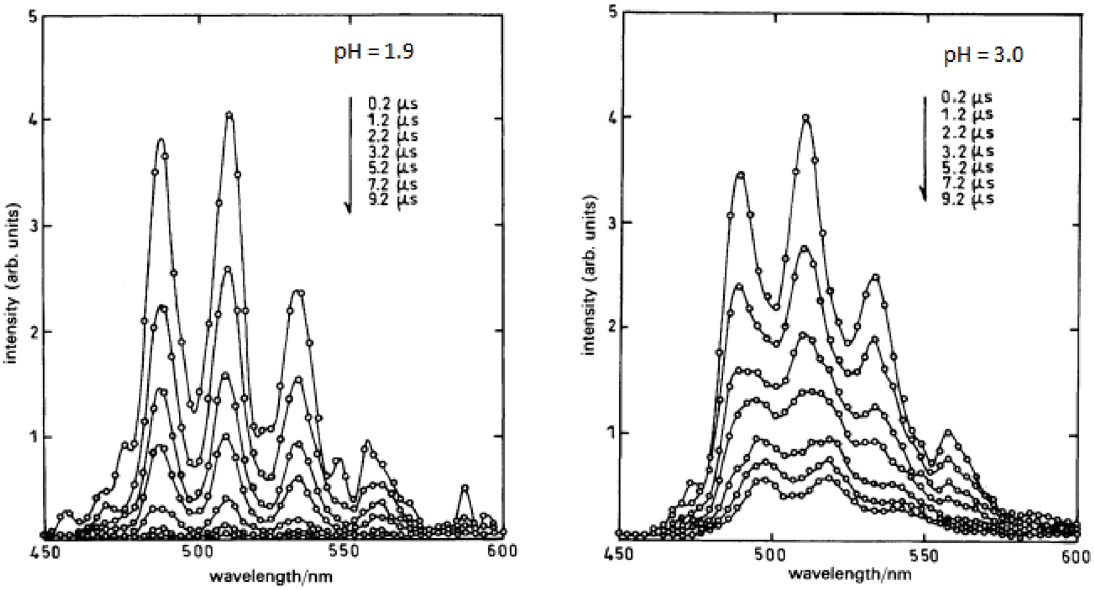

Figure 19: Time-resolved fluorescence of uranyl ion at pH = 1.9 (left) and pH = 3.0 (right).[35]

The time-resolved spectrum of the uranyl ion at pH = 1.9 showed only a decrease in intensity with time, while the spectrum of the uranyl ion at pH = 3.0 showed both a decrease in intensity and a significant shift of major peaks to higher wavelength. The spectrum at pH = 3.0 clearly indicated that two components with different lifetimes were present, which were attributed to the short-lived aqueous UO_2^{2+} component and the much longer lived $[UO_2(OH)_2]^{2+}$ component. The spectrum at pH = 1.9 exhibited only the short lived aqueous UO_2^{2+} component.

The lifetime of uranyl emission is dependent on anion coordination. The lifetime of the uranyl ion in aqueous media with fluoride, sulphate and phosphate have been investigated.[36] Table 4 shows the results obtained in the experiment, which showed significant increase in lifetime after addition of fluoride and phosphate and a moderate increase upon the addition of sulphate.

Acid added + substrate	Lifetime (µs)
0.1M $HClO_4$	2.1
0.1M $HClO_4$ + 0.9M $NaClO_4$	2.4
1M $HClO_4$	6.8
1M $HClO_4$ + 1M $NaClO_4$	7.0
1M $HClO_4$ + 1M $NaHSO_4$	11.1
1M H_2SO_4	10.8
1M $HClO_4$ + 1M NaF	159
1M $HClO_4$ + 1M H_3PO_4	190
1M H_3PO_4	187
1M H_3PO_4 + 1M $NaNO_3$	140

Table 4: Lifetimes of uranyl + acid and substrate

The effect of the addition of fluoride was investigated by analysing the lifetimes of the emissions at various concentrations. At low concentration (<10 mM fluoride) there were two distinct emissions detected, one had a lifetime of 2.4 µs and the second a lifetime of 75 µs. The rapid decay component was attributed to the emission of the uranyl aqua ion, while the longer decay was attributed to the 1:1 uranyl-fluoro complex. A further increase in concentration of fluoride resulted in a component which had a longer lifetime yet (150 µs), which was attributed to the emission of a 1:2 uranyl-fluoro complex. Further increasing the concentration of fluoride did not affect the lifetime, due primarily to the fact that the 1:3 and 1:4 uranyl-fluoro complexes have a similar lifetime. The reason for the increase in lifetime was attributed to the quenching of the emission by water. With increased amount of fluoride the quenching of the emission by water became less effective, resulting in longer lifetime emissions. Further work by the same group investigated water quenching of uranyl emission, exploring a potential electron transfer mechanism as the source of the quenching.[37]

1.3 Organic lumophores

1.3.1 Triarylimidazole (lophine)

The triarylimidazole motif will be used extensively during the course of the thesis and so a brief background will now be given. Subsequent chapters will also address more details of the chemistry of this molecule. The first triarylimidazole (**6**) was isolated in 1877 by Radziszewski through the condensation of a 1,2-dicarbonyl compound with an aldehyde and ammonia (Scheme 1).[38] The reaction can be considered to take two steps, in the first step a diimine is formed, and in the second step the diimine condenses with the aldehyde to form the imidazole. This synthesis is sometimes referred to as the Debus-Radziszewski imidazole synthesis.[39]

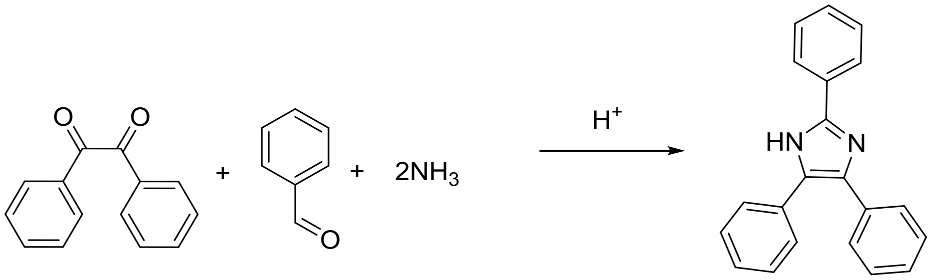

6

Scheme 1: Formation of triphenylimidazole

Further work by F. R. Japp helped develop the understanding of the reaction, as he successfully formed an imidazole using phenanthraquinone and proposed a chemical equation for the reaction (Equation 11). [40]

$$\underset{\text{phenanthraquinone}}{C_{14}H_8O_2} + \underset{\text{salicylaldehyde}}{C_7H_6O_2} + 2NH_3 \longrightarrow C_{21}H_{14}N_2O + 3H_2O$$

Equation 11

In addition, Japp also successfully proposed a structure for the imidazole, which correctly placed the double bonds in the imidazole ring as well as the hydrogen atom.[41]

The initial work by Radziszewski also noted that this type of molecule displays chemiluminescence (i.e. the emission of light when undergoing a chemical reaction). Radziszewski stated that in the presence of air and a strong base “lophine” yielded ammonia, benzoic acid, and enough light to illuminate the surroundings. The luminescent properties of triarylimidazole have since been the subject of much interest. A study in 1964 by White and Harding suggested that the origin of the chemiluminescence was the formation and subsequent decomposition of a peroxide.[42] In order to determine this, a series of substituted imidazoles were prepared along with a peroxide-containing analogue (Figure 20).

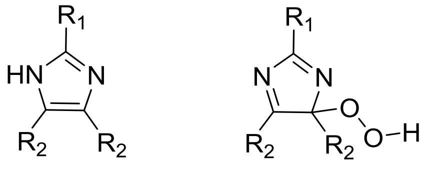

a: $R_1 = R_2 = C_6H_5$

b: $R_1 = p\text{-}CH_3OC_6H_4$, $R_2 = C_6H_5$

c: $R_1 = R_2 = p\text{-}CH_3OC_6H_4$

d: $R_1 = p\text{-}(CH_3)_2NC_6H_4$, $R_2 = C_6H_5$

e: $R_1 = p\text{-}(CH_3)_2NC_6H_4$, $R_2 = p\text{-}CH_3OC_6H_4$

Figure 20: Molecular structures of imidazole and peroxide-imidazole

All of the imidazole compounds listed displayed chemiluminescence when reacted with base and oxygen, and all of the peroxides also yielded light upon reaction with base alone. Each of the imidazole- peroxide imidazole analogues displayed similar emission wavelengths, indicating that in each case a common light emitter was involved.

In the last thirty years the chemiluminescent properties of triarylimidazole have been investigated for practical purposes, including metal ion detection and biological detection.[43-48] The use of triarylimidazole derivatives as analytical tools was reviewed in 2002 and has highlighted its suitability for the determination of Co(II) and Cr(VI).[49] For instance it was discovered by Marino *et al*. that trace amounts of Co(II) enhanced the chemiluminescent (CL) reaction in basic hydrogen peroxide solutions. This method was hampered slightly by interference by other metal ions, in particular Mg(II).[47]

1.3.2 Chemosensing using the triarylimidazole motif

The 2,4,5-triphenylimidazole chromophoric motif has attracted much attention due to its fluorescence and chemiluminescence attributes, which has analytical applications as a result of the ability to tune the optical properties through the nature of the imidazole substituents.[49-51] For instance, a molecule containing a 2,4,5-triphenylimidazole (colloquially knows as lophine) skeleton, “DIBI”, has been used to detect terminal alkenes (Scheme 2).[52]

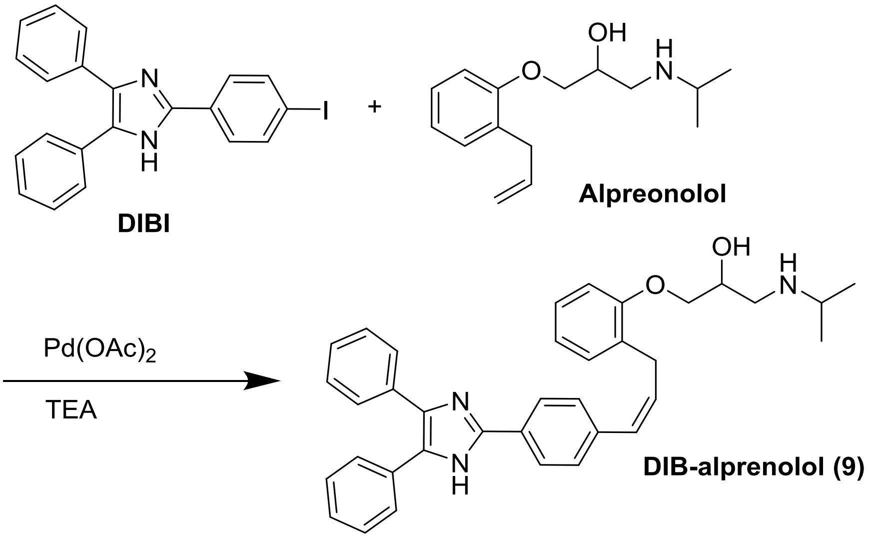

Scheme 2: Reaction scheme for formation of DIB-alprenolol (**9**) modified from [52]

Using alprenolol as a model for terminal alkene-containing molecules, the reaction proceeds via a Heck coupling reaction forming DIB-alprenolol. The fluorescence-labelled DIB-alprenolol was easily detected in the presence of biological components, suggesting possible applications as a detection method for alprenolol and similar compounds such as oxprenolol, levallorphan and cholecalciferol in biological systems.

1.3.3 Fused imidazo[4,5-*f*]-1,10-phenanthroline complexes.

This thesis will include the isolation of a wide range of highly fluorescent molecules and their coordination chemistry to rhenium, therefore a coordination site on the fluorescent molecule is necessary. The fused imidazo[4,5-*f*]-1,10-phenanthroline unit (**10**) is a diimine-based analogue that incorporates the same chromophoric motif (Figure 21). The presence of the diimine unit has allowed a number of studies on coordination chemistry of the ligand. For example, it has been investigated with visible light absorbing Ir(III)[53], Ru(II)[54] and Pt(II)[55] complexes, as well as utilised in the development of a sensor for Co(II).[56]

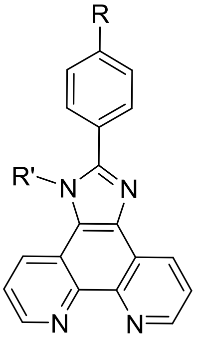

10

Figure 21: Fused imidazo[4,5-*f*]-1,10-phenanthroline, **10**

Complexes of the type *fac*-{Re(CO)$_3$} incorporating a fused imidazo[4,5-*f*]-1,10-phenanthroline unit provides access to a series of complexes with photophysical properties which has biological applications. The excited ^{3}MLCT state can be accessed and the associated emission has a large Stokes' shift and an enhanced lifetimes which are desired attributes for biological applications.[57] Re(I) complexes coordinated to 2,2′-bipyridine and 1,10-phenanthroline based ligands have been well established and investigated, as have their photophysics, which generally originate from the MLCT (metal to ligand charge transfer) excited states that involve the singular accepting diimine ligand.[26,58,59]

Shavaleev and Nazeeruddin have recently displayed potential applications of fused imidazo[4,5-*f*]-1,10-phenanthroline iridium complexes in orange light-emitting electrochemical cells.[53]

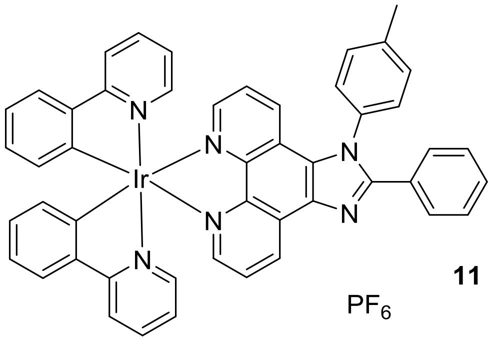

11

Figure 22: Molecular structure of **11**

The complex was found to absorb light at $\lambda > 450$ nm and a molar absorption coefficient of $\varepsilon < 1.4\times10^3$ $M^{-1}cm^{-1}$. This was assigned to a (Ir-phenyl)-to-lophine charge transfer. The complex exhibited yellow-orange phosphorescence in DCM with a λ_{max} at 583 nm, a quantum yield (Φ) of 43% and a relatively long lifetime of 910 ns. The complex was successfully incorporated into electrochemical cells, providing a fast, efficient and long lived orange light-emitting cells.

Zhao and co-workers have also reported the Ir(III) complexes of related ligands incorporating a terminal coumarin chromophore conjugated to the imidazole core; these complexes demonstrated significant photogeneration of singlet oxygen following irradiation with visible light.[60]

Metal bound nitrosyl groups have been investigated in the framework of [Ru(terpy)(L)(NO)]$^{n+}$

(where terpy = 2,2':6',2"-terpyridine, L = 2-phenylimidazo[4,5-f]1,10-phenanthroline, **12**) (Figure 23).[54]

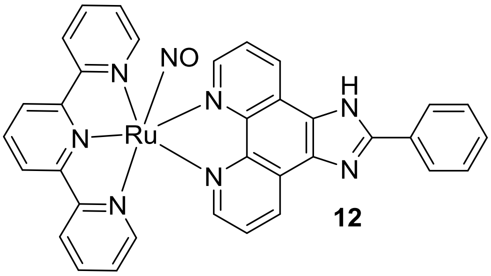

12

Figure 23: Molecular structure of **12**

The work demonstrated that the "terpy" and "lophine" coligands in the complex framework facilitates the stabilisation of the nitrosyl group in both the NO$^+$ and NO$^·$ redox states.

The detection of Co^{2+} ions have been explored by exploiting the optical properties of fused imidazo[4,5-*f*]-1,10-phenanthroline complexes.[56] Significant reduction in the electronic absorption intensity upon addition of Co^{2+} to a buffered dimethylformamide (DMF) solution of 2-(2-pyridine)imidazo[4,5-*f*]-1,10-phenanthroline, **13** was observed, with little or no changes observed with addition of other biologically important molecules such as Na$^+$, K$^+$, Mg^{2+}, Ba^{2+}, Co^{2+}, Ni^{2+}, Cu^{2+}, Ag$^+$, Zn^{2+}, and Hg^{2+} (Figure 24).

Specifically, a 5 x 10^{-5} M solution of Co^{2+} would quench the fluorescence of the ligand by 81%, however the same concentration solutions of the ions mentioned previously would result in quenching of the order of 6-31 %. Of vital importance to the effectiveness of this ligand as a fluorescent metal ion detector is the ability for it to distinguish between the target analyte (i.e. Co^{2+}) and other metal ions which may be in the solution. Such considerations are also important for the work undertaken in this thesis, as ultimately the ligands presented may be evaluated for their use in the detection of low-level alpha emitters such as uranyl, and as such their interactions with other metal ions should also be considered for comparison.

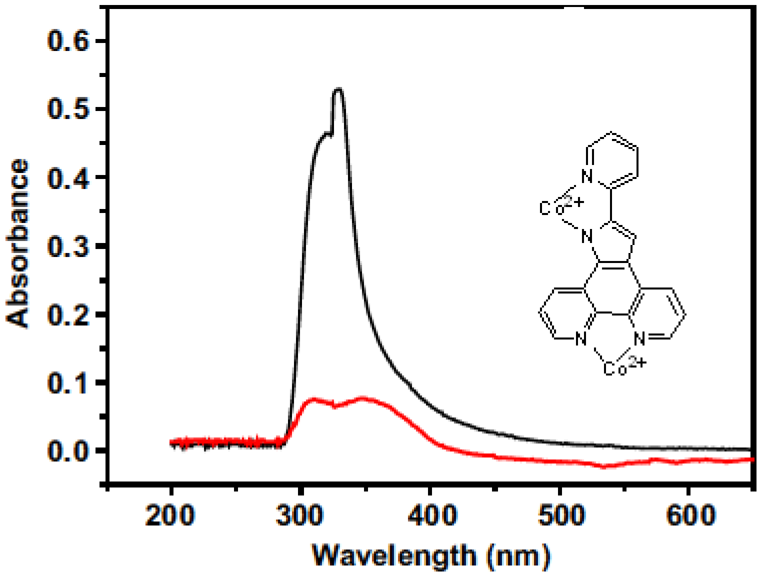

Figure 24: Electronic absorption spectra to determine presence of Co^{2+}

1.4 Analytical techniques

The following section will give a brief overview of the other analytical techniques employed during the course of this thesis.

1.4.1 NMR spectroscopy

Nuclear Magnetic Resonance (NMR) spectroscopy is one of the most useful tools for an analytical chemist, as it can be used to determine the structure and chemical environment of certain molecules. It utilises the interaction of a magnetic field with a property that some nuclei have called “spin”. Numerous nuclei have the property called spin such as ^{1}H, ^{13}C and ^{31}P. Quantum mechanics tells us that a nucleus with a spin *I* will have 2*I*+1 possible orientations. For example, ^{1}H has an *I* value of ½, therefore it has two possible orientations (+ ½ and – ½ , Figure 25). Without a magnetic field these states are degenerate, however upon application of a magnetic field they occupy two distinct energy levels.

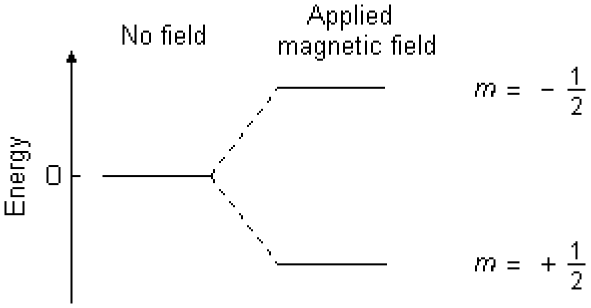

Figure 25: Splitting of energy levels with magnetic field. [61]

The lower state (m = + ½) will contain slightly more nuclei than the higher level as described by the Boltzmann distribution. If radio frequency (rf) radiation is absorbed by the nucleus then the magnetic moment of spins in line with the magnetic field will "flip" in order to oppose the magnetic field (i.e. occupies the higher energy state, Figure 26).

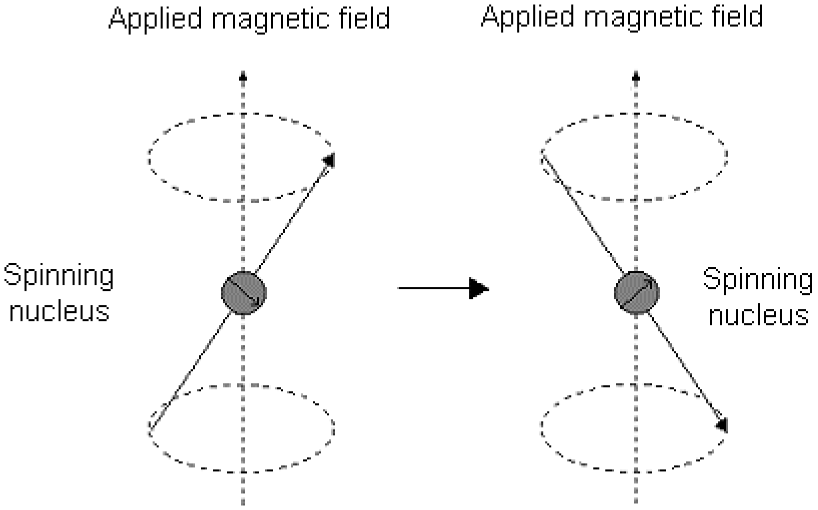

Figure 26: "Flip" of the magnetic moment of a nucleus.[61]

If the energy levels have exactly the same population and there is no net change in the population of either energy level then the spin system is termed as "saturated".

After the sample is irradiated it is allowed to relax back to its original state, which it can do through spin-lattice relaxation and spin-spin relaxation. During this time the spectrometer will monitor the absorption and emission of rf energy and transmit the data as an NMR spectrum. The relaxation time is crucial as a quick relaxation time will result in less spin saturation and a quicker collection of data, however too quick and it can lead to line broadening in the spectrum. The relaxation time of ^1H is relatively quick therefore it has a quick acquisition time and spin-spin coupling can be observed.

The spectrum provides useful of information about the location of a nucleus in a molecule through its chemical shift and (if present) spin-spin coupling. Firstly chemical shift relates to the exact position of the resonance on the spectrum. This is influenced by electrons in the vicinity of the nucleus in question. Electrons have their own spin independent of the nucleus and this is in the opposite direction to that of the applied magnetic field. This spin “shields” the nucleus which means the applied field strength must be increased in order for the nucleus to absorb at its transition frequency. This causes what is called an “upfield” shift which is observed in the spectrum. Conversely, if electrons are drawn away form a nucleus, for instance if it was near an electron withdrawing group, then the nucleus will be *deshielded* and there will be a downfield shift in the resonance. This information is useful as it may provide clues to the location of a nucleus within a molecule.

Spin-spin coupling refers to the splitting of the energy levels as a result of the spin of nearby nuclei. For example, if a ^1H nucleus is in the proximity of non-equivalent ^1H nuclei then its resonance may be split in relation to the number of other nuclei. For instance, in ethanol CH_3CH_2OH, the equivalent ^1H nuclei in the CH_3 unit will give a signal through interaction with the magnetic field which will then be split by the ^1H nuclei in the CH_2 unit according to the 2nI+1 rule (where n = number of nuclei and I = spin of nuclei), into a triplet. Similarly the nuclei of the CH_2 unit will also be split by the CH_3 unit resulting in a quartet. The strength of this coupling is expressed by coupling constants, J, which are determined by the frequency difference between the split resonances. For ethanol, the coupling constant is exactly the same value for the triplet and the quartet as they originate from the same energy gap.

1.4.1.1 Instrumentation and conditions

All ^1H and $^{13}C\{^1H\}$ NMR spectra were obtained at Cardiff University chemistry department on NMR-FT Bruker 250, 400 or 500 spectrometers and recorded in an appropriate solvent (i.e. $CDCl_3$, MeOD, d^6-DMSO, D_2O). ^1H and $^{13}C\{^1H\}$NMR chemical shifts (δ) were determined relative to internal TMS and are given in ppm.

1.4.2 Electronic Absorption Spectroscopy

Much of electronic absorption spectroscopy uses the same theory as described in section 1.1, which will not be repeated here. This technique measures the absorbance of molecules that absorb energy in the UV region of the electromagnetic spectrum. Absorbance is directly proportional to the pathlength l, and the concentration of the absorbing species c. The Beer-Lambert law states that:

$$A = \varepsilon c l$$

Equation 12

Where ε is the *molar absorptivity coefficient.* The spectra obtained using this technique will exhibit bands which correspond to transitions of an electron from a ground state to an excited state. These transitions follow the same selection rules as outlined in section 1.1.3. Absorptions which break the selection rules can still be observed (e.g. such as those which are relaxed by heavy atom spin-orbit coupling) however they will have a much lower ε value compared to transitions that do not break the selection rules. Numerous transitions can be observed using this technique, including $\pi \rightarrow \pi^*$ and $n \rightarrow \pi^*$ transitions which are commonly observed in organic compounds and charge transfer absorptions, which require an electron-donating component and an electron accepting component.

1.4.2.1 Instrumentation and conditions

Electronic absorption studies were performed using a Jasco V-570 spectrophotometer in an appropriate solvent (10^{-5} M) at 298 K.

1.4.3 IR spectroscopy

Infrared spectroscopy is the analysis of the interaction between infrared radiation and a molecule. The vibration spectrum of a compound is obtained by exposing a sample to infrared radiation and recording the variation of transmission with frequency.[62] A low transmission percentage indicates that the radiation of that frequency is being absorbed by the molecule.

IR radiation of certain frequencies causes excitation of the vibrations of covalent bonds within a molecule, it is at these frequencies that the radiation is absorbed. These vibrations include the stretching and bending modes (Figure 27), and other more energetic modes such as twisting, rocking and scissoring.

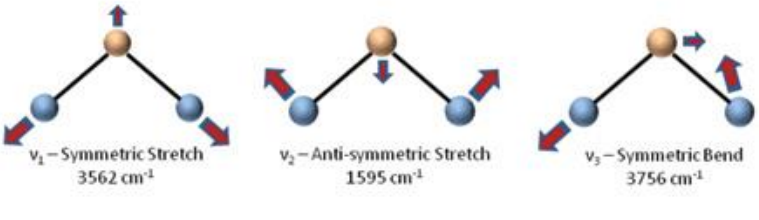

Figure 27: Bending and stretching modes of a non-linear triatomic molecule.[63]

A typical IR spectrum will analyse between about 4000 cm^{-1} to 400 cm^{-1} (wavenumbers), and is best utilised as a complimentary tool to confirm the presence of functional groups in a molecule. The region from 400cm^{-1} to ≈ 1000 cm^{-1} is known as the “fingerprint” region which often contains numerous bands that cannot be differentiated. The region from 1000 cm^{-1} to 4000 cm^{-1}, sometimes known as the “functional group region” is usually the region which provides the most useful information. This is due to the fact that functional groups often exhibit bands at specific frequencies in this region, and as such they can be easily identified. A selection of examples is shown in Table 5.

Functional group	Absorption wavenumbers (cm^{-1})
Alkyl C-H stretch	**2950-2850**
O-H stretch (alcohol)	**3550-3200**
O-H stretch (carboxylic acid)	**3000-2500**
N-H stretch (amine)	**3500-3300**
C=O stretch (aldehyde)	**1740 - 1690**
C=O stretch (ketone)	**1750-1680**
C=O stretch (ester)	**1750-1735**
C=O stretch (carboxylic acid)	**1780-1710**
C=O stretch (amide)	**1690-1630**

Table 5: Summary of common absorptions

The infrared spectrum of hexanoic acid (Figure 28) displays numerous stretches and bends that are typical for the various functional groups.

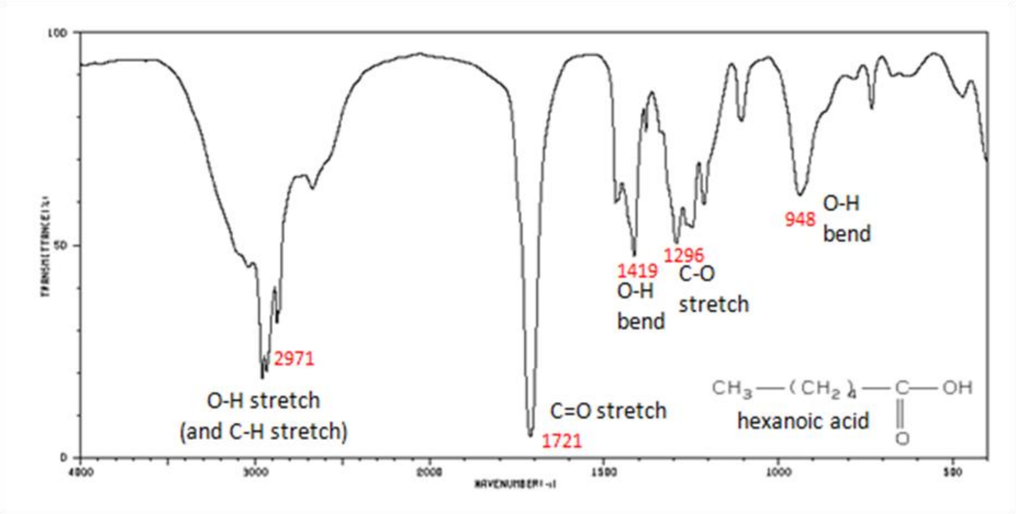

Figure 28: Typical IR spectrum.[64]

1.4.3.1 Instrumentation and conditions

Infrared spectra were obtained at 298 K where the solid sample is mixed with KBr and pressed as plates unless otherwise noted. Spectra were obtained on a Jasco FT/IR-660 plus spectrometer.

1.4.4 Mass spectrometry

Mass spectrometry is a technique used to accurately determine the mass to charge ratio (m/z), and thereby the molecular weight of a sample. Figure 29 depicts a standard mass spectrometer. A sample being analysed will first be vaporised, then ionised, accelerated, deflected and finally detected.

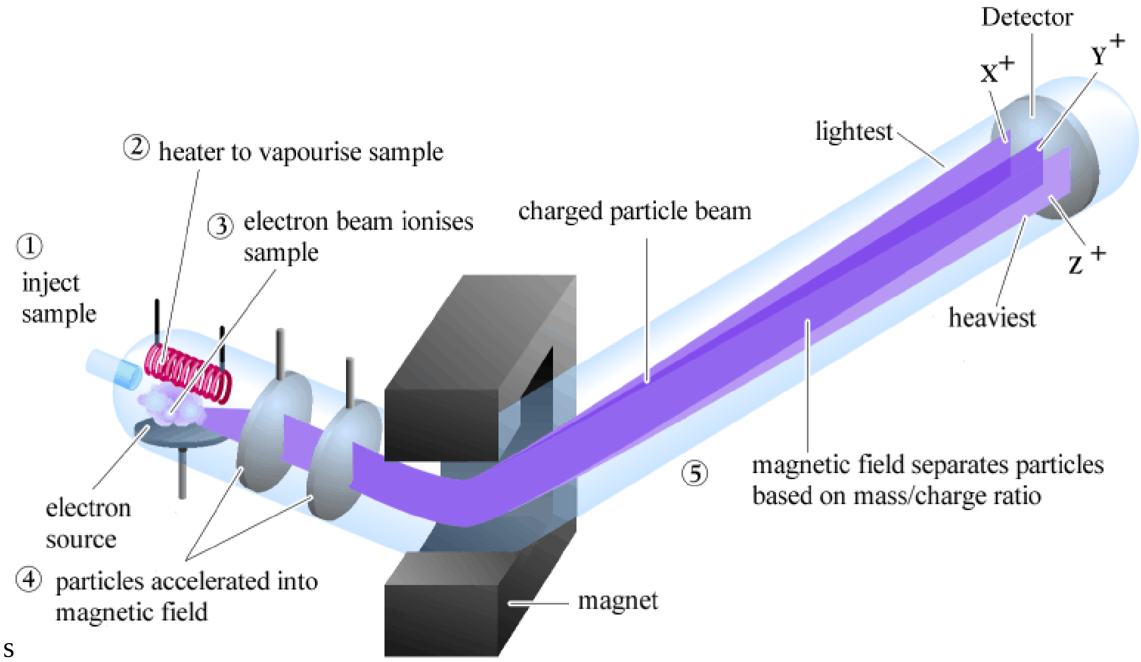

Figure 29: Diagram of a typical mass spectrometer.[65]

A typical mass spectrometer always contains the following components.

1) A heater to vaporise the sample
2) A vacuum pump to remove any air particles to avoid collisions
3) A source to ionise the sample (e.g. electron gun)
4) An electric field to accelerate the sample
5) An electromagnet to form a magnetic field to deflect the ionised particles.
6) A detector which analyses the deflected particles according to their mass/charge ratio

1.4.4.1 Ion sources

Ions can be formed in a variety of ways such as electron ionisation (EI), chemical ionisation (CI), fast atom bombardment (FAB), matrix-assisted laser desorption ionisation (MALDI) and many more.

1.4.4.2 Electron ionisation (EI)

The most common ionisation method, particularly for organic materials is electron ionisation (EI) which is achieved through interaction between an electron beam and the vaporised sample. This causes an ejection of an electron from the analyte which is then deflected and detected. Electron ionisation is a relatively harsh method, and if the analyte is not stable after ionisation it may fragment into smaller and more stable ions. If the $[M]^+$ ion is stable enough it will be visible in the spectrum.

1.4.4.3 Chemical ionisation (CI)

Chemical ionisation is a far less harsh method of obtaining analyte ions, and is generally achieved through interaction of the analyte with a molecular ion. For example methane can be ionised to form CH_3^+ or CH_5^+, these can then collide with a theoretical molecule AB to form $[AB\text{-}H]^+$ or $[AB+H]^+$. Commonly the $[M+H]^+$ ion is the heaviest ion found using this technique.

1.4.4.4 Electrospray ionisation (ESI)

Electrospray ionisation is an extremely “soft” technique that is used on molecules with large molecular weight such as proteins and other complex biological molecules. ESI involves the introduction of the analyte in very low concentration into a metal capillary. A very high voltage is then passed through the capillary causing the sample to become ionised and disperse into small droplets in the mass spectrometer. The droplets become smaller in size as the solvent evaporates, leaving the analyte intact as a charged ion.

1.4.4.5 Fast atom bombardment

Fast atom bombardment (FAB) is another relatively soft technique in mass spectrometry which involves the bombarding of the target sample protected in a matrix under vacuum by inert atoms, often noble gases such as xenon and argon. The high energy atoms desorb positive and negative ions from the surface of the matrix creating a ionised sample which is then detected.

1.4.4.6 Instrumentation and conditions

Low resolution mass spectra were obtained by the staff of Cardiff University using the appropriate methods. High-resolution mass spectra were aquired at the ESPRC National Mass Spectrometry Service at Swansea University.

1.4.5 Small Angle Neutron Scattering (SANS)

Small angle neutron scattering is an analytical technique that can probe structures at length scales from 1nm to more than 100 nm.[66] This technique relies on the elastic scattering of neutrons to provide a scattering pattern. These patterns can be analysed to provide information about the size, shape and orientation of the sample. During the experiment a beam of neutrons is directed at the sample, most of which pass through the sample onto the detector without deviation owing to neutrons very high penetrative abilities. However a small amount of neutrons may interact with a nucleus resulting in the elastic scattering of the neutrons (Figure 30). Neutrons do not interact with electrons so scattering is due to the nature of the nucleus of the isotope in the sample. The refractive index θ, is directly related to the scattering length density "δ" of an isotope, and is a measure of the interaction between a neutron and a nucleus.

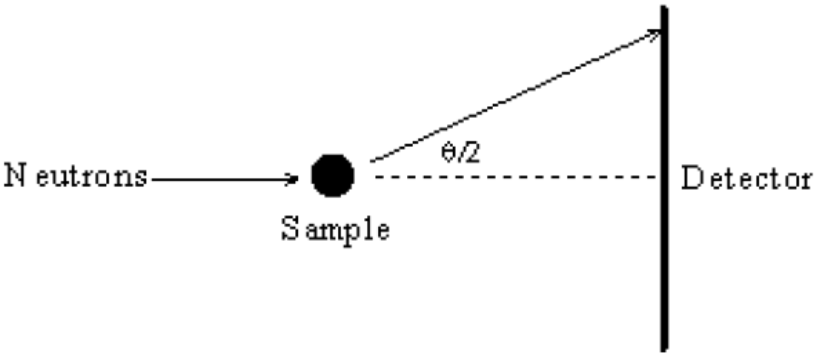

Figure 30: Diagram depicting the theory of neutron scattering .[67]

Hydrogen and deuterium have vastly different δ values (Table 6), where protic values are typically small and negative and deuterated values are large and positive.

Solvent	**δ (protonated) ($x10^{10}cm^{-2}$)**	**δ (deuterated) ($x10^{10}cm^{-2}$)**
Water	**-0.56**	**+6.38**
Octane	**-0.53**	**+6.43**
Cyclohexane	**-0.28**	**+6.70**
Toluene	**+0.94**	**+5.66**
Chloroform	**+2.39**	**+3.16**

Table 6: Scattering length densities. Data from [66]

This difference in scattering length density is of great importance as it allows us to undergo contrast experiments. These experiments involve substituting deuterated components with protic components and through comparison with controls, gather information regarding the protic components size and location. For example, in a system where core-shell particles are in a continuous phase, contrast experiments can be used to highlight the size of the components of the particle by alternating protic and deuterated components within the particle (Figure 31).

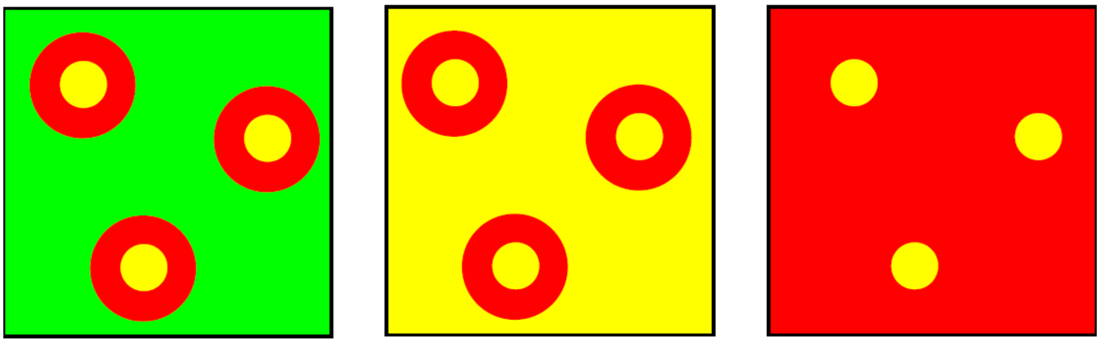

Natural contrast

r solvent = r core
(shell visible)

r solvent = r shell
(core visible)

Figure 31: Example of a contrast experiment.[68]

SANS can be used to analyse many systems such as polymers, biological molecules, nanoparticles and microemulsions (which incorporate core-shell particles as shown in Figure 31).

1.4.5.1 Instrumentation and conditions

Small-angle neutron scattering (SANS) measurements were performed on the fixed-geometry, time-of-flight LOQ diffractometer (ISIS spallation neutron source, Oxfordshire, UK). The microemulsion solutions were placed in 1 or 2mm pathlength quartz cuvettes (Hellma) and mounted in aluminium holders on top of an enclosed, computer-controlled sample changer. All experiments were undertaken at 25°C, and the experimental measuring times were between 20 and 40 minutes.

1.4.6 Luminescence instrumentation and conditions

Photophysical data was obtained on a JobinYvon-Horiba Fluorolog spectrometer fitted with a JY TBX picosecond photodetection module in the appropriate solvent. Emission spectra were uncorrected and excitation spectra were instrument corrected. The pulsed source was a Nano-LED configured for 295, 372 or 459 nm output operating at 1MHz. Luminescence lifetime profiles were obtained using the JobinYvon-Horiba FluoroHub single photon counting module and the data fits yielded the lifetime values using the provided DAS6 deconvolution software. The statistical method used is an iterative least squares reconvolution, where the goodness of fit is quantified by χ^2 (a value ≈ 1 is taken to indicate a good quality fit). The decay profiles were assumed to be mono-exponential (single lifetime component) where the application of a bi-exponential model resulted in no improvement of the fit as indicated by χ.

1.4.7 X-ray Diffraction

X-ray crystallography is a technique used to determine the molecular structure of a crystal, in which an X-ray beam is diffracted when it encounters an area of high electron density around an atom. Figure 32 shows a diagram depicting the diffraction of X-rays by a crystal. A crystal incorporates a layered structure with interspacial distances of "d". As the X-ray beam encounters "scatterers" (i.e. areas of high electron density surrounding atoms) they are diffracted at an incident angle of θ. These diffracted beams can interact with each other either destructively (in which case they are not observed) or constructively in which case they are visible as a diffraction pattern. The diffraction pattern is collected on a detector as the sample is slowly rotated and more data is collected. This data is collected computationally to produce a model of the molecular structure of the crystal.

Bragg's equation connects the x-ray wavelength, the spacing "*d*" and the incident angle θ.

$$n\lambda = 2d\sin\theta$$

Equation 13: Bragg's Law

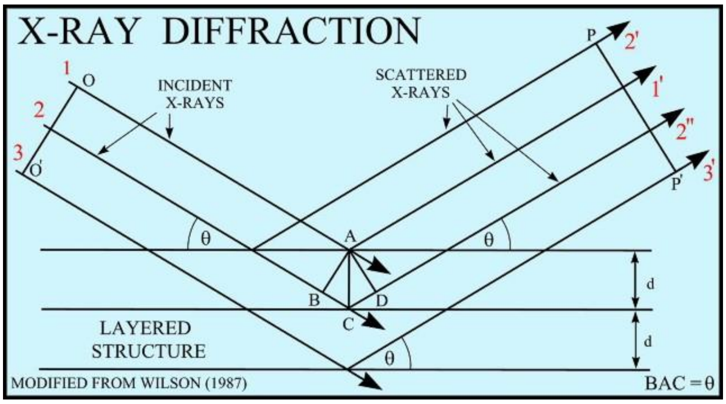

Figure 32: Diagram showing the processes occurring in X-ray diffraction[69]

1.5 Aims

The aims of the work described in this thesis were the synthesis and characterisation of a range of triarylimidazole (lophine) species with the purpose of coordination to metals. Numerous substituents were incorporated into the lophine molecule, with the intention of exploring how alterations to the functional groups of lophine will affect solubility and electronic behaviour. This "tuning" of the molecule was investigated through a myriad of spectroscopic techniques, at the forefront of them electronic absorption and luminescence spectroscopy. It was hoped that a greater understanding of how these systems work and behave electronically in various solvents would be established. In order to provide a coordination site for metal complexation, lophines were designed to incorporate a phenanthroline moiety, and in some instances catechol and terpyridine moieties.

Coordination chemistry of new ligands was undertaken to form Re(I) complexes in order to explore how the photophysical behaviour of the well-established Re(I)-diimine species vary with alterations to the lophine structure. Among the topics that were discussed included emission wavelength, lifetimes and solvatochromism.

As has previously been discussed the photophysical and luminescent properties of uranyl complexes is relatively unexplored in comparison to trivalent lanthanides and *d*-block metal complexes. Exploring these aspects of uranyl chemistry could prove useful, not only to further understand the electronics of the uranyl cation, but also for practical purposes such as detection. Probing uranyl directly is not necessarily the most effective way of detection, therefore this study investigated the effect of coordinating lophine to uranyl as molecular "tags" in order to probe the electronic properties of the system. Different functional groups were employed in order to alter solubility, emission and reactivity. Through investigations of the uranyl species with these “tuneable” ligands, it was hoped that a library of emission wavelengths would be created that will table emission wavelengths of specific ligands with uranyl, in order to provide a detection method.

The behaviour of uranyl ion in micellar environment was also explored, with potential applications as a pre-concentration method for detection of low-level amounts in solution, including environmental samples. These systems were explored through small angle neutron scattering (SANS) and through the luminescence spectroscopy, in order to elucidate the partitioning of the uranyl ion in a micelle with a variety of O and N-donor ligands.

1.6 References

(1) http://www.southampton.ac.uk/~chemlab/useful/lum/lum.htm (accessed 13/02/2014).

(2) Atkins, P.; De Paula, J. *Atkins' Physical Chemistry, 8th Edition, Oxford University Press* **2006**.

(3) http://webcache.googleusercontent.com/search?q=cache:http://wwwchem.uwimona.edu.jm/courses/selrules.html (accessed 9/2/14).

(4) http://www2.chemistry.msu.edu/faculty/reusch/virttxtjml/photchem.htm (accessed 7/2/14).

(5) Atkins, P.; de Paula, J.; Friedman, R. *Quanta, Matter, and Change: A Molecular approach to physical chemistry; W. H. Freeman, New York*

2009.

(6) Lakowicz, J. R. *Principles of Fluorescence Spectroscopy, Plenum Press, New York* **1983**.

(7) Stokes, G. G. *Phil. Trans. R. Soc. London* **1852**, *142*, 463.

(8) http://www.answers.com/topic/stokes.

(9) Grewer, C.; Brauer, H. *J. Phys. Chem.* **1994**, *98*, 4230.

(10) Wilkinson, F. *Pure & Appl. Chem.* **1997**, *69*, 851.

(11) Kautsky, H. *Trans. Faraday Soc.* **1939**, *35*, 216.

(12) Sun, M.; Song, P. S. *Photochem. Photobiol.* **1977**, *25*, 3.

(13) Lohse, P. W.; Kuhnt, J.; Druzhinin, S. I.; Scholz, M.; Ekimova, M.; Oekermann, T.; Lenzer, T.; Ouma, K. *Phys. Chem. Chem. Phys.* **2011**, *13*, 19632.

(14) Evans, R. C.; Douglas, P.; Winscom, C. J. *Coordin. Chem Rev.* **2006**, *250*, 2093.

(15) Forster, T. *Discuss. Faraday Soc.* **1959**, *27*, 7.

(16) Dexter, D. L. *J. Chem. Phys.* **1953**, *21*, 836.

(17) Baldo, M. A.; Thompson, M. E.; Forrest, S. R. *Pure Appl. Chem.* **1999**, *71*, 2095.

(18) Lo, K. K.-W.; Louie, M.-W.; Zhang, K. Y. *Coordin. Chem Rev.* **2010**, *254*, 2603.

(19) Chen, H.; Zhao, Q.; Wu, Y.; Li, F.; Yang, H.; Yi, T.; Huang, C. *Inorg. Chem.* **2007**, *46*, 11075.

(20) Brulatti, P.; Gildea, R. J.; Howard, J. A. K.; Fattori, V.; Cocchi, M.; Williams, J. A. G. *Inorg. Chem.* **2012**, *51*, 3813.

(21) Baba, A. I.; Shaw, J. R.; Simon, J. A.; Thummel, R. P.; Schmehl, R. H. *Coordin. Chem Rev.* **1998**, *171*, 43.

(22) Ciobotaru, I. C.; Polosan, S.; Ciobotaru, C. C. *J. Lumin.* **2014**, *145*, 259.

(23) Nguyen, T. T.; Martin, J. C. *J. Am. Chem. Soc.* **1980**, *102*, 7383.

(24) Ayala, N. P.; Flynn Jr., C. M.; Sacksteder, L.; Demas, J. N.; DeGraff, B. A. *J. Am. Chem. Soc.* **1990**, *112*, 3837.

(25) Striplin, D. R.; Crosby, G. A. *Coordin. Chem Rev.* **2001**, *211*, 163.

(26) Wrighton, M.; Morse, D. L. *J. Am. Chem. Soc.* **1974**, *96*, 998.

(27) Worl, L. A.; Duesing, R.; Chen, P.; Ciana, L. D.; Meyer, T. J. *J. Chem. Soc. Dalton Trans.* **1991**, 849.

(28) Bagnall, K. W. **1972**, Elsevier Publishing.

(29) Cotton, S. *Lanthanide and actinide chemistry* **2007**, John Wiley and sons ltd.

(30) Duff, M. C.; Morris, D. E.; Hunter, D. B.; Bertsch, P. M. *Geochim. Cosmochim. Ac.* **2000**, *64*, 1535.

(31) Natrajan, L. S. *Coordin. Chem Rev.* **2012**, *256*, 1583.

(32) McGlynn, S. P.; Smith, J. K. *J. Mol. Spectrosc.* **1961**, *6*, 164.

(33) McGlynn, S. P.; Smith, J. K.; Neely, W. C. *J. Chem. Phys.* **1961**, *35*, 105.

(34) Meinrath, G. *Freiberg On-line Geosci.* **1998**, *1*, 1.

(35) Park, Y.-Y.; Sakai, Y.; Abe, R.; Ishii, T.; Harada, M.; Kojima, T.; Tomiyasu, H. *J. Chem. Soc. Faraday Trans.* **1990**, *86*, 55.

(36) Moriyasu, M.; Yokoyama, Y.; Ikeda, S. *J. Inorg. Nucl. Chem.* **1977**, *39*, 2199.

(37) Moriyasu, M.; Yokoyama, Y.; Ikeda, S. *J. Inorg. Nucl. Chem.* **1977**, *39*, 2211.

(38) Radziszewski, B. *Chem. Ber.* **1877**, *10*, 70.

(39) Plater, M. J. *Bull. Hist. Chem.* **2008**, *33*, 76.

(40) Japp, F. R. *J. Chem. Soc. Trans.* **1881**, *39*, 225.

(41) Japp, F. R.; Streatfield, F. W. *J. Chem. Soc. Trans.* **1882**, *41*, 146.

(42) White, E. H.; Harding, M. J. C. *J. Am. Chem. Soc.* **1964**, *86*, 5686.

(43) Kamidate, T.; Yamaguchi, K.; Segawa, T.; Watanabe, H. *Anal. Sci.* **1989**, *5*, 429.

(44) Macdonald, A.; Chain, K. W.; Nieman, T. A. *Anal. Chem.* **1979**, *51*, 2077.

(45) Marino, D. F.; Ingle Jr., J. D. *Anal. Chem.* **1981**, *53*, 294.

(46) Nakashima, K.; Yamasaki, H.; Shimoda, R.; Kuroda, N.; Akiyama, S.; Baeyens, W. R. G. *Biomed. Chromatogr.* **1997**, *11*, 63.

(47) Marino, D. F.; Wolff, F.; Ingle Jr., J. D. *Anal. Chem.* **1979**, *51*, 2051.

(48) Yamaguchi, S.; Kishikawa, N.; Ohyama, K.; Ohba, Y.; Kohno, M.; Masuda, T.; Takadate, A.; Nakashima, K.; Kuroda, N. *Anal. Chim. Acta.* **2010**, *665*, 74.

(49) Nakashima, K. *Biomed. Chromatogr.* **2003**, *17*, 83.

(50) Boyatzis, S.; Nikokavouras, J. *J. Photoch. Photbio. A.* **1988**, *44* 335

(51) Fridman, N.; Kaftory, M.; Eichen, Y.; Speiser, S. *J. Mol. Struct.* **2009**, *917*, 101.

(52) Kishikawa, N.; Ohkuma, M.; Wada, M.; Ohyama, K.; Ikeda, R.; Nakashima, K.; Kuroda, N. *J. Chromatogr. A.* **2011**, *1218*, 3002.

(53) Tordera, D.; Pertegas, A.; Shavaleev, N. M.; Scopelliti, R.; Orti, E.; Bolink, H. J.; Baranoff, E.; Gratzel, M.; Nazeeruddin, M. K. *J. Mater. Chem.* **2012**, *22*, 19264.

(54) Maji, S.; Sarkar, B.; Patra, M.; Kumar Da, A.; Mobin, S. M.; Kaim, W.; Kumar Lahiri, G. *Inorg. Chem.* **2008**, *47*, 3218.

(55) Shavaleev, N. M.; Adams, H.; Weinstein, J. A. *Inorg. Chim. Acta.* **2007**, *360*, 700.

(56) Wang, X.; Zheng, W.; Lin, H.; Liu, G.; Chen, Y.; Fang, J. *Tetrahedron Lett.* **2009**, *50*, 1536.

(57) Lo, K. K.-W.; Tsang, K. H.-K.; Hui, W.; Zhu, N. *Inorg. Chem.* **2005**, *44*, 6100.

(58) Striplin, D. R.; Crosby, G. A. *Chem. Phys. Lett.* **1994**, *221*, 426.

(59) Fredericks, S. M.; Luong, J. C.; Wrighton, M. S. *J. Am. Chem. Soc.* **1979**, *101*, 7415.

(60) Sun, J.; Zhao, J.; Guo, H.; Wu, W. *Chem. Commun.* **2012**, *48*, 4169.

(61) http://teaching.shu.ac.uk/hwb/chemistry/tutorials/molspec/nmr1.htm (accessed 12/02/2014).

(62) Atkins, P.; Overton, T.; Rourke, J.; M., W.; Armstrong, F. *Inorganic Chemistry, 4th Edition, OUP Oxford* **2006**.

(63) http://discover.osa.org/ accessed (16/02/2014).

(64) www.chemwiki.ucdavis.edu (accessed 16/02/2014).

(65) http://www.mhhe.com/physsci/chemistry/carey/student/olc/ch13ms.html (accessed 16/2/14).

(66) http://www.isis.stfc.ac.uk/instruments/small.

(67) http://www.isis.stfc.ac.uk/groups/large.

(68) http://www.ncnr.nist.gov/summerschool/ss08/pdf/SANS_NR_Intro.pdf accessed (16/02/2014).

(69) http://pubs.usgs.gov/of/2001/of01.

Chapter 2: Synthesis and investigation of luminescent rhenium(I) complexes of substituted imidazole[4,5-*f*]-1,10-phenanthroline derivatives

2.1 Introduction

In this chapter, eight novel diimine ligands were coordinated to the *fac*-[Re(CO_3)Br] core for investigation into luminescent responses to variations of functional groups. Four of the isolated complexes incorporated halide functional groups, whilst four incorporated different alkyl groups and extended chromophores. All complexes and ligands were fully characterised using a range of spectroscopic techniques. Crystal structures were also obtained for complexes [ReBr$(CO)_3$(**21**)], [ReBr$(CO)_3$(**23**)] and [ReBr$(CO)_3$(**25**)].

2.2 Properties and applications of [Re$(CO)_3$(diimine)]$^+$ complexes

Chapter 1 has provided the general background of the history and basic photophysical properties of Re-diimine complexes, therefore the introduction to this chapter will focus on the potential applications of rhenium tricarbonyl diimine complexes, and also how the photophysical properties can be altered with alterations to substituents located on the Re$(CO)_3$ core.

2.2.1 Effects of ligand substitution on the Re$(CO)_3$ core

Substituents directly coordinated to the Re-tricarbonyl core can have an effect on the nature of the emission of a [Re$(CO)_3$(diimine)] species, as shown by Demas and Degraff. [1] Incorporation of long chain alkyl substituents to the metal core of *fac*-[(Re(bpy)$(CO)_3$L]$^+$ (where L = $NC(CH_2)_nCH_3$, n = 0-17, bpy = 2,2′-bipyridine) has been shown to increase excited state lifetimes in a range of solvents with an increase in chain length. As there cannot be any appreciable inductive effect from the alkyl chain to affect the CT excited state, the increase in excited state lifetimes was attributed to the "foldback" of the alkyl chain over the bipyridine moiety of the molecule. The excitation resides in the metal-bipyridine portion of the molecule, and therefore it must be changes to this area which lead to perturbation of CT excited-state properties. It was concluded that the "foldback" of the alkyl chain over one face of the bipyridine moiety, and the resultant displacement of solvent from the local environment yielded different decay constants (τ). Further effects of changes to ligands directly attached to the Re(I) centre have been explored, displaying small changes to emission wavelengths, and in some cases emission can be switched to ligand-localized phosphorescence on cooling to 77K.[2]

2.2.2 Biological applications of *fac*-[Re(diimine)(CO_3)L]$^{0/+}$ complexes

The work undertaken on the photophysical properties of Re(I)-1,10-phenanthroline complexes has led to much research in the area of biological applications. Shown in Figure 33 are two complexes isolated in 1995 with the purpose of examining their DNA-binding abilities.[3]

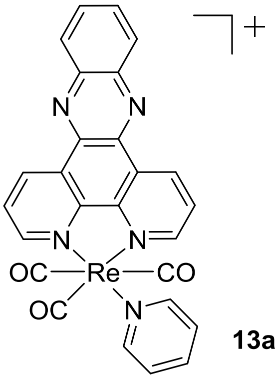

13a

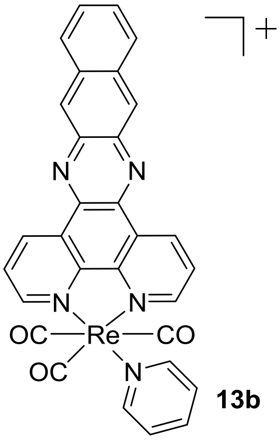

13b

Figure 33: Molecular structures of [Re(dppz)$(CO)_3$(py)]$^+$, **13a** and [Re(dppn)$(CO)_3$(py)]$^+$, **13b**

Both complexes exhibited low energy absorptions at 380 – 450 nm which were attributed to a mixture of d(Re)$\rightarrow\pi^*$ (diimine) MLCT and $\pi\rightarrow\pi^*$ diimine IL (intra-ligand) transitions. Emissions were found to be 556 nm and 588 nm in CH_2Cl_2 for **13a** and **13b**, respectively. Intercalation of these complexes into DNA (calf thymus) caused an enhancement in emission when excited at 350 nm, demonstrating its use as an efficient DNA sensor. Enhancement of the emission intensity is attributed to the intercalation process, which positions the complex in a hydrophobic pocket, isolating the rhenium complex from water that would otherwise quench the emission.

The biological applications of Re(I) polypyridyl complexes usually involve exploiting the ^{3}MLCT emission properties of rhenium(I).[4] Isothiocyanate and maleimide complexes have proven useful as amine and sulfhydryl specific luminescent biological labels.[5] A series of such complexes of the style [Re(CO_3)(N^N)(py-3-NCS)](CF_3SO_3) and [Re(N^N)(CO_3)(py-3-mal)](CF_3SO_3) were isolated, incorporating 1,10-phenanthroline, 2,2′-bipyridine and biquinoline derivatives (Figure 34). Electron donating and withdrawing substituents were again employed on the 1,10-phenanthroline derivatives in order to “tune” the optical properties of the system (py-3-NCS = 3-isothiocyanatopyridine; py-3-mal = 3-maleimidopyridine).

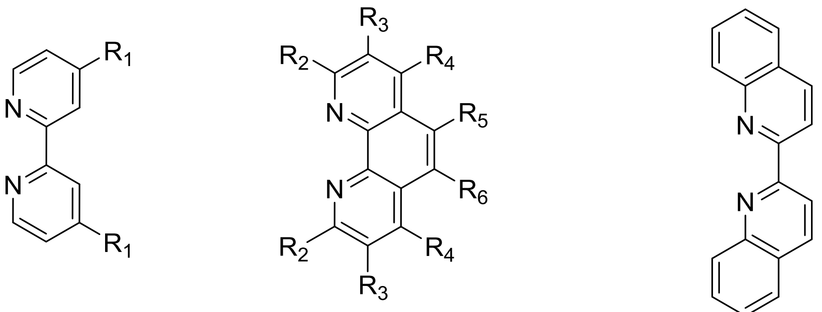

14a: R_1 = H
14b: $R_1 = CH_3$
14c: $R_1 = C(CH_3)_3$

15a: All H
15b: $R_2 = CH_3$
15c: $R_4 = CH_3$
15d: $R_4 = C_6H_5$
15e: $R_2 = CH_3$, $R_4 = C_6H_5$
15f: $R_3 = R_4 = CH_3$
15g: $R_5 = C_6H_5$
15h: R_5 = Cl

16

* R subtituents = H unless otherwise stated

Figure 34: Diimine ligands incorporated into the complexes

Upon irradiation, all ligands displayed intense and long-lived emission, originating from an excited state of ^{3}MLCT ($d\pi(\mathrm{Re})\rightarrow\pi^*(\mathrm{N^\wedge N})$) character. It was observed that ligands with electron-donating substituents on the diimine moiety emitted at a higher energy than those with electron-withdrawing substituents, or ligands that were more conjugated. Bioconjugation studies were undertaken for these complexes. The universal M13 reverse sequencing primer was labelled with [Re(**14a**)(CO_3)(py-3-NCS)](CF_3SO_3) and the resultant labelled species (Re-M13) was isolated and exhibited yellow luminescence at a wavelength of 548 nm (Figure 35) . Similarly, maleimide-containing Re complex was found to undergo addition reactions to form stable thioethers and as such was suitable to label an oligonucleotide, a cysteine-containing tripeptide glutathione and the serum albumins HSA and BSA (Human Serum Albumin and Bovine Serum Albumin respectively). All labelled molecules showed intense and long-lived ^{3}MLCT emission upon photoexcitation, and displayed promise as bio-detectors.[6]

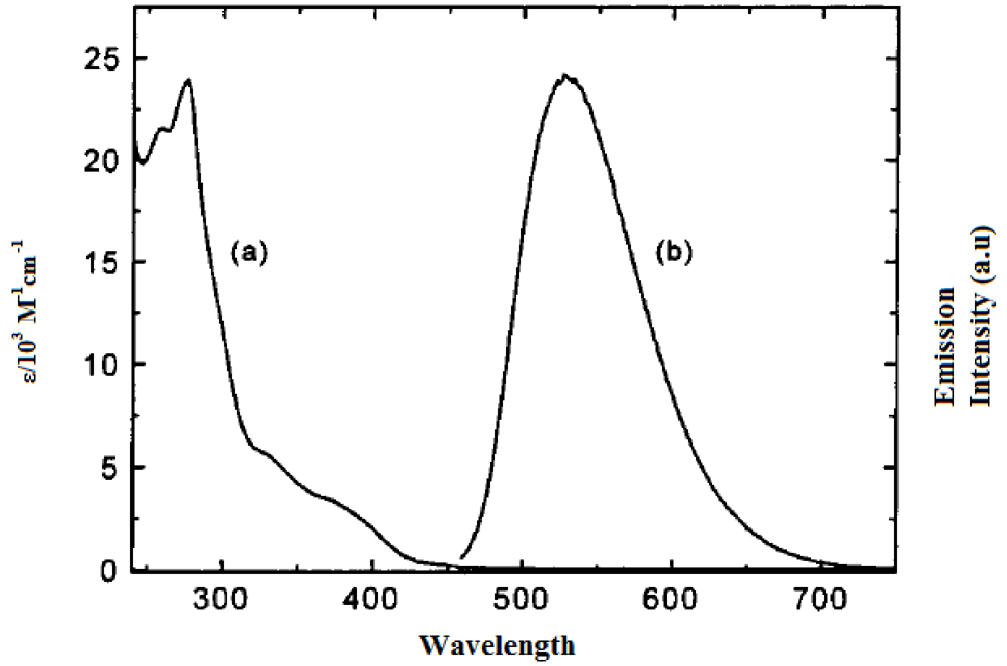

Figure 35: Electronic absorption (a) and emission spectrum (b) of [Re(**14a**)(CO_3)(py-3-mal)](CF_3SO_3).[6]

2.2.3 Photoswitchable luminescence of rhenium(I) tricarbonyl diimines

Switchable on/off emissions have become an increasingly important aspect of Re(I) tricarbonyl complexes, with applications in high density information storage.[7] Gray and Winkler explored the use of 1,2-di-(4-pyridyl)ethylene (dpe) as a potential method for luminescence on/off switching. Dpe can undergo reversible *trans-cis* photoisomerization upon UV excitation, and in this case coordination of dpe to a rhenium(I) tricarbonyl diimine core results in an emissive complex in its cis conformation (on, **17b**) and a non-emissive trans complex (off, **17a**)(Figure 36).

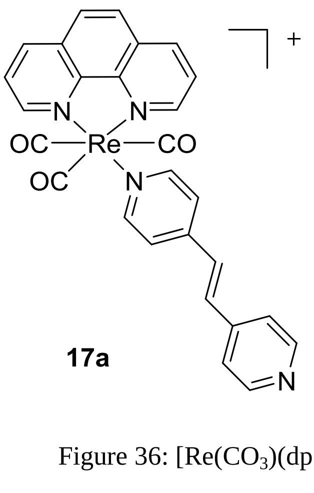

17a

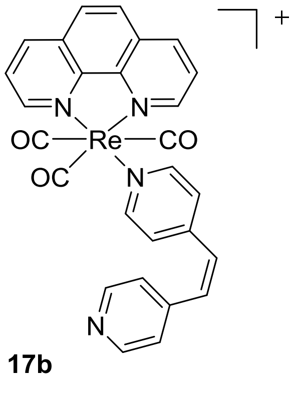

17b

Figure 36: [Re(CO_3)(dpe)(phen)]$^+$ *trans* (**17a**) and *cis* (**17b**)

The electronic absorption spectra showed that the absorption associated with the lowest spin-allowed transition of protonated *trans*-dpe was located at ≈ 317 nm, which is in a similar range for typical

MLCT excitations in $[ReL(CO)_3X]^{0/+}$. Typically, *cis*-stilbenes/stilbazoles have higher energy $\pi\rightarrow\pi^*$ transitions due to the twisting of the benzene/pyridine moieties, while the more planar trans-stilbenes/stilbazoles have a lower energy $\pi\rightarrow\pi^*$ transition. This distinction is crucial to these complexes behaving as photoswitches. Iha and Meyer have shown the lowest-lying excited state in the trans-dpe complex is primarily dpe-localized, for which radiative decay is negligible.[8] In uncomplexed trans-dpe 90% of photoexcited molecules return to the ground state via nonradiative relaxation (Figure 37). This however is not true for the *cis*-dpe complex, which has a higher energy π^* (dpe) excited state which is higher than the excited MLCT, therefore the lowest excited state has more MLCT character which allows radiative decay to compete with the nonradiative relaxation processes.

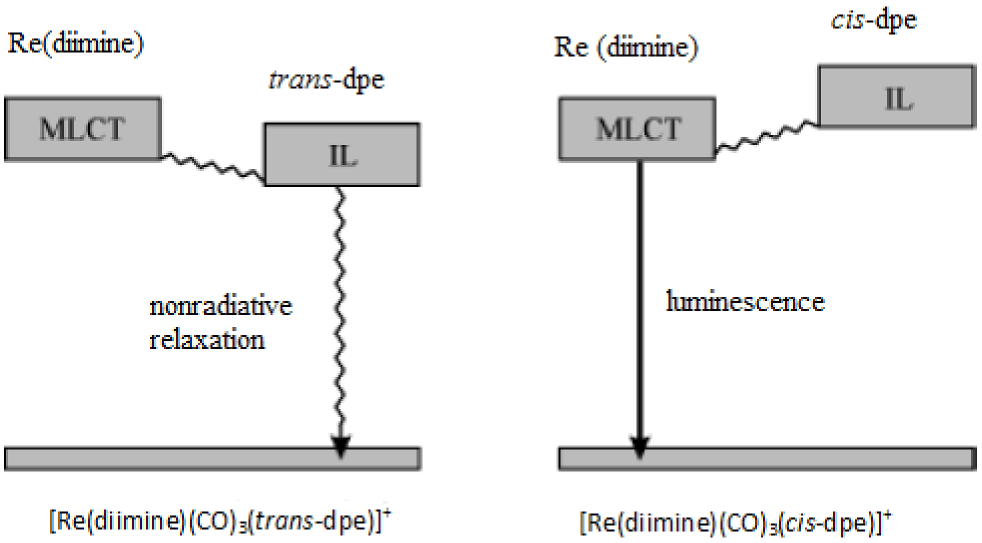

Figure 37: Scheme depicting radiative and non-radiative relaxation in **17a** and **17b**. [7]

Irradiation of the stable ambient temperature *trans*-dpe complex at 350 nm leads to photoisomerization to the *cis*-dpe complex which results in the on-switching of the yellow fluorescence. This can be “turned off” by irradiation at 250 nm, which causes reverse *cis-trans* isomerisation and switches off the yellow luminescence (Figure 38).

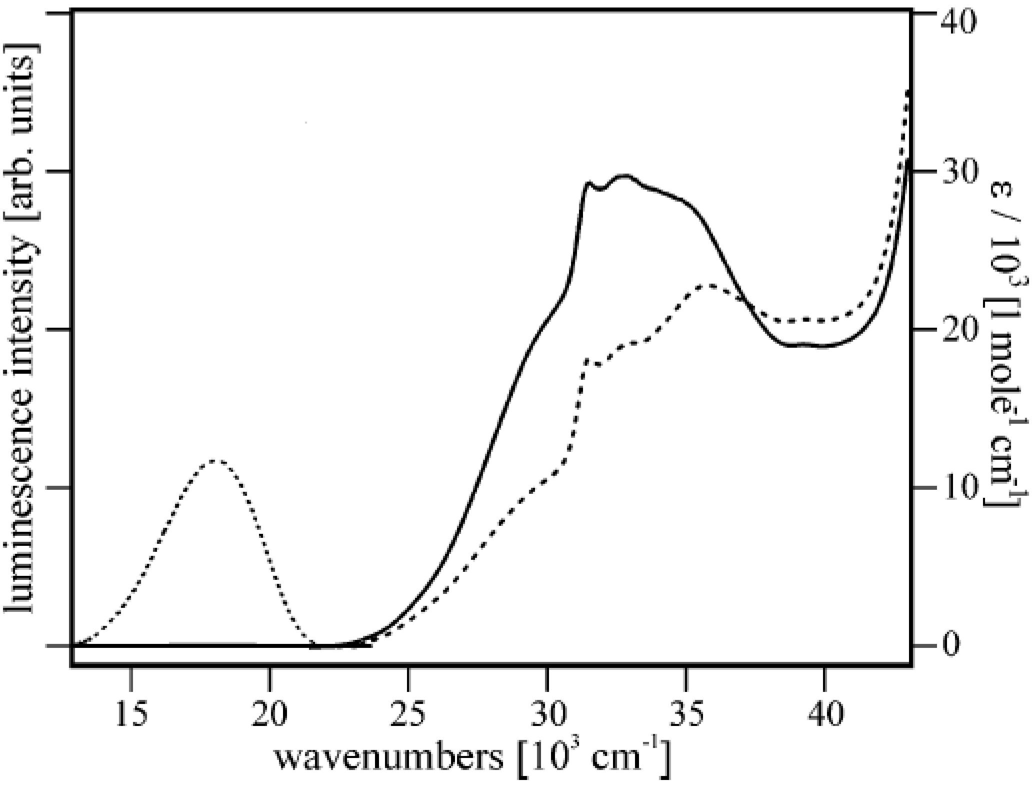

Figure 38: Absorption an emission spectra of **17a** (solid line) and **17b** (dashed line). [7]

2.2.4 Applications of $[Re(CO_3)(diimine)]^+$ complexes as electroluminescent devices

Electroluminescence (EL) and electroluminescent devices have been the subject of interest since the discovery of the first organic light-emitting EL devices 25 years ago.[9,10] Chan and co-workers explored the potential advantages of using Re(I) complexes in EL devices, synthesising a tri-functional complex (Figure 39).[11]

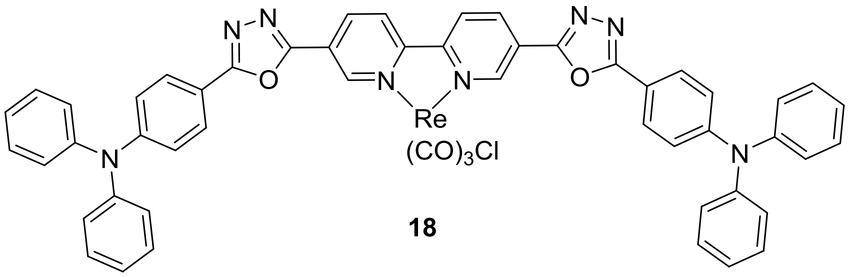

18

Figure 39: Light emitting complex **18**

The ligand incorporated three functional groups, the hole-transporting triphenylamine, the electron-transporting oxadiazole moieties, and the 2,2′-bipyridyl unit which provided a binding site to form light emitting complexes, using metals such as Re(I) and Ru(II). Electronic absorption spectra of the complex showed absorption due to MLCT at 478 nm, a lower energy than is usually expected for

Re(I) tricarbonyl diimine complexes. This was attributed to the electron-withdrawing effect of the oxadizole moiety which lowered the π^* energy level.

2.2.5 OLED (organic light emitting diode) devices

The identification of novel phosphorescent materials has garnered significant interest due to their potential applications as Organic Light-Emitting Diodes (OLEDs). Early OLEDs largely consisted of small organic molecules which emitted light through fluorescence. Under excitation, both triplet and singlet excited states are formed; therefore harvesting luminescence from only singlet electrons significantly limits the luminescence efficiency in purely fluorescent devices.

As a triplet emitter Re(I)tricarbonyl diimine complexes are suitable for use as OLED devices. Several have been reported, including by Wang and co-workers who prepared a yellow OLED based on [Re(t-Bubpy)$(CO)_3$Cl], **19a** (t-Bubpy = 4,4′-bi(*tert*-butyl)-2,2′-bipyridine) (Figure 40) with an efficiency of up to 1061mW^{-1}.[12] Energy transfer from a $BePP_2$, **19b** (PP = 2-(2-hydroxyphenyl pyridine)) to the [Re(t-Bubpy)$(CO)_3$Cl] codeposited films were explored via photoluminescence and electroluminescence. EL emission peaks varied with different composition % of [Re(t-Bubpy)$(CO)_3$Cl], ranging from 560 nm at 100% to 535nm at 3%. It was observed that a higher EL efficiency was observed for the codeposited films where the **19a** wt.% was higher (≈ 90%).

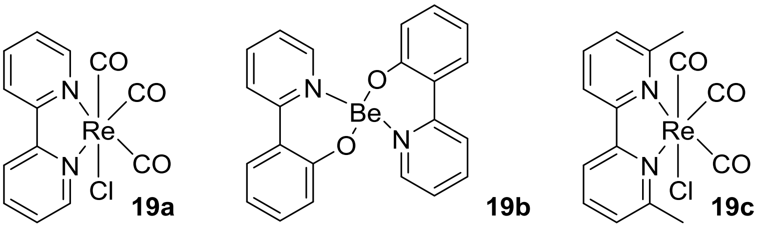

Figure 40: Molecular structures of **19a**,**19b** and **19c**

Li and co-workers have also reported highly efficient devices based on **19a** and [Re(dmphen)$(CO)_3$Cl], **19c** doped in dicarbazole host material.[13] Both materials displayed electroluminescence at 10 and 6 wt.% respectively at 6 V (Figure 41).

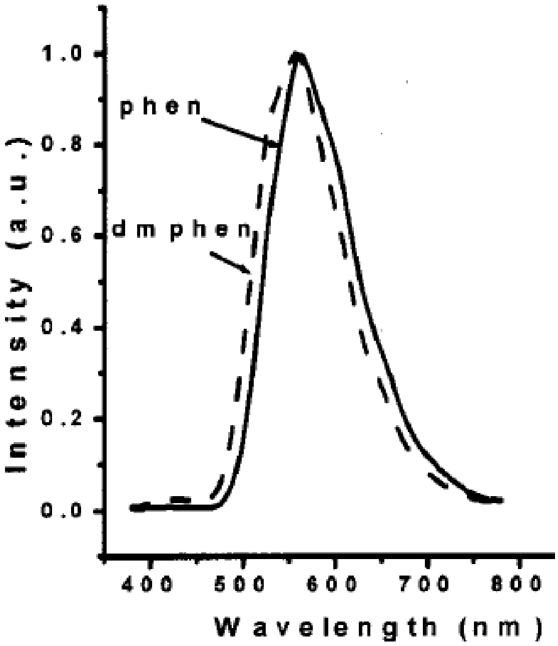

Figure 41: The electroluminescence spectra of OLEDs based on **19a** and **19c** at the concentration of 10 and 6 % in CBP at 6 V, respectively.[13]

The maximum efficiency and brightness achieved from the devices based on **19a** and **19c** are 6.67 cd/A and 2769 cd/m^2, and 7.15 cd/A and 3686 cd/m^2, respectively. These values indicates high performance, as devices based on osmium complexes only reach an efficiency of < 2 cd/A.[14] However it was noted that contrary to other electrophosphorescent devices which achieve maximum efficiencies at very low current density (< 0.1 mA/cm^2), **19a** and **19c** required between 1 and 10 mA/cm^2. The low efficiency at low current density was attributed to the leak current which could be overcome by improving the fabricating technique.

2.3 Aims

The aims of the project will be developed through the following key areas:

-The synthesis and characterisation of novel heterocyclic chromophoric “lophine” ligands with tuneable optical properties as fluorescent “tags”.

-Investigation of the photophysical properties of these ligands, with particular focus on the changes in optical properties with alterations in R and R′ groups.

-The synthesis and characterisation of novel rhenium complexes allowing investigation of photophysical aspects.

-Obtaining x-ray crystal structures of the novel rhenium complexes to allowing insight into the structure of complexes and how this may affect phosphorescence emission.

2.4 Results and discussion

2.4.1 Isolated ligands

Listed in Figure 42 are compounds which were isolated in this chapter, along with their designated number for reference.

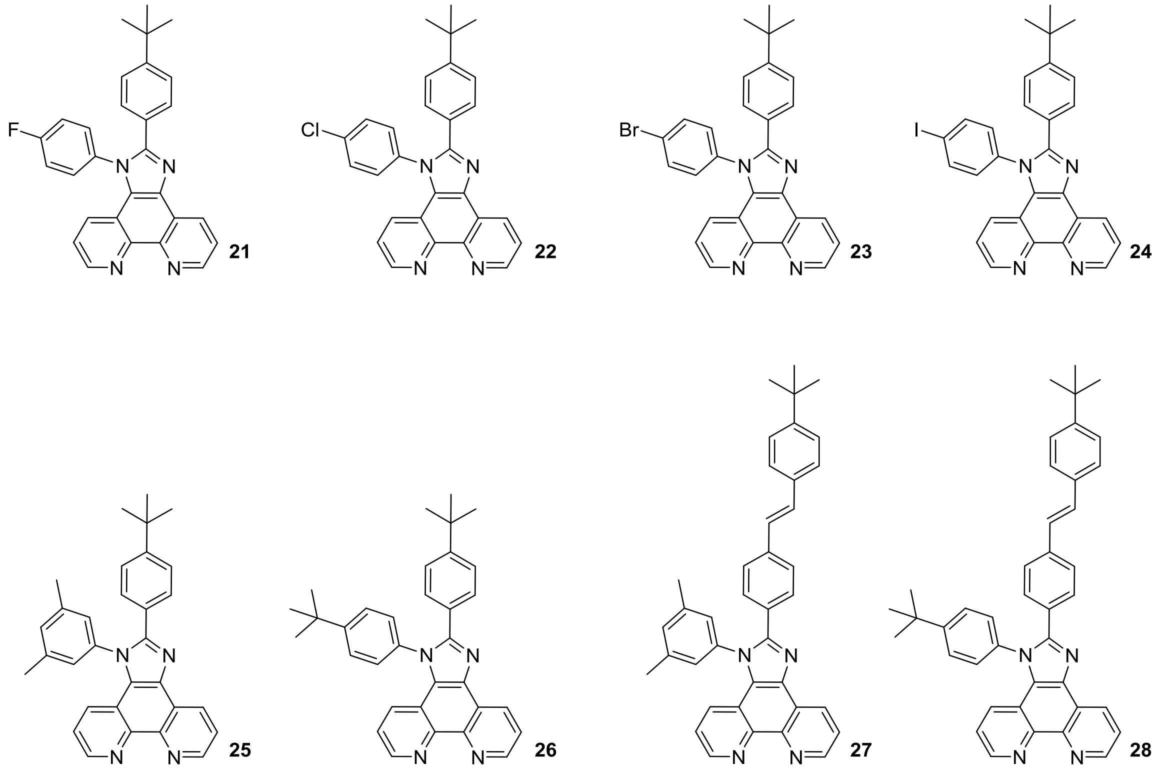

Figure 42: Isolated ligands

2.4.2 Ligand synthesis

This chapter presents a study of fused imidazo[4,5-*f*]-1,10-phenanthroline ligands and their subsequent reactions to form Re(I) complexes. The ligands have been designed with differing functional groups in order to explore changes in solubility, and also to investigate the effect of functional groups on the electronics and optical properties of the systems. All ligands have been fully characterised using a variety of spectroscopic and analytical techniques, confirming the proposed structures in each case. All relevant supporting data is presented in the experimental section (2.7).

Scheme shows the general scheme for the formation of fused imidazo[4,5-*f*]-1,10 phenanthroline “lophine” ligands, **20**.

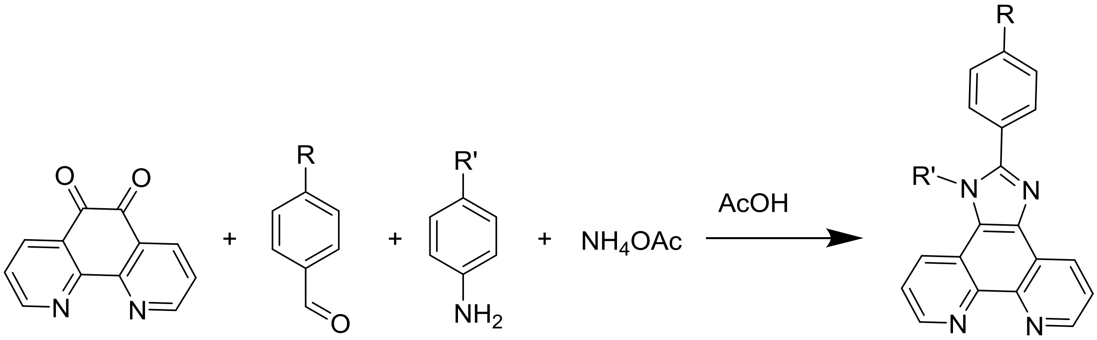

20

Scheme 3: Synthesis of fused imidazo[4,5-*f*]-1,10-phenanthroline

Ligands **21-28** were isolated in moderate-to-good yields according to adaptations of previously reported approaches, involving the 3 hour reflux in acetic acid of equivalent amounts of 1,10-phenanthroline-5,6-dione, a benzaldehyde derivative and an aniline with excess ammonium acetate.[15] Table shows the range of R and R′ groups utilised for all the isolated ligands in this chapter. Yields were found to vary from 28% - 90% as a result of changes to the R and R′ substituents. Ligands **21-24** incorporated halides into the R′ side-arm, and a significant difference in percentage yield were observed, with the fluoro-containing molecule being isolated in a significantly lower yield. A possible explanation for this is the effect of the halide group on the aniline derivative ($X-C_6H_4NH_2$ where X = F, Cl, Br or I). In general, aniline reacts as a base in a similar way to primary amines by exploiting the lone pair of the nitrogen to accept a hydrogen ion. However, anilines are far less reactive than amines due to delocalisation of the nitrogen lone pair. This results in the lone pair electrons being less readily available and reduced reactivity as a nucleophile. Fluorine is extremely electronegative and as such attracts electron density towards itself. As a result this may reduce the electron density around the nitrogen lone pair and result in increased reactivity of the aniline as a base compared to the other halide molecules. This may increase the amount of side reactions that occur (e.g. with the 1,10-phenanthroline-4,5-dione) and as such reduce the overall yield percentage, although it is difficult to prove that this is the case. Fluorine is significantly more electronegative which may explain why the yield values of Cl, Br and I are closer together, although there is still a general trend of increasing yield.

Ligand	R	R′	Yield (%)
21	4-^{t}Bu	4-FC_6H_4	28
22	4-^{t}Bu	4-ClC_6H_4	51
23	4-^{t}Bu	4-BrC_6H_4	49
24	4-^{t}Bu	4-IC_6H_4	63
25	4-^{t}Bu	3,5-MeC_6H_3	67
26	4-^{t}Bu	4-^{t}BuC_6H_4	57
27	4-^{t}Bustyr*	3,5-MeC_6H_3	90
28	4-^{t}Bustyr*	4-^{t}BuC_6H_4	29

Table 7: Isolated ligands **21-28**

Yield differences of **25-28** may be attributed to differences in solubility of the isolated products. 3,5-dimethyl phenyl containing **25** and **27** both were isolated in higher yields than the 4-^{t}butyl analogues, and were isolated with relative ease.

Element	Electronegativity (Pauling scale)
F	3.98
Cl	3.16
Br	2.96
I	2.66

Table 8: Electronegativity values

*

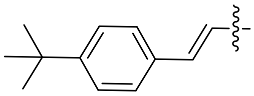

= 4-^{t}Bustyr

Ligands **21-28** were isolated as pale off-white or light yellow powders through washing with copious amounts of water followed by extraction into CH_2Cl_2 or $CHCl_3$. The ligands showed good solubility in common organic solvents, imparted by the functionalised aryl groups.

2.4.3 Characterisation of the ligands

^{1}H and ^{13}C NMR spectra of ligands **21-28** have been obtained in $CDCl_3$ at 298 K. As an example, the ^{1}H NMR spectrum of **27** is shown in Figure 43. ^{1}H NMR Peaks in the aliphatic region at 1.33 and 2.43 ppm show the presence of the t-butyl and dimethyl groups. At 7.12 ppm there is a clear roofed pair of doublets, corresponding to the alkene protons located on the axial t-butyl styrene moiety. In the aromatic region there are numerous signals, some of which overlap, however clearly distinct at 9.0-9.2 ppm are three signals, two of which correspond to protons which are the closest in proximity to the highly electronegative and deshielding imines of the phenanthroline. The other signal corresponds to the phenanthroline proton which lies closest to the R′ groups as a result of deshielding from the substituted imidazole.

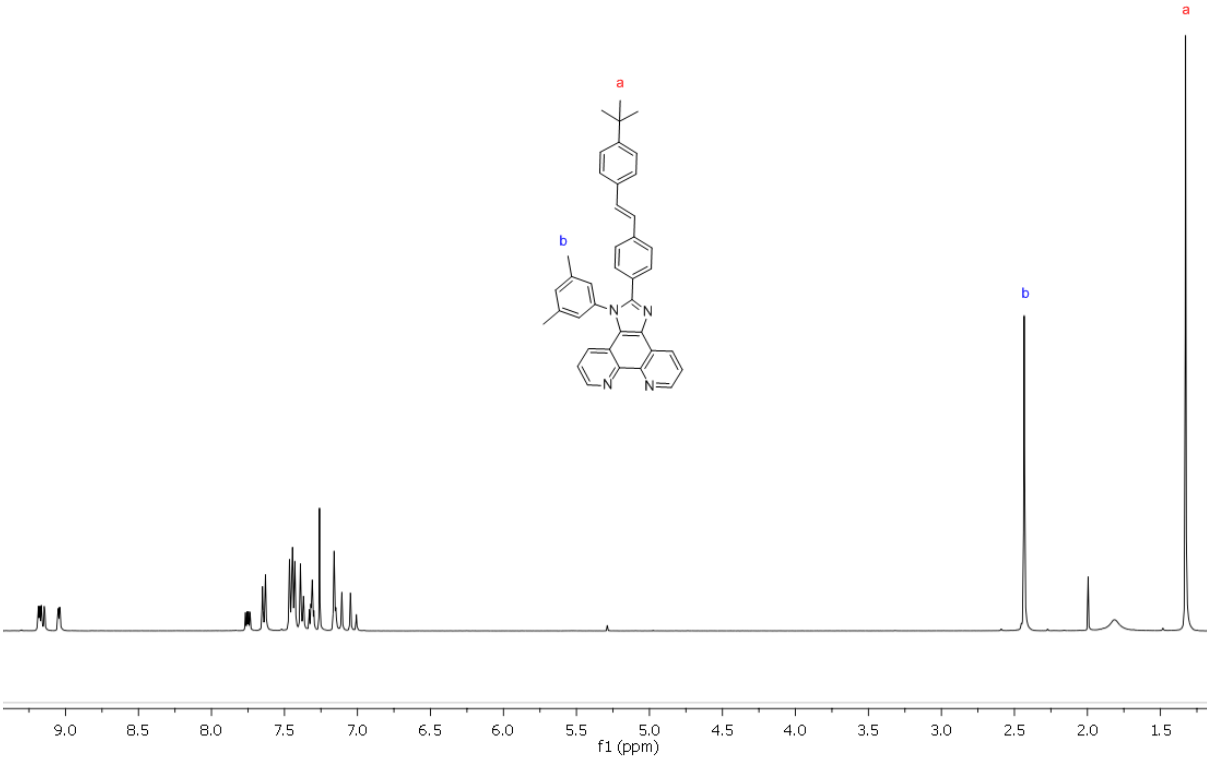

Figure 43: NMR spectrum of **27**. (# = residual solvent peaks, * = $CDCl_3$)

The ^{13}C NMR spectra of the isolated compounds are complicated as the lack of symmetry (with the exception of σ_h) in the molecule leads to many signals in the aromatic region (150-100 ppm). In addition many of the carbon atoms are quaternary and as such may not appear with great intensity on the spectra. The aliphatic carbons are easily identifiable.

High-resolution ES mass spectrometry confirmed the presence of the molecular ions in each case as $[M]^+$. Isotopic patterns were observed for the halide-containing **21-24** consistent with that expected.

Infrared spectra were obtained on KBr plates for each ligand, for which few notable peaks were observed. Each compound had a band at ≈ 2900 cm^{-1}, corresponding to an alkyl C-H stretch and numerous bands in the “fingerprint” region of the spectra. No starting material benzaldehyde, aniline or ketone peaks were observed for any of the compounds.

2.4.4 Electronic Absorption Spectroscopy

Electronic absorption spectroscopy in $CHCl_3$ at 298 K of the isolated ligands showed bands in the region of 275 nm assigned to $\pi \rightarrow \pi^*$ absorptions with a high extinction coefficient expected of an extended conjugated framework. Table 9 shows the absorption wavelengths, molar absorption coefficient values and emission wavelengths of **21-28.**

Compound Number	R	R′	Absorption λ_{max} /nm (ε/$M^{-1}cm^{-1}$)	Emission λ_{max}/nm
21	4-^{t}Bu	4-FC_6H_4	278 (25000), 315 (sh) (14600)	409
22	4-^{t}Bu	4-ClC_6H_4	275 (26700), 311 (sh) (17800), 368 (sh) (3000)	411
23	4-^{t}Bu	4-BrC_6H_4	279 (25000), 321 (sh) (15200)	411
24	4-^{t}Bu	4-IC_6H_4	276 (30100), 318 (sh) (17100)	410
25	4-^{t}Bu	3,5-MeC_6H_3	278 (42365), 319 (sh) (19912), 376 (sh) (1330)	415
26	4-^{t}Bu	4-$^tBuC_6H_4$	275 (39500), 368 (2300)	415
27	4-^{t}Bustyr	3,5-MeC_6H_3	289 (28800), 345 (19600)	425
28	4-^{t}Bustyr	4-$^tBuC_6H_4$	288 (28200), 344 (34100)	456

Table 9: λ_{max} (abs) and λ_{max} (em) for **21-28** in $CHCl_3$ at 298 K

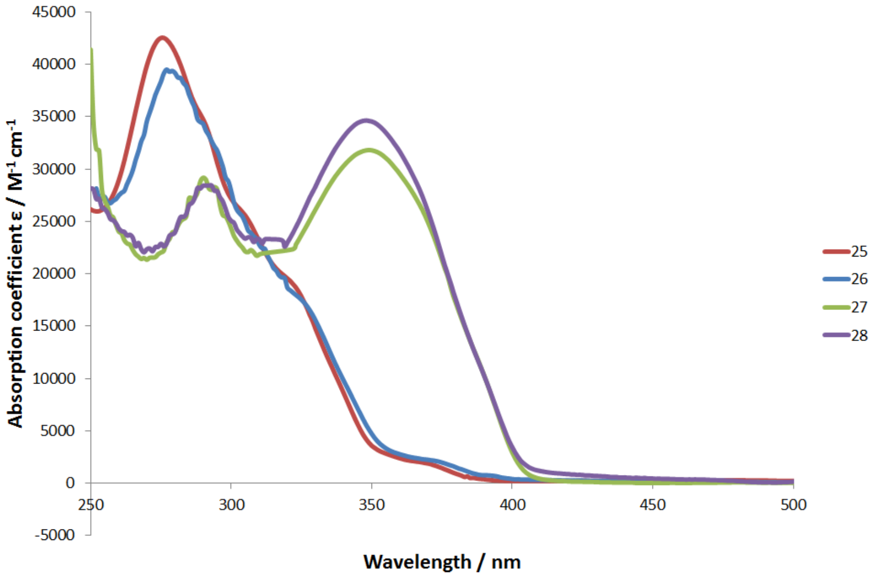

Figure 44: UV-vis absorption spectra of **25-28** in $CHCl_3$ at 298 K

All ligands have high extinction coefficients ranging from 14,500 to 42,400 $M^{-1}cm^{-1}$, with the halide-containing **21-24** having similar extinction coefficients and a λ_{max} at about 275 nm. These results are comparable to previously explored fused and non-fused lophines.[16,17] The 4-^{t}Bustyr containing lophines **27** and **28** both displayed lower-energy absorptions at ≈ 350 nm. These can be attributed to the extended conjugation of these chromophores, which renders the π^* orbital of these ligands to be more stabilised compared to **25** and **26**.

All ligands were found to be emissive (λ_{ex} = 375 nm), with small to moderate Stokes' shifts, and relatively short lifetimes were observed in the region of 1-4 ns, attributed to the efficient process of the spin allowed relaxation of an excited singlet state to a ground state configuration. The emission wavelengths of **21-24** were found to be nearly identical (in the region of 409-411 nm), indicating that the halides on the pendant side-arm (R′) had little or no effect on the photophysical properties of the fluorophore, suggesting the "tuning" of the optical properties of the molecule may be a result of changes to the apical position of the "R" group. Previous research has shown that different substituents on the apical group can affect the photophysics of a lophine. [16] Figure 45 shows the normalised emission spectra of **25-28**.

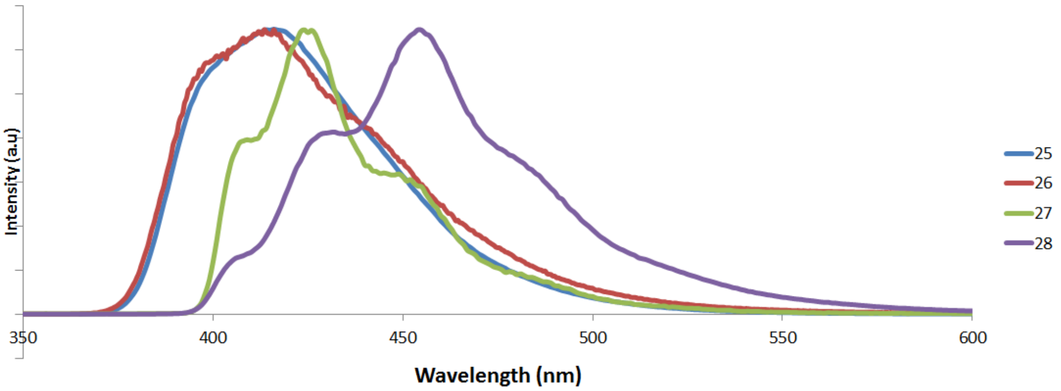

Figure 45: Emission Spectra of **25-28** in $CHCl_3$ at 298 K

The ligand pair of **25** and **26** also displayed no change in emission with the change of the R′ group, with both appearing as broad peaks. Unlike ligands **21-26**, ligands **27** and **28** showed significant variation in both the emission wavelength and appearance of the emission peak, which are very sensitive to the nature of the incorporated substituents. **28** is bathochromically shifted to about 455 nm, which is a shift of about 30 nm compared to the analogous **27** which contains a different R′ group. This implies that R and R′ do not always have an independent effect on fluorescence, and that a combination of the two may alter emission. Both t-butyl styrene containing ligands **27** and **28** show vibronic structures superimposed upon the peak appearances centred at 424 and 453 nm, respectively, suggesting rigidity of the chromophore.

2.5 Coordination chemistry of 21-28 with Re(I)

The coordination chemistry of the ligands **21-28** was explored with Re(I), wherein heating stoichiometric equivalents of ligand and $ReBr(CO)_5$ in toluene for 24 hr produced the desired complexes as powder of the general formulation *fac*-$[ReBr(CO)_3(N^\wedge N)]$ (where N^N = **21-28**, Scheme 4).

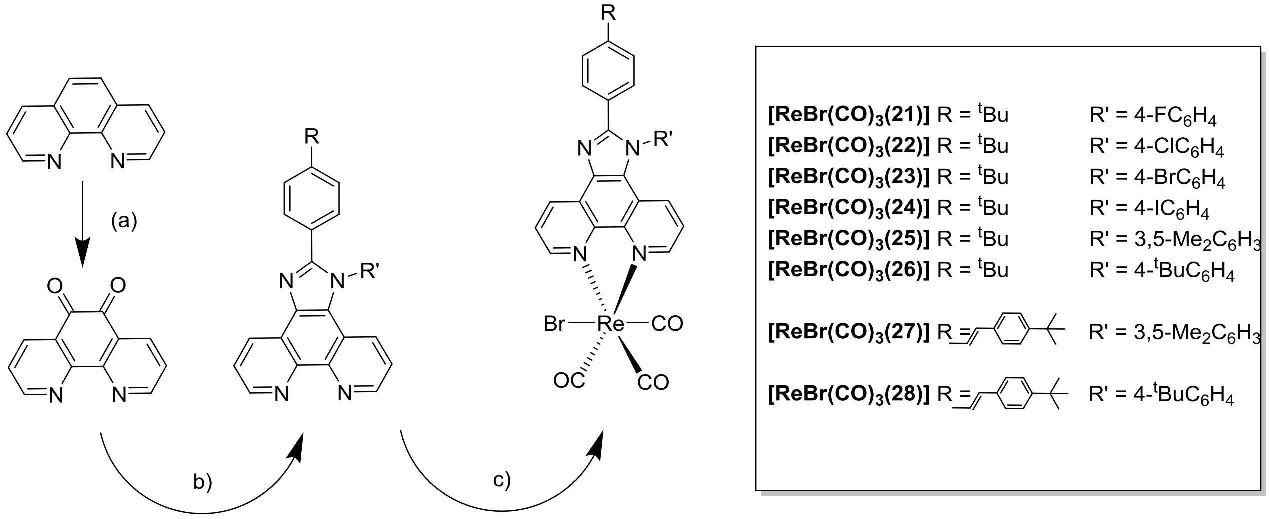

Scheme 4: Route to the new complexes. a) conc. H_2SO_4/ conc.HNO_3 b)R^1-NH_2, R^2-C_5H_6(CHO), NH_4OAc, AcOH, c) $Re(CO)_5Br$, toluene, Δ.

2.5.1 Characterisation of the complexes

^{1}H and ^{13}C{^{1}H} NMR spectra of all *fac*-[Re(CO)$_3$Br(N^N)] complexes were obtained, with significant chemical shift variations confirming coordination to rhenium. The ^{1}H NMR spectrum of the complexes show the most significant shifts belonged to the protons in closest proximity to the rhenium metal, which leads to proton deshielding and a down field shift (Figure 46). For example, ligand **25** shows a shift of the phenanthroline aromatic protons from 9.1 to 9.4 ppm. The observed shifts are similar to those observed for coordination of bipy to Re(I), which also exhibited a shift of the doublets associated with bipy.[18] The ^{1}H NMR spectrum of these complexes also seems to imply that there is free rotation about the apical C-C bond and also about the side-arm C-C bond. This is evident in the fact that peaks attributed to equivalent aromatic protons on the aryl rings as well as the aliphatic groups (^{t}Butyl and 3,5 dimethyl) appear in the NMR spectrum as singular sharp peaks in contrast to multiple or broadened peaks, as was observed for the free ligand.

^{13}C NMR spectroscopy also provides evidence for successful coordination of Re as evidenced by slight change in the chemical shifts of the aromatic carbons. Additionally, there are peaks visible at 190-197 ppm in some of the complexes which correspond to the C≡O coordinated to the rhenium metal. This is not seen in some of the complexes which were not of a sufficiently high concentration due to the fact that these carbons are quaternary and bonded to extremely electron withdrawing groups.

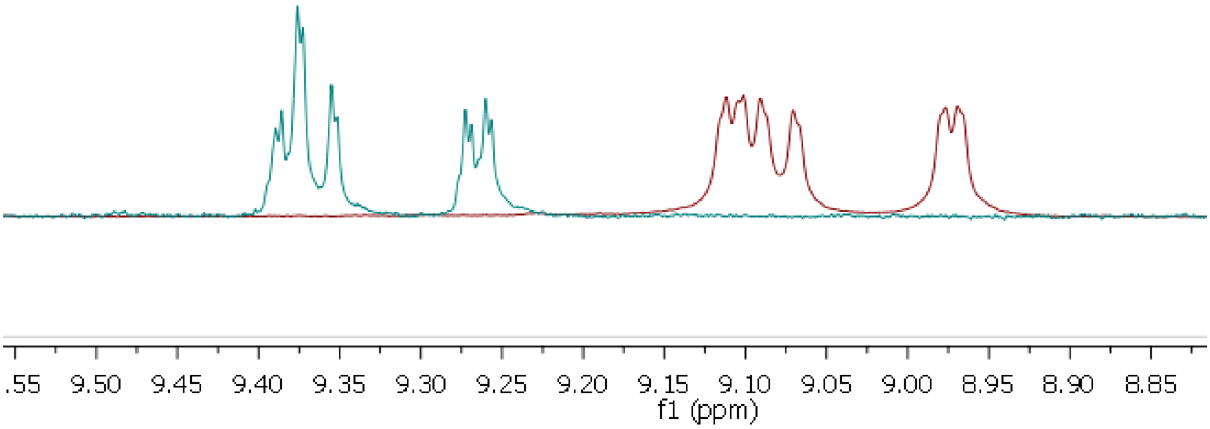

Figure 46: NMR spectrum of **25** (red line) and [Re(CO)$_3$Br(**25**)] (blue line).

Solid-state IR studies were conducted on the complexes commonly revealing three bands (Figure 47), the two lower frequency absorptions often overlapping, suggesting the local symmetry can be approximated to C_s (2A′ + A″) as expected for the facially capped coordination geometry. The absorption frequencies did not change drastically with a change in the coordinating lophine.[19]

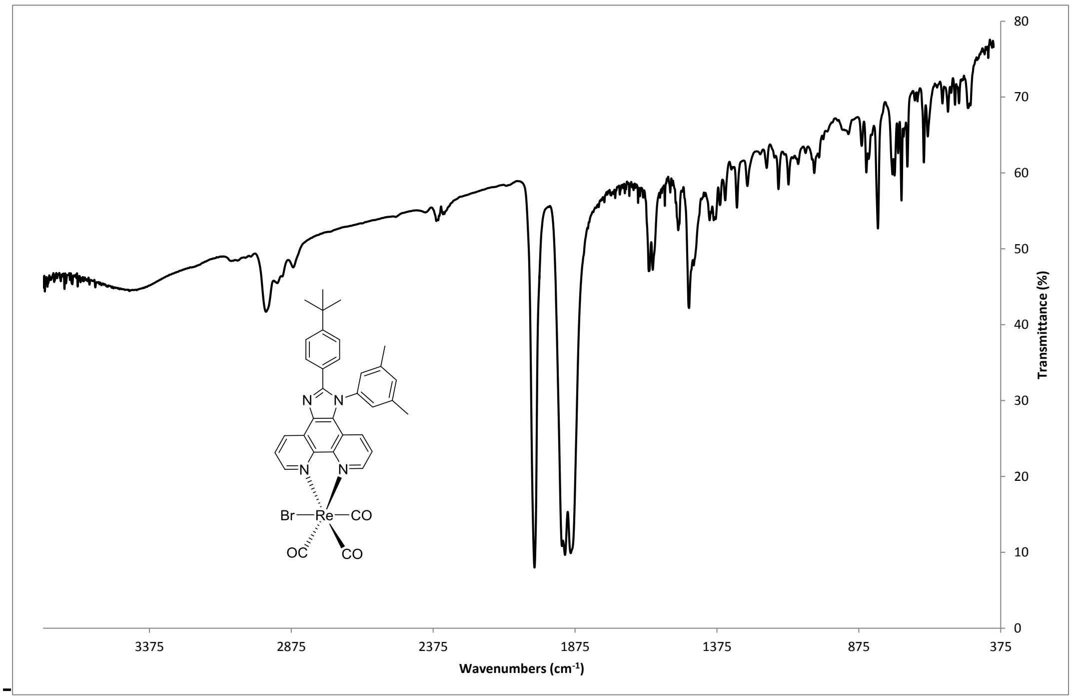

Figure 47: IR spectrum of complex [Re(CO)$_3$(**24**)Br]

HR electrospray mass spectrometry (positive mode) showed that the neutral complexes fragmented in a predictable manner, substituting the axially coordinated bromide anion with carrier solvent derived MeCN, resulting in an overall cationic species [Re(CO)$_3$(MeCN)(N^N)]$^+$, with an isotopic distribution consistent for rhenium.

2.5.2 Structural studies

Single crystal X-ray diffraction studies were undertaken on three complexes, ***fac*-[ReBr(CO)$_3$(21)]**, ***fac*-[ReBr(CO)$_3$(23)]** and ***fac*-[ReBr(CO)$_3$(25)]**. Suitable crystals were obtained by the slow evaporation of a chloroform solution of the complex solution over a period of 72 h. ***fac*-[ReBr(CO)$_3$(21)]** **c**rystallised as a chloroform sesquihydrate solvate in C2/c symmetry, ***fac*-[ReBr(CO)$_3$(23)]** crystallised as a chloroform di-solvate in P1 symmetry, whilst ***fac*-[ReBr(CO)$_3$(25)]** crystallised in P-1 symmetry as a partial water-hexane solvate. The structures are very similar and only ***fac*-[ReBr(CO)$_3$(23)]** will be described in detail, with the structures of ***fac*-[ReBr(CO)$_3$(21)]** and ***fac*-[ReBr(CO)$_3$(25)]** being summarised in the Supporting Information. The parameters associated with the data collection for ***fac*-[ReBr(CO)$_3$(23)]** are shown in Table 10, and Figure 48 illustrates the structure of ***fac*-[ReBr(CO)$_3$(23)]** in the solid-state with selected bond length and angle data. Here we observe octahedral coordination geometry as expected for a d^6 Re(I) complex, with **23** chelating *trans* to two carbonyl ligands, with the third CO ligand and bromide donors occupying axial positions. Bond lengths and angles are typical for a {ReBr(CO)$_3$} complex of a chelating diimine.[19,20] For all the complexes ***fac*-[ReBr(CO)$_3$(21)]**, ***fac*-[ReBr(CO)$_3$(23)]** and ***fac*-[ReBr(CO)$_3$(25)]** disorder was observed for the axial bromide and axial carbonyl ligands. The imidazo[4,5-*f*]-1,10-phenanthroline core of the ligand framework is essentially co-planar with the 'Re(CO)$_2$' fragment of the complex, whilst the *p*-^{t}Bu-phenyl group deviates from co-planarity with the heterocyclic core of the ligand with a torsion angle of 20.3°; the *p*-bromophenyl group is almost orthogonal to the ligand core with a torsion angle of 81.8°. The packing of ***fac*-[ReBr(CO)$_3$(23)]** revealed no significant π-stacking interactions and a hydrogen bonding interaction (2.412 Å) between the axial carbonyl ligand and a chloroform molecule of solvation.

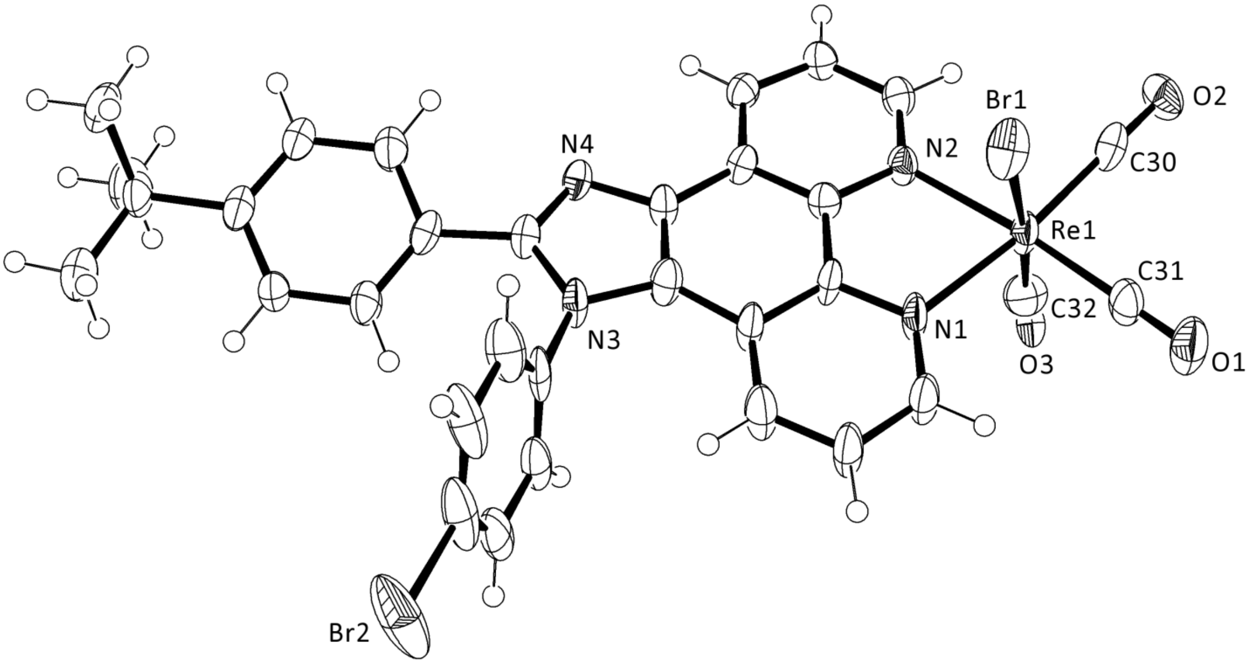

Figure 48: Ortep3 plot of complex ***fac*-[ReBr(CO)$_3$(23)]**. Ellipsoids are drawn at 50% probability. Selected data - bond lengths (Å): Re1-Br1, 2.5528(17); Re1-N1, 2.169(7); Re1- N2, 2.176(6); Re1-C30, 1.935(10); Re1-C32, 1.926(10); Re1-C31, 1.913(9); C30-O1 1.141(11); C31-O2 1.162(11); C32-O3 1.086(10). Bond angles(°) C31-Re1-C32, 92.2(9); C31-Re1-C30, 87.2(4); C32-Re1-C30, 91.7(8); C31-Re1-N1, 98.3(3); C32-Re1-N1, 92.8(8); C30-Re1-N1, 172.8(3); C31-Re1-N2, 173.4(3); C32-Re1-N2, 89.8(8); C30-Re1-N2, 99.0(3); N1-Re1-N2, 75.3(2); C31-Re1-Br1, 90.6(3); C32-Re1-Br1, 175.1(8); C30-Re1-Br1, 92.4(3); N1-Re1-Br1, 82.9(2); N2-Re1-Br1, 87.01(19). Note that Br1 and the axial carbonyl ligand (C32-O3) are disordered.

Table 10: Crystal data and structure refinement parameters for ***fac*-[ReBr(CO)$_3$(23)].**

CCDC Reference	942268
Chemical formula	$C_{32}H_{23}Br_2N_4O_3Re\cdot 2(CHCl_3)$
M_r	1096.30
Crystal system, space group	Triclinic, $P1$
Temperature (K)	150
a, b, c (Å)	10.9351 (4), 12.5833 (4), 14.5001 (5)
α, β, γ (°)	103.635 (2), 97.470 (2), 99.604 (2)
V (Å^3)	1881.71 (11)
Z	2
Radiation type	Mo $K\alpha$
μ (mm^{-1})	5.82
Crystal size (mm), description	0.40 × 0.20 × 0.10, yellow plate
Index ranges	$h = -12 \leq h \leq 12, -15 \leq k \leq 14, -16 \leq l \leq 17$
Absorption correction	Empirical (using intensity measurements) *DENZO*/*SCALEPACK*
T_{min}, T_{max}	0.204, 0.594
No. of measured, independent and observed [$I > 2\sigma(I)$] reflections	12296, 6820, 4870
R_{int}	0.056
$(\sin \theta/\lambda)_{max}$ (Å^{-1})	0.610
$R[F^2 > 2\sigma(F^2)]$, $wR(F^2)$, S	0.048, 0.121, 1.03
No. of reflections/parameters/restraints	6820/520/155
H-atom treatment	H-atom parameters constrained
$\Delta\rho_{max}$, $\Delta\rho_{min}$ (e Å^{-3})	1.31, −1.68

X-ray Structure of *fac*-[ReBr(CO)$_3$(21)]

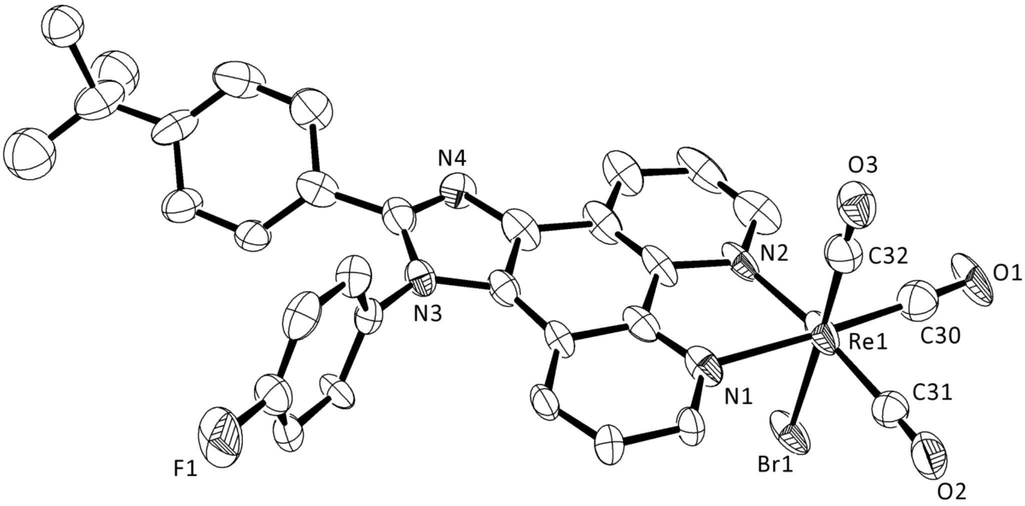

Figure 49: Ortep3 plot of complex Y. Ellipsoids are drawn at 30% probability. Hydrogen atoms omitted for clarity. Selected data – bond lengths (Å): Re1-Br1, 2.579(2); Re1-N1, 2.177(12); Re1-N2, 2.102(16); Re1-C30, 1.93(2); Re1-C31, 1.940(19); C32- Re1 1.920(10); C30-O1, 1.14(2); C31-O2, 1.132(19); C32- O3, 1.091(10); C30-O1, 1.14(2); C31-O2, 1.132(19); C32- O3, 1.091(10). Bond angles (°):C32-Re1-C30 90.2(11); C32-Re1-C31 87.4(11); C30-Re1-C31 86.9(8); C32-Re1-N2 94.9(10); C30-Re1-N2 99.0(6); C31-Re1-N2 173.7(6); C32A-Re1-N1 89(4); C32-Re1-N1 93.1(9); C30-Re1-N1 173.8(7); C31-Re1-N1 98.5(7); N2-Re1-N1 75.5(5); C32-Re1-Br1 178.1(9); C30-Re1-Br1 91.6(6); C31-Re1-Br1 93.5(5); N2-Re1-Br1 84.1(3); N1-Re1-Br1 85.1(3). Note that Br1 and the axial carbonyl ligand (C32-O3) are disordered. There is also rotational disorder within the *tert*-butyl group.

Table 11: Crystal data and structure refinement parameters for ***fac*-[ReBr(CO)$_3$(21)].**

CCDC Reference	942267
Chemical formula	$C_{32}H_{23}BrFN_4O_3Re\cdot1.54(H_2O)\cdot CHCl_3$
M_r	943.81
Crystal system, space group	Monoclinic, *C*2/*c*
Temperature (K)	150
a, *b*, *c* (Å)	21.3850 (6), 13.5594 (6), 24.8012 (10)
β (°)	92.823 (2)
V (Å^3)	7182.8 (5)
Z	8
Radiation type	Mo *K*α
μ (mm^{-1})	4.77
Crystal size (mm), description	0.25 × 0.25 × 0.20, yellow block
Index ranges	$h = -27 \leq h \leq 27, -16 \leq k \leq 17, -32 \leq l \leq 32$
Absorption correction	Empirical (using intensity measurements) *DENZO*/*SCALEPACK*
T_{min}, T_{max}	0.382, 0.449
No. of measured, independent and observed [$I > 2\sigma(I)$] reflections	13791, 8126, 4925
R_{int}	0.064
$(\sin \theta/\lambda)_{max}$ (Å^{-1})	0.649
$R[F^2 > 2\sigma(F^2)]$, $wR(F^2)$, S	0.094, 0.234, 1.02
No. of reflections/parameters/restraints	8126/528/193
H-atom treatment	H-atom parameters constrained
$\Delta\rho_{max}$, $\Delta\rho_{min}$ (e Å^{-3})	2.82, −4.06

X-ray Structure of *fac*-[ReBr(CO)$_3$(25)]

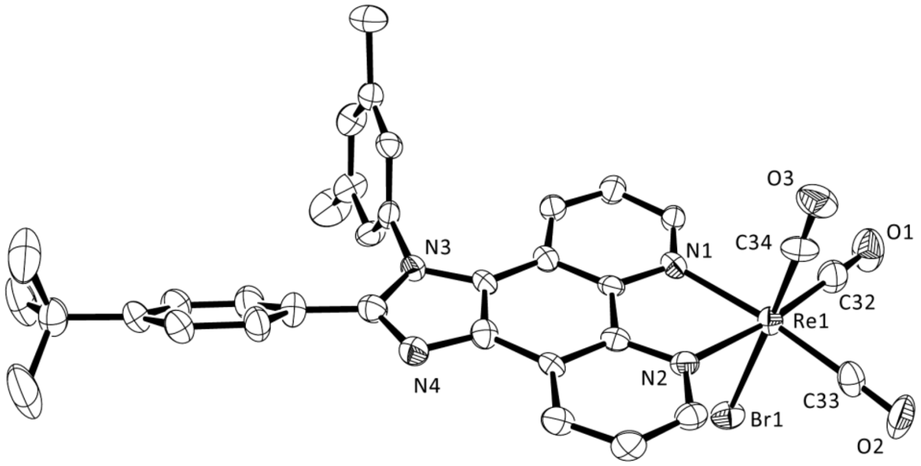

Figure 50: Ortep3 plot of complex ***fac*-[ReBr(CO)$_3$(25)]**. Ellipsoids are drawn at 50% probability. Hydrogen atoms omitted for clarity. Selected data – bond lengths (Å):

Table 12: Crystal data and structure refinement parameters for ***fac*-[ReBr(CO)$_3$(25)].**

CCDC reference	946891
Chemical formula	$C_{34}H_{28}BrN_4O_3Re\cdot0.16(C_6H_{14})\cdot0.34(H_2O)$
M_r	826.97
Crystal system, space group	Triclinic, *P*-1
Temperature (K)	150
a, *b*, *c* (Å)	12.7327 (5), 16.1447 (6), 18.1453 (5)
α, β, γ (°)	110.645 (2), 104.457 (2), 99.474 (2)
V (Å^3)	3246.0 (2)
Z	4
Radiation type	Mo *K*α
μ (mm^{-1})	5.02
Crystal size (mm)	0.30 × 0.05 × 0.05
Absorption correction	Empirical (using intensity measurements) *DENZO*/*SCALEPACK*
T_{min}, T_{max}	0.315, 0.788
No. of measured, independent and observed [$I > 2\sigma(I)$] reflections	21084, 14435, 9962
R_{int}	0.059
$(\sin \theta/\lambda)_{max}$ (Å^{-1})	0.650
$R[F^2 > 2\sigma(F^2)]$, $wR(F^2)$, S	0.069, 0.160, 1.03
No. of reflections/parameters/restraints	14435/903/270
H-atom treatment	H-atom parameters constrained
	$w = 1/[\sigma^2(F_o^2) + (0.0429P)^2 + 39.073P]$ where $P = (F_o^2 + 2F_c^2)/3$
$\Delta\rho_{max}$, $\Delta\rho_{min}$ (e Å^{-3})	1.47, −2.06

2.5.3 Electronic absorption spectroscopy and luminescent studies

Two main absorption characteristics are observed for the Re(I) complexes of ligands **21-28**. The first is a metal-perturbed ligand-based absorption ($\pi\rightarrow\pi^*$), which - similarly to the free ligand - has a relatively high extinction coefficient. Intra-ligand imidazole based $n\rightarrow\pi^*$ may also contribute to the low-energy tail of the absorption, with its characteristic low extinction coefficient.[21] The second characteristic is that of a ^{1}MLCT absorption, observed as promotion of an electron from the rhenium *d* orbital to a vacant π^* orbital on the ligand (Re(d)$\rightarrow\pi^*$), and at low energy with the longest wavelength observed at >400 nm as a broad shoulder (Figure 51).

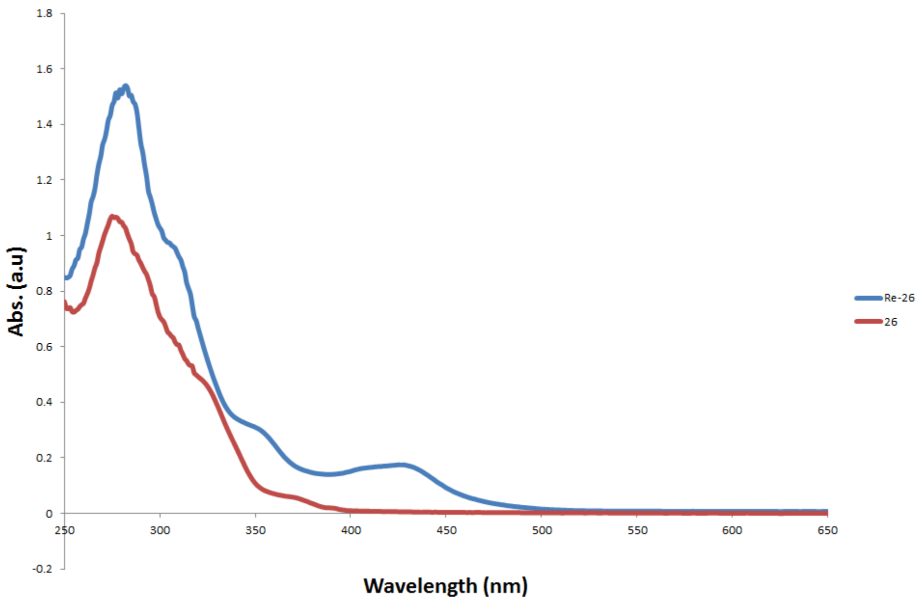

Figure 51: Electronic absorption spectra of **26** (red line) and [Re(CO)$_3$Br(**26**)] (blue line) in CHCl$_3$ at 298K

Complex Number	R	R′	Absorption (λ_{max}/nm)	Emission (λ_{max}/nm)	τ (ns)
Re(CO)$_3$Br(**21**)	4-^{t}Bu	4-FC$_6$H$_4$	276, 362, 410	586	156
Re(CO)$_3$Br(**22**)	4-^{t}Bu	4-ClC$_6$H$_4$	277, 339, 423	588	169
Re(CO)$_3$Br(**23**)	4-^{t}Bu	4-BrC$_6$H$_4$	277, 338, 423	572	178
Re(CO)$_3$Br(**24**)	4-^{t}Bu	4-IC$_6$H$_4$	277, 337, 423	591	149
Re(CO)$_3$Br(**25**)	4-^{t}Bu	3,5-MeC$_6$H$_3$	282, 349, 423	581	158
Re(CO)$_3$Br(**26**)	4-^{t}Bu	4-^{t}BuC$_6$H$_4$	279, 352, 419	581	162
Re(CO)$_3$Br(**27**)	4-^{t}Bustyr	3,5-MeC$_6$H$_3$	288, 342, 423	578	185
Re(CO)$_3$Br(**28**)	4-^{t}Bustyr	4-^{t}BuC$_6$H$_4$	271, 338, 419	505	1.1

Table 13: Photophysical data for Re(I) complexes, obtained in MeCN/ CHCl$_3$

Re complexes of **21-27** displayed relatively long lived orange-yellow emission at 570-590 nm. This is a relatively low energy emission which is attributed to relaxation of an excited triplet state to a singlet ground state (^{3}MLCT phosphorescence). Emission in this region is a commonly observed for Re complexes of 1,10-phenanthroline and 2,2′-bipy based derivatives.[19,22] The lower energy associated with this emission is reflected in the longer emission wavelength and relatively large Stokes' shift compared to the free ligand. The deactivation of the triplet state to a singlet state is also a spin-forbidden process which leads to an enhanced lifetime and phosphorescence. Table 13 shows lifetimes for [Re(CO)$_3$Br(**21-27**)] are in the region of 150-185 ns (compared to 1-4 ns for the free ligands).

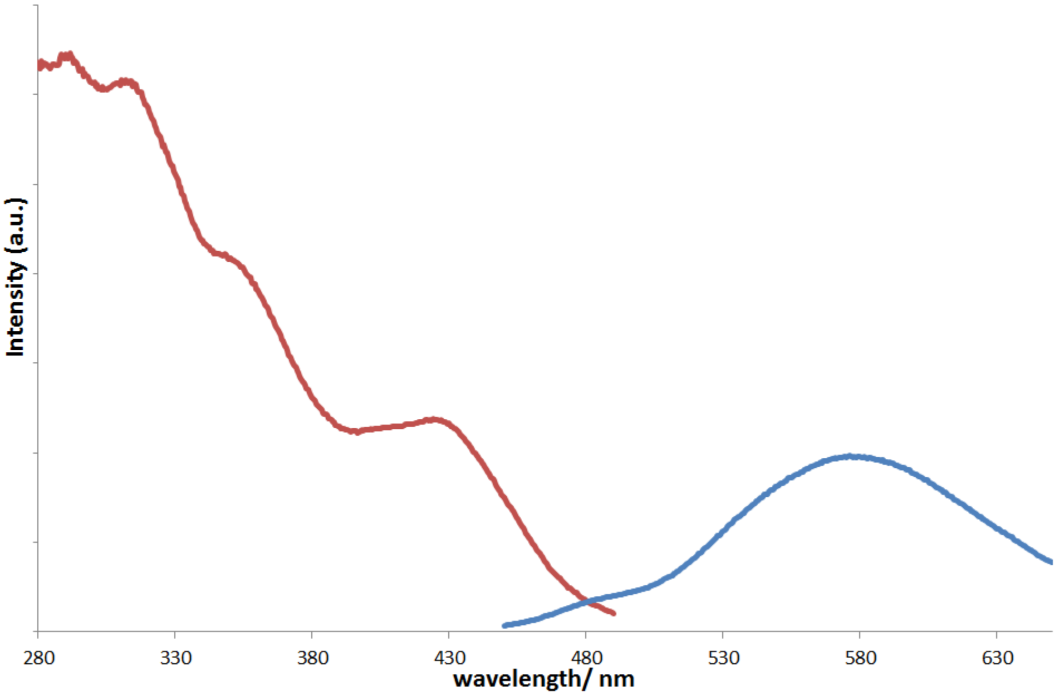

Figure 52: Excitation (red) and emission spectra (blue) of [Re(CO)$_3$(**21**)Br] in CHCl$_3$ at 298 K

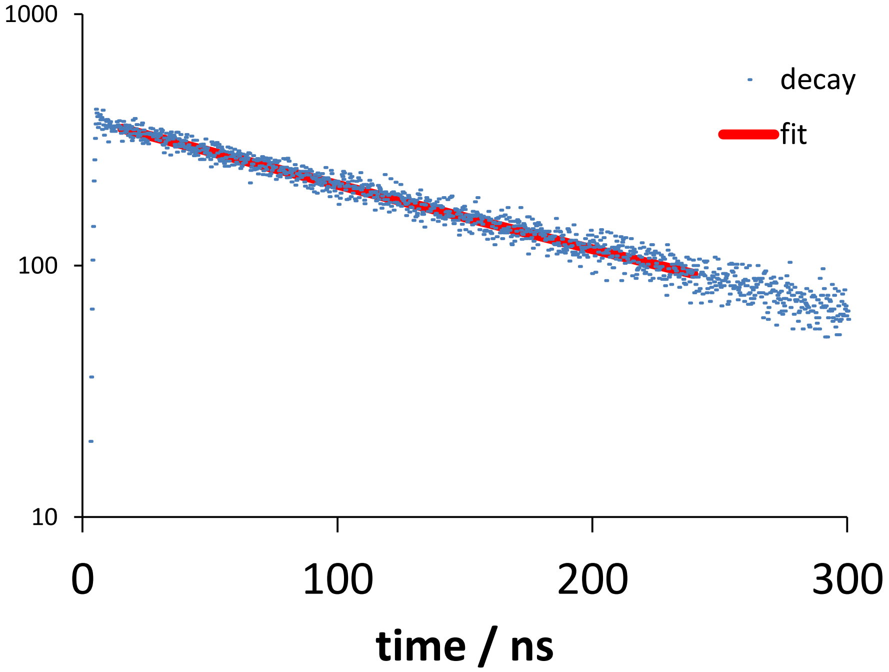

Figure 53: Lifetime decay spectrum of [Re(CO)$_3$Br(**25**)] in CHCl$_3$ at 298 K

In comparison to the emission wavelengths and lifetimes observed for the other rhenium coordinated ligands, [Re(CO)$_3$Br(**28**)] yielded anomalous results. Although fully characterised through NMR and

IR spectroscopies, as well as high-resolution mass spectrometry, it does not share the same photophysical characteristics attributed to the other ligands. An emission wavelength value of 505 nm is significantly red-shifted from the emission of the free ligand, however is still significantly shorter than the other observed wavelengths of these ligand types. Emission lifetime at this wavelength was also found to be very short (≈ 1ns), confirming that the emission observed is indeed a metal-perturbed ligand-based emission. Further dilution of the complex did not yield different results, ruling out aggregation in solution. After a repeated measurement using MeCN as a solvent, with a significantly higher excitation wavelength (467 nm), a new band was observed at ca. 560 nm. A lifetime decay profile was obtained in $CHCl_3$ (λ_{em} = 560 nm) and was fitted to a biexponential yielding two distinct lifetime values of 0.9 and 348 ns. These parameters are ascribed to a dual emissive compound where both ligand-centred and MLCT states contribute; the observation of longer-lived component was consistent with ^{3}MLCT. Therefore the emission observed for this complex is ascribed to a dual-emissive species, where the ^{3}MLCT is quenched through non-radiative processes.

The reasons behind this complex having different photophysical attributes compared to $[ReBr(CO)_3($**27**$)]$ is unclear. It was not expected for the R′ group to have much, if any, impact on the luminescence properties of the complex, yet the luminescence spectra and decay profiles of the two complexes are vastly different (the decay profile of $[ReBr(CO)_3($**28**$)]$ is shown in Figure 54Figure).

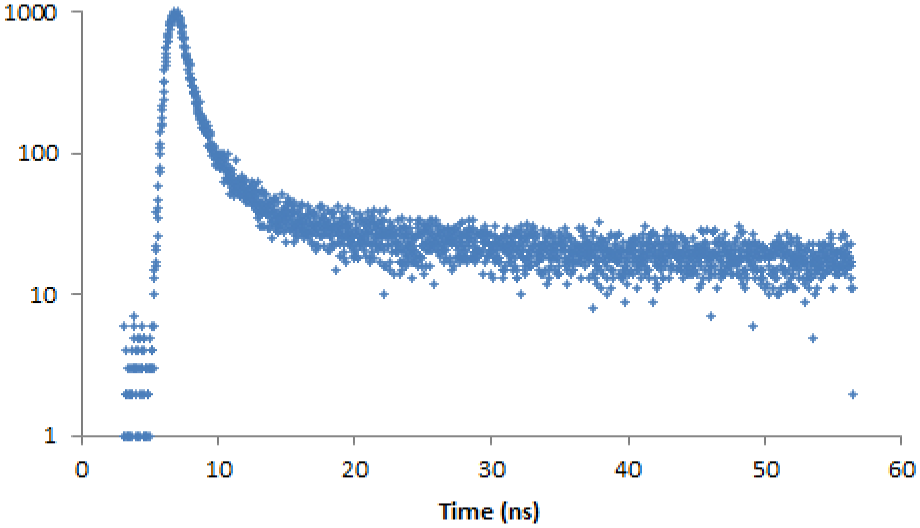

Figure 54: Decay profile of $[ReBr(CO)_3$**28**$]$ obtained in $CHCl_3$ at 298K

.

It is possible to speculate that the differences may be a result of impure $[ReBr(CO)_3$**28**$]$ affecting the luminescence properties, possibly by quenching the long-lived phosphorescence. It may be beneficial for future work with this complex to obtain a complete elemental analysis in order to further confirm the purity of the sample. Should it be confirmed that the sample is completely pure the nature of the luminescence of [ReBr(CO)$_3$(**27**)] and [ReBr(CO)$_3$(**28)**] could be affected by the nature of the R′ group, possibly with its interaction with solvent. Future work to determine this would be to obtain luminescence spectra in various solvents and comparing and contrasting the emission profiles and decay lifetimes. It has already been observed that the use of MeCN as a solvent resulted in different spectra for [ReBr(CO)$_3$(**28**)] compared to CHCl$_3$, and therefore other solvents may provide more information about the nature of the emission. It is worth noting that there is the possibility of ligand exchange between the bromide and the acetonitrile which could affect the nature of the emission. This could again be confirmed by isolating the analogous acetonitrile complex and obtaining its emission and decay profiles in MeCN.

The lifetimes of the halide-containing Re complexes of **21-24** do show some variation in lifetimes and emission wavelength, however there is no discernible connection between the electronegativity of the halides and the lifetime. Comparing this data and that of the **25/26** and **27/28** pair shows that the influence of the R′ group on emission can be difficult to predict, and that it is the interplay of R and R′ that can determine overall fluorescence.

2.6 Conclusions

A series of fused imidazo[4,5-*f*]-1,10-phenanthroline ligands and the associated Re(CO$_3$)Br(N^N) complexes have been isolated. All compounds have been fully characterised via ^{1}H and ^{13}C{^{1}H} NMR spectroscopy, IR, and electronic absorption spectroscopies, as well as high resolution mass spectrometry Fluorescence emission studies have shown all compounds to be emissive, with the emission wavelength of free lophines **21-28** appearing to be sensitive to variations of the apical R group and, in the case of 4-^{t}Bustyr containing lophines, also the R′ group. Seven of the isolated rhenium complexes showed expected emission as a result of relaxation from an excited triplet state due to ^{3}MLCT, also showing the expected enhanced lifetime associated with a spin-forbidden process. An anomalous result was seen however for [Re(CO)$_3$Br(**28**)], for which an emission at ≈ 500 nm was observed. Further investigation of the emission confirmed that it was not as a result of a ^{3} MLCT, and has been tentatively assigned an intra-ligand $\pi \rightarrow \pi^*$ metal perturbed emission. Excitation at a higher wavelength in CHCl$_3$ did reveal a second emission at a lower energy, and when the lifetime of this emission was examined a dual-emissive species was observed, incorporating a short lifetime ligand-based emission and also a longer lived ^{3}MLCT emission. Crystal structures of three of the rhenium complexes, incorporating ligands **21, 23** and **25**, have been obtained revealing the expected structural conformation in each case.

2.7 Experimental

Synthesis of 1,10-phenanthroline-5,6-dione

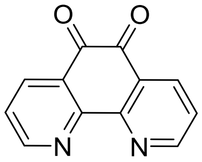

Concentrated sulphuric acid (98% w/v, 40 ml) and concentrated nitric acid (69% w/v, 20 ml) were added to a loosely stoppered round bottom flask equipped with a condenser and cooled in an ice bath. Finely ground 1,10-phenanthroline (4 g, 0.022 mol) and sodium bromide (4 g, 0.039 mol) were added slowly and reaction mixture was heated and stirred under a nitrogen atmosphere at 100°C for 4hrs. After cooling to room temperature the reaction mixture was poured into crushed ice (200 g). Sodium hydroxide pellets (18 g) were added slowly in small portions and further sodium hydroxide as an aqueous solution was slowly added to achieve neutrality (approximately 75 ml of a 40% w/v solution was required). The solution was extracted with chloroform (3 × 150 ml), the combined organic layers were washed with saturated brine (100 ml) and dried ($MgSO_4$) and the volatiles removed *in vacuo,* to yield a bright yellow solid (yield = 3.80 g). This material had identical spectroscopic properties to that reported in the literature and was used without further purification.

Synthesis of 21

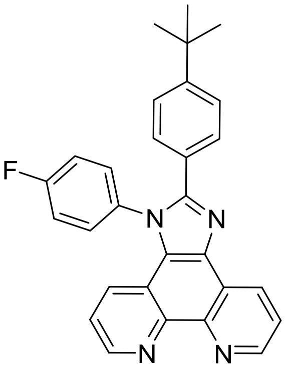

1,10-phenanthroline-5,6-dione (0.500 g, 2.38 mmol), 4-fluoroaniline (0.264 g, 2.38 mmol), 4-tert-butylbenzylaldehyde (0.386 g, 2.38 mmol) and ammonium acetate (1.83 g, 23.7 mmol) were added to acetic acid (10 ml) in a round bottomed flask. The reaction was allowed to stir and refluxed at 125 °C for the duration of 3hrs. The reaction mixture was poured into ice water (200 ml), neutralised with ammonium hydroxide. Hypochlorite solution (2 drops, 4-20 % w/w) was used to remove impurities by oxidation, and the resulting orange solution was extracted into dichloromethane (3 × 50 ml), dried ($MgSO_4$) and the volatiles removed *in vacuo*. The crude product was recrystalised from acetonitrile and filtered using a sinter, dried under vacuum and afforded the title compound, as a pale yellow powder (yield = 0.300 g). ^{1}H NMR (250 MHz, $CDCl_3$): δ 9.08-8.92 (2H, m, phen-*H*), 9.05 (1H, dd, *J* = 4.05, 1.33 Hz, phen-*H*), 7.47 (1H, dd, *J* = 6.25, 2.56 Hz, Ar-*H*), 7.45-7.23 (10H, m, Ar-*H*), 1.35 (9H, s, Ar-$C(CH_3)_3$ ppm. ^{13}C{H} NMR (62.5 MHz, $CDCl_3$): δ 152.8, 152.5, 149.1, 147.9, 144.9, 144.4, 136.2, 134.1, 130.9, 130.8, 130.6, 129.0, 128.8, 127.7, 126.8, 125.6, 124.0, 123.6, 122.2, 119.8, 118.6, 117.9, 117.5, 34.7, 31.2 ppm. HRMS (ES)(%): found *m/z* = 447.1977; $\{C_{29}H_{24}N_4F\}^+$ requires 447.1980. IR (KBr plates) 3419, 3056, 2962, 2904, 2871, 1511, 1225, 741 cm^{-1}. UV-vis λ_{max} (ε / M^{-1} cm^{-1}) ($CHCl_3$): 278 (25000), 315 (sh) (14600) nm.

Synthesis of 22

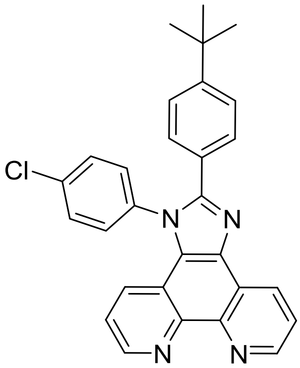

This material was prepared by a similar method to **21** using 1,10-phenanthroline-5,6-dione (0.500 g, 2.37 mmol), 4-chloroaniline (0.304 g, 2.37 mmol), 4-tert-butylbenzylaldehyde (0.386 g, 2.38 mmol) and ammonium acetate (1.83 g, 23.7 mmol). The crude product was recrystalised from acetonitrile affording the title compound, as pale green powder. (yield = 0.560 g) ^{1}H NMR (250 MHz, $CDCl_3$): δ 9.24-9.12 (2H, m, phen-*H*), 9.02 (1H, dd, *J* = 4.05, 1.33 Hz, phen-*H*), 7.65 (1H, dd, *J* = 6.25, 2.56 Hz, Ar-*H*), 7.43-7.21 (10H, m, Ar-*H*), 1.24 (9H, Ar-C(C*H*$_3$)$_3$ ppm. ^{13}C{H} NMR (62.5 MHz, $CDCl_3$): δ 152.8, 152.3, 149.1, 147.9, 144.8, 144.3, 136.6, 136.2, 130.8, 130.5, 130.3, 129.0, 127.7, 126.7, 126.6, 123.9, 123.6 122.2, 119.6, 109.9, 34.8, 31.2 ppm. HRMS (ES)(%): found *m/z* = 463.1679 $\{C_{29}H_{24}N_4Cl\}^+$ requires 463.1684. IR (KBr plates) 3419, 3086, 3017, 2961, 2901, 2866, 2357, 1560, 1492, 839, 745 cm^{-1}. UV-vis λ_{max} (ε / M^{-1} cm^{-1}) ($CHCl_3$): 275 (26700), 311 (sh) (17800), 368 (sh) (3000) nm.

Synthesis of 23

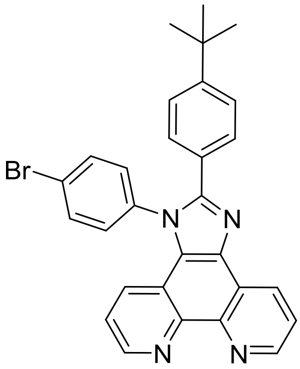

This material was prepared by a similar method to **21** using 1,10-phenanthroline-5,6-dione (0.500 g, 2.37 mmol), 4-bromoaniline (0.409 g, 2.38 mmol), 4-tert-butylbenzylaldehyde (0.386 g, 2.38 mmol) and ammonium acetate (1.83 g, 23.7 mmol). The crude product was recrystalised from acetonitrile affording the title compound, as an off white powder (yield = 0.590 g). ^{1}H NMR (250 MHz, $CDCl_3$): δ 9.13-8.94 (2H, m, phen-*H*), 9.04 (1H, dd, *J* = 4.05, 1.33 Hz, phen-*H*), 7.68 (1H, dd, *J* = 6.25, 2.56 Hz, Ar-*H*), 7.7-7.24 (10H, m, Ar-*H*), 1.24 (9H, s, Ar-C(C*H*$_3$)$_3$) ppm. ^{13}C{H} NMR (62.5 MHz, $CDCl_3$): δ 152.7, 152.1, 148.9, 147.8, 144.6, 144.2, 137.1, 136.1, 133.7, 130.5, 130.4, 128.9, 127.6, 126.6, 126.4, 125.5, 124.2, 123.8, 123.5, 122.1, 119.5, 109.9, 34.7, 31.1 ppm. HRMS (ES)(%): found *m/z* = 507.1173; $\{C_{29}H_{24}N_4Br\}^+$ requires 507.1179. IR (KBr plates) 3010, 2955, 2361, 1479, 839, 813, 741 cm^{-1}. UV-vis λ_{max} (ε / M^{-1} cm^{-1}) ($CHCl_3$): 279 (25000), 321 (sh) (15200) nm.

Synthesis of 24

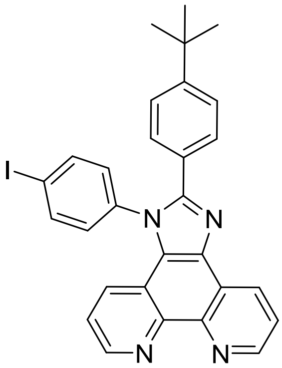

This material was prepared by a similar method to **21** using 1,10-phenanthroline-5,6-dione (0.500 g, 2.37 mmol), 4-iodoaniline (0.521 g, 2.38 mmol), 4-tert-butylbenzylaldehyde (0.386 g, 2.38 mmol) and ammonium acetate (1.83 g, 23.7 mmol). The crude product was recrystalised from acetonitrile and filtered using a sinter, dried under vacuum and afforded the title compound, as a white powder (yield = 0.838 g). ^{1}H NMR (250 MHz, $CDCl_3$): δ 9.24-9.12 (2H, m, phen-*H*), 9.02 (1H, dd, *J* = 4.05, 1.33 Hz, phen-*H*), 7.40 (1H, dd, *J* = 6.25, 2.56 Hz, Ar-*H*), 7.92-7.21 (10H, m, Ar-*H*), 1.24 (9H, s, Ar-C(C*H*$_3$)$_3$) ppm. ^{13}C{H} NMR (62.5 MHz, $CDCl_3$): δ 152.7, 152.1, 149.0, 147.8, 144.7, 144.3, 139.7, 137.8, 136.2, 130.7, 130.5, 128.9, 127.7, 126.6, 126.5, 125.6, 123.8, 123.5, 122.2, 119.6, 95.9, 82.5, 40.1, 34.8, 31.2 ppm. HRMS (ES)(%): found *m/z* = 555.1034; $\{C_{29}H_{24}N_4I\}^+$ requires 555.1040. IR (KBr plates) 3010, 2956, 1478, 1393, 893, 813 cm^{-1}. UV-vis λ_{max} (ε / M^{-1} cm^{-1}) ($CHCl_3$): 276 (30100), 318 (sh) (17100) nm.

Synthesis of 25

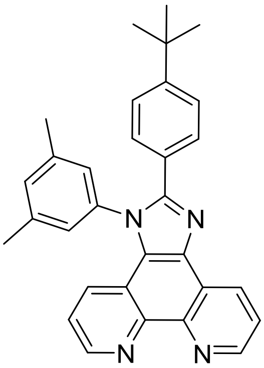

This material was prepared by a similar method to **21** using 1,10-phenanthroline-5,6-dione (0.500 g, 2.38 mmol), 3,5-dimethylaniline (0.291 g, 2.4 mmol), 4-tert-butylbenzylaldehyde (0.389 g, 2.4 mmol) and ammonium acetate (1.83 g, 23.7 mmol) using 2 M NaOH to neutralise the quenched reaction mixture. The resulting off-white solid was recrystalised using acetonitrile to give the product as white powder (yield = 0.73 g). ^{1}H NMR (400 MHz, $CDCl_3$): δ 9.15 (2H, ddd, *J* = 9.78, 6.21, 1.68 Hz, phen-*H*), 9.03 (1H, dd, *J* = 4.26, 1.53 Hz, phen-*H*), 7.73 (1H, dd, *J* = 8.08, 4.38 Hz, Ar-*H*), 7.59 (2H, d, *J* = 8.48 Hz, Ar-*H*), 7.42 (1H, dd, *J* = 8.41, 1.52 Hz, Ar-*H*), 7.38-7.27 (4H, m, Ar-*H*), 7.15 (2H, s, Ar-*H*), 2.42 (6H, s, Ar-C*H*$_3$), 1.29 (9H, s, Ar-C(C*H*$_3$)$_3$) ppm. ^{13}C{^{1}H} NMR (101 MHz, $CDCl_3$): δ 152.3, 151.8, 148.7, 147.6, 144.7, 144.2, 140.4, 137.8, 135.9, 131.8, 130.4, 128.6, 128.0, 127.0, 126.8, 126.1, 125.3, 123.9, 123.3, 122.0, 119.9, 34.6, 31.0, 21.3 ppm. MS (ES)(%): found *m/z* = 457.2385 [M+H]$^+$; $\{C_{31}H_{29}N_4^+\}$ requires 457.2387. IR (KBr plates): 2948, 2358, 2341, 1611, 1597, 1568, 1511, 1499, 1470, 1391, 1364, 1340, 1305, 1267, 1195, 1154, 1115, 1079, 1022, 998, 872, 847, 841, 808, 744 cm^{-1}. UV-vis λ_{max} (ε / M^{-1} cm^{-1}) ($CHCl_3$): 278 (42400), 319 (sh) (20000), 376 (sh) (1330) nm.

Synthesis of 26

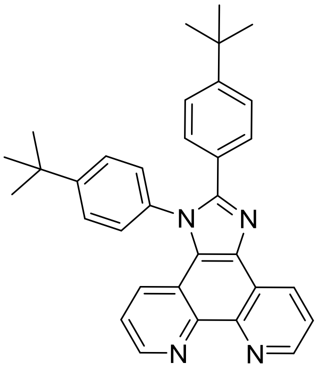

This material was prepared by a similar method to **21** using 1,10-phenanthroline-5,6-dione (0.300 g, 1.43 mmol), 4-*tert*-butyl-aniline (0.213 g, 1.43 mmol), 4-tert-butylbenzylaldehyde (0.232 g, 1.43 mmol) and ammonium acetate (1.10 g, 14.3 mmol). The product was initially obtained crude as a brown oil which was recrystalised using acetonitrile and water to give the product as a pale brown powder (yield = 0.392 g). ^{1}H NMR (400 MHz, $CDCl_3$): δ 9.15 (2H, ddd, *J* = 9.85, 6.23, 1.76 Hz, phen-*H*), 9.03 (1H, dd, *J* = 4.29, 1.61 Hz, phen-*H*), 7.74 (1H, dd, *J* = 8.09, 4.38 Hz, Ar-*H*), 7.68-7.60 (2H, m, Ar-*H*), 7.53 (2H, d, *J* = 8.54 Hz, Ar-*H*), 7.47-7.38 (3H, m, Ar-*H*), 7.30 (3H, td, *J* = 8.46, 5.54 Hz, Ar-*H*), 1.46 (9H, s, Ar-$C(CH_3)_3$), 1.29 (9H, s, Ar-$C(CH_3)_3$) ppm. $^{13}C\{^1H\}$ NMR (101 MHz, $CDCl_3$): δ 192.6, 169.0, 154.2, 152.8, 152.7, 149.2, 148.1, 147.4, 145.1, 144.7, 136.5, 136.4, 135.9, 135.7, 130.9, 130.1, 129.2, 128.6, 128.5, 127.8, 127.4, 127.4, 126.7, 126.4, 126.1, 125.8, 125.5, 124.4, 123.9, 122.6, 120.4, 120.2, 102.1, 35.5, 35.1, 31.8, 31.6 ppm. HRMS (ES)(%): found *m/z* = 485.2694 $[M+H]^+$;$\{C_{33}H_{33}N_4^+\}$ requires 485.2700. IR (KBr plates): 2961, 1686, 1605, 1510, 1464, 1442, 1363, 1266, 1107, 1061, 1018, 837, 802, 739 cm^{-1}. UV-vis λ_{max} (ε / M^{-1} cm^{-1}) ($CHCl_3$): 275 (39500), 368 (2300) nm.

Synthesis of 27

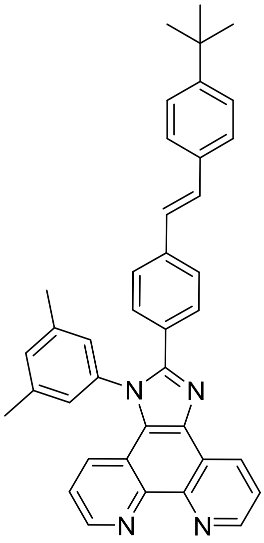

This material was prepared by a similar method to **21** using 1,10-phenanthroline-5,6-dione (0.8 g, 3.8 mmol), 3,5-dimethylaniline (0.461 g, 3.8 mmol), 4-*tert*-butylstyryl-benzaldehyde (1 g, 3.8 mmol) and ammonium acetate (2.91 g, 37.8 mmol). The off-brown solid was recrystallised using acetonitrile to give the product as a brown powder (yield = 1.9 g). ^{1}H NMR (400 MHz, $CDCl_3$): δ 9.17 (2H, ddd, *J* = 9.72, 6.17, 1.61 Hz, phen-*H*), 9.04 (1H, dd, *J* = 4.23, 1.47 Hz, phen-*H*), 7.75 (1H, dd, *J* = 8.08, 4.38 Hz, Ar-*H*), 7.64 (2H, d, *J* = 8.34 Hz, Ar-*H*), 7.55-7.45 (5H, m, Ar-*H*), 7.38 (2H, d, *J* = 8.38 Hz, Ar-*H*), 7.31 (2H, dd, *J* = 8.29, 4.40 Hz, Ar-*H*), 7.19-6.98 (4H, m, Ar-H and C=C*H*), 2.43 (6H, s, Ar-CH_3), 1.33 (9H, s, Ar-C(CH_3)$_3$) ppm. ^{13}C{^{1}H} NMR (101 MHz, $CDCl_3$): δ 152.0, 151.6, 149.4, 148.2, 145.2, 144.8, 141.0, 138.7, 138.3, 136.4, 134.6, 132.5, 131.0, 130.1, 129.7, 129.1, 128.6, 127.5, 127.3, 126.8, 126.7, 126.6, 126.1, 124.4, 123.9, 122.6, 120.4, 35.1, 31.7, 21.8 ppm. HRMS (ES)(%): found *m/z* = 558.2781 $[M+H]^+$; {$C_{39}H_{34}N_4$} requires 558.2778. IR (KBr plates): 3025, 2949, 2865, 1627, 1601, 1562, 1511, 1469, 1447, 1392, 1270, 1184, 1152, 1109, 1076, 1017, 961, 947, 867, 844, 803, 742 cm^{-1}. UV-vis λ_{max} (ε / M^{-1} cm^{-1}) ($CHCl_3$): 289 (28800), 345 (19600) nm.

Synthesis of 28

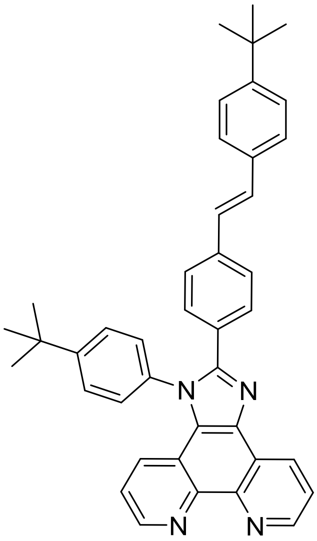

This material was prepared by a similar method to **21** using 1,10-phenanthroline-5,6-dione (0.300 g, 1.43 mmol), 4-*tert*-butyl-aniline (0.213 g, 1.43 mmol), 4-*tert*-butylstyryl-benzaldehyde (0.378 g, 1.43 mmol) and ammonium acetate (1.10 g, 14.3 mmol). The resulting brown oil was recrystalised from ethanol to give the product as brown powder (yield = 0.240 g). ^{1}H NMR (250 MHz, $CDCl_3$): δ 9.17-9.06 (2H, m, phen-*H*), 8.98 (1H, dd, *J* = 4.31, 1.66 Hz, phen-*H*), 7.69 (1H, dd, *J* = 8.10, 4.41 Hz, Ar-*H*), 7.59 (2H, d, *J* = 8.54 Hz, Ar-*H*), 7.52 (2H, d, *J* = 8.45 Hz, Ar-*H*), 7.43-7.20 (10H, m, Ar-*H*), 7.01 (2H, dd, *J* = 16.39, 16.38 Hz, C=C*H*), 1.40 (9H, s, Ar-C(CH_3)$_3$), 1.26 (9H, s, Ar-C(CH_3)$_3$) ppm. ^{13}C{^{1}H} NMR (101 MHz, $CDCl_3$): δ 192.1, 154.3, 152.4, 152.2, 151.6, 149.4, 148.2, 145.2, 144.8, 144.1, 138.7, 136.5, 135.6, 135.5, 134.6, 134.2, 132.4, 131.0, 130.7, 130.1, 129.8, 129.0, 128.6, 128.5, 127.9, 127.5, 127.3, 127.2, 127.1, 126.9, 126.8, 126.7, 126.2, 126.1, 124.4, 123.9, 122.6, 120.3, 120.2, 35.5, 35.1, 31.8, 31.7 ppm. HRMS (ES)(%): m/z = 587.3162 $[M+H]^+$. {$C_{41}H_{39}N_4^+$} requires 587.3169. IR (KBr plates): 2960, 1707, 1598, 1565, 1509, 1462, 1442, 1266, 1105, 963, 845, 740 cm^{-1}. UV-vis λ_{max} (ε / M^{-1} cm^{-1}) ($CHCl_3$): 288 (28200), 344 (34100) nm.

Synthesis of [ReBr(CO)$_3$(21)]

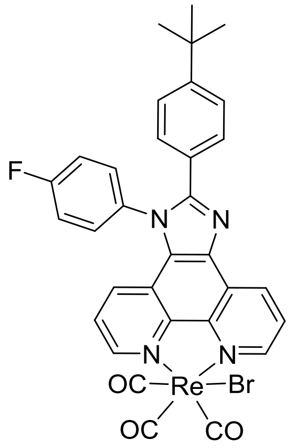

[Re(CO)$_5$Br] (0.05 g, 0.12 mmol) was added to **21** (0.06 g, 0.13 mmol) in toluene (10 ml) and stirred at 100 °C overnight. The reaction was filtered and washed with toluene (10 ml) and petroleum ether (10 ml) to give the product as a yellow solid (yield = 0.090 g). ^{1}H NMR (250 MHz, CDCl$_3$): δ 9.34-9.27 (2H, m, phen-*H*), 9.32 (1H, dd, *J* = 4.05, 1.33Hz, phen-*H*), 7.88 (1H, dd, *J* = 6.25, 2.56 Hz, Ar-*H*), 7.56-7.31 (10H, m, Ar-*H*), 1.25 (9H, s, Ar-C(C*H*$_3$)$_3$) ppm. ^{13}C{H} NMR (125.7 MHz, CDCl$_3$): δ 197, 189, 165, 163, 155, 154, 152, 151, 145, 145, 133, 133, 131, 130. 130, 130, 130, 129, 127, 126, 126, 126, 125, 122, 118, 118, 118, 66, 35, 31, 15 ppm. HRMS (ES)(%): found *m/z* = 795.0551; $\{C_{32}H_{24}BrFN_4O_3{}^{185}Re^+\}$ requires 795.0540. IR (KBr plates): 2961, 2021, 1921, 1887, 1600, 1510, 1473, 1448, 1384, 1323, 1302, 1265, 1225, 1154, 1092 cm^{-1}. UV-vis (ε / M^{-1} cm^{-1}) (CHCl$_3$): 276 (32000), 362 (25000), 410 (3400) nm.

Synthesis of [ReBr(CO)$_3$(22)]

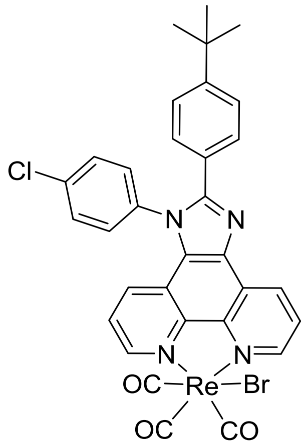

The title compound was prepared using [Re(CO)$_5$Br] (0.05 g, 0.12 mmol) and **22** (0.055 g, 0.12 mmol) to give the product as a yellow solid (yield = 0.089 g). ^{1}H NMR (250 MHz, CDCl$_3$): δ 9.47-

9.31 (2H, m, phen-*H*), 9.39 (1H, dd, *J* = 4.05, 1.33 Hz, phen-*H*), 7.98 (1H, dd, *J* = 6.25, 2.56 Hz, Ar-*H*), 7.75-7.42 (10H, m, Ar-*H*), 1.35 (9H, s, Ar-C(CH_3)$_3$) ppm. ^{13}C{H} NMR (62.5 MHz, $CDCl_3$): δ 154.4, 153.8, 151.8, 150.8, 145.3, 145.0, 137.2, 135.5, 132.9, 131.4, 131.3, 130.0, 129.8, 129.0, 127.0, 126.1, 126.1, 125.8, 125.6, 124.9 121.9, 34.9, 31.1 ppm. HRMS (ES)(%): found *m/z* = 833.0055; {$C_{32}H_{23}BrClN_4O_3Na^{185}Re^+$} requires 833.0064. IR (KBr plates) 2963, 2021, 1920, 1886, 1601, 1493, 1383, 1302, 1269, 1157, 1092, 1018, 844 cm^{-1}. UV-vis (ε / M^{-1} cm $^{-1}$) ($CHCl_3$): 277 (87900), 339 (sh) (11200), 423 (5800) nm.

Synthesis of [ReBr(CO)$_3$(23)]

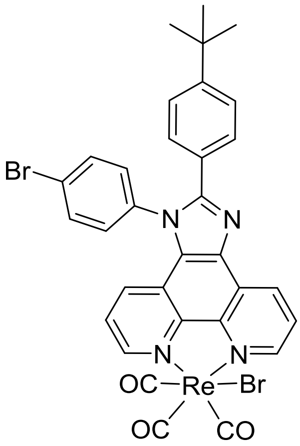

The title compound was prepared using [Re(CO)$_5$Br] (0.05 g, 0.12 mmol) and **23** (0.060 g, 0.14 mmol) to give the product as a yellow solid (yield = 0.081 g). ^{1}H NMR (250 MHz, $CDCl_3$): δ 9.33-9.22 (2H, m, phen-*H*), 9.26 (1H, dd, *J* = 4.05, 1.33 Hz, phen-*H*), 8.00 (1H, dd, *J* = 6.25, 2.56 Hz, Ar-*H*), 7.97-7.23 (10H, m, Ar-*H*), 1.26 (9H, s, Ar-C(CH_3)$_3$) ppm. ^{13}C{^{1}H} NMR (101 MHz, $CDCl_3$): δ 197.0, 154.5, 153.9, 151.9, 150.9, 145.5, 145.1, 137.1, 136.3, 134.6, 134.4, 133.0, 130.4, 130.1, 129.8, 129.1, 127.1, 126.3, 126.2, 126.0, 125.8, 125.4, 125.0, 122.0, 35.0, 31.2 ppm. HRMS (ES)(%): found *m/z* = 876.9559; {$C_{32}H_{23}Br_2N_4O_3Na^{185}Re^+$} requires 876.9559. IR (KBr plates): 2962, 2020, 1919, 1885, 1709, 1600, 1489, 1475, 1448, 1382, 1302, 1269, 1157, 1068, 1015, 1015, 987, 844 cm^{-1}. UV-vis (ε / M^{-1} cm $^{-1}$) ($CHCl_3$): 277 (43400), 338 (sh) (7900), 423 (3800) nm.

Synthesis of [ReBr(CO)$_3$(24)]

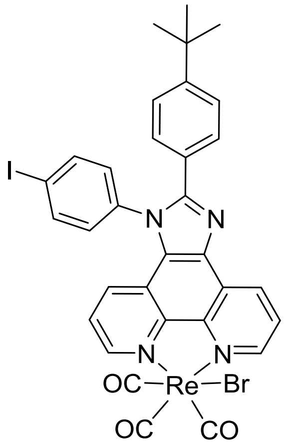

The title compound was prepared using [Re(CO)$_5$Br] (0.05 g, 0.12 mmol) and **24** (0.060 g, 0.14 mmol) to give the product as a yellow solid (yield = 0.101 g). ^{1}H NMR (250 MHz, CDCl$_3$): δ 9.43-9.32 (2H, m, phen-*H*), 9.38 (1H, dd, *J* = 4.05, 1.33 Hz, phen-*H*), 7.96 (1H, dd, *J* = 6.25, 2.56 Hz, Ar-*H*), 7.99-7.42 (10H, m, Ar-*H*), 1.30 (9H, s, Ar-C(C*H*$_3$)$_3$) ppm. ^{13}C{^{1}H} NMR (63 MHz, CDCl$_3$): δ 153.9, 151.9, 150.9, 145.5, 145.1, 137.1, 136.3, 134.6, 134.4, 133.0, 130.4, 130.1, 129.8, 129.1, 127.1, 126.3, 126.2, 126.0, 125.8, 125.4, 125.0, 122.0, 35.0, 31.2 ppm. HRMS (ES)(%): found *m/z* = 924.9411; {$C_{32}H_{23}BrIN_4O_3Na^{185}Re^+$} requires 924.9420. IR (KBr plates): 2962, 2024, 1900, 1600, 1487, 1448, 1399, 1383, 1340, 1302, 1267, 1012, 987, 843 cm^{-1}. UV-vis (ε / M^{-1} cm $^{-1}$) (CHCl$_3$): 277 (85800), 337 (sh), (14800), 423 (6900) nm.

Synthesis of [ReBr(CO)$_3$(25)]

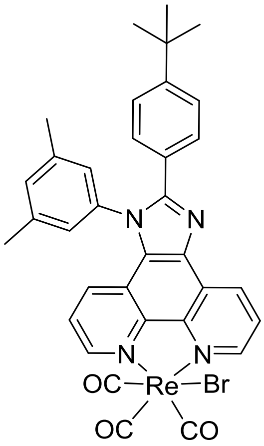

Into a round bottom flask was added **25** (0.056 g, 0.123 mmol), [Re(CO)$_5$Br] (0.05 g, 0.123 mmol) and toluene (30ml) and then the reactants were left at reflux for 3 hours. The solvent was removed *in vacuo* to yield orange oil. CHCl$_3$ was added (2 ml) and was precipitated from hexane to give the product as a yellow powder (yield = 0.065 g). ^{1}H NMR (400 MHz, CDCl$_3$): δ 9.42-9.31 (2H, m, phen-*H*), 9.26 (1H, dd, *J* = 4.97, 1.45 Hz, phen-*H*), 7.94 (1H, dd, *J* = 8.23, 5.17 Hz, Ar-*H*), 7.66-7.61 (2H, m, Ar-*H*), 7.54 (2H, ddd, *J* = 13.57, 8.56, 3.21 Hz, Ar-*H*), 7.40 (3H, d, *J* = 8.56 Hz, Ar-*H*), 7.18 (2H, d, *J* = 7.62 Hz, Ar-*H*), 2.48 (3H, s, Ar-C*H*$_3$), 2.46 (3H, s, Ar-C*H*$_3$), 1.32 (9H, s, Ar-C(C*H*$_3$)$_3$) ppm. ^{13}C{^{1}H} NMR (101 MHz, CDCl$_3$): δ 154.0, 153.8, 151.7, 150.7, 145.4, 145.1, 141.5, 141.3, 136.8, 133.0, 132.9, 130.2, 128.9, 127.3, 126.0, 125.9, 125.8, 125.6, 124.9, 122.1, 34.9, 31.1, 21.4 ppm. HRMS (ES)(%): found *m/z* = 827.0765; {$C_{34}H_{28}BrN_4O_3Na^{185}Re^+$} requires 827.0767. IR (KBr plates): 2964, 2017, 1910, 1890, 1615, 1601, 1511, 1473, 1386, 1363, 1345, 1304, 1267, 1199, 1158, 1122, 1031, 864, 848, 807 cm^{-1}. UV-vis λ_{max} (ε / M^{-1} cm^{-1}) (CHCl$_3$): 282 (53600), 316 (32300), 349 (9300), 423 (4900) nm.

Synthesis of [ReBr(CO)$_3$(26)]

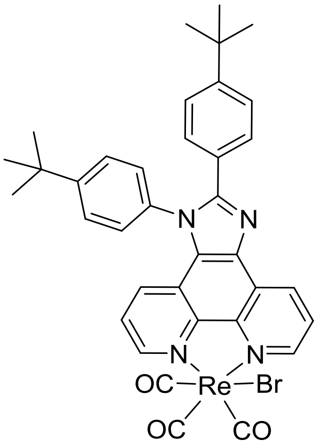

Into a round bottom flask was added **26** (0.060 g, 0.123 mmol), [Re(CO)$_5$Br] (0.050 g, 0.123 mmol), and toluene (30 ml). The reaction mixture was left at reflux for 3 hours. The solvent was removed *in vacuo* to yield a yellow solid. CHCl$_3$ was added (2 ml) and product was precipitated from hexane to give the product as a yellow powder (yield = 0.090 g). ^{1}H NMR (400 MHz, CDCl$_3$: δ 9.34-9.26 (2H, m, phen-*H*), 9.22-9.14-9.13 (1H, m, phen-*H*), 7.91-7.85 (1H, m, Ar-*H*), 7.71-7.60 (2H, m, Ar-*H*), 7.57-7.45 (2H, m, Ar-*H*), 7.45-7.37 (2H, m, Ar-*H*), 7.35-7.26 (2H, m, Ar-*H*), 7.22-7.17 (2H, m, Ar-*H*), 1.49 (9H, s, Ar-C(C*H*$_3$)$_3$), 1.31 (9H, s, Ar-C(C*H*$_3$)$_3$) ppm. ^{13}C{^{1}H} NMR (101 MHz, CDCl$_3$): δ 197.21, 189.3, 155.2, 154.8, 153.9, 152.0, 150.9, 145.7, 134.7, 133.3, 130.4, 129.3, 128.4, 128.3, 128.2, 127.8, 126.7, 126.4, 126.0, 125.2, 122.6, 35.7, 35.3, 31.8, 31.5 ppm. HRMS (ES)(%): found *m/z* = 833.1260; {$C_{36}H_{33}O_3N_4Br^{185}Re$} requires 833.1260. IR (KBr plates): 2962, 2019, 1917, 1893, 1599, 1509, 1446, 1364, 1266, 1107, 812 cm^{-1}. UV-vis λ_{max} (ε / M^{-1} cm^{-1}) (CHCl$_3$): 279 (63800), 306 sh (40400), 352 sh (12500), 419 (7100) nm.

Synthesis of [ReBr(CO)$_3$(27)]

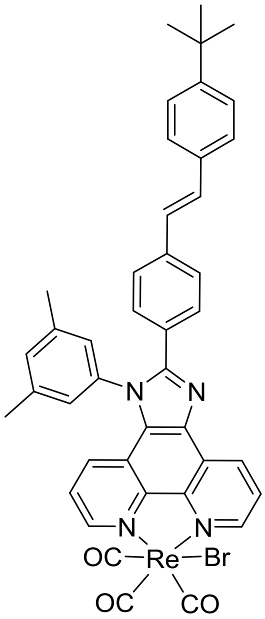

Into a round bottom flask was added **27** (0.069 g, 0.123 mmol), [Re(CO)$_5$Br] (0.050 g, 0.123 mmol), and toluene (30 ml) and the reactants were left at reflux for 3 hours. The solvent was removed *in vacuo* to yield an orange oil. CHCl$_3$ was added (2 ml) and a green solid was precipitated from hexane to give the product as a green powder (yield = 0.080 g). ^{1}H NMR (400 MHz, CDCl$_3$): δ 9.42-9.32 (2H, m, phen-*H*), 9.27 (1H, dd, *J* = 5.04, 1.28 Hz, phen-*H*), 7.95 (1H, dd, *J* = 8.22, 5.14 Hz, Ar-*H*), 7.67 (2H, d, *J* = 8.40 Hz, Ar-*H*), 7.60 (1H, dd, *J* = 8.55, 1.31 Hz, Ar-*H*), 7.54-7.43 (5H, m, Ar-*H*), 7.40 (2H, d, *J* = 8.58 Hz, Ar-*H*), 7.21-6.99 (5H, m, Ar-*H* and C=C*H*), 2.54-2.33 (6H, m, Ar-C*H*$_3$), 1.34 (9H, s, Ar-C(C*H*$_3$)$_3$) ppm. ^{13}C{^{1}H} NMR (101 MHz, CDCl$_3$): δ 197.3, 189.5, 154.1, 152.0, 151.9, 151.0, 145.7, 145.4, 141.9, 141.6, 139.6, 137.4, 137.1, 134.4, 133.3, 133.2, 130.7, 130.6, 129.8, 129.5, 129.4, 129.0, 128.0, 127.9, 127.0, 126.9, 126.9, 126.6, 126.4, 126.3, 126.2, 126.0, 125.7, 125.3, 122.5, 35.1, 31.7, 21.9 ppm. HRMS (ES)(%): found *m/z* = 929.1236; {$C_{42}H_{34}BrN_4O_3Na^{185}Re^+$} requires 929.1236. IR (KBr plates): 3769, 2020, 1917, 1900, 1600, 1471, 843 cm^{-1}. UV-vis λ_{max} (ε / M^{-1} cm^{-1}) (CHCl$_3$): 288 (47600), 342 (28100), 423 (8400) nm.

Synthesis of [ReBr(CO)$_3$(28)]

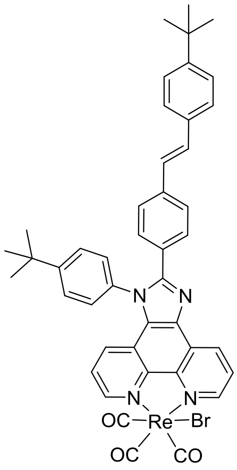

Into a round bottom flask was added lophine L8 (0.072 g, 0.123 mmol), [Re(CO)$_5$Br] (0.050 g, 0.123 mmol), and toluene (30 ml). The reactants were left at reflux for 3 hours. The solvent was removed *in vacuo* to yield a yellow solid. CHCl$_3$ was added (2 ml) and product was precipitated from hexane to give yellow solid. The solid was washed with ethanol and collected the product as a yellow powder (yield = 0.080 g). ^{1}H NMR (400 MHz, CDCl$_3$): δ 9.36-9.25 (2H, m, phen-*H*), 9.19 (1H, d, *J* = 5.02 Hz, phen-*H*), 7.88 (1H, dd, *J* = 8.20, 5.18 Hz, Ar-*H*), 7.65 (2H, d, *J* = 8.57 Hz, Ar-*H*), 7.60-7.47 (3H, m, Ar-*H*), 7.47-7.29 (9H, m, Ar-*H*), 7.03 (2H, dd, *J* = 45.72, 16.33 Hz, C=C*H*), 1.42 (9H, s, Ar-C(CH_3)$_3$), 1.27 (9H, s, Ar-C(CH_3)$_3$) ppm. ^{13}C{^{1}H} NMR (101 MHz, CDCl$_3$): δ 155.4, 154.5, 151.8, 151.1, 145.9, 145.3, 139.8, 137.1, 134.7, 134.4, 133.4, 133.4, 130.8, 130.5, 130.0, 128.6, 128.5, 128.4, 128.2, 128.0, 127.9, 127.1, 126.9, 126.7, 126.4, 126.2, 125.2, 122.6, 35.8, 35.2, 31.9, 31.7 ppm. HRMS (ES)(%): found *m/z* = 935.1730; {$C_{44}H_{39}N_3O_3Br^{185}Re$} requires 937.1730. IR (KBr plates): 2960, 2018, 1892, 1600, 1509, 805 cm^{-1}. UV-vis λ_{max} (ε / M^{-1} cm^{-1}) (CHCl$_3$): 271 (34100), 299 (31000), 338 (30500), 419 sh (6300) nm.

2.8 Supplementary data

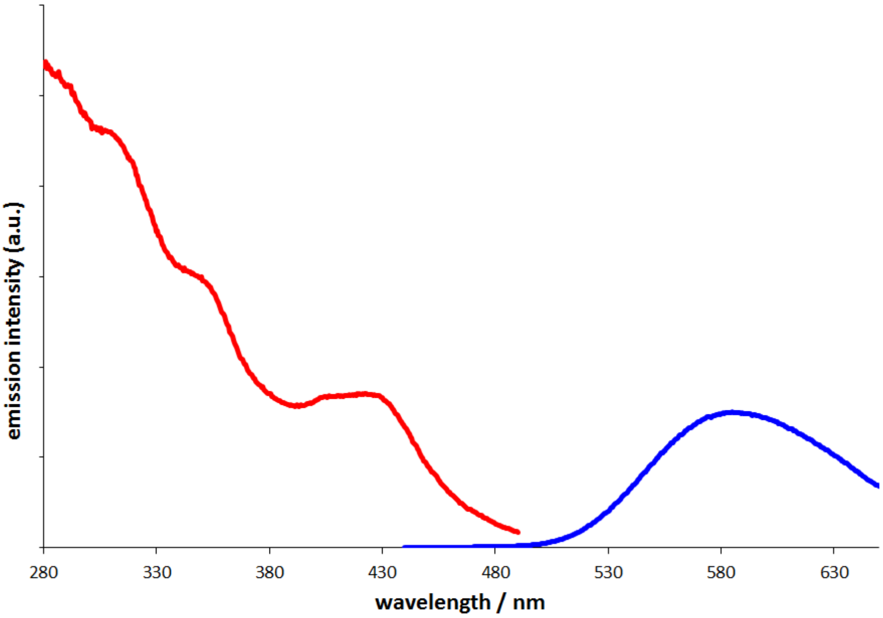

Figure 55: Excitation (red) and emission spectra of [Re(CO)$_3$(**22**)Br] obtained in CHCl$_3$

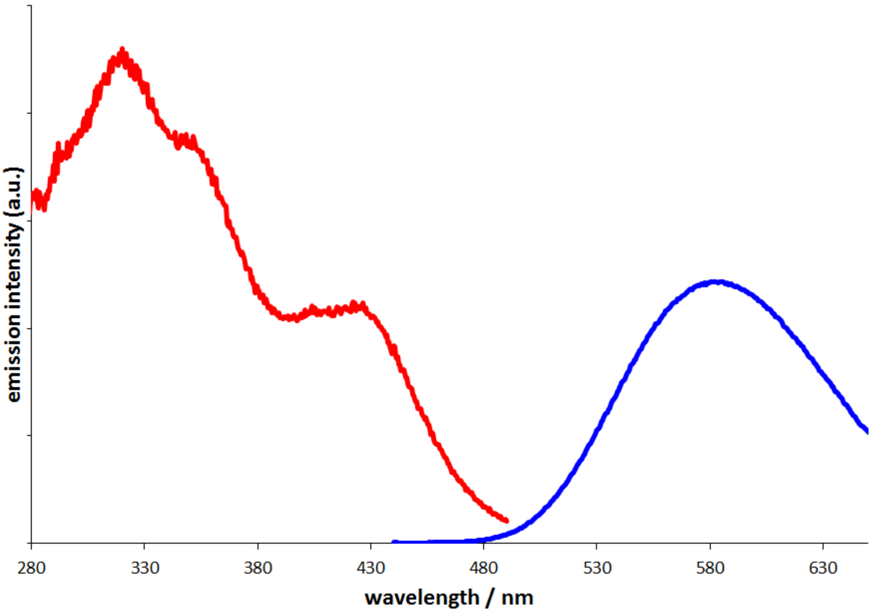

Figure 56: Excitation (red) and emission spectra of [Re(CO)$_3$(**23**)Br] obtained in CHCl$_3$

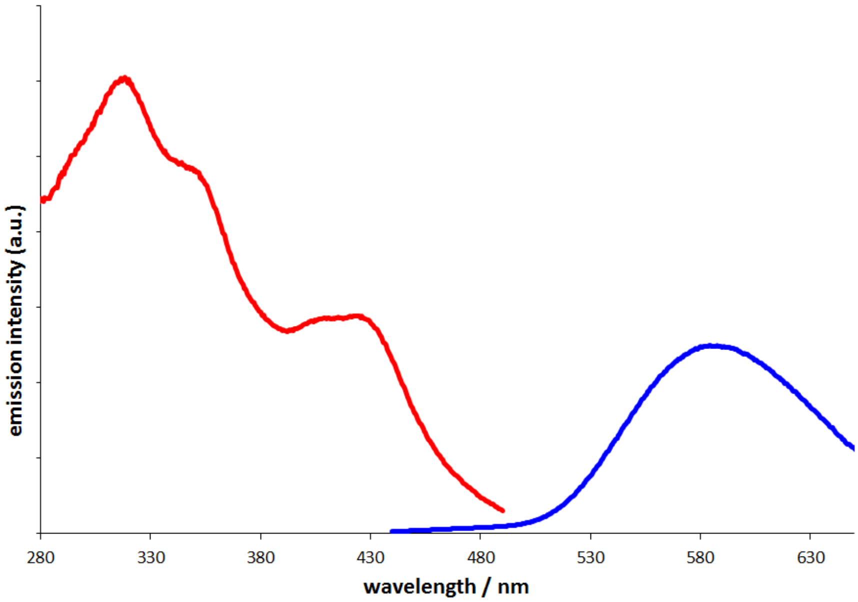

Figure 57: Excitation (red) and emission spectra of [Re(CO)$_3$(**24**)Br] obtained in CHCl$_3$

2.9 References

(1) Reitz, G. A.; Dressick, W. J.; Demas, J. N. *J. Am. Chem. Soc.* **1986**, *108*, 5345.

(2) Sacksteder, L.; Zipp, A. P.; Brown, E. A.; Streich, J.; Demas, J. N.; DeGraff, B. A. *Inorg. Chem.* **1990**, *29*, 4335.

(3) Yam, V. W.; Lo, K. K.; Cheung, K.; Kong, R. *J. Chem. Soc. Chem. Commun.* **1995** 1191.

(4) Lo, K. K.; Zhang, K. Y.; Li, S. P. *Eur. J. Inorg. Chem.* **2011**, 3551.

(5) Lo, K. K.; Hui, W.-K.; Chung, C.-K.; Tsang, K. H.; Ng, D. C.; Zhu, N.; Cheung, K.-K. *Coordin. Chem Rev.* **2005**, *249*, 1434.

(6) Lo, K. K.; Hui, W.-K.; Ng, D. C.; Cheung, K. *Inorg. Chem.* **2002**, *41*, 40.

(7) Wenger, O. S.; Henling, L. M.; Day, M. W.; Winkler, J. R.; Gray, H. B. *Inorg. Chem.* **2004**, *43*, 2043.

(8) Dattelbaum, D. M.; Itokazu, M. K.; Iha, N. Y. M.; Meyer, T. J. *J. Phys. Chem. A.* **2003**, *107*, 4092.

(9) Burroughes, J. H.; Bradley, D. D. C.; Brown, A. R.; Marks, R. N.; Mackay, K.; Friend, R. H.; Burns, P. L.; Holmes, A. B. *Nature* **1990**, *347*, 539.

(10) Tang, C. W.; VanSlyke, S. A. *Appl. Phys. Lett.* **1987**, *51*, 913.

(11) Gong, X.; Ng, P. K.; Chan, W. K. *Adv. Mater.* **1998**, *10*, 1337.

(12) Li, Y.; Liu, Y.; J., G.; Wu, F.; Tian, W.; Li, B.; Wang, Y. *Synth. Met.* **2001**, *118*, 175.

(13) Li, F.; Zhang, M.; Cheng, G.; Feng, J.; Zhao, Y.; Ma, Y. G.; Lui, S. Y.; Shen, J. C. *Appl. Phys. Lett.* **2004**, *84*, 148.

(14) Ma, Y. G.; Zhang, H. Y.; Shen, J. C.; Che, C. M. *Synth. Met.* **1998**, *94*, 245.

(15) Steck, E. A.; Day, A. R. *J. Am. Chem. Soc.* **1943**, *65*, 452.

(16) Fridman, N.; Kaftory, M.; Eichen, Y.; Speiser, S. *J. Mol. Struct.* **2009**, *917*, 101.

(17) Feng, K.; Hsu, F.-L.; Van DerVeer, D.; Bota, K.; Bu, X. R. *J. Photoch. Photbio. A.* **2004**, *165*, 223.

(18) V. P. Boricha; S. Patra; Y. S. Chouhan; P. Sanavada; E. Suresh; Paul, P. *Eur. J. Inorg. Chem.* **2009**, 1256.

(19) F. L. Thorp-Greenwood; M. P. Coogan; A. J. Hallett; Laye, R. H.; Pope, S. J. A. *J. Organomet. Chem.* **2009**, *694* 1400.

(20) Veroni, I.; Mitsopoulou, C. A.; Lahoz, F. J. *J. Organomet. Chem.* **2008**, *693*, 2451.

(21) Sun, S. S.; Lees, A. J. *J. Am. Chem. Soc.* **2000**, *122*, 8956.

(22) Wrighton, M.; Morse, D. L. *J. Am. Chem. Soc.* **1974**, *96*, 998.

Chapter 3 Synthesis and characterisation of fluorescent hydroxy and methoxy-substituted imidazole[4,5-f]-1,10-phenanthroline derivatives and their Re(I) carbonyl complexes

3.1 Introduction

In this chapter, a series of novel diimine ligands have been coordinated to the *fac*-[Re(CO_3)Br] core for investigation into luminescent responses to variations of functional groups. The isolated complexes incorporated either methoxybenzene or hydroxybenzene derivatives. Analogous molecules containing a non-coordinating phenanthrene moiety were also isolated and compared to their 1,10-phenanthroline containing analogues. All complexes and ligands were fully characterised using a range of spectroscopic techniques. Crystal structures were also obtained for complexes *fac*-[ReBr$(CO)_3$**(47)**], *fac*-[ReBr$(CO)_3$**(49)**] and *fac*-[ReBr$(CO)_3$**(52)**].

3.2 1,2-dihydroxybenzene derivatives

1,2-dihydroxybenzene, also known as catechol, and catechol-containing molecules have recently proved to be useful for the detection of a variety of metal ions.[1] Among the metals suitable for detection via binding with catechol are group 13 metals,[2] Fe,[3] U,[4] and also a range of lanthanide ions.[1] In many of these examples the metal ions were detected through quenching of fluorescence upon coordination of the metal ion. For example, Al^{3+}, Ga^{3+} and In^{3+} were all detected through the use of a fluorescent catechol-containing ligand (Figure 58).[2]

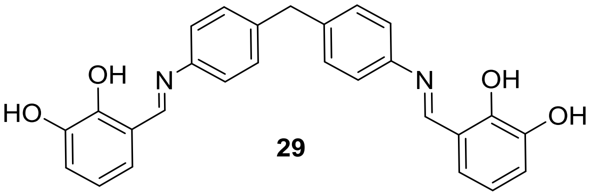

29

Figure 58: Molecular structure of fluorescent catechol, **29**

It was found that the free ligand was only weakly emissive due to the competition between the intramolecular photo-induced proton transfer (PPT) and the photo-induced electron transfer (PET) from the imines. Upon deprotonation with tetrabutylammonium hydroxide, the photo-induced proton transfer was prevented, leading to an increase in emission intensity. Upon coordination to the trivalent metal nitrates, this emission is quenched (Figure 59).

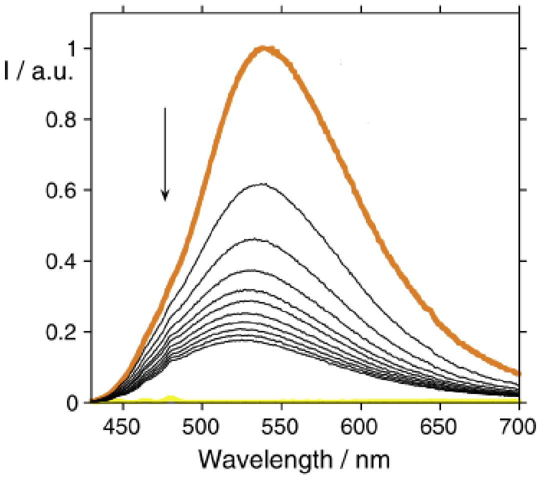

Figure 59: Fluorometric titrations of ligand **29** (yellow line) in CH_3CN as a function of added Al^{3+}, after addition of 4 equivalents of $Bu_4N(OH)$ (orange line).[2]

This effect in solution is due to the coordination of the oxygen atoms and the uncoordinated nitrogen donor atoms present in the ligands, activating the quenching through the PET phenomena.

3.3 Optical properties of catechol-containing molecules

The optical properties of catechol have been previously investigated.[5] The solvatochromism of nine push-pull substituted catechol derivatives has previously been explored in a range of 39 solvents.[6] Examples are shown in Figure 60.

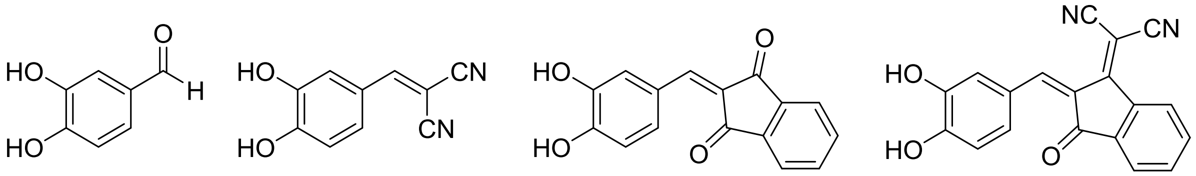

30a **30b** **30c** **30d**

Figure 60: Molecular structure of a range of catechols

It was observed for each catechol derivative that the shortest wavelength absorption occurred in the least polar solvents (e.g. $CHCl_3$). The largest bathochromic shift was then observed for the most polar solvents such as DMSO and hexamethyl-phosphoric triamide (HMPA). Additional absorbtion bands were also observed for 3,4-dihydroxy benzaldehyde as a result of hydrogen bond formation and deprotonation with increasing solvent polarity.

3.4 Dihydroxy 3,4-dihydroxy-imidado[4,5-*f*][1,10]-phenanthroline complexes for pH monitoring

Catechol derivatives have been utilised as fluorescent chemosensors for wide-range pH monitoring.[7] Lophine-based catechol complexes have also proven useful pH sensors, with the protonation/deprotonation of the phenol groups leading to a change in emission intensities as well as emission wavelength.[8] For example, a ruthenium complex containing a 3,4-dihydroxy-imidado[4,5-*f*][1,10]-phenanthroline moiety (**31**) was isolated and its luminescence emission explored at varying pH. It was reported that the complex showed an emission maximum ≈ 620 nm, which is characteristic of luminescence derived from a triplet MLCT (d(Ru)$\rightarrow\pi^*$(ligand) transition. It was observed that the emission intensity was dependent upon pH, with the intensities reducing upon deprotonation (i.e. from pH1→pH14). Additionally, there was a slight blue shifting of the λ_{max} upon deprotonation. It was concluded that the deprotonated phenol group resulted in almost complete quenching of the Ru(II) emission due to the PET process. It was also observed that at a constant pH, addition of DNA to this complex resulted in quenching of the emission, implying that the complex intercalated with DNA.

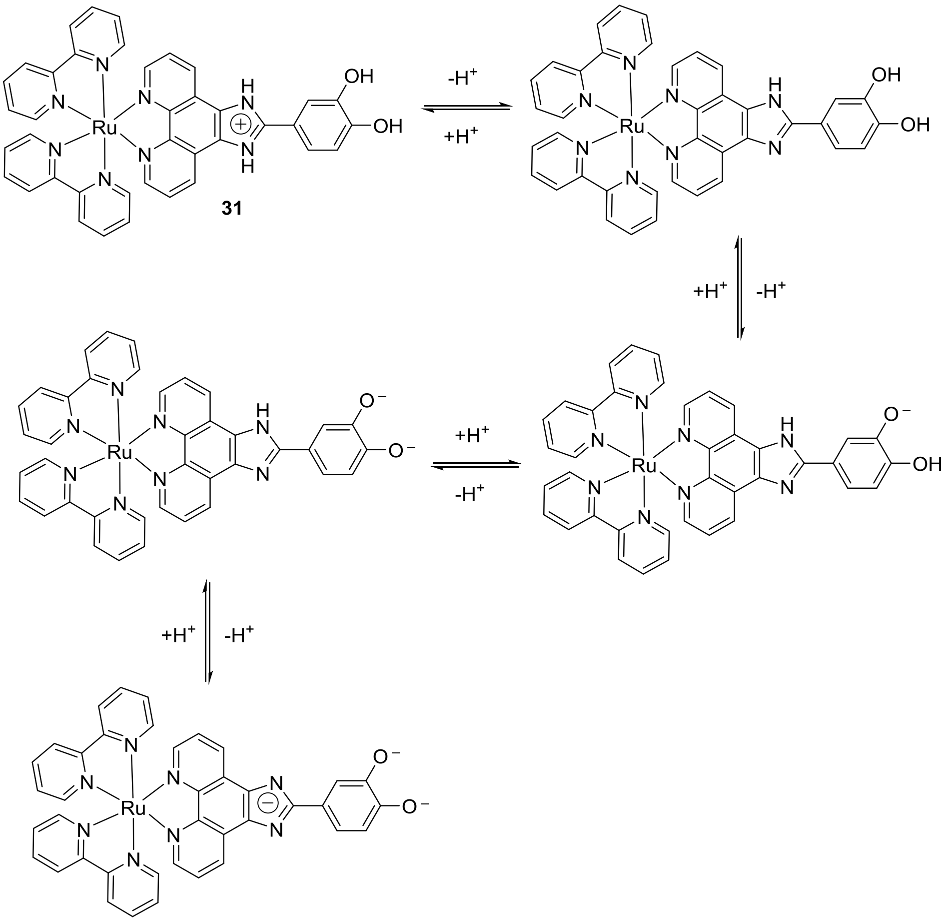

Figure 61: Protonation/ deprotonation process of **31**. [8]

3.5 Luminescent properties of phenanthrene

Much of this chapter will discuss the use of catechol based lophines that incorporate a phenanthrene core instead of a 1,10-phenanthroline core. Compounds which incorporate both the phenanthrene moiety and catechol are not commonly found in the literature, however the fluorescent and phosphorescent attributes of phenanthrene based compounds are well known. Early investigations of the luminescent and electronic properties of phenanthrene included studies on fluorescence emission,[9] polarization of the luminescence,[10] and the generation and lifetimes of the phenanthrene triplet state.[11-13] Recently, the luminescence of phenanthrene has been investigated for applications including OLEDs[14-16] and metal coordination/detection, including Au, [17]Hg^{2+},[18] and Re(I).[19]

3.5.1 Phenanthrene-based OLEDs

Conjugated polymers, such as polyfluorenes (PFs), which have large band gaps are ideal molecules for blue-light emitting OLEDs. However, one of the problems of using polyfluorenes is their tendency to generate long wavelength emission around 550 nm either during annealing or passage of current, turning the desired blue emission colour into the undesired blue-green emission.[14] This blue-light emitter has been stabilised by incorporating a repeat phenanthrene unit, **32**, which maintains the desired blue emission (Figure 62).

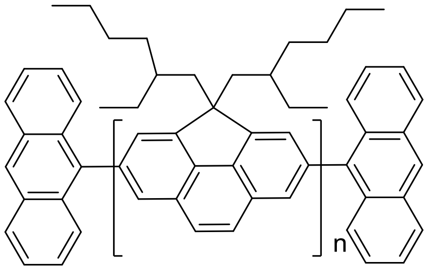

32

Figure 62: Molecular structure of poly(2,6-(4,4-bis(2-ethylhexyl)-4H-cyclopenta[*def*]phenanthrene)), **32**

32 (PCCP) showed high maximum brightness and high efficiency, and displayed stabilized blue electroluminescence (EL) without a lower energy emission band.

3.5.2 Metal complexes/sensing

Phenanthrene has in the last ten years been incorporated into chromophoric systems in order to exploit its luminescence traits.[17,18,19] Although phenanthrene does not contain any heteroatoms for coordination to metals, it is often used to extend the conjugation of the system, or indeed to act as the chromophore on its own. For example, in 2008 a phenanthrene containing gold complex (Figure 63, **33**) was reported to exhibit intense blue-green emission.[17]

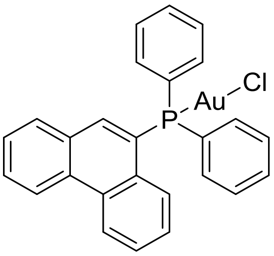

33

Figure 63: Molecular structure of gold complex **33**

The Au was coordinated by reaction of $AuCl(Me_2S)$ and 9-diphenylphosphinophenanthrene. The emission spectra of the free ligand showed a broad featureless band centred at ca. 550 nm. This band was tentatively assigned as an intramolecular charge-transfer of (ICT) from the diphenyl phosphino group to the phenanthrene unit. This assignment was partly based on a significant red-shift of the emission in polar solvents, which is indicative of a charge-transfer process. The emission spectra of **33** displayed a blue-green emission at ca. 500 nm at 297 K in degassed 2-MeTHF. This emission was attributed to room temperature phosphorescence from the phenanthrene chromophore. This was based on the extended measured lifetime (22 μs) which indicated a spin-forbidden relaxation process that led to a longer emission lifetime. Additionally, it was assigned a phenanthrene based emission as the vibronic structure of the band was similar to the vibronic structure observed for free phenanthrene at 77 K. The Au atom appeared to have a marked effect on the phosphorescence, as upon coordination the radiative rate constant (k_f) increased four-fold, indicating a large heavy atom effect of the gold on the phenanthrene.

3.6 DNA binding ability of dihydroxy 3,4-dihydroxy-imidado[4,5-*f*][1,10]-phenanthroline complexes

The DNA binding abilities of Ru(II)[8,20] and Co(III)[21,22] catechol-"lophine" complexes have been an area of interest recently. For example, the suitability of the use of catechol as a DNA "molecular light switch" has been investigated.[22] It was found that the incorporation of a cobalt catechol-lophine complex $[Co(bipy)_2(ODHIP)]^{3+}$ (Figure 64), **34** (where ODHIP = 3,4-dihydroxyl-imidazo[4,5-*f*][1,10]phenanthroline) into calf thymus (ct) DNA led to hypochromism and a bathochromic shift in the absorption spectrum, and an increase in intensity of the fluorescence emission (Figure 65). The increase in emission intensity was attributed to the complex being "shielded" from water by the DNA, which reduced quenching. The additional binding site imparted by the catechol moiety was also exploited, as successful coordination of Cu^{2+} led to the quenching of the fluorescence (i.e. fluorescence could be switched "off") in ct DNA.

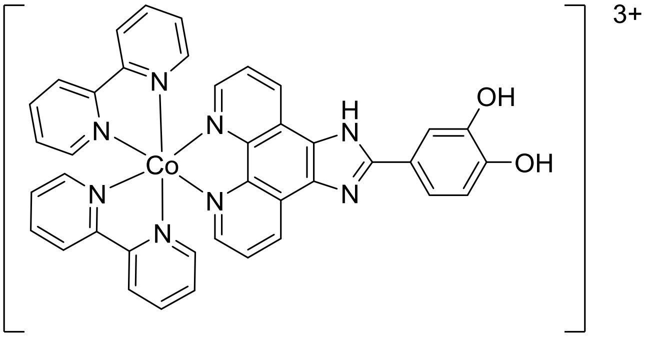

Figure 64: Co complex **34** used as a “DNA molecular light switch”

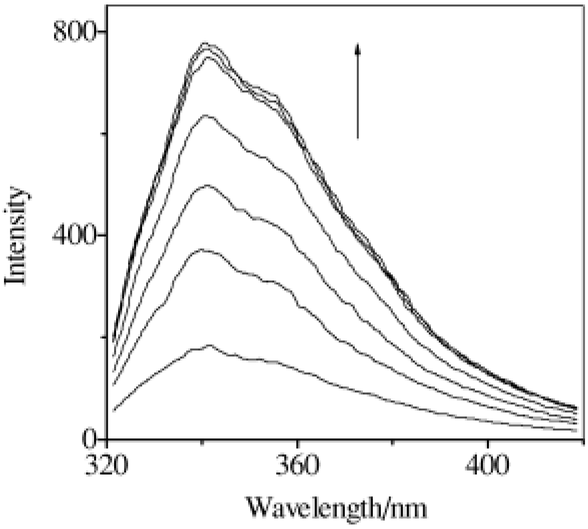

Figure 65: Emission intensity as a function of increasing concentration of DNA

3.7 Aims

The aims of this chapter will be achieved through the following key areas:

- Isolate and characterise a series of methoxy based “lophine” chromophores.
- Isolate and characterise a series of “catechol” based “lophine” chromophores.
- Isolate both phenanthrene and phenanthroline based molecules of the above.
- Coordination investigation with the Re(I) tricarbonyl core (with the phenanthroline-based ligands)
- Explore optical properties of the ligands and their associated complexes.
- Investigate solvatochromism for the hydroxy-containing molecules.

3.8 Results and Discussion

3.8.1 List of isolated compounds

Listed in Figure 66 are the compounds which were isolated in this chapter, along with their designated number for reference.

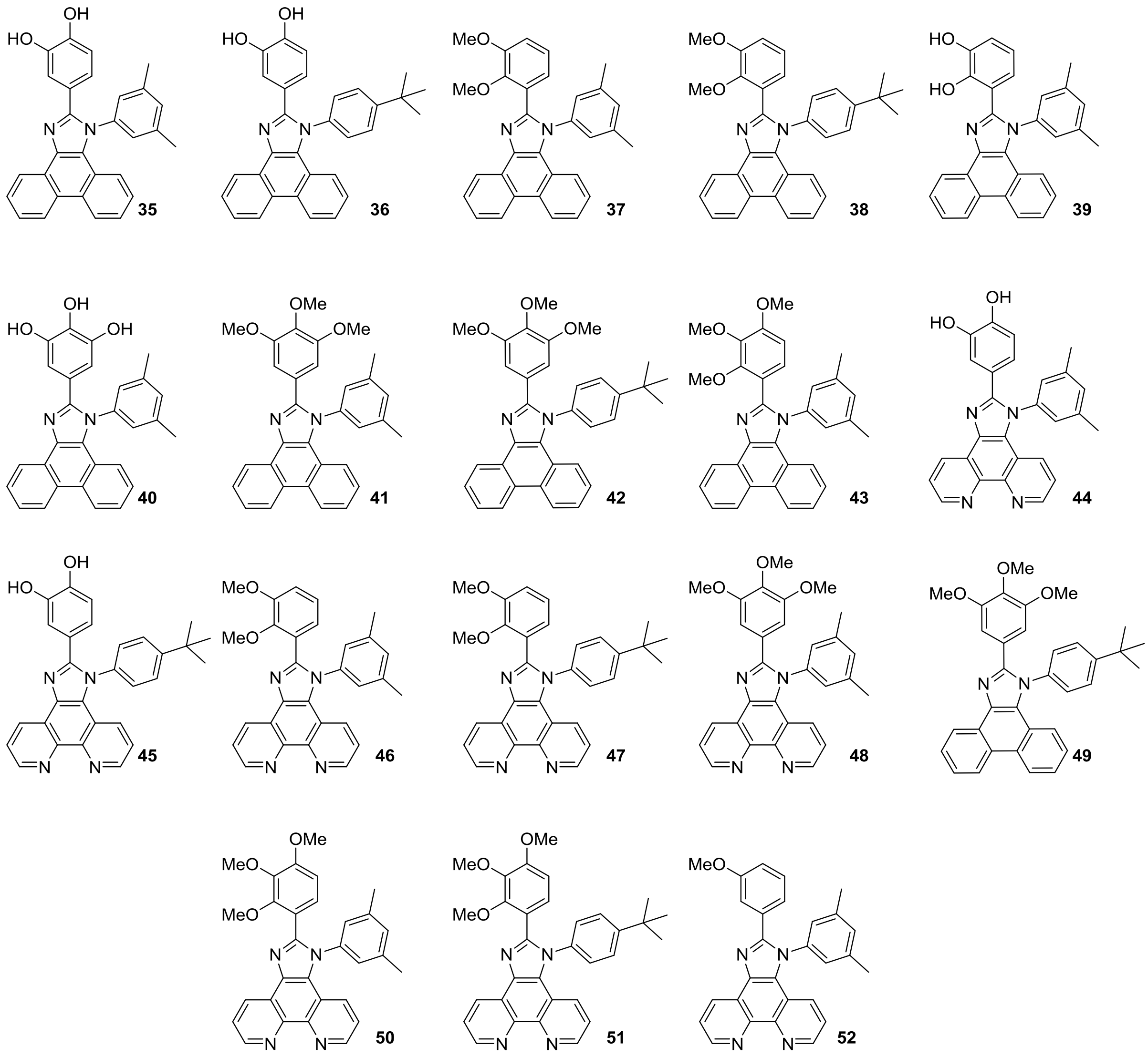

Figure 66: List of isolated ligands

This chapter presents a study of methoxy and hydroxy substituted fused imidazo[4,5-*f*]-1,10-phenanthroline and phenanthrene ligands and their subsequent reactions to form Re(I) complexes. All ligands and complexes have been fully characterised, with x-ray crystal structures obtained for *fac*-[ReBr(CO)$_3$(**47**)], *fac*-[ReBr(CO)$_3$(**49**)] and *fac*-[ReBr(CO)$_3$(**52**)].

3.8.2 Synthesis of the ligands

All compounds with the exception of **39** and **40** were isolated through a similar method to that previously described in chapter 2, using the appropriate methoxy or hydroxy derived benzaldehyde. However isolation of some compounds proved difficult through this method, in particular 2,3-hydroxy derivatives, due to solubility issues as well as steric constraints. Potentially, there was also a formation of a tautomer which could reduce the reactivity of the benzaldehyde (Figure 67).

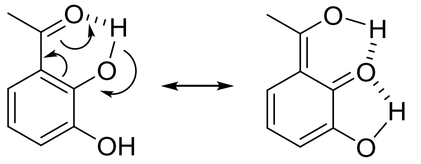

Figure 67: Possible Tautomer

This was circumvented through the isolation of the analogous 2,3-methoxy derivative, and its subsequent demethylation with BBr_3 using known techniques.[23-26] Although generally the 2,3-dimethoxy derivatives displayed lower yields, most likely due to steric constraints reducing reactivity, they did provide a synthetic pathway to the 2,3-hydroxy derivatives.

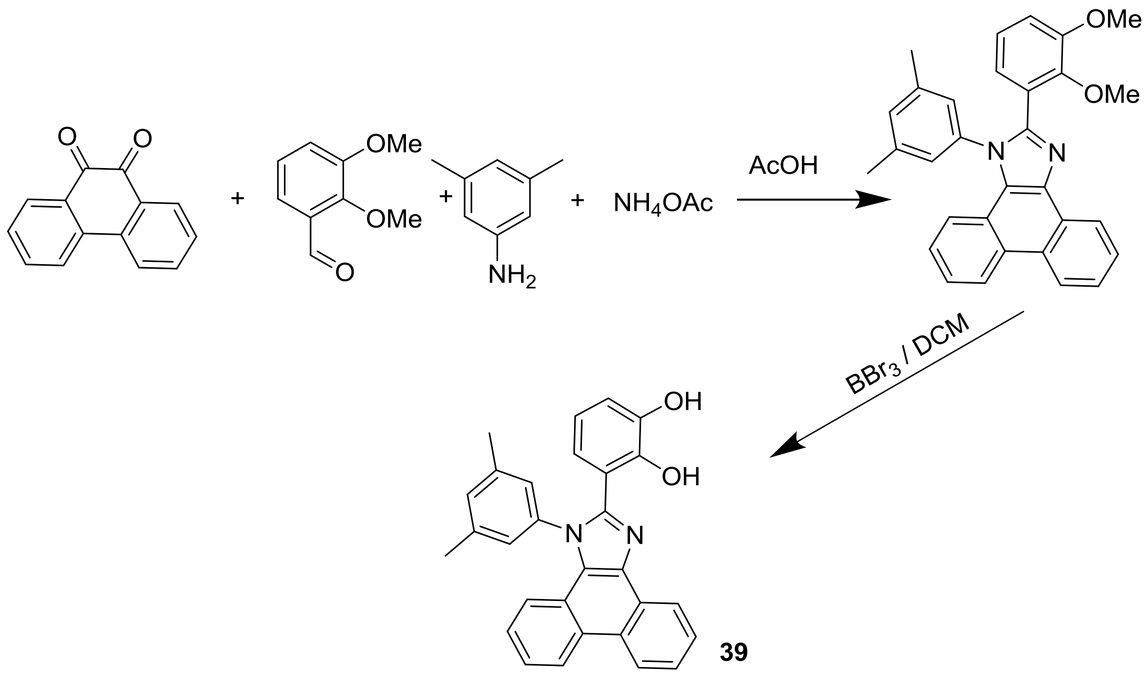

Scheme 5: Formation of **39** through demethylation.

Generally, the hydroxy-containing lophines had reduced solubility in less polar solvents (although in some instances were sparingly soluble in $CHCl_3$), and in most cases characterisation was carried out in polar solvents such as MeOH or DMSO. All compounds were isolated as light brown or off-white powders. Table 14 displays the yields of the isolated compounds. Ligands were isolated in poor-to-moderate yields, most likely related to varying difficulties in isolating the compounds due to different solubilities.

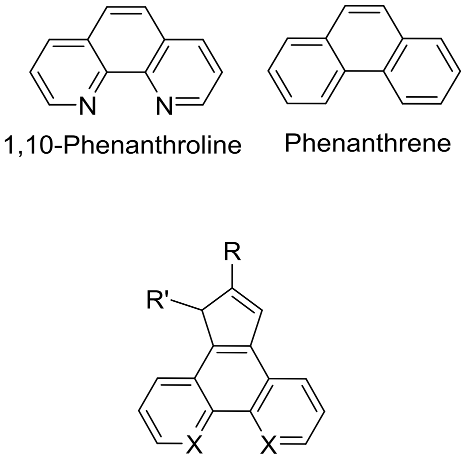

Figure 68: General formulation of the isolated lophines

Compound Number	Core	R	R′	Yield (%)
35	Phenanthrene	3,4-dihydroxy	3,5-diMe	32
36	Phenanthrene	3,4-dihydroxy	4-^{t}Bu-Ph	42
37	Phenanthrene	2,3-dimethoxy	3,5-diMe	61
38	Phenanthrene	2,3-dimethoxy	4-^{t}Bu-Ph	71
39	Phenanthrene	2,3-dihydroxy	3,5-diMe	52
40	Phenanthrene	3,4,5-trihydroxy	3,5-diMe	76
41	Phenanthrene	3,4,5-trimethoxy	3,5-diMe	90
42	Phenanthrene	3,4,5-trimethoxy	4-^{t}Bu-Ph	56
43	Phenanthrene	2,3,4-trimethoxy	3,5-diMe	30
44	1,10-Phen	3,4-dihydroxy	3,5-diMe	56
45	1,10-Phen	3,4-dihydroxy	4-^{t}Bu-Ph	41
46	1,10-Phen	2,3-dimethoxy	3,5-diMe	59
47	1,10-Phen	2,3-dimethoxy	4-^{t}Bu-Ph	50
48	1,10-Phen	3,4,5-trimethoxy	3,5-diMe	85
49	1,10-Phen	3,4,5-trimethoxy	4-^{t}Bu-Ph	54
50	1,10-Phen	2,3,4-trimethoxy	3,5-diMe	41
51	1,10-Phen	2,3,4-trimethoxy	4-^{t}Bu-Ph	34
52	1,10-Phen	3-methoxy	3,5-diMe	49

Table 14: Isolated ligands and their yields

3.8.3 Characterisation of the ligands

All isolated compounds were investigated via ^{1}H and ^{13}C{^{1}H} NMR spectroscopy. The characteristics of the ^{1}H NMR spectra are similar to those described in chapter 2, with the loss of a benzaldehyde peak at ca. 10 ppm, and the observation of signals at ca. 8.5-9.5 ppm assigned to phenanthroline/phenanthrene aromatic protons.

The ^{1}H NMR spectrum of **41** is shown in Figure 69 which displayes distinctive signals at 3.6-3.8 ppm which are attributed to protons of the OMe substituents of the molecule. Two signals were observed for the three methoxy groups present, with one of the signals integrating to twice that of the other. The presence of only two signals indicates that there is free rotation around the apical C-C bond, and it can also be predicted that the equivalent MeO groups were those in the “3” and “5” positions, whilst those situated on the “4” position MeO are chemically distinct from those two. The appearance of only one signal for the methyl groups (c) also indicates free rotation of the R′ sidearm.

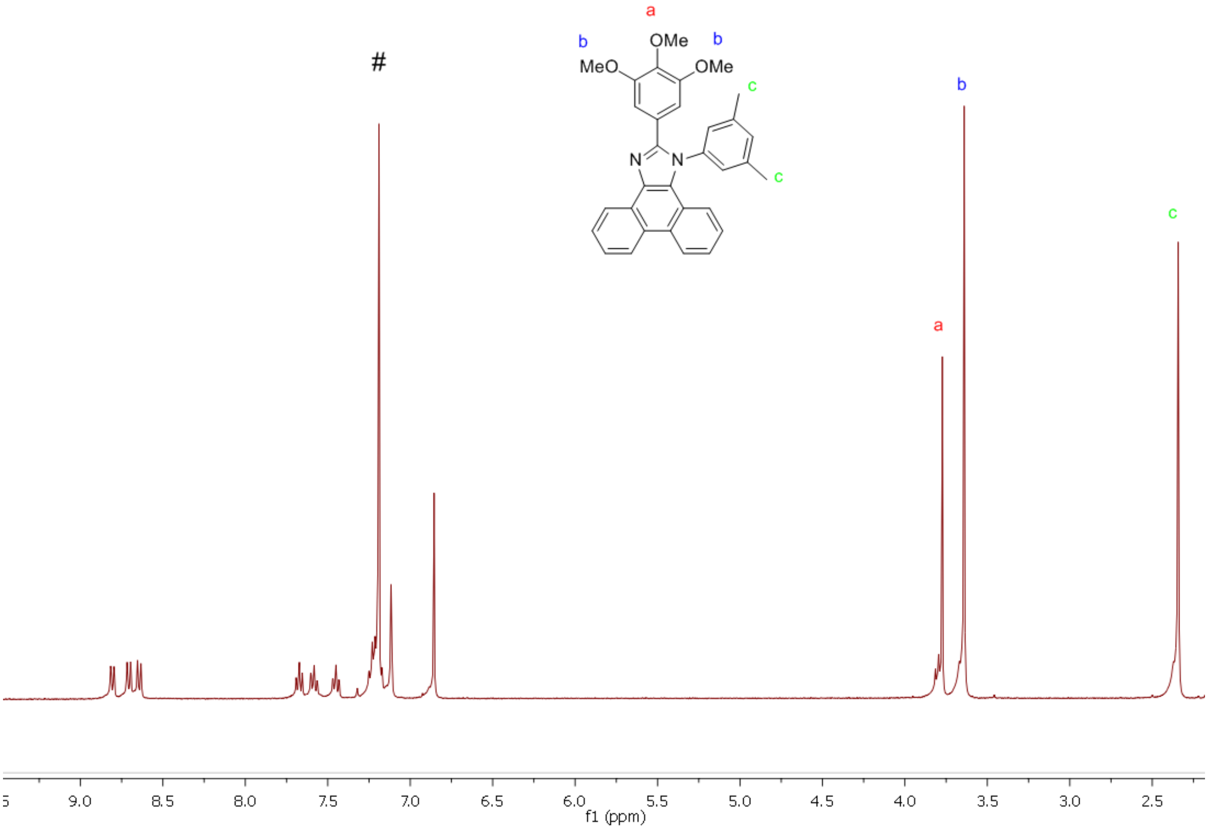

Figure 69: ^{1}H NMR spectrum of **41** obtained in $CDCl_3$ at 298K

The ^{1}H NMR spectrum of the analogous demethylated lophine (Figure 70) suggests the formation of the correct compound, with the loss of the signal for the MeO groups at 3.6-3.8 ppm. After demethylation, the solubility of the tris-hydroxy lophine in $CHCl_3$ was poor therefore the NMR sample was prepared in d_6-DMSO. A broad signal was observed for the OH groups at ≈ 9.5 ppm, which are almost hidden due to extensive broadening of the signal. No OH peak was visible when the sample was run in MeOD. Hydroxy originating signals were also barely visible for lophine **36**, which contains a dihydroxy group and was soluble in $CDCl_3$, appearing as a very broad peak between 9.1 and 9.3 ppm. Chemical shifts were also observed in the aromatic region, with the three resonances previously observed at 8.6-9.0 ppm appearing as two resonances at ≈ 8.6 and 9.1 ppm. This is likely a result of a change of solvent resulting in different chemical shifts for the aromatic protons.

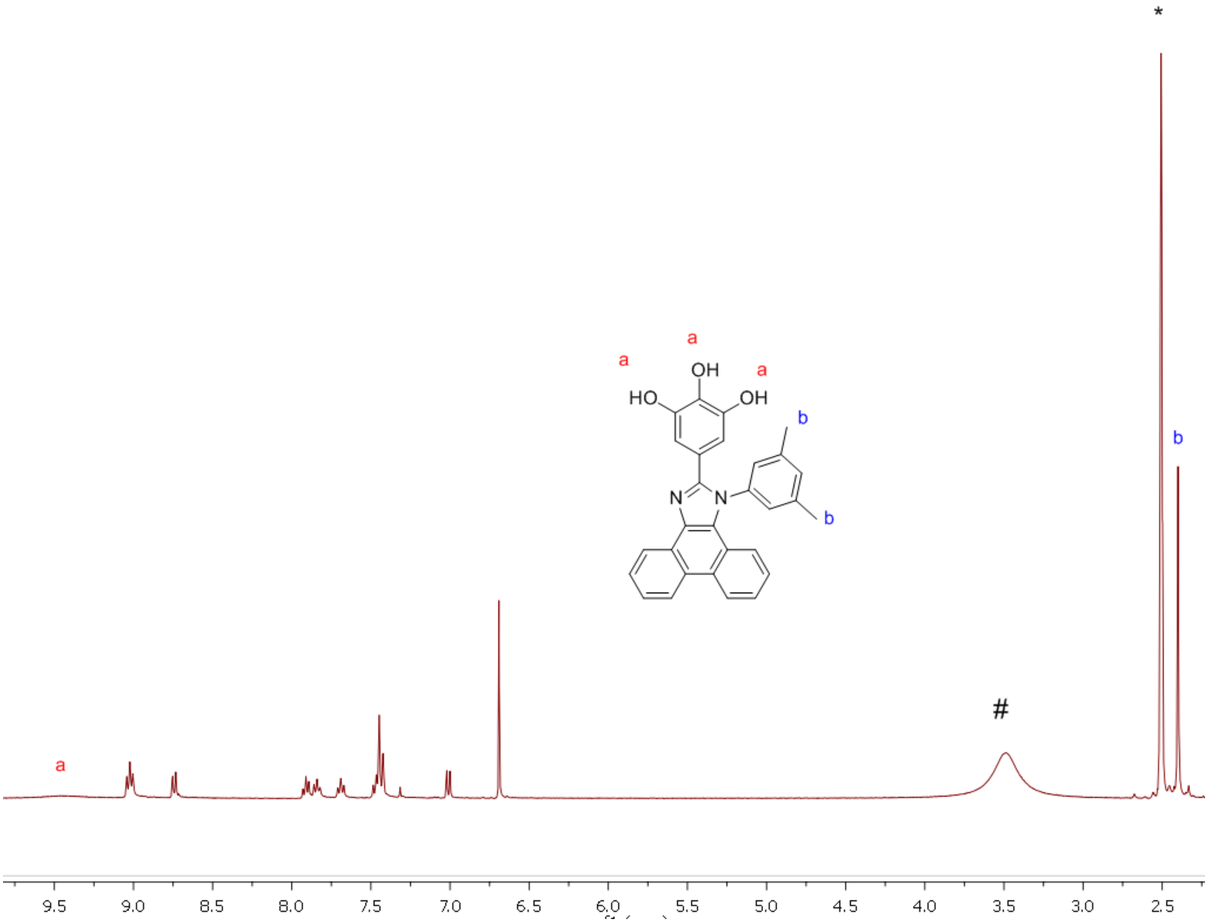

Figure 70: NMR spectrum of **40** in DMSO at 298K, # = residual solvent, * =d^6-DMSO

The $^{13}C\{^1H\}$ NMR spectra of the compounds again showed numerous signals in the aromatic region (~100-155 ppm in $CDCl_3$). Even though the isolated compounds were unsymmetric, it is likely that free rotation around the apical C-C bond and the side-arm N-C bond leads to chemical equivalency of pairs of carbon atoms. In addition, the presence of numerous quaternary carbon atoms may result in weak signals which were not observed in the spectra. Observed in the aliphatic region of the $^{13}C\{^1H\}$ NMR spectra were carbons associated with the O-CH_3 substituents, as well as alkyl carbons associated with the R′ groups. In each instance the $^{13}C\{^1H\}$ NMR confirmed the number of OMe environments that were visible in the ^1H NMR spectrum, again implying a free rotation around the apical C-C bond.

High resolution electro-spray mass spectrometry confirmed in each case the presence of the protonated molecular ion. Infrared spectra were obtained on KBr plates for each ligand, for which few notable peaks were observed. Each compound had a band at ≈ 2900 cm^{-1}, corresponding to an alkyl C-H stretch and numerous bands in the "fingerprint" region of the spectra. No starting material benzaldehyde, aniline or ketone peaks were observed for any of the compounds.

3.8.4 Electronic Absorption Spectroscopy of the ligands

Shown in Table 15 are the UV-vis absorption data for compounds **35-52**.

Compound Number	**Core**	**R**	**R′**	**Absorption λ_{max} /nm (ε/M^{-1}cm^{-1})**	**Solvent**
35	Phenanthrene	3,4-dihydroxy	3,5-diMe	299 (27,100), 357 (8300)	MeOH
36	Phenanthrene	3,4-dihydroxy	4-^{t}Bu-Ph	263 (115,800), 325(sh) (25,500), 360 (8500), 456 (1700)	$CHCl_3$
37	Phenanthrene	2,3-dimethoxy	3,5-diMe	260 (87,000), 280 (sh) (39,400), 339 (sh) (4091), 357 (3900)	$CHCl_3$
38	Phenanthrene	2,3-dimethoxy	4-^{t}Bu-Ph	260 (88,000), 281 (sh) (37,400), 304 (sh) (17,400), 339 (3200), 356 (3800)	$CHCl_3$
39	Phenanthrene	2,3-dihydroxy	3,5-diMe	262 (47,200), 285(sh) (17,500), 365 (8800)	DMSO
40	Phenanthrene	3,4,5-trihydroxy	3,5-diMe	257 (24,300), 304 (8700), 356 (2500)	MeOH
41	Phenanthrene	3,4,5-trimethoxy	3,5-diMe	263 (59,600), 317 (24,200), 361 (sh) (11,200)	$CHCl_3$
42	Phenanthrene	3,4,5-trimethoxy	4-^{t}Bu-Ph	263 (63,400), 317 (24,700), 362 (sh) (10,200)	$CHCl_3$
43	Phenanthrene	2,3,4-trimethoxy	3,5-diMe	258 (85,200), 280 (s) (26,000), 306	$CHCl_3$

				(sh) (13,900)	
44	1,10-Phen	3,4-dihydroxy	3,5-diMe	262(sh) (54,200), 280 (58,500), 304 (sh)(46,300)	DMSO
45	1,10-Phen	3,4-dihydroxy	4-^{t}Bu-Ph	276 (31,800), 316(sh) (15,500), 423 (3100)	CHCl$_3$
46	1,10-Phen	2,3-dimethoxy	3,5-diMe	256 (55,600), 276 (sh) (42,500), 312 (14,000)	CHCl$_3$
47	1,10-Phen	2,3-dimethoxy	4-^{t}Bu-Ph	270 (97,600), 352 (sh) (2500)	CHCl$_3$
48	1,10-Phen	3,4,5-trimethoxy	3,5-diMe	278 (54,900), 325(sh) (11,600), 368 (sh) (1600)	CHCl$_3$
49	1,10-Phen	3,4,5-trimethoxy	4-^{t}Bu-Ph	281 (46,000), 314 (sh) (25,300), 361 (sh) (1600)	CHCl$_3$
50	1,10-Phen	2,3,4-trimethoxy	3,5-diMe	258 (53,900), 275(sh) (45,900), 314(sh) (9900), 362 (1600)	CHCl$_3$
51	1,10-Phen	2,3,4-trimethoxy	4-^{t}Bu-Ph	270 (77,900), 427 (sh) (2000)	CHCl$_3$
52	1,10-Phen	3-methoxy	3,5-diMe	273 (30,300), 313(sh) (15,300), 359 (sh) (1900)	CHCl$_3$

Table 15: Electronic absorption data for the isolated ligands

The discussion of the electronic absorption spectra of compounds **35-52** can be divided into three sections. The first is the effect of a phenanthrene core on the absorption of the molecule compared to a 1,10-phenanthroline core. The second is the differences observed for the methoxy and hydroxy containing molecules. Finally, the effect of the R′ sidearm on the absorption properties will be discussed.

The optical properties of phenanthrene and 1,10-phenanthroline are subtly distinct from each other. Although the electronic spectrum of 1,10-phenanthroline does bear some marked similarities, phenanthrene shows more pronounced vibrational structure, while the vibrational structure of 1,10-phenanthroline is more solvent-dependent.[27] Additionally it was found that 1,10-phenanthroline and phenanthrene emit at 378 and 350 nm respectively in cyclohexane, indicating that the energy of the $\pi\rightarrow\pi^*$ transition is greater for phenanthrene than 1,10-phenanthroline.

The observed λ_{max} values for the phenanthrene-containing **35-43** species were in the high energy end of the spectrum (≈ 260 nm) with large associated molar absorption coefficients. These observations are consistent with a high energy $\pi\rightarrow\pi^*$ transition expected of a highly conjugated π framework. Also visible in many of these spectra are lower energy peaks or shoulders with low molar absorption (ε) coefficients (1000-300 $M^{-1}cm^{-1}$) attributed to an intramolecular $n\rightarrow\pi^*$ transition. Lophines **35** and **40** both show anomalous results in absorption energy, and particularly in the value of the molar absorption coefficients. Molar absorption coefficients of 27,100 $M^{-1}cm^{-1}$ and 24,300 $M^{-1}cm^{-1}$ are observed respectively, which is drastically lower than the highest value molar absorption coefficient of the phenanthrene containing lophines, which has a value of 115,800 $M^{-1}cm^{-1}$. These observations are most likely a result of solvent polarity. Interactions between solute and solvent can affect peak position, profile and intensity, and in this case it is most likely hydrogen bonding between the hydroxy substituents and MeOH that is the cause of different spectra.[28] A high molar absorption coefficient (115,800 $M^{-1}cm^{-1}$) is observed at 263 nm for the di-hydroxy containing **36** in $CHCl_3$**,** however when the same chromophore is investigated in MeOH a molar absorption coefficient of 59,300 $M^{-1}cm^{-1}$ and a slight blue-shift is observed at 257 nm. This suggests that the polarity of the solvent has a significant influence on absorption intensity as well as potential hydrogen bonding from the solute. Hydrogen bonding can affect the absorption spectra by assisting electron migration, stabilizing some resonance structures, and also by the amount of aggregation of the solute in solution. For example poly(propylene-oxide)-poly(p-phenylene-ethynylene) block copolymers show less aggregation in $CHCl_3$ compared to MeOH/hexane and MeOH/water. [28] This aggregation of the solute in the latter two solvent systems led to a hypsochromic shift and a 50 % reduction in absorption intensity, largely due to the less solvated aromatic poly(p-phenylene-ethynylene) moiety of the molecule. These observations are similar to those observed for chromophore **36** which also showed a roughly 50 % decrease in intensity and a slight hypsochromic shift. Figure 71 shows the absorptions spectra of **37, 39** and **46**.

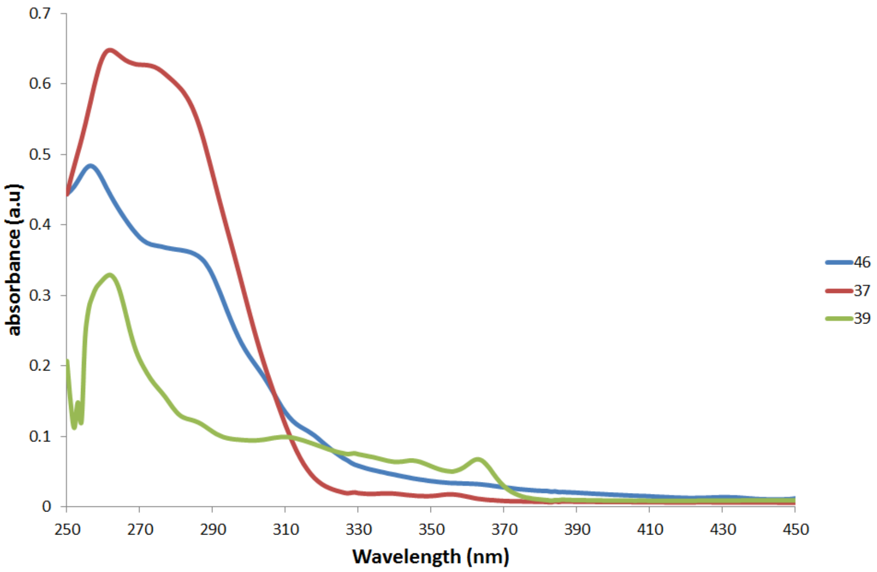

Figure 71: Electronic Absorption spectrum of **46**, **37** (both $CHCl_3$) and **39** (DMSO) at 298K

All 1,10-phenanthroline-containing molecules show high energy $\pi \rightarrow \pi^*$ transitions, between 256 and 281 nm. Similarly to the phenanthrene based molecules, $n \rightarrow \pi^*$ transitions are also visible as weak peaks or shoulders at lower energy. Compounds **44-52** have increased solubility in $CHCl_{3,}$ which implies the 1,10-phenanthroline moiety imparts increased solubility in less polar solvents. In general the molar absorption coefficients are lower for **44-52** in comparison to their phenanthrene analogues. This may be attributed to solute-solute interactions as well as solute-solvent interactions. The imines of the phenanthroline unit may hydrogen bond to other molecules as well as the solvent leading to aggregation and a reduction in absorption intensity.

It is difficult to compare the absorption spectra of the hydroxy and methoxy containing lophines directly as often they have different solubilities. The **37**/**39** and **41**/**40** analogous pairs display lower molar absorption coefficients in the hydroxy analogues and in the case of **40** a slight blue-shift of the absorption maxima. The $CHCl_3$ soluble **36** has a large molar absorption coefficient (115,800 $M^{-1}cm^{-1}$), and similar absorption maxima compared to dimethoxy-containing lophines.

The number of methoxy substituents does not appear to affect either the absorption maxima or the molar absorption coefficient of the molecule, although the two highest molar absorption coefficients were observed for **37** and **38** which are both 2,3-dimethoxy containing and phenanthrene based lophines.

Alterations to the R′ group in the phenanthrene-containing compounds did not induce any changes to the resultant absorption spectra. For example, the analogous pairs **37**/**38** and **41**/**42** showed little change in the absorption maxima wavelength or molar absorption coefficient. However, these observations were not repeated for the 1,10-phenanthroline containing analogous pairs **46**/**47** and **50**/**51,** which show a significant bathochromic shift and hyperchromism when a 4-^{t}Bu-Ph moiety was incorporated in place of a 3,5-diMe R′ group. This indicated that 1,10-phenanthroline-based chromophores were more sensitive to alterations to their optical properties through the R′ group than the phenanthrene analogues.

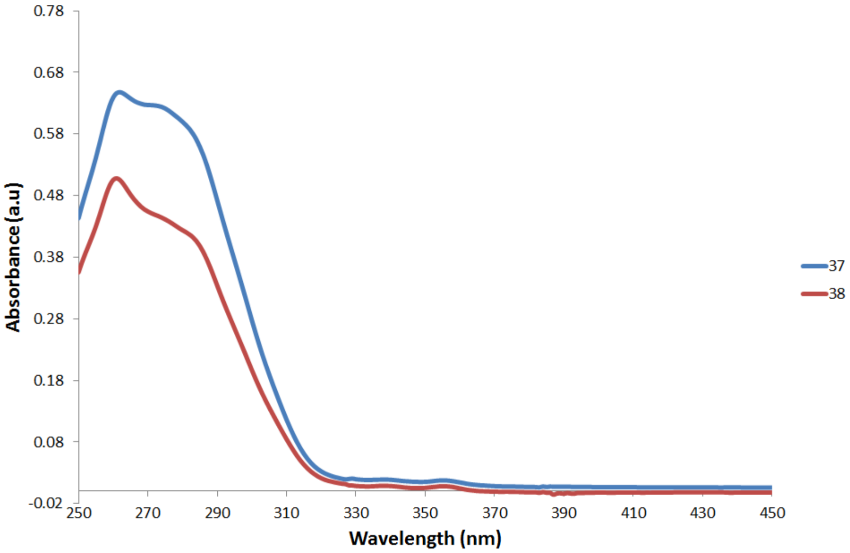

Figure 72: Absorption spectra of **37** (blue line) and **38** (red line) (both contain a phenanthrene core) in $CHCl_3$ at 298K

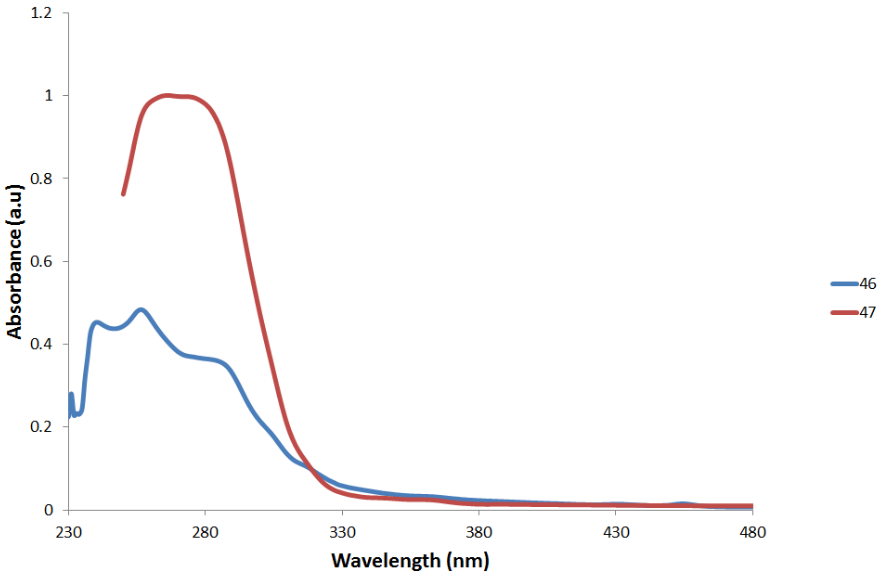

Figure 73: Absorption Spectra of **46** (blue line) and **47** (red line) (both contain a phenanthroline core) in $CHCl_3$ at 298K

3.8.5 Luminescent properties of the ligands

Table 16 shows λ_{ex}, λ_{em} and emission lifetime (τ) for compounds **35-52**.

Compound Number	Core	R	R′	Solvent	λ_{ex} (nm)	λ_{em} (nm)	τ (ns)
35	Phenanthrene	3,4-dihydroxy	3,5-diMe	DMSO	260	406	6.6
36	Phenanthrene	3,4-dihydroxy	4-^{t}Bu-Ph	$CHCl_3$	276	390	2.9
37	Phenanthrene	2,3-dimethoxy	3,5-diMe	$CHCl_3$	243	388	4.7
38	Phenanthrene	2,3-dimethoxy	4-^{t}Bu-Ph	$CHCl_3$	240	380	5.0
39	Phenanthrene	2,3-dihydroxy	3,5-diMe	DMSO	285	384	4.2
40	Phenanthrene	3,4,5-trihydroxy	3,5-diMe	DMSO	377	416	3.2
41	Phenanthrene	3,4,5-trimethoxy	3,5-diMe	$CHCl_3$	237	392	2.9
42	Phenanthrene	3,4,5-trimethoxy	4-^{t}Bu-Ph	$CHCl_3$	239	392	3.0
43	Phenanthrene	2,3,4-trimethoxy	3,5-diMe	$CHCl_3$	239	388	3.9
44	1,10-Phen	3,4-dihydroxy	3,5-diMe	$CHCl_3$	258	423	4.1
45	1,10-Phen	3,4-dihydroxy	4-^{t}Bu-Ph	$CHCl_3$	263	417	4.0
46	1,10-Phen	2,3-dimethoxy	3,5-diMe	$CHCl_3$	240	400	3.3
47	1,10-Phen	2,3-dimethoxy	4-^{t}Bu-Ph	$CHCl_3$	242	399	3.3
48	1,10-Phen	3,4,5-trimethoxy	3,5-diMe	$CHCl_3$	244	421	4.3
49	1,10-Phen	3,4,5-trimethoxy	4-^{t}Bu-Ph	$CHCl_3$	244	419	4.2
50	1,10-Phen	2,3,4-trimethoxy	3,5-diMe	$CHCl_3$	244	411	3.6
51	1,10-Phen	2,3,4-trimethoxy	4-^{t}Bu-Ph	$CHCl_3$	329	416	3.6
52	1,10-Phen	3-methoxy	3,5-diMe	$CHCl_3$	356	415	3.5

Table 16: Luminescent data for the ligands **35-52**

All ligands were found to be fluorescently emissive, with small to moderate Stokes' shifts, and relatively short lifetimes were observed in the region of 3-7 ns, attributed to the efficient process of the relaxation of an excited singlet state to a relaxed ground state configuration. The emission/excitation spectrum of ligand **38** is shown in Figure 74.

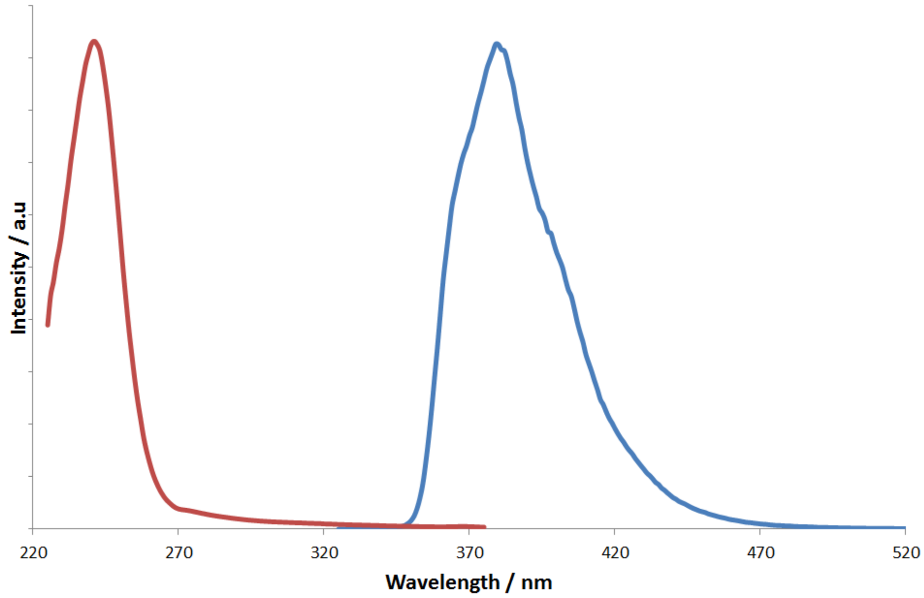

Figure 74: Normalised excitation (red) and emission (blue) spectrum of **38** ($CHCl_3$ at 298 K)

Differences between the emission wavelengths of phenanthroline and phenanthrene-based lophines were observed, with the phenanthrene-based lophines emitting at about 20 nm less than their phenanthroline analogues in some cases. A lower energy emission was observed for the phenanthroline compounds indicating a stabilised LUMO or the HOMO is destabilised for the phenanthrene-based lophines relative to the phenanthroline-based analogues. This is consistent with previously reported observations of the emission properties of phenanthroline and phenanthrene derivatives.[27] Unlike free phenanthrene, no significant vibrational structure was seen for either phenanthrene or phenanthroline based lophines **35-52**, showing a lack of structural rigidity in the compounds. The lower wavelength emission observed for the phenanthrene-containing chromophores compared to the 1,10-phenanthroline-based chromophores was similar to that reported in the literature.

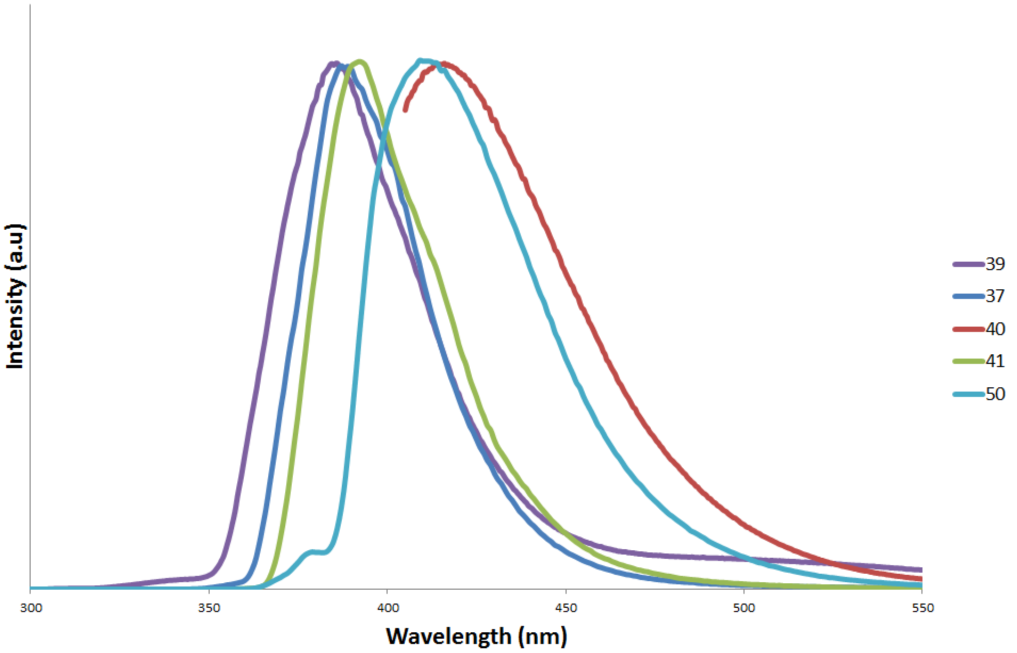

Figure 75: Normalised emission spectra for selected lophines

As discussed in chapter 2, contributions to the fluorescence spectra of these molecules appear to be more dependent on the influence of the apical R group, and not the R′ group. This is evident in this class of molecules. Although there were slight changes of emission with changes in the R′ group in some cases, overall a greater variation in emission wavelength was observed with changes to the R group.

The lack of solubility of the hydroxy-derived compounds in $CHCl_3$ made them difficult to compare to the methoxy-derived lophines. Compounds **35** and **40** show a lower energy emission, possibly due to the effects of the solvent. Compound **36** (Figure 76) is a di-hydroxy containing lophine, but has increased solubility in a range of solvents imparted by its aryl R′ group (again demonstrating the ability to tune the solubility of these types of molecules). It was therefore prudent to explore the effects of solvent polarity on these types of ligand using this molecule, the results of which are displayed in Table 17.

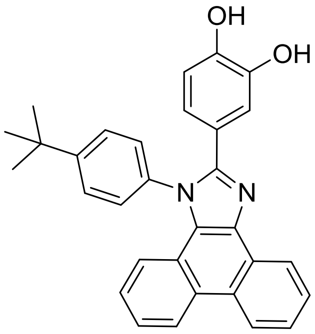

Figure 76: Molecular structure of **36**

Solvent	Emission / nm	Excitation /nm
CHCl3	390	276
MeOH	390	230
Acetone	393	222
EtOH	392	245
MeCN	395	230
DMSO	404	249

Table 17: Effect of solvent on emission wavelength of **36**

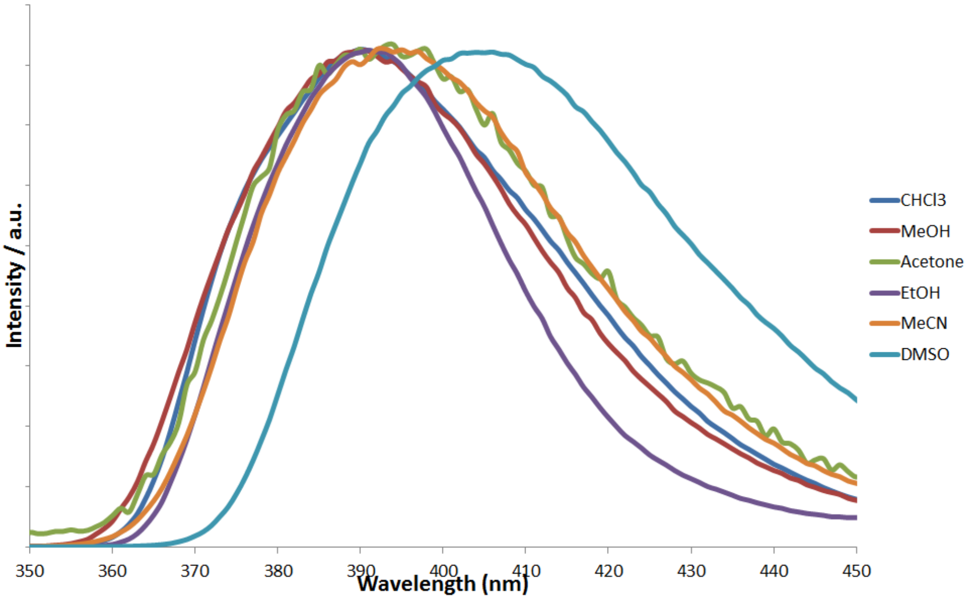

Figure 77: Normalised emission spectra of **36** in various solvents

Figure 77 shows that there is a subtle trend of increasing wavelength emission with an increase in solvent polarity. The observed solvatochromism indicated that in this compound there was an element of charge transfer to the electronic transition, the energy of which will be affected by the polarity of the solvent and its interactions with the catechol moiety. The observed results were similar to those reported in the literature, with a bathochromic shift of the catechol with increasing solvent polarity, with lower energy light emitted with increasing polarity due to hydrogen bond formation.[6] It should be noted that the low resolution appearance of the spectra obtained in acetone and MeCN was due to the weak signal obtained in these solvents, which give them a less defined appearance when normalised compared to the spectra obtained in other solvents.

3.9 Coordination chemistry of 44-52 with Re (I)

The coordination chemistry of the 1,10-phenanthroline-containing ligands (**44-52**) was explored with Re(I), wherein heating stoichiometric equivalents of ligand and ReBr(CO)$_5$ in toluene for 24 hr produced the desired complexes as powder of the general formulation *fac*-[ReBr(CO)$_3$(N^N)] (where N^N = **44-52**), in moderate to good yields. All complexes were characterised via ^{1}H and ^{13}C{H} NMR spectroscopy (where solubility allowed), electronic absorption and IR spectroscopy and high resolution mass spectrometry. Luminescence studies were also undertaken to explore the optical properties of these complexes. Shown in Scheme 6 is a general scheme for the formation of the complexes, together with a list of all isolated complexes.

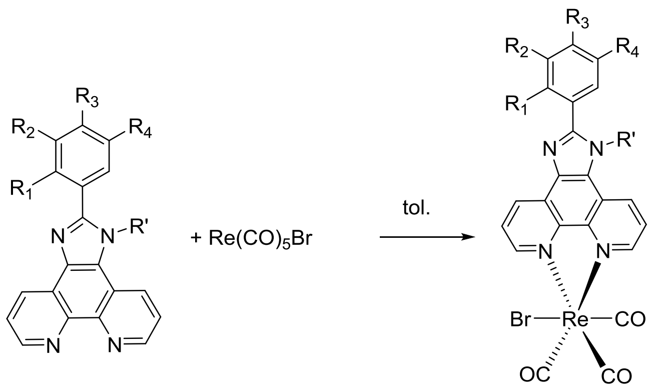

ReBr(CO)$_3$(44) R_1= R_4= H.R_2=R_3 = OH. R' = 3,5-diMe-Ph

ReBr(CO)$_3$(45) R_1= R_4= H.R_2=R_3 = OH. R' = 4-^{t}Bu-Ph

ReBr(CO)$_3$(46) R_1=R_2= OMe. R_3=R_4=H. R' = 3,5-diMe-Ph

ReBr(CO)$_3$(47) R_1=R_2= OMe. R_3=R_4=H. R' = 4-^{t}Bu-Ph

ReBr(CO)$_3$(48) R_1 = H. R_2=R_3=R_4=OMe. R' = 3,5-diMe-Ph

ReBr(CO)$_3$(49) R_1 = H. R_2=R_3=R_4=OMe. R' = 4-^{t}Bu-Ph

ReBr(CO)$_3$(50) R_1=R_2=R_3=OMe. R_4=H. R' = 3,5-diMe-Ph

ReBr(CO)$_3$(51) R_1=R_2=R_3=OMe. R_4=H. R' = 4-^{t}Bu-Ph

ReBr(CO)$_3$(52) R_2=OMe, R_1=R_3=R_4=H.R' = 3,5-diMe-Ph

Scheme 6: Formation of complexes of the type *fac*-[ReBr(CO)$_3$(N^N)]

3.9.1 Characterisation of the complexes

^{1}H NMR spectroscopic studies confirmed the successful formation of the Re(I) complexes in each instance due to significant downfield shifting of the ligand based proton resonances. The protons most influenced by the deshielding effect of the Re(I) centre were the phenanthroline protons. For example, free ligand **46** displays signals at 9.05-9.17 ppm which correspond to protons located on the phenanthroline. At 3.80 and 3.85 are signals which correspond to OCH$_3$ protons, and at 2.30 ppm is a singlet corresponding to the methyl groups on the R′ substituent. From 6.90 to 7.71 ppm are aromatic protons of the apical group and the R′ phenyl rings. Upon coordination to rhenium there is a clear shift in some of the signals due to deshielding of the electron withdrawing Re(I) group. The most pronounced of these shifts are observed for the phenanthroline protons (from 9.17-9.37 ppm), with smaller shifts observed for the other aromatic protons (for example from 7.50 to 7.66). No chemical shift is observed for the OMe groups or alkyl groups due to their distance away from the Re(I) centre.

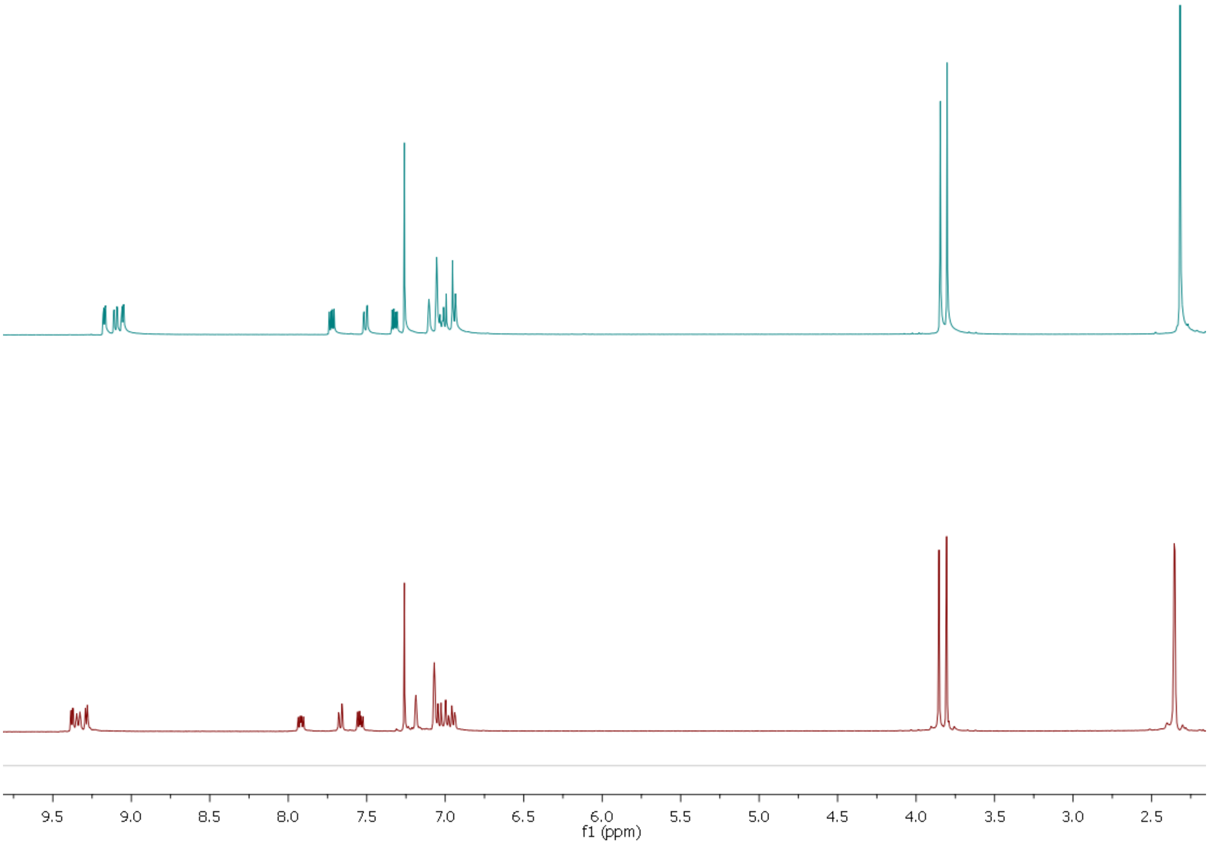

Figure 78: ^{1}H NMR spectra of **46** (blu**e)** and [ReBr(CO)$_3$**(46)]** (red) in CDCl$_3$ at 298 K

Slight changes in the chemical shifts of carbon resonances were also observed in the ^{13}C{^{1}H} NMR spectra. For example free lophine **46** contained numerous carbon signals in the aromatic region, with the furthest downfield shifted carbon at 153.0 ppm and the further upfield aromatic proton at 114.6 ppm. Upon coordination the furthest downfield shifted aromatic carbon remains at 153.0 ppm, however many other signals have undergone a downfield chemical shift including the most upfield signal from 114.6 to 115.3 ppm. Also observable in some of the samples run at a higher concentration were three weak signals associated with the quaternary, highly deshielded carbons of the carbonyl groups coordinated to the rhenium centre. Two of the three observed signals are very close in proximity in the spectrum (~197 ppm), whilst the third is less downfield shifted (~189 ppm). This suggests two carbonyl groups in similar chemical environments, with a third carbonyl group in a different environment. This is confirmed in the crystal structure (to be discussed in section 3.9.2).

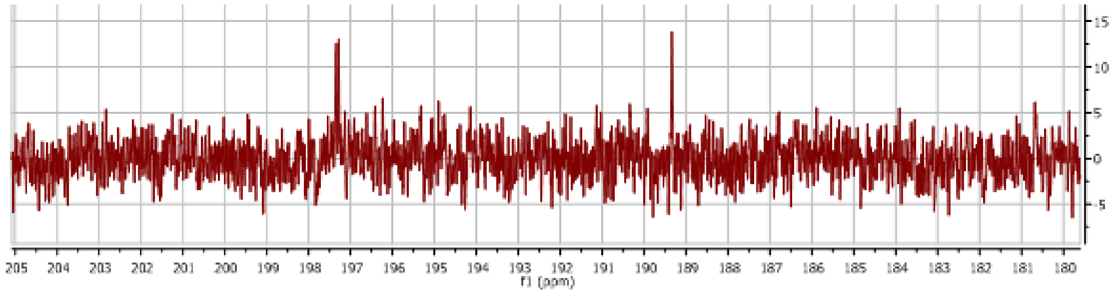

Figure 79: Observed carbonyl resonances in $^{13}C\{^1H\}$ NMR spectrum of $[ReBr(CO)_3($**46**$)]$ in $CDCl_3$ at 298K

All complexes were examined via solid state IR and commonly showed either three distinct bands or two, one of which was significantly broadened. The local symmetry of the *fac*-tricarbonyl core can be approximated to a C_s point group, and as a consequence three bands are expected (2A’ and A’’). The absorption frequencies did not change drastically with a change in the coordinating lophine. A broad peak due to O-H stretches is observed at ≈ 3500 cm^{-1} for catechol-containing lophines (Figure 80).

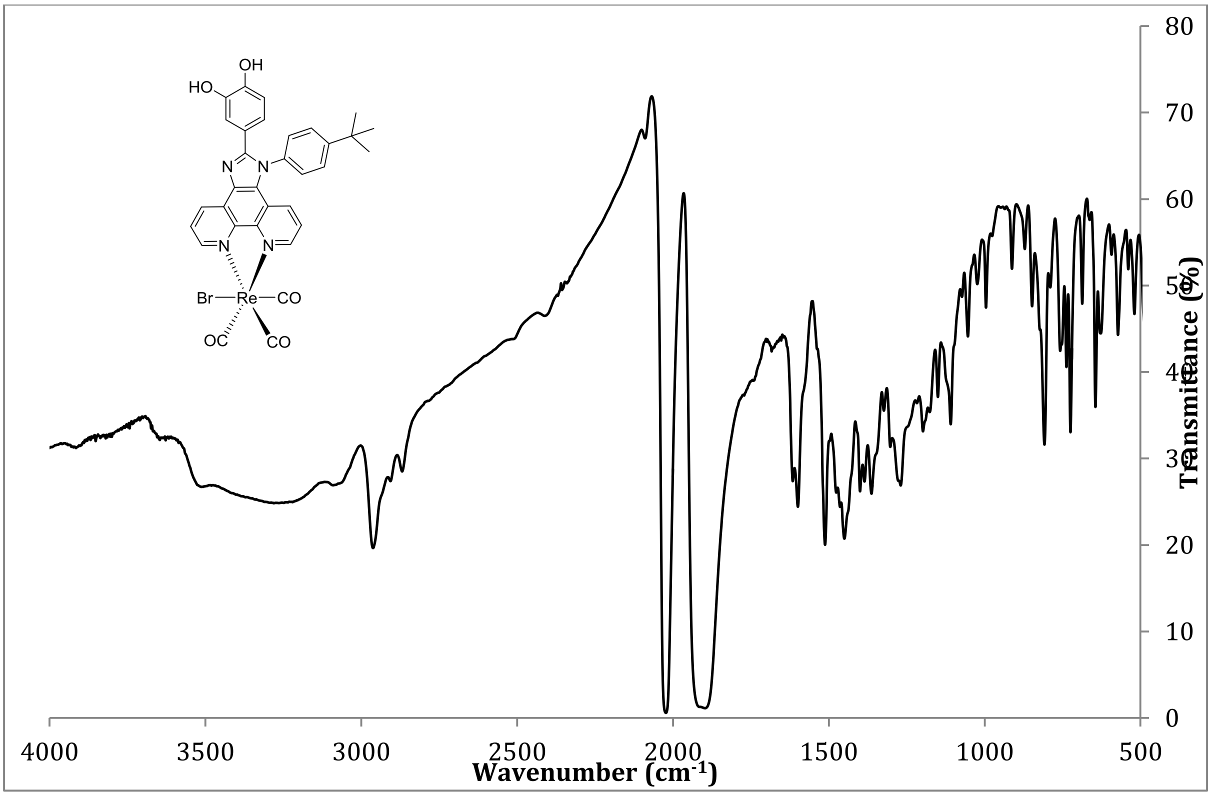

Figure 80: IR spectrum of $[ReBr(CO)_3($**45**$)]$

HR electrospray mass spectrometry (positive mode) showed that the neutral complexes fragmented in a predictable manner, showing both the protonated fragment and substituting the axially coordinated bromide anion with carrier solvent derived MeCN, resulting in an overall cationic species [Re(CO)$_3$(MeCN)(N^N)]$^+$, with an isotopic distribution consistent for rhenium. Figure 81 shows the observed data of [ReBr(CO)$_3$(**49**)] along with the theoretical isotope model.

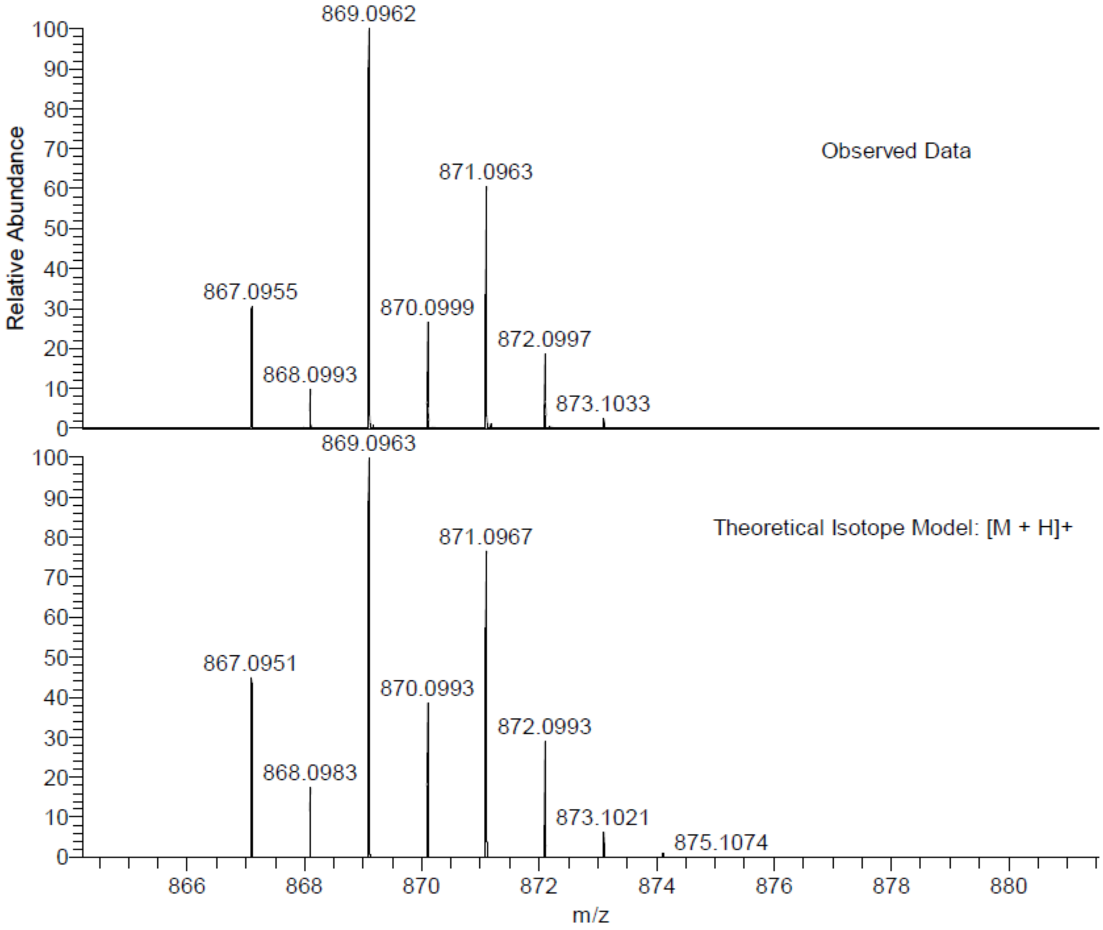

Figure 81: Mass spectrometry data for [ReBr(CO)$_3$(**49**)]

3.9.2 Structural Studies

Single crystal X-ray diffraction studies were undertaken on three complexes, ***fac*-[ReBr(CO)$_3$(47)]**, ***fac*-[ReBr(CO)$_3$(49)]** and ***fac*-[ReBr(CO)$_3$(52)]**. Suitable crystals were obtained by the slow diffusion of hexane into a toluene solution of the complex solution over a period of 72 h. ***fac*-[ReBr(CO)$_3$(47)]** crystallised in P-1 symmetry, ***fac*-[ReBr(CO)$_3$(49)]** crystallised in P21/c symmetry. The parameters associated with the data collection for ***fac*-[ReBr(CO)$_3$(49)]** are shown in Table 18, and Figure 82 illustrates the structure of ***fac*-[ReBr(CO)$_3$(49)]** in the solid-state with selected bond length and angle data. The structure of ***fac*-[ReBr(CO)$_3$(49)]** displays octahedral coordination geometry as expected for a d^6 Re(I) complex, with **49** chelating *trans* to two carbonyl ligands, with the third CO ligand and bromide donors occupying axial positions. Bond lengths and angles are typical for a {ReBr$(CO)_3$} complex of a chelating diimine.[29,30] The imidazo[4,5-*f*]-1,10-phenanthroline core of the ligand framework is essentially co-planar with the 'Re$(CO)_2$' fragment of the complex, whilst the trimethoxy-phenyl group deviates from co-planarity with the heterocyclic core of the ligand with a torsion angle of 25.0°; the *p*-^{t}butylphenyl group is almost orthogonal to the ligand core with a torsion angle of 81.8°. The ^{t}butyl group is disordered due to rotation. An increased torsion angle (away from planarity) is observed (65.8°) for the apical substituent "R" of ***fac*-[ReBr(CO)$_3$(47)]** compared to ***fac*-[ReBr(CO)$_3$(49)].** This is most likely due to the ortho-positioning of the methoxy substituent on the apical phenyl in ***fac*-[ReBr(CO)$_3$(47)]**, which bears only a H atom for ***fac*-[ReBr(CO)$_3$(49)].** The added steric clashing that would be involved with the sidearm R′ group results in significant rotation of the apical group. An increased torsion angle away from planarity such as this reduces the effective conjugation of the molecule. Contrastingly, ***fac*-[ReBr(CO)$_3$(52)]** contains the least steric bulk of each of the complexes, with only one methoxy group located in the meta position relative to the imidazole core. This has a torsion angle of only 9.0°, meaning it is almost co-planar with the rest of the chromophore. There appears to therefore to be a trend of increasing planarity with the positions of the substituents, with ***fac*-[ReBr(CO)$_3$(47)]** having the largest angle deviation away from planarity due to steric bulk in the ortho position of the apical phenyl group, and ***fac*-[ReBr(CO)$_3$(52)]** the closest to planarity due to the positioning of its sole methoxy substituent in the meta position. It is important not to over-analyse these results as they only provide information of the structure in the solid-state crystal, and not in solution. In particular inter-ligand interactions may affect the conformation of these complexes in the solid state, but not in a dilute solution. However, the structures do provide valuable information about intra-ligand interactions, in particular between R group substituents and the imidazole ring.

Table 18**.** Crystal data and structure refinement details

Empirical formula	$C_{35}H_{30}BrN_4O_6Re$	
Formula weight	868.74	
Temperature	100(2) K	
Wavelength	0.71075 Å	
Crystal system	Monoclinic	
Space group	$P21/c$	
Unit cell dimensions	a = 11.686(5) Å	α = 90°
	b = 12.634(5) Å	β = 93.380(7)°
	c = 24.0993(10) Å	γ = 90°
Volume	3552(2) $Å^3$	
Z	4	
Density (calculated)	1.625 Mg / m^3	
Absorption coefficient	4.594 mm^{-1}	
F(000)	1704	
Crystal	Block; yellow	
Crystal size	$0.05 \times 0.02 \times 0.02$ mm^3	
θ range for data collection	2.98 – 25.03°	
Index ranges	$-13 \le h \le 13$, $-15 \le k \le 15$, $-27 \le l \le 28$	
Reflections collected	50295	
Independent reflections	6268 [R_{int} = 0.1013]	
Completeness to θ = 25.03°	99.8 %	
Absorption correction	Semi–empirical from equivalents	
Max. and min. transmission	0.9137 and 0.8028	
Refinement method	Full-matrix least-squares on F^2	
Data / restraints / parameters	6268 / 30 / 461	
Goodness-of-fit on F^2	1.171	
Final R indices [$F^2 > 2\sigma(F^2)$]	$R1$ = 0.0669, $wR2$ = 0.1591	
R indices (all data)	$R1$ = 0.0790, $wR2$ = 0.1665	
Largest diff. peak and hole	1.399 and –0.774 e $Å^{-3}$	

Diffractometer: *Rigaku AFC12* goniometer equipped with an enhanced sensitivity (HG) *Saturn724+* detector mounted at the window of an *FR-E+ SuperBright* molybdenum rotating anode generator with VHF *Varimax* optics (70µm focus). **Cell determination and data collection**: *CrystalClear-SM Expert 2.0 r11* (Rigaku, 2011). **Data reduction, cell refinement and absorption correction**: *CrystalClear-SM Expert 2.0 r13* (Rigaku, 2011). **Structure solution**: *SHELXS97* (Sheldrick, G.M. (2008). Acta Cryst. A64, 112-122**Structure refinement**: *SHELXL97* (Sheldrick, G.M. (2008). Acta Cryst. A64, 112-122). **Graphics:** *OLEX2* (Dolomanov, O. V., Bourhis, L. J., Gildea, R. J., Howard, J. A. K. & Puschmann, H. (2009). J. Appl. Cryst. 42, 339-341).

Special details:
Examined crystal was a very small fragment from cluster of microcrystalline material.
In the crystal structure tert-butyl group is disordered due to rotation. The disordered group has been modelled over two positions.
Structure contains relatively small accessible voids containing very diffused electron density (solvent). PLATON/SQUEEZE routine was used.

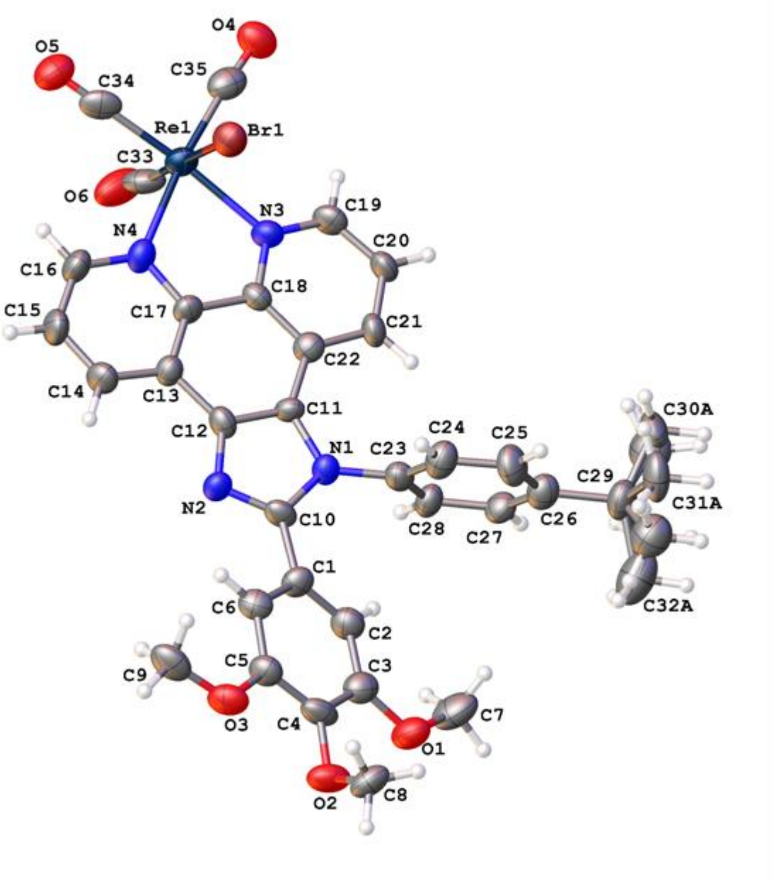

Figure 82: Ortep3 plot of complex ***fac*-[ReBr(CO)$_3$(49)]**. Ellipsoids are drawn at 50% probability. Selected data - bond lengths (Å): C33–Re1, 1.942(13); C34–Re1, 1.958(12); C35–Re1, 1.935(12); N3–Re1, 2.184(7); N4–Re1, 2.174(8); Br1–Re1, 2.6431(12). Bond angles(°): O6–C33–Re1, 173.8(9); O5–C34–Re1, 179.3(10); O4–C35–Re1, 175.6(9); C19–N3–Re1, 125.3(6); C18–N3–Re1, 115.9(6); C16–N4–Re1, 126.6(6); C17–N4–Re1, 116.1(6); C35–Re1–C33, 86.9(4); C35–Re1–C34, 89.7(4); C33–Re1–C34, 88.4(4); C35–Re1–N4, 173.5(4); C33–Re1–N4, 93.9(4); C34–Re1–N4, 96.7(3); C35–Re1–N3, 98.0(4); C33–Re1–N3, 97.0(4); C34–Re1–N3, 170.8(3); N4–Re1–N3, 75.5(3); C35–Re1–Br1, 95.3(3); C33–Re1–Br1, 177.8(3); C34–Re1–Br1, 91.6(3); N4–Re1–Br1, 83.9(2); N3–Re1–Br1, 82.8(2).

The parameters associated with the data collection for ***fac*-[ReBr(CO)$_3$(47)]** are shown in Table 19, and Figure 83 illustrates the structure of ***fac*-[ReBr(CO)$_3$(47)]** in the solid-state with selected bond length and angle data.

Table 19: Crystal data and structure refinement details.

Empirical formula	$C_{34}H_{28}BrN_4O_5Re$	
Formula weight	838.71	
Temperature	100(2) K	
Wavelength	0.71075 Å	
Crystal system	Triclinic	
Space group	$P{-}1$	
Unit cell dimensions	a = 11.1587(8) Å	α = 111.784(8)°
	b = 13.0479(10) Å	β = 110.740(8)°
	c = 13.1431(10) Å	γ = 97.685(7)°
Volume	1582.4(2) $Å^3$	
Z	2	
Density (calculated)	1.760 Mg / m^3	
Absorption coefficient	5.150 mm^{-1}	
F(000)	820	
Crystal	Column; yellow	
Crystal size	$0.27 \times 0.06 \times 0.06$ mm^3	
θ range for data collection	2.58 – 27.55°	
Index ranges	$-14 \le h \le 13$, $-16 \le k \le 16$, $-13 \le l \le 17$	
Reflections collected	19955	
Independent reflections	7218 [R_{int} = 0.0468]	
Completeness to θ = 27.55°	98.9 %	
Absorption correction	Semi−empirical from equivalents	
Max. and min. transmission	0.7475 and 0.3369	
Refinement method	Full-matrix least-squares on F^2	
Data / restraints / parameters	7218 / 0 / 411	
Goodness-of-fit on F^2	0.998	
Final R indices [$F^2 > 2\sigma(F^2)$]	$R1$ = 0.0333, $wR2$ = 0.0800	
R indices (all data)	$R1$ = 0.0412, $wR2$ = 0.0832	
Largest diff. peak and hole	2.086 and −2.054 e $Å^{-3}$	

Diffractometer: *Rigaku AFC12* goniometer equipped with an enhanced sensitivity (HG) *Saturn724+* detector mounted at the window of an *FR-E+ SuperBright* molybdenum rotating anode generator with HF *Varimax* optics (100µm focus). **Cell determination and data collection**: *CrystalClear-SM Expert 2.0 r11* (Rigaku, 2011). **Data reduction, cell refinement and absorption correction**: *CrystalClear-SM Expert 2.0 r13* (Rigaku, 2011). **Structure solution**: *SHELXS97* (Sheldrick, G.M. (2008). Acta Cryst. A64, 112-122). **Structure refinement**: *SHELXL97* (Sheldrick, G.M. (2008). Acta Cryst. A64, 112-122). **Graphics:** *OLEX2* (Dolomanov, O. V., Bourhis, L. J., Gildea, R. J., Howard, J. A. K. & Puschmann, H. (2009). J. Appl. Cryst. 42, 339-341).

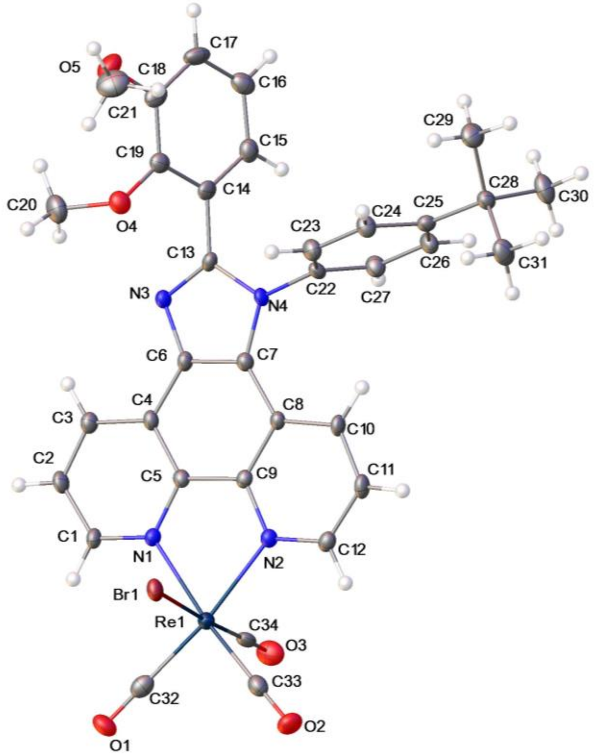

Figure 83: Ortep3 plot of complex ***fac*-[ReBr(CO)$_3$(47)]**. Ellipsoids are drawn at 50% probability. Selected data - bond lengths (Å): C32–Re1, 1.931(4); C34–Re1, 1.926(4); C33–Re1, 1.908(4); Br1–Re1, 2.6332(5); N1–Re1, 2.171(3); N2–Re1, 2.177(3). Bond angles(°): O1–C32–Re1, 178.7(3); O3–C34–Re1, 177.2(4); O2–C33–Re1, 177.7(4); C1–N1–Re1, 125.7(3); C5–N1–Re1, 115.8(2); C12–N2–Re1, 125.2(3); C9–N2–Re1, 116.0(2); C33–Re1–C34, 90.55(17); C33–Re1–C32, 89.01(17); C34–Re1–C32, 88.91(17); C33–Re1–N1, 171.05(13); C34–Re1–N1, 95.09(14); C32–Re1–N1, 98.01(15); C33–Re1–N2, 97.57(15); C34–Re1–N2, 93.49(14); C32–Re1–N2, 172.96(15); N1–Re1–N2, 75.20(12); C33–Re1–Br1, 90.24(12); C34–Re1–Br1, 177.25(11); C32–Re1–Br1, 93.74(12); N1–Re1–Br1, 83.81(8); N2–Re1–Br1, 83.79(8).

The parameters associated with the data collection for ***fac*-[ReBr(CO)$_3$(52)]** are shown in Table 20, and Figure 84 illustrates the structure of ***fac*-[ReBr(CO)$_3$(52)]** in the solid-state with selected bond length and angle data.

Table 20: Crystal data and structure refinement details.

Empirical formula	$C_{31}H_{22}BrN_4O_4Re$	
Formula weight	780.64	
Temperature	100(2) K	
Wavelength	0.71075 Å	
Crystal system	Triclinic	
Space group	P–1	
Unit cell dimensions	a = 11.4724(8) Å	α = 66.902(4)°
	b = 11.5525(8) Å	β = 67.901(4)°
	c = 13.8552(10) Å	γ = 89.984(5)°
Volume	1541.45(19) $Å^3$	
Z	2	
Density (calculated)	1.682 Mg / m^3	
Absorption coefficient	5.278 mm^{-1}	
F(000)	756	
Crystal	Block; Yellow	
Crystal size	0.07 × 0.04 × 0.04 mm^3	
θ range for data collection	2.98 – 25.02°	
Index ranges	$-13 \le h \le 13$, $-12 \le k \le 13$, $-16 \le l \le 16$	
Reflections collected	16846	
Independent reflections	5427 [R_{int} = 0.0310]	
Completeness to θ = 25.02°	99.4 %	
Absorption correction	Semi–empirical from equivalents	
Max. and min. transmission	0.8166 and 0.7089	
Refinement method	Full-matrix least-squares on F^2	
Data / restraints / parameters	5427 / 768 / 480	
Goodness-of-fit on F^2	0.796	
Final R indices [$F^2 > 2\sigma(F^2)$]	$R1$ = 0.0599, $wR2$ = 0.1455	
R indices (all data)	$R1$ = 0.0785, $wR2$ = 0.1609	
Largest diff. peak and hole	3.316 and –3.122 e $Å^{-3}$	

Diffractometer: *Rigaku AFC12* goniometer equipped with an enhanced sensitivity (HG) *Saturn724+* detector mounted at the window of an *FR-E+ SuperBright* molybdenum rotating anode generator with VHF *Varimax* optics (70µm focus). **Cell determination and data collection**: *CrystalClear-SM Expert 2.0 r11* (Rigaku, 2011). **Data reduction, cell refinement and absorption correction**: *CrystalClear-SM Expert 2.0 r13* (Rigaku, 2011). **Structure solution**: *SHELXS97* (Sheldrick, G.M. (2008). Acta Cryst. A64, 112-122). **Structure refinement**: *SHELXL97* (Sheldrick, G.M. (2008). Acta Cryst. A64, 112-122).

Special details:
Sample contains dry crystalline material grown on the bottom of the vial which had to be scratched out . Tiny crystalline fragments were poor quality., however good enough to collect X-ray data.
Crystal structure exhibits significant amout of molecular disorder. In the structure two phenyl rings were modelled over two positions. AFIX 66, SIMU/DELU and EADP restraints have been used to maintain sensible geometry and to modell appropriately displacement parameters.
Structure contains small accessible voids with very diffused electron density (solvent), which was impossible to assign and PLATON/SQUEEZE routine was used to remove it. This improves overall model and led structure refinement to convergence.

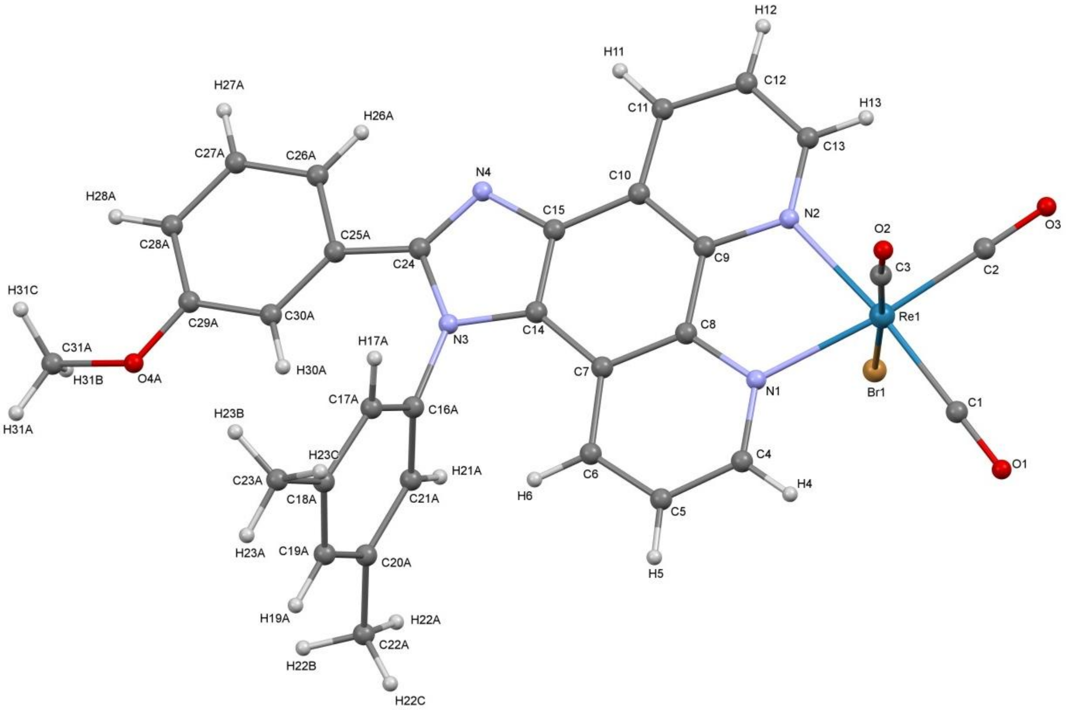

Figure 84: Ortep3 plot of complex ***fac*-[ReBr(CO)$_3$(52)]**. Ellipsoids are drawn at 50% probability. Selected data - bond lengths (Å): Re1–C2, 1.903(14); Re1–C1, 1.921(12); Re1–C3, 1.932(17); Re1–N2, 2.161(7); Re1–N1, 2.179(10); Re1–Br1, 2.6229(14). Bond angles(°): C2–Re1–C1, 87.3(6); C2–Re1–C3, 88.6(6); C1–Re1–C3, 92.7(7); C2–Re1–N2, 97.5(4); C1–Re1–N2, 172.4(7); C3–Re1–N2, 93.2(4); C2–Re1–N1, 172.7(4); C1–Re1–N1, 99.6(6); C3–Re1–N1, 93.7(5); N2–Re1–N1, 75.4(3); C2–Re1–Br1, 93.9(4); C1–Re1–Br1, 89.1(6); C3–Re1–Br1, 177.0(4); N2–Re1–Br1, 84.8(2); N1–Re1–Br1, 83.6(2); C13–N2–Re1, 125.9(6); C9–N2–Re1, 115.7(5); C4–N1–Re1, 126.3(8); C8–N1–Re1, 115.9(6).

3.9.3 Electronic Absorption Spectroscopy of the complexes

Electronic absorption spectra have been obtained for complexes [ReBr(CO)$_3$(**44-52**)] at 297K in CHCl$_3$. Results are tabulated below along with luminescence data (Table 21).

Complex	R	R′	Solvent	λ_{max} (nm)	λ_{ex} (nm)	λ_{em} (nm)	τ (ns)
[ReBrCO$_3$(44)]	3,4-dihydroxy	3,5-diMe	CHCl$_3$	275 (45,800), 308(sh) (30,000), 359(sh) (10,000), 418 (5700)	364	580	166
[ReBrCO$_3$(45)]	3,4-dihydroxy	4-^{t}Bu-Ph	CHCl$_3$	276 (38,600), 357(sh) (8500), 418 (6200)	363	587	156
[ReBrCO$_3$(46)]	2,3-dimethoxy	3,5-diMe	CHCl$_3$	261 (77,700), 287 (sh) (46,800), 414 (6500)	265	578	168
[ReBrCO$_3$(47)]	2,3-dimethoxy	4-^{t}Bu-Ph	CHCl$_3$	262 (115,800), 418 (1800)	268	580	163
[ReBrCO$_3$(48)]	3,4,5-trimethoxy	3,5-diMe	CHCl$_3$	278 (30,200), 347(sh) (8600), 425 (3700)	265	579	163
[ReBrCO$_3$(49)]	3,4,5-trimethoxy	4-^{t}Bu-Ph	CHCl$_3$	278 (46,700), 341 (sh) (14,700), 426 (6000)	264	580	158
[ReBrCO$_3$(50)]	2,3,4-trimethoxy	3,5-diMe	CHCl$_3$	239 (55,800), 261 (85,700), 295 (sh) (38,400), 417 (6300)	375	580	149
[ReBrCO$_3$(51)]	2,3,4-trimethoxy	4-^{t}Bu-Ph	CHCl$_3$	274, 408 (3800)	345	584	149
[ReBrCO$_3$(52)]	3-methoxy	3,5-diMe	CHCl$_3$	274 (49 300), 292 (sh) (33 600), 421 (4800)	333	582	170

Table 21: Electronic spectroscopy data for Re complexes

Two main absorption characteristics are observed for each of complexes. The first are high energy $\pi\rightarrow\pi^*$ transitions expected for an extended π framework (λ_{max} at $\approx$ 260–310 nm), the second characteristic is that of a ^{1}MLCT absorption (Re(d)$\rightarrow\pi^*$) with the longest wavelengths observed at >400 nm as broad shoulders. This data is similar to that obtained for rhenium complexes isolated in the previous chapter. Although band assignments are similar for related complexes, for instance [Re(CO)$_3$Cl(phen)], there are contrasting values for both the band positions and their molar absorption. [Re(CO)$_3$Cl(phen)] possessed bands at 270 nm with a molar absorption of 30,600 M^{-1}cm^{-1} ($\pi\rightarrow\pi^*$), which is similar to many of the isolated complexes discussed, however the ^{1}MLCT absorption (Re(d)$\rightarrow\pi^*$) for [Re(CO)$_3$Cl(phen)] is at 383 nm which is a significantly higher energy absorption compared to the value of the lophine derived complexes ($\approx$ 415 nm).[31] The molar absorption coefficient of [Re(CO$_3$)Cl(phen)] is close to values observed for the isolated complexes

(≈ 4000 $M^{-1}cm^{-1}$). In general, there are no significant changes in absorption wavelength or of the molar absorption coefficient values associated with the $\pi\rightarrow\pi^*$ transition upon coordination of Re(I). All ^{1}MLCT absorption values for the isolated complexes are close in value for both absorption wavelength and absorption strength.

3.9.4 Luminescence studies

Re complexes of the ligands all showed emission at ≈ 580 nm attributed to the ^{3}MLCT transition. The formation of the triplet state leads to a larger Stokes' shift in comparison to the corresponding free ligands. Emission lifetimes for these complexes are also increased dramatically due to the deactivation of the excited triplet state being a spin-forbidden process. Typical lifetimes were obtained ca. 150-170 ns, which are typical of neutral Re-phen based lumophores.[30,32] Excitation wavelengths appear to be affected by changes in the apical R group as opposed to the R′ group (see Table 21). This can lead to a large Stokes' shift (Figure 85) or a small Stokes' shift (Figure 86). There does not appear to be a definite relationship between the excitation wavelength and the nature of the R substituent, both hydroxy and some methoxy derived complexes display smaller Stokes' shifts, and the positioning of the substituents on the phenyl R group can display either shorter or longer excitation wavelengths.

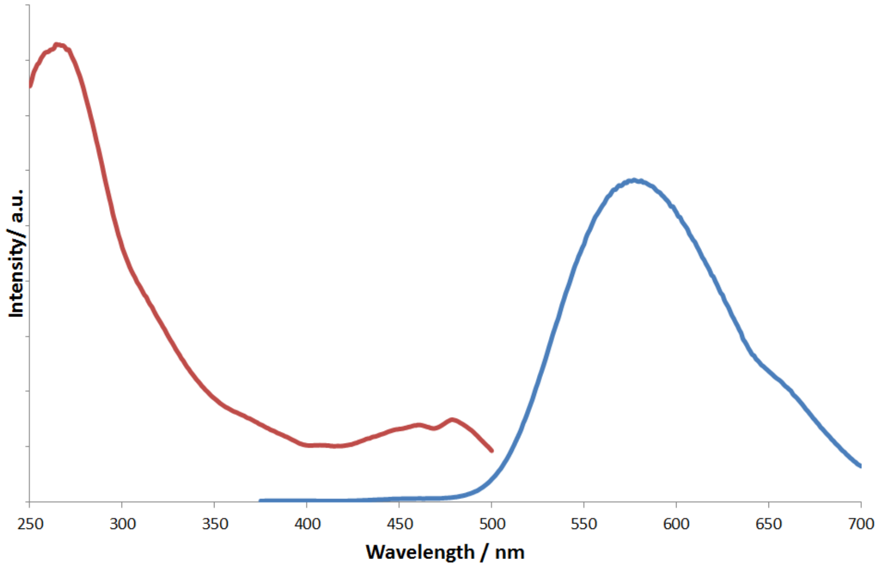

Figure 85: Emission (blue) and excitation (red) spectra of complex [ReBr$(CO)_3$**(46)**] in $CHCl_3$ at 298K

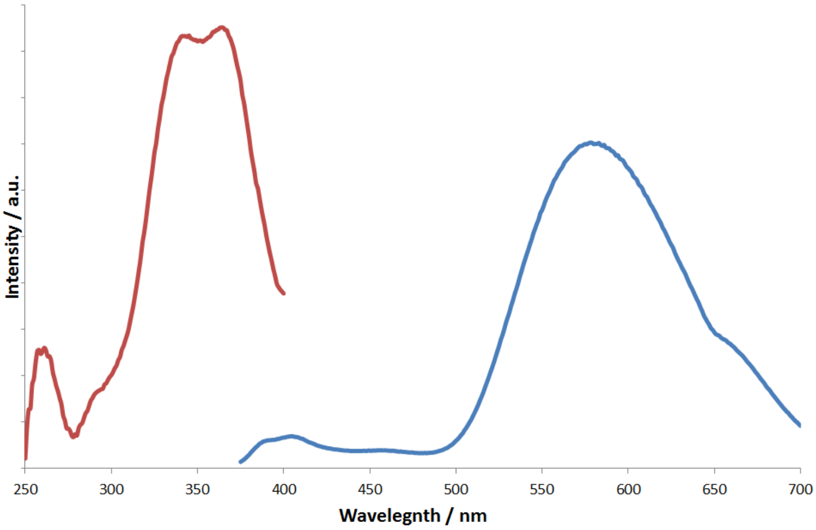

Figure 86: Emission (blue) and excitation (red) spectra of complex [ReBr(CO)$_3$(**44**)] in CHCl$_3$ at 298K

From the data, R′ does not appear to have much influence on the lifetime of the emission, as evidenced that there is not a significant increase in the lifetime values between the analogous pairs of [ReBr(CO)$_3$(**44/45**)], [ReBr(CO)$_3$(**46/47**)], [ReBr(CO)$_3$(**48/49**)] or [ReBr(CO)$_3$(**50/51**)]. The largest variation was observed for the [ReBr(CO)$_3$(**44/45**)] pair which has a difference of 10 ns, which is not significant when experimental errors are accounted for. All other complex pairs had a lifetime difference of 5 ns or less which does not suggest any influence of the R′ group on the emission lifetimes. The R group may have an effect on the emission lifetimes as evidenced by the slightly differing values for each complex pair. The lowest value is for the [ReBr(CO)$_3$(**50/51**)] pair (149 ns), while the highest values are for the [ReBr(CO)$_3$(**44/45**)] pair (166/156 ns). There is not a large difference between these two sets of lifetimes, however it may indicate that the lifetimes may be more sensitive to changes of the R group than the R′ group.

3.10 Conclusions

A series of hydroxy and methoxy substituted imidazo[4,5-*f*]-1,10-phenanthroline and phenanthrene (lophine) ligands have been isolated and fully characterised. The optical properties of these molecules have been investigated and compared by electronic absorption spectroscopy, fluorescence emission spectroscopy, and emission lifetime measurements. Differences in the optical propeties due to changes in the phenanthrene/ 1,10 phenanthroline core, the nature of the R group, the nature of the solvent used and- to a lesser degree- in changes to the R′ group were observed. The isolation of the catechol derived lophines provides an additional binding site for metals.

A series of Re(I) complexes, incorporating the 1,10-phenanthroline derived lophines were isolated and fully characterised. X-ray crystal structures were obtained for two examples, which showed varying degrees of torsion away from planarity of apical R group from the imidazole-phenanthroline moiety of the molecule. The degree of the torsion angle appears to result directly from the position of the substituents on the R group. Electronic absorption spectra, fluorescence emission spectra and emission lifetimes were obtained for each complex and in each case showed an absorption band at ≈ 415 nm, emission at 580 nm, and extended lifetimes (149 – 165 ns), all of which arise from ^{3}MLCT.

3.11 Experimental

Synthesis of 35

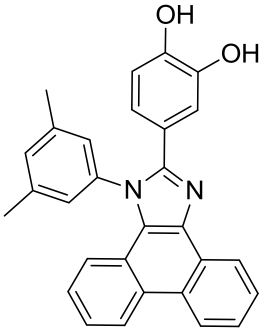

Into a round bottom flask was added NH_4OAc (1.11 g, 14.4 mmol), 3,4-dihydroxy benzaldehyde (0.199g, 1.44 mmol), 9,10-phenanthrenedione (0.300g, 1.44 mmol), 3,5-dimethylaniline (0.18 ml, 1.44 mmol) and acetic acid (30ml) and then the reaction mixture was left at reflux for 3 hours. Upon cooling, the product was precipitated from water (50 ml). The light brown precipitate was extracted with chloroform (2 × 150 ml). The combined organics were washed with water (3 × 50ml) and brine (1 × 50 ml), and then dried and the volatiles removed *in vacuo*. The resulting brown oil was recrystalised using chloroform and hexane to give product (**35**) as a brown powder (0.200g, 0.47 mmol). ^{1}H NMR (250 MHz, DMSO) δ 8.86 (2H, dd, *J* = 11.2, 8.6 Hz, phen-*H*), 8.62 (1H, d, phen-*H*), 7.83 – 7.58 (2H, m, Ar-*H*), 7.51 (1H, t, *J* = 7.4 Hz, Ar-*H*), 7.39 – 7.19 (5H, m, Ar-*H*), 7.07 (1H, d, *J* = 7.9 Hz, Ar-*H*), 6.79 (1H, dd, *J* = 8.2, 1.9 Hz, Ar-*H*), 6.64 (1H, d, *J* = 8.3 Hz, Ar-*H*), 2.37 (6H, s, (Ar-CH_3)) ppm. ^{13}C{^{1}H} NMR (101 MHz, DMSO) δ 150.9, 146.6, 145.0, 139.7, 138.4, 136.2, 131.5, 128.2, 127.6, 127.5, 127.4, 126.8, 126.6, 126.5, 125.5, 124.9, 124.4, 123.7, 122.6, 122.0, 121.4, 120.5, 120.2, 119.3, 116.9, 115.2, 20.8 ppm. HRMS (ES)(%): found *m/z* = 430.1671[M]$^+$;{$C_{29}H_{22}N_2O_2^+$} requires 430.1676. IR (KBr plates): 3490 (w), 2916 (w), 1609 (s), 1570 (w), 1521 (m), 1492 (m), 1453 (s), 1389 (w), 1357 (s), 1268 (s), 1231 (s), 1195 (w), 1116 (w), 1024 (w), 967 (w), 918 (w), 868 (m), 820 (w) 756 (s), 751 (s) cm^{-1}. UV-vis λ_{max} (ε / M^{-1} cm $^{-1}$) (MeOH): 299 (27 100), 357 (8300) nm.

Synthesis of 36

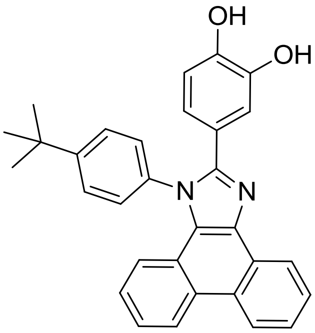

This material was prepared by a similar method to **35** using 3,4-dihydroxy benzaldehyde (0.199 g, 1.44 mmol), 9,10-phenanthrenedione (0.300 g, 1.44 mmol), 4-tertbutylaniline (0.23 ml, 1.44 mmol), and ammonium acetate (1.11 g, 14.4 mmol). The crude product was recrystalised from chloroform and hexane to give product (**36**) as a brown powder (0.275 g, 0.47 mmol). ^{1}H NMR (400 MHz, DMSO) δ 8.87 (2H, dd, *J* = 18.2, 8.4 Hz, phen-*H*), 8.64 (1H, d, *J* = 7.9 Hz, phen-*H*), 8.32 (1H, s, Ar-*H*), 7.75 (1H, t, *J* = 7.5 Hz, Ar-*H*), 7.67 (2H, m, Ar-*H*), 7.52 (3H, m, Ar-*H*), 7.32 – 7.23 (1H, m, Ar-*H*), 7.15 (1H, d, *J* = 2.0 Hz, Ar-*H*), 7.00 (1H, m, Ar-*H*), 6.71 (1H, dd, *J* = 8.3, 2.1 Hz, Ar-*H*), 6.61 (1H, d, *J* = 8.3 Hz, Ar-*H*), 1.41 (9H, s, Ar-CH(C*H*$_3$)$_3$) ppm. ^{13}C{^{1}H} NMR (101 MHz, DMSO) δ 152.7, 151.2, 146.4, 145.0, 136.3, 135.9, 128.6, 128.2, 127.5, 127.4, 127.0, 126.8, 126.6, 125.5, 124.9, 124.5, 123.6, 122.6, 121.9, 121.40, 120.5, 120.1, 116.9, 115.1, 34.8, 31.2 ppm. HRMS (ES)(%): found *m/z* = 457.1910 [M - H]$^-$. {$C_{31}H_{25}N_2O_2^-$} requires 457.1922. IR (KBr plates): 2964 (m), 1699 (m), 1617 (m), 1521 (m), 1452 (s), 1393 (w), 1356 (m), 1286 (m), 1229 (w), 1110 (w), 996 (w), 843 (w), 818 (w), 755 (s), 733 (s) cm^{-1}. UV-vis λ_{max} (ε / M^{-1} cm $^{-1}$) (CHCl$_3$): 263 (115 800), 325(sh) (25 500), 360 (8500), 456 (1700) nm.

Synthesis of 37

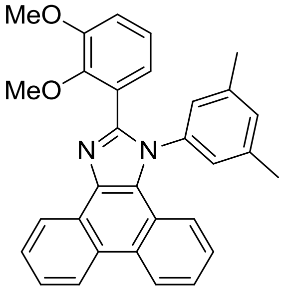

This material was prepared by a similar method to **35** using 2,3-dimethoxy benzaldehyde (0.239 g, 1.44 mmol), 9,10-phenanthrenedione (0.300 g, 1.44 mmol), 3,5-dimethylaniline (0.18 ml, 1.44 mmol) and ammonium acetate (1.11 g, 14.4 mmol). The crude product was recrystalised from chloroform and hexane to give product (**37**) as a light brown powder (0.400 g, 0.87 mmol). ^{1}H NMR (400 MHz, CDCl$_3$) δ 8.86 (1H, d, *J* = 7.6 Hz, phen-*H*), 8.77 (1H, d, *J* = 8.3 Hz, phen-*H*), 8.72 (1H, d, *J* = 8.3 Hz, phen-*H*), 7.78 – 7.68 (1H, m, Ar-*H*), 7.68 – 7.60 (1H, m, Ar-*H*), 7.56 – 7.47 (1H, m, Ar-*H*), 7.37 – 7.21 (3H, m, Ar-*H*), 7.09 – 6.86 (4H, m, Ar-*H*), 3.83 (6H, d, *J* = 10.3 Hz, Ar-O-C*H*$_3$), 2.31 (6H, s, Ar-C*H*$_3$) ppm. ^{13}C{^{1}H} NMR (101 MHz, CDCl$_3$) δ 152.5, 149.2, 148.5, 139.1, 137.7, 137.0, 130.9, 129.0, 128.1, 127.5, 127.4, 127.2, 126.2, 126.0, 125.3, 124.8, 124.0, 123.8, 123.5, 123.1, 122.7, 121.1, 113.9, 61.5, 55.9, 21.2 ppm. HRMS (ES)(%): found *m/z* = 459.2061 [M + H]$^+$.{$C_{29}H_{27}N_2O_2^+$} requires 459.2067. IR (KBr plates): 2940 (w), 1607 (m), 1581 (m), 1527 (w), 1507 (w), 1478 (s), 1462 (s), 1427 (m), 1381 (w), 1346 (w), 1327 (w), 1271 (s), 1230 (m), 1203 (w), 1170 (w), 1126 (w), 1082 (s), 1047 (w), 994 (m), 884 (w), 864 (w), 759 (s) cm^{-1}. UV-vis λ_{max} (ε / M^{-1} cm $^{-1}$) (CHCl$_3$): 260 (87,000), 280 (sh) (39,400), 339 (sh) (4100), 357 (3900) nm.

Synthesis of 38

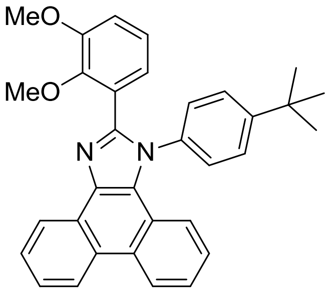

This material was prepared by a similar method to **35** using, 2,3-dimethoxy benzaldehyde (0.239 g, 1.44 mmol), 9,10-phenanthrenedione (0.300 g, 1.44 mmol), 4-tertbutylaniline (0.23 ml, 1.44 mmol) and ammonium acetate (1.11 g, 14.4 mmol). The crude product was recrystalised using chloroform and hexane to give product (**38**) as an off-white powder (0.500g, 0.79 mmol). ^{1}H NMR (400 MHz, CDCl$_3$) δ 8.86 (1H, d, *J* = 7.2 Hz, phen-*H*), 8.78 (1H, d, *J* = 8.4 Hz, phen-*H*), 8.72 (1H, d, *J* = 8.3 Hz, phen-*H*), 7.73 (1H, t, *J* = 7.5 Hz, Ar-*H*), 7.65 (1H, t, *J* = 7.5 Hz, Ar-*H*), 7.51 (1H, t, *J* = 7.6 Hz, Ar-*H*), 7.44 (3H, d, *J* = 8.4 Hz, Ar-*H*), 7.36 (3H, d, *J* = 8.3 Hz, Ar-*H*), 7.30 – 7.24 (1H, m, Ar-*H*), 7.20 (1H, m, Ar-*H*), 7.05 – 6.97 (2H, m, Ar-H), 6.93 (1H, dd, *J* = 6.9, 2.8 Hz, Ar-*H*), 3.83 (3H, s, Ar-O-C*H*$_3$), 3.77 (3H, s, Ar-O-C*H*$_3$), 1.35 (9H, s, Ar-C(C*H*$_3$)$_3$) ppm. ^{13}C{^{1}H} NMR (101 MHz, CDCl$_3$) δ 152.7, 152.5, 149.5, 148.5, 135.4, 129.2, 128.4, 128.1, 127.8, 127.4, 126.4, 125.5, 125.0, 124.2, 124.1, 123.9, 123.3, 122.9, 121.2, 114.1, 61.7, 56.1, 35.0, 31.5 ppm. HRMS (ES)(%): found *m/z* = 487.2378 [M + H]$^+$. {$C_{33}H_{31}O_2N_2$}$^+$ requires 487.2380. IR (KBr plates): 2960 (w), 1613 (w), 1580 (w), 1509 (m), 1478 (s), 1460 (s), 1424 (w), 1385 (w), 1304 (w), 1261 (s), 1234 (w), 1205 (w), 1107 (w), 1079 (s), 1052 (m), 1011 (m), 990 (w), 869 (w), 843 (w), 756 (s), 744 (s), 727 (s) cm^{-1}. UV-vis λ_{max} (ε / M^{-1} cm^{-1}) (CHCl$_3$): 260 (88,000), 281 (sh) (37,400), 304 (sh) (17,400), 339 (3200), 356 (3800) nm.

Synthesis of 39

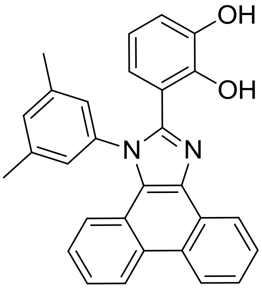

Into a round bottom flask was added lophine **37,** (0.360g, 0.79 mmol), 1M BBr_3 in DCM solution (2.73 ml, 2.73 mmol) and DCM (10 ml) at 0^{o}C. The solution was allowed to reach room temperature with stirring for 24 hrs. The resultant solution was quenched with water. All solvents were then removed *in vacuo* and the brown solid precipitated from ethanol and diethyl ether to give product (**39**) as a light brown powder (0.176g). ^{1}H NMR (400 MHz, MeOD) δ 8.96 – 8.87 (m, 2H, phen-*H*), 8.49 – 8.41 (m, 1H, phen-*H*), 7.89 – 7.81 (2H, m, Ar-*H*), 7.72 (1H, t, *J* = 7.4 Hz, Ar-*H*), 7.45 – 7.32 (4H, m, Ar-*H*), 7.19 (1H, d, *J* = 7.9 Hz, Ar-*H*), 7.00 (1H, dd, *J* = 8.0, 1.4 Hz, Ar-*H*), 6.92 (1H, dd, *J* = 7.9, 1.3 Hz, Ar-*H*), 6.76 (1H, t, *J* = 7.9 Hz, Ar-*H*), 2.40 (6H, s, Ar-C*H*$_3$) ppm. Insufficient solubility for ^{13}C{^{1}H} NMR. HRMS (ES)(%): found *m/z* = 431.1752; {$C_{29}H_{23}N_2O_2^+$} requires 431.1754. IR (KBr plates): 3193 (bs), 1652 (w), 1616 (m), 1590 (m), 1557 (m), 1509 (m), 1475 (s), 1309 (m), 1279 (m), 1242 (m), 1183 (w), 1169 (m), 1040 (w), 964 (w), 816 (m), 753 (s) cm^{-1}. UV-vis λ_{max} (ε / M^{-1} cm $^{-1}$) (DMSO): 262 (47 200), 285(sh) (17 500), 365 (8800) 262 (47 200), 285(sh) (17 500), 365 (8800) nm.

Synthesis of 40

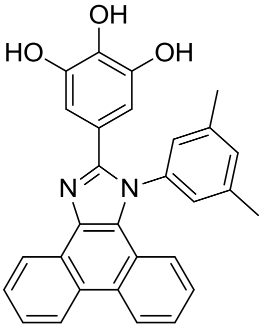

Into a round bottom flask was added lophine **41,** (0.200 g, 0.41 mmol), 1M BBr_3 in DCM solution (1.271 ml, 1.271 mmol) and DCM (10 ml) at 0^{o}C. The solution was allowed to reach room temperature with stirring for 24 hrs. The resultant solution was quenched with water. All solvents were then removed *in vacuo* and the product (**40**) precipitated from methanol and diethyl ether to give a light brown powder (0.140 g). ^{1}H NMR (400 MHz, MeOD) δ 8.94 (2H, dd, *J* = 9.2, 3.3 Hz, phen-*H*), 8.63 – 8.51 (1H, m, phen-*H*), 7.85 (2H, m, Ar-*H*), 7.75 – 7.65 (1H, m, Ar-*H*), 7.51 – 7.32 (4H, m, Ar-*H*), 7.18 (1H, d, *J* = 7.6 Hz, Ar-*H*), 6.69 (1H, s, Ar-*H*), 2.46 (6H, s, Ar-C*H*$_3$) ppm. ^{13}C{^{1}H} NMR (101 MHz, DMSO) δ 149.0, 146.0, 140.1, 137.1, 135.5, 132.8, 129.2, 128.5, 127.9, 127.8, 127.1, 126.5, 126.1, 124.9, 124.4, 122.3, 121.0, 120.7, 109.8, 21.0 ppm. HRMS (ES)(%): found *m/z* = 447.1699 [M+H]$^+$;{$C_{29}H_{23}N_2O_3^+$} requires 447.1703. IR (KBr plates): 3235 (bs), 1703 (w), 1638 (m), 1616 (s), 1538 (w), 1512 (s), 1482 (m), 1456 (w), 1314 (s), 1190 (m), 1038 (m), 1011 (m), 852 (w), 758 (m), 723 (m) cm^{-1}. UV-vis λ_{max} (ε / M^{-1} cm^{-1}) (MeOH): 257 (24 300), 304 (8700), 356 (2500) nm.

Synthesis of 41

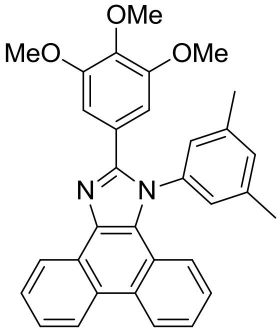

This material was prepared by a similar method to **35** using 2,3,4-trimethoxy benzaldehyde (0.283 g, 1.44 mmol), 9,10-phenanthrenedione (0.300 g, 1.44 mmol), 3,5-dimethylaniline (0.18 ml, 1.44 mmol) and ammonium acetate (1.11g 14.4 mmol). The crude product was recrystallised using chloroform and hexane to give product (**41**) as a white powder (0.630g, 1.29 mmol). ^{1}H NMR (400 MHz, $CDCl_3$) δ 8.88 (1H, dd, *J* = 7.9, 1.1 Hz, phen-*H*), 8.78 (1H, d, *J* = 8.3 Hz, phen-*H*), 8.71 (1H, d, *J* = 8.1 Hz, phen-*H*), 7.77 – 7.71 (1H, m, Ar-*H*), 7.65 (1H, m, Ar-*H*), 7.56 – 7.49 (1H, m, Ar-*H*), 7.33 – 7.23 (3H, m, Ar-*H*), 7.18 (2H, s, Ar-*H*), 6.92 (2H, s, Ar-*H*), 3.84 (3H, s, Ar-O-CH_3), 3.70 (6H, s, Ar-O-CH_3), 2.41 (6H, s, Ar-CH_3). ^{13}C{^{1}H} NMR (101 MHz, $CDCl_3$) δ 152.9, 150.3, 140.4, 139.0, 138.6, 131.5, 129.4, 128.4, 128.3, 127.4, 126.8, 126.5, 125.7, 125.3, 125.0, 124.2, 123.3, 123.2, 122.8, 121.1, 106.7, 61.1, 55.9, 21.4 ppm. HRMS (ES)(%): found *m/z* = 489.2167 [M + H]$^+$; {$C_{32}H_{28}N_2O_3$}$^+$ requires 489.2173. IR (KBr plates): 3006 (wb), 1587 (s), 1570 (m), 1532 (w), 1513 (m), 1484 (s), 1463 (s), 1416 (m), 1376 (w), 1345 (m), 1280 (w), 1249 (m), 1235 (m), 1186 (w), 1124 (s), 1026 (w), 1009 (w), 862 (w), 763 (s), 729 (s) cm^{-1}. UV-vis λ_{max} (ε / M^{-1} cm^{-1}) ($CHCl_3$): 263 (59 600), 317 (24 200), 361 (sh) (11 200) nm.

Synthesis of 42

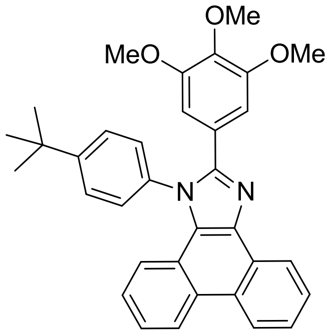

The material was prepared by a similar method to **35** using 3,4,5-trimethoxybenzaldehyde (0.283 g, 1.44 mmol), 9,10-phenanthrenedione (0.300 g, 1.44 mmol), 4-terbutylaniline (0.23 ml, 1.44 mmol) and ammonium acetate (1.11g, 14.4 mmol). The crude product was recrystallised from chloroform and hexane to give product (**42)** as a white powder (0.390g). ^{1}H NMR (400 MHz, $CDCl_3$) δ 8.88 (dd, *J* = 8.0, 1.1 Hz, 1H, phen-*H*), 8.77 (d, *J* = 8.4 Hz, 1H, phen-*H*), 8.71 (1H, d, *J* = 8.3 Hz, phen-*H*), 7.78 – 7.71 (1H, m, Ar-*H*), 7.69 – 7.62 (3H, m, Ar-*H*), 7.55 – 7.45 (3H, m, Ar-*H*), 7.32 – 7.23 (2H, m, Ar-*H*), 6.85 (2H, s, Ar-*H*), 3.84 (3H, s, Ar-O-CH_3), 3.67 (6H, s, Ar-O-CH_3), 1.44 (9H, s, Ar-C(CH_3)$_3$) ppm. ^{13}C NMR (101 MHz, $CDCl_3$) δ 153.3, 152.9, 150.4, 138.5, 137.2, 136.5, 129.3, 128.7, 128.4, 128.3, 127.4, 127.3, 126.4, 125.8, 125.7, 125.0, 124.2, 123.2, 123.2, 122.8, 121.0, 119.8, 106.6, 61.0, 56.0, 35.2, 31.5 ppm. HRMS (ES)(%): found *m/z* = 517.1475 $[M + H]^+$; $\{C_{34}H_{33}N_3O_2\}^+$ requires 517.2486. IR (KBr plates): 2956 (m), 1587 (m), 1571 (w), 1510 (s), 1475 (s), 1450 (s), 1412 (s), 1346 (w), 1327 (w), 1269 (w), 1240 (m), 1189 (w), 1124 (s), 1065 (w), 1005 (m), 881 (w), 843 (w), 752 (s), 724 (s) cm^{-1}. UV-vis λ_{max} (ε / M^{-1} cm $^{-1}$) ($CHCl_3$): 263 (63 400), 317 (24 700), 362 (sh) (10 200) nm.

Synthesis of 43

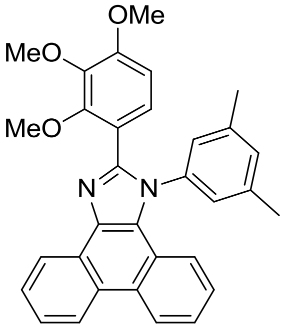

This material was prepared by a similar method to **35** using 2,3,4-trimethoxy benzaldehyde (0.283 g, 1.44 mmol), 9,10-phenanthrenedione (0.300g, 1.44 mmol), 3-5-dimethylaniline (0.18 ml, 1.44 mmol) and ammonium acetate (1.11 g, 14.4 mmol). The crude product was recrystallised using chloroform and hexane to give product (**43**) as a light brown powder (0.210 g, 0.43 mmol). ^{1}H NMR (400 MHz, $CDCl_3$) δ 8.84 (1H, dd, *J* = 8.0, 1.1 Hz, phen-*H*), 8.78 (1H, d, *J* = 8.3 Hz, phen-*H*), 8.72 (1H, d, *J* = 8.2 Hz, phen-*H*), 7.77 – 7.67 (1H, m, Ar-*H*), 7.63 (1H, m, Ar-*H*), 7.56 – 7.47 (1H, m, Ar-*H*), 7.34 – 7.27 (2H, m, Ar-*H*), 7.08 (4H, m, Ar-*H*), 6.62 (1H, d, *J* = 8.6 Hz, Ar-*H*), 3.85 (3H, s, Ar-O-C*H*$_3$), 3.77 (6H, d, *J* = 7.4 Hz, Ar-O-C*H*$_3$), 2.31 (6H, s, Ar-CH$_3$) ppm. ^{13}C{^{1}H} NMR (101 MHz, $CDCl_3$) δ 154.9, 152.9, 149.6, 141.7, 139.0, 138.0, 137.1, 130.8, 129.1, 128.2, 127.8, 127.3, 126.8, 126.3, 126.2, 125.4, 124.8, 124.1, 123.2, 122.9, 121.3, 118.2, 106.7, 61.5, 61.0, 56.1, 21.3 ppm. HRMS (ES)(%): found *m/z* = 489.2163 [M + H]$^+$. $\{C_{32}H_{29}N_2O_3\}^+$ requires 489.2173. IR (KBr plates): 2961 (w), 1600 (s), 1532 (w), 1509 (m), 1464 (s), 1411 (m), 1380 (w), 1345 (w), 1325 (w), 1292 (s), 1233 (m), 1214 (m), 1094 (s), 1064 (m), 1006 (m), 881 (w), 758 (s), 726 (s) cm^{-1}. UV-vis λ_{max} (ε / M^{-1} cm $^{-1}$) ($CHCl_3$): 258 (85 200), 280 (s) (26 000), 306 (sh) (13 900) nm.

Synthesis of 44

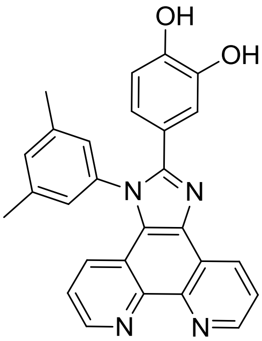

This material was prepared by a similar method to **35** using, 3,4-dihydroxy benzaldehyde (0.198 g, 1.43 mmol), 1,10-phenanthroline-5,6-dione (0.300 g, 1.43 mmol), 3,5-dimethylaniline (0.18 ml, 1.43 mmol) and ammonium acetate (1.10 g, 14.3 mmol). The crude product was recrystallised using chloroform and hexane to give product (**44**) as a brown powder (0.346g, 0.80 mmol). ^{1}H NMR (400

MHz, DMSO) δ 9.06 (1H, d, *J* = 3.0 Hz, phen-*H*), 8.97 (1H, d, *J* = 7.7 Hz, phen-*H*), 8.92 (1H, d, *J* = 3.1 Hz, phen-*H*), 7.85 (1H, dd, *J* = 7.8, 4.3 Hz, Ar-*H*), 7.48 (1H, dd, *J* = 8.4, 4.2 Hz, Ar-*H*), 7.37 (1H, s, Ar-*H*), 7.32 (3H, m, Ar-*H*), 7.22 (1H, d, *J* = 1.9 Hz, Ar-*H*), 6.81 (1H, dd, *J* = 8.3, 1.9 Hz, Ar-*H*), 6.66 (1H, d, *J* = 8.3 Hz, Ar-*H*), 2.38 (6H, s, Ar-C*H*$_3$) ppm. ^{13}C{^{1}H} NMR (101 MHz, DMSO) δ 152.1, 148.4, 147.3, 146.9, 145.0, 143.7, 143.6, 143.5, 140.1, 137.8, 134.9, 134.8, 131.8, 127.3, 126.2, 123.7, 123.4, 122.6, 120.9, 120.5, 119.5, 116.8, 115.3, 20.8 ppm. HRMS (ES)(%): found *m/z* = 433.1658[M + H]$^+$. $\{C_{27}H_{20}N_4O_2\}^+$ requires 433.1659. IR (KBr plates): 3155 (bs), 1610 (m), 1601 (m), 1567 (m), 1510 (m), 1484 (s), 1425 (m), 1392 (w), 1343 (m), 1287 (s), 1240 (s), 1115 (w), 1081 (w), 1023 (w), 888 (m), 830 (m), 808 (m), 740 (s) cm^{-1}. UV-vis λ_{max} (ε / M^{-1} cm $^{-1}$) (DMSO) 262(sh) (54 200), 280 (58 500), 304 (sh)(46 300) nm.

Synthesis of 45

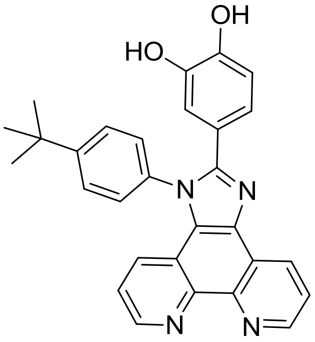

This material was prepared by a similar method to **35** using 3,4-dihydroxy benzaldehyde (0.198 g, 1.43 mmol), 1,10-phenanthroline-5,6-dione (0.300g, 1.43 mmol), 4- terbutylaniline (0.23 ml, 1.43 mmol) and ammonium acetate (1.10 g, 14.3 mmol). The crude product was recrystalised using chloroform and hexane to give product (**45**) as a brown/green powder (0.270 g, 0.80 mmol). ^{1}H NMR (400 MHz, MeOD) δ 9.01 (2H, m, phen-*H*), 8.92 – 8.84 (1H, m, phen-*H*), 7.84 – 7.67 (3H, m, Ar-*H*), 7.55 – 7.30 (4H, m, Ar-*H*), 7.07 (1H, d, *J* = 2.1 Hz, Ar-*H*), 6.82 (1H, dd, *J* = 8.2, 2.1 Hz, Ar-*H*), 6.69 (1H, d, *J* = 8.2 Hz, Ar-*H*), 1.45 (9H, s, Ar-C(C*H*$_3$)$_3$) ppm. ^{13}C{^{1}H} NMR (101 MHz, MeOD) δ 155.12, 154.60, 149.25, 148.42, 148.30, 146.37, 144.68, 144.38, 136.15, 135.75, 131.51, 129.55, 129.24, 128.45, 127.40, 126.51, 124.81, 123.56, 122.75, 121.66, 120.96, 120.78, 117.93, 115.92, 35.94, 31.74 ppm. HRMS (ES)(%): found *m/z* = 461.1976 [M + H]$^+$; $\{C_{29}H_{25}N_4O_2\}^+$ requires 461.1972. IR (KBr plates): 3058 (bw), 2961 (m), 1598 (m), 1576 (w), 1563 (w), 1511 (s), 1464 (w), 1438 (m), 1392 (w), 1364 (w), 1267 (s), 1110(w), 1033 (w), 993 (w), 910 (w), 808 (m), 740 (s) cm^{-1}. UV-vis λ_{max} (ε / M^{-1} cm $^{-1}$) (CHCl$_3$): 276 (31 800), 316(sh) (15 500), 423 (3100) nm.

Synthesis of 46

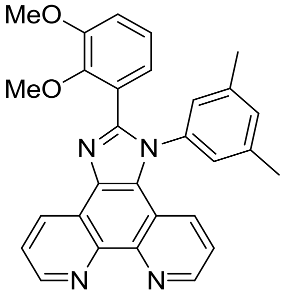

This material was prepared by a similar method to **35** using 2,3-dimethoxy benzaldehyde (0.237 g, 1.43 mmol), 1,10-phenanthroline-5,6-dione (0.300 g, 1.43 mmol), 3,5-dimethylaniline (0.18 ml, 1.43 mmol) and ammonium acetate (1.10 g, 14.3 mmol). The crude product was recrystalised using chloroform and hexane to give product (**46**) as an off-white powder (0.390g, 0.85 mmol). ^{1}H NMR (400 MHz, $CDCl_3$) δ 9.17 (1H, dd, *J* = 4.4, 1.8 Hz, phen-*H*), 9.10 (1H, dd, *J* = 8.1, 1.8 Hz, phen-*H*), 9.05 (1H, dd, *J* = 4.3, 1.6 Hz, phen-*H*), 7.72 (1H, dd, *J* = 8.1, 4.4 Hz, Ar-*H*), 7.51 (1H, dd, *J* = 8.4, 1.6 Hz, Ar-*H*), 7.32 (1H, dd, *J* = 8.4, 4.3 Hz, Ar-H), 7.10 (1H, s, Ar-*H*) 7.07 – 6.90 (5H, m, Ar-*H*), 3.85 (3H, s, Ar-O-C*H*$_3$), 3.80 (3H, s, Ar-O-C*H*$_3$), 2.32 (6H, s, Ar-C*H*$_3$). ^{13}C{^{1}H} NMR (101 MHz, $CDCl_3$) δ 153.0, 149.2, 148.7, 148.3, 140.0, 137.3, 136.1, 131.9, 130.9, 128.8, 126.7, 126.1, 125.6, 124.5, 124.1, 124.0, 123.9, 122.6, 120.3, 118.0, 114.6, 62.0, 56.4, 21.7 ppm. HRMS (ES)(%): found *m/z* = 461.1968 $[M + H]^+$. $\{C_{29}H_{25}N_4O_2\}^+$ requires 461.1972. IR (KBr plates): 2937 (s), 1594 (m), 1562 (m), 1521 (w), 1502 (m), 1475 (s), 1420 (w), 1393 (w), 1377 (w), 1341 (w), 1263 (s), 1233 (w), 1168 (w), 1083 (s), 1045 (m), 999 (m), 856 (w), 824 (m), 809 (m), 742 (s) cm^{-1}. UV-vis λ_{max} (ε / M^{-1} cm $^{-1}$) ($CHCl_3$): 256 (55 600), 276 (sh) (42 500), 312 (14 000) nm.

Synthesis of 47

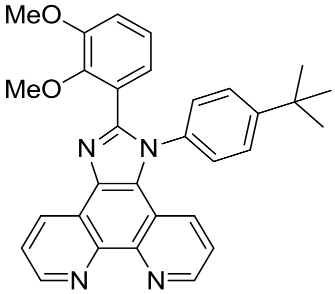

This material was prepared by a similar method to **35** using 2,3-dimethoxy benzaldehyde (0.237 g, 1.43 mmol), 1,10-phenanthroline-5,6-dione (0.300g, 1.43 mmol), 4-tertbutylaniline (0.23 ml, 1.43 mmol) and ammonium acetate (1.10 g, 14.3 mmol). The crude product was recrystalised using chloroform and hexane to give product (**47**) as an off-white powder (0.350 g, 0.72 mmol). ^{1}H NMR (400 MHz, $CDCl_3$) δ 9.24 – 9.20 (1H, m, phen-*H*), 9.16 (1H, d, *J* = 6.8 Hz, phen-*H*), 9.08 (1H, dd, *J* = 4.3, 1.5 Hz, phen-*H*), 7.77 (1H, dd, *J* = 8.1, 4.4 Hz, Ar-*H*), 7.51 – 7.42 (3H, m, Ar-*H*), 7.39 – 7.29

(3H, m, Ar-*H*), 6.99 (3H, m, Ar-*H*), 3.83 (3H, s, Ar-O-C*H*$_3$), 3.77 (3H, s, Ar-O-C*H*$_3$), 1.35 (9H, s, Ar-C(C*H*$_3$)$_3$) ppm. ^{13}C{^{1}H} NMR (101 MHz, CDCl$_3$) δ 153.1, 152.6, 150.8, 148.8, 148.3, 148.0, 144.8, 144.3, 135.9, 134.4, 130.6, 128.3, 127.7, 126.7, 126.5, 125.4, 124.2, 123.9, 123.7, 123.5, 122.2, 120.0, 114.3, 61.6, 56.0, 35.0, 31.4 ppm. HRMS (ES)(%): found *m/z* = 489.2280 [M + H]$^+$;{$C_{31}H_{29}N_4O_2$}$^+$ requires 489.2285. IR (KBr plates): 2958 (m), 1599 (m), 1578 (m), 1560 (m), 1511 (s), 1465 (s), 1389 (w), 1339 (w), 1304 (w), 1263 (s), 1238 (w), 1131 (w), 1083 (s), 1071 (s), 1052 (s), 1004 (s), 989 (s), 872 (w), 847 (w), 818 (m), 806 (m), 797 (m), 785 (m) cm^{-1}. UV-vis λ_{max} (ε / M^{-1} cm $^{-1}$) (CHCl$_3$): 270 (97 600), 352 (sh) 2500 nm.

Synthesis of 48

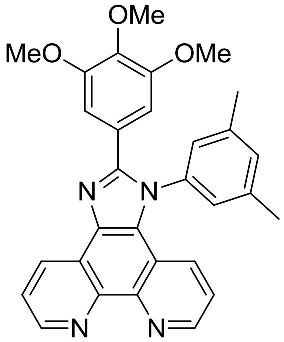

This material was prepared by a similar method to **35** using 3,4,5-trimethoxy benzaldehyde (0.281g, 1.43 mmol), 1,10-phenanthroline-5,6-dione (0.300 g, 1.43 mmol), 3,5-dimethylaniline (0.18 ml, 1.43 mmol) and ammonium actetate (1.10 g, 14.3 mmol). The crude product was recrystalised using chloroform and hexane to give product (**48**) as a brown powder (0.600 g, 1.22 mmol). ^{1}H NMR (400 MHz, CDCl$_3$) δ 9.19 (1H, dd, J = 4.4, 1.8 Hz, phen-*H*), 9.15 (1H, dd, J = 8.1, 1.8 Hz, phen-*H*), 9.06 (1H, dd, J = 4.3, 1.6 Hz, phen-*H*), 7.76 (1H, dd, J = 8.1, 4.4 Hz, Ar-*H*), 7.51 (1H, dd, J = 8.4, 1.6 Hz, Ar-*H*), 7.36 – 7.30 (2H, m, Ar-*H*), 7.20 (2H, s, Ar-*H*), 6.93 (2H, s, Ar-*H*), 3.86 (3H, s, Ar-O-C*H*$_3$), 3.72 (6H, s, Ar-O-C*H*$_3$), 2.43 (6H, s, Ar-C*H*$_3$) ppm. ^{13}C{^{1}H} NMR (101 MHz, CDCl$_3$) δ 152.97, 151.60, 148.90, 147.97, 144.65, 144.13, 140.92, 139.01, 138.27, 135.76, 131.98, 130.92, 128.37, 127.10, 126.33, 125.03, 124.01, 123.64, 122.43, 120.02, 106.50, 61.05, 55.95, 21.41 ppm. HRMS (ES)(%): found *m/z* = 491.2076 [M+H]$^+$; {$C_{30}H_{27}N_4O_3$}$^+$ requires 491.2078. IR (KBr plates): 2935 (w), 1661 (w), 1588 (m), 1561 (w), 1523 (w), 1480 (m), 1418 (m), 1346 (w), 1247 (w), 1236 (w), 1126 (s), 1025 (w), 1000 (w), 804 (w), 738 (s) cm^{-1}. UV-vis λ_{max} (ε / M^{-1} cm $^{-1}$) (CHCl$_3$): 278 (54 900), 325(sh) (11 600), 368 (sh) (1600) nm.

Synthesis of 49

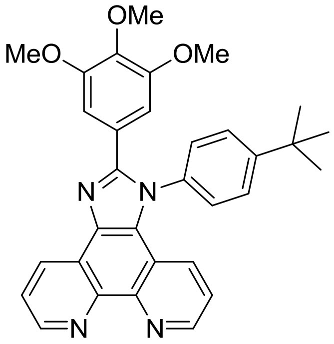

This material was prepared by a similar method to **35** using 3,4,5-trimethoxy benzaldehyde (0.281g, 1.43 mmol), 1,10-phenanthroline-5,6-dione (0.300 g, 1.43 mmol), 4-tertbutylaniline (0.23 ml, 1.43 mmol) and ammonium acetate (1.10 g, 14.3 mmol). The crude product was recrystalised using chloroform and hexane to give product (**49**) as a brown powder (0.400 g, 0.77 mmol). ^{1}H NMR (400 MHz, $CDCl_3$) δ 9.16 (2H, m, phen-*H*), 9.04 (1H, dd, *J* = 4.3, 1.6 Hz, phen-*H*), 7.75 (1H, dd, *J* = 8.1, 4.4 Hz, Ar-*H*), 7.70 – 7.65 (2H, m, Ar-*H*), 7.54 – 7.46 (3H, m, Ar-*H*), 7.34 – 7.28 (2H, m, Ar-*H*), 6.84 (2H, s, Ar-*H*), 3.84 (3H, s, Ar-O-C*H*$_3$), 3.67 (6H, s, Ar-O-C*H*$_3$), 1.44 (9H, s, Ar-C(C*H*$_3$)$_3$). ^{13}C{^{1}H} NMR (101 MHz, $CDCl_3$) δ 153.9, 152.9, 151.6, 148.9, 147.9, 144.7, 144.2, 138.9, 135.8, 135.6, 130.7, 128.3, 128.1, 127.6, 126.9, 125.0, 123.9, 123.5, 122.3, 119.9, 106.4, 61.0, 55.9, 35.2, 31.4 ppm. HRMS (ES)(%): found *m/z* = 519.2386 $[M + H]^+$. $\{C_{32}H_{31}N_4O_3\}^+$ requires 519.2391. IR (KBr plates): 2965 (w), 1584 (m), 1559 (m), 1511 (s), 1473 (s), 1404 (m), 1344 (w), 1294 (w), 1247 (m), 1234 (m), 1187 (w), 1128 (s), 1069 (w), 1003 (m), 853 (m), 805 (m), 741 (s) cm^{-1}. UV-vis λ_{max} (ε / M^{-1} cm^{-1}) ($CHCl_3$): 281 (46 100), 314 (sh) (25 300), 361 (sh) (1600) nm.

Synthesis of 50

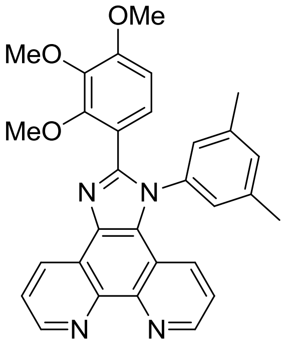

This material was prepared by a similar method to **35** using, 2,3,4-trimethoxy benzaldehyde (0.280 g, 1.43 mmol), 1,10-phenanthroline-5,6-dione (0.300 g, 1.43 mmol), 3,5-dimethylaniline (0.18 ml, 1.43 mmol) and ammonium acetate (1.10 g, 14.3 mmol). The crude product was recrystalised using chloroform and hexane to give product (**50**) as a brown powder (0.290g, 0.59 mmol). ^{1}H NMR (400

MHz, $CDCl_3$) δ 9.18 (1H, dd, *J* = 4.4, 1.7 Hz, phen-*H*), 9.11 (1H, dd, *J* = 8.1, 1.7 Hz, phen-*H*), 9.07 (1H, dd, *J* = 4.3, 1.6 Hz, phen-*H*), 7.74 (1H, dd, *J* = 8.1, 4.4 Hz, Ar-*H*), 7.56 (1H, dd, *J* = 8.4, 1.6 Hz, Ar-*H*), 7.34 (1H, dd, *J* = 8.4, 4.3 Hz, Ar-*H*), 7.09 (4H, m, Ar-*H*), 6.64 (1H, d, *J* = 8.6 Hz, Ar-*H*), 3.86 (3H, s, Ar-O-C*H*$_3$), 3.77 (6H, d, *J* = 1.5 Hz, Ar-O-C*H*$_3$), 2.33 (6H, s, Ar-C*H*$_3$) ppm. $^{13}C\{^1H\}$ NMR (101 MHz, $CDCl_3$) δ 186.6, 175.4, 155.3, 152.7, 151.0, 148.8, 147.9, 144.3, 143.8, 141.9, 139.5, 137.0, 135.5, 131.4, 131.0, 128.6, 126.6, 126.2, 125.8, 124.1, 123.6, 122.4, 120.0, 117.0, 106.8, 61.4, 60.9, 56.1, 21.3 ppm. HRMS (ES)(%): found *m/z* = 491.2069 $[M + H]^+$. $\{C_{30}H_{27}N_4O_3\}^+$ requires 491.2078. IR (KBr plates): 2935 (w), 2556 (w), 1750 (w), 1714 (s), 1612 (s), 1599 (s), 1563 (m), 1531 (w), 1510 (m), 1472 (s), 1429 (w), 1383 (w), 1341 (w), 1293 (s), 1233 (s), 1099 (s), 1061 (m), 1037 (s), 921 (m), 890 (m), 827 (s), 804 (s), 738 (s) cm^{-1}. UV-vis λ_{max} (ε / M^{-1} cm^{-1}) ($CHCl_3$): 258 (53 900), 275(sh) (45 900), 314(sh) (9900), 362 (1600) nm.

Synthesis of 51

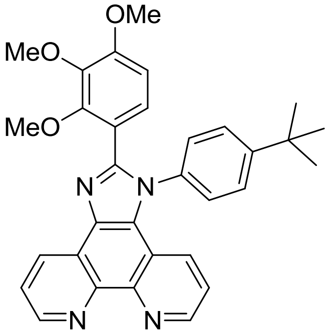

This material was prepared by a similar method to **35** using 2,3,4-trimethoxy benzaldehyde (0.280 g, 1.43 mmol), 1,10-phenanthroline-5,6-dione (0.300 g, 1.43 mmol), 4-tertbutylaniline (0.23 ml, 1.43 mmol) and ammonium acetate (1.10 g, 14.3 mmol). The crude product was recrystalised using chloroform and hexane to give product (**51**) as a light brown powder (0.250 g, 0.48 mmol). ^1H NMR (400 MHz, $CDCl_3$) δ 9.17 (1H, dd, *J* = 4.4, 1.8 Hz, phen-*H*), 9.11 (1H, dd, *J* = 8.1, 1.8 Hz, phen-*H*), 9.05 (1H, dd, *J* = 4.3, 1.6 Hz, phen-*H*), 7.73 (1H, dd, *J* = 8.1, 4.4 Hz, Ar-*H*), 7.58 (1H, dd, *J* = 8.4, 1.6 Hz, Ar-*H*), 7.49 – 7.45 (2H, m, Ar-*H*), 7.35 – 7.29 (3H, m, Ar-*H*), 7.17 (1H, d, *J* = 8.5 Hz, Ar-*H*), 6.67 (1H, d, *J* = 8.6 Hz, Ar-*H*), 3.87 (3H, s, Ar-O-C*H*$_3$), 3.68 (6H, d, *J* = 5.5 Hz, Ar-O-C*H*$_3$), 1.36 (9H, s, Ar-C(CH_3)$_3$) ppm. ^{13}C NMR (101 MHz, $CDCl_3$) δ 155.3, 153.0, 152.5, 151.3, 148.9, 148.0, 144.8, 144.3, 141.8, 135.9, 134.6, 130.7, 128.5, 127.9, 126.8, 126.4, 126.4, 124.2, 123.6, 122.2, 120.0, 117.4, 107.0, 61.4, 61.0, 56.2, 35.0, 31.4 ppm. HRMS (EI)(%): found *m/z* = 519.2380; $\{C_{32}H_{31}N_4O_3\}$ requires 519.2380. IR (KBr plates): 2960 (s), 2017 (w), 1915 (w), 1601 (m), 1561 (w), 1512 (m), 1464 (s), 1410 (m), 1340 (w), 1293 (s), 1222 (w), 1095 (s), 1070 (m), 1037 (m), 1013 (m), 985 (w), 807 (w), 748 (s), cm^{-1}. UV-vis λ_{max} (ε / M^{-1} cm^{-1}) ($CHCl_3$): 270 (77 900), 427 (sh) (2000) nm.

Synthesis of 52

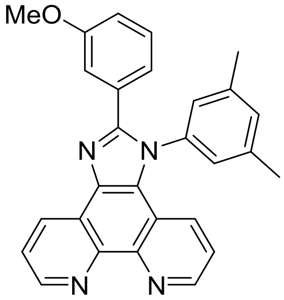

This material was prepared by a similar method to **35** using 3-methoxy benzaldehyde (0.17 ml, 1.43 mmol), 1,10-phenanthroline-5,6-dione (0.300 g, 1.43 mmol), 3,5-dimethylaniline (0.18 ml, 1.43 mmol) and ammonium acetate (1.10 g, 14.3 mmol). The crude product was recrystalised using chloroform and hexane to give product (**52**) as an off-white powder (0.300 g, 0.697 mmol). ^{1}H NMR (250 MHz, $CDCl_3$) δ 9.23 – 9.12 (2H,m ,phen-*H* ,), 9.05 (1H, dd, *J* = 4.3, 1.6 Hz, phen-*H*), 7.76 (1H dd, *J* = 8.1, 4.4 Hz, Ar-*H*), 7.47 (1H, dd, *J* = 8.4, 1.6 Hz, Ar-*H*), 7.38 – 7.11 (6H, m, Ar-*H*), 6.96 – 6.85 (1H, m, Ar-*H*), 3.73 (3H, s, Ar-OC*H*$_3$), 2.42 (6H, s, Ar-C*H*$_3$) ppm. ^{13}C NMR (101 MHz, $CDCl_3$) δ 159.3, 151.8, 149.0, 147.9, 144.9, 144.4, 140.6, 137.9, 135.9, 132.00, 131.2, 130.6, 129.4, 128.3, 127.1, 126.2, 124.0, 123.5, 122.2, 121.6, 120.00, 115.9, 113.9, 55.2, 21.4 ppm. HRMS (EI)(%): found *m/z* = 520.1897; {$C_{34}H_{24}N_4O_2$} requires 520.1899. IR (KBr plates): 3043 (w), 2949 (w), 1601 (s), 1559 (m), 1522 (w), 1503 (m), 1485 (m), 1460 (m), 1439 (m), 1340 (w), 1246 (s), 1219 (w), 1149 (w), 1078 (w), 1034 (s), 864 (m), 829 (m), 819 (m), 793 (s) cm^{-1}. UV-vis λ_{max} (ε / M^{-1} cm $^{-1}$) ($CHCl_3$): 273 (30 300), 313 (sh) (15 300), 359 (sh), 1850 nm.

Synthesis of [ReBr(CO)$_3$(44)]

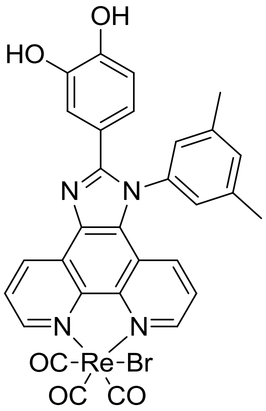

Into a round bottom flask was added lophine (**44**) (0.053 g, 0.123 mmol), pentacarbonylbromorhenium (0.05 g, 0.123 mmol) and toluene (30ml) and the reactants were left at reflux for 3 hours. The solvent was removed *in vacuo* to yield orange oil. $CHCl_3$ was added (2ml) and was precipitated from hexane to give product [ReBr(CO)$_3$(**44**)] as a yellow/green powder (0.065g). ^{1}H

NMR (400 MHz, DMSO) δ 9.52 (1H, bs, Ar-O*H*), 9.43 (1H, d, *J* = 5.1 Hz, phen-*H*), 9.34 (1H, d, *J* = 8.2 Hz, phen-*H*), 9.29 (2H, m, phen-*H*, Ar-O*H*), 8.18 (1H, dd, *J* = 8.2, 5.2 Hz, Ar-*H*), 7.84 (1H, dd, *J* = 8.6, 5.1 Hz, Ar-*H*), 7.56 (1H, d, *J* = 8.6 Hz, Ar-*H*), 7.43 (2H, s, Ar-*H*), 7.36 (1H, s, Ar-*H*), 7.26 (1H, d, *J* = 1.9 Hz, Ar-*H*), 6.87 (1H, dd, *J* = 8.3, 1.8 Hz, Ar-*H*), 6.69 (1H, d, *J* = 8.3 Hz, Ar-*H*), 2.40 (6H, d, *J* = 2.7 Hz, Ar-C*H*$_3$). ^{13}C{^{1}H} NMR (101 MHz, DMSO) δ 154.0, 152.1, 151.1, 147.5, 145.2, 143.9, 143.9, 140.5, 140.4, 136.9, 135.5, 132.9, 132.3, 130.2, 127.0, 126.1, 126.0, 125.9, 125.3, 121.6, 120.8, 120.1, 117.9, 116.8, 115.4, 20.9 ppm. HRMS (ES)(%): found *m/z* = 803.0035 [M + Na]$^+$; {$C_{30}H_{20}BrN_4NaO_5{}^{185}Re$}$^+$ requires 803.0039. IR (KBr plates): 2921 (w), 2023 (s), 1913 (s), 1884 (s), 1616 (w), 1593 (w), 1516 (w), 1447 (w), 1273 (w), 819 (w) cm^{-1}. UV-vis λ_{max} (ε / M^{-1} cm^{-1}) (CHCl$_3$): 275 (45 800), 308(sh) (30 000), 359(sh) (10 000), 418 (5700) nm.

Synthesis of [ReBr(CO)$_3$(45)]

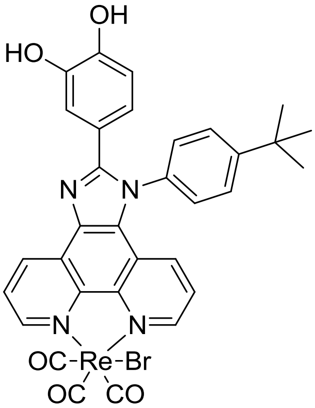

The title compound was prepared in a similar manner to [ReBr(CO)$_3$**(44)**] using lophine (**45**) (0.057 g, 0.123 mmol) and pentacarbonylbromorhenium (0.05 g, 0.123 mmol) to give the product [ReBr(CO)$_3$(**45**)] as a yellow/green solid (0.080 g). ^{1}H NMR (400 MHz, CDCl$_3$) δ 9.34 (1H, s, phen-*H*), 9.28 – 9.10 (2H, m, phen-*H*), 7.81 (2H, m, Ar-*H*), 7.64 (2H, d, *J* = 8.7 Hz, Ar-*H*), 7.49 (3H, m, Ar-*H*), 7.13 (1H, bs, Ar-*H*), 6.50 (1H, bs, Ar-*H*), 6.21 (1H, bs, Ar-*H*), 1.48 (6H, s, Ar-C(C*H*$_3$)$_3$) ppm. Insufficient solubility for ^{13}C{^{1}H} NMR. HRMS (ES)(%): found *m/z* = 807.0366 [M + H]$^+$; {$C_{32}H_{23}BrN_4O_5{}^{185}Re$} requires 807.0387. IR (KBr plates): 2022 (s), 1896 (bs), 1599 (m), 1511 (m), 1450 (m), 1399 (w), 1362 (w), 1269 (w), 1108 (w), 808 (m), 724 (m) cm^{-1}. UV-vis λ_{max} (ε / M^{-1} cm^{-1}) (CHCl$_3$): 276 (38 600), 357(sh) (8500), 418 (6200) nm.

Synthesis of [ReBr(CO)$_3$(46)]

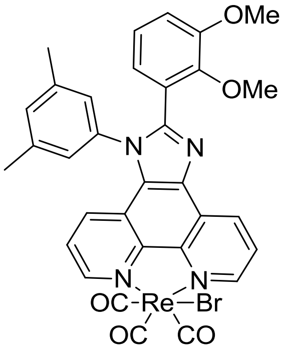

The title compound was prepared in a similar manner to [ReBr(CO)$_3$**(44)**] using lophine (**46**) (0.057 g, 0.123 mmol) and pentacarbonylbromorhenium (0.05 g, 0.123 mmol) to give the product [ReBr(CO)$_3$(**46**)] as a green solid (0.085 g). ^{1}H NMR (400 MHz, CDCl$_3$) δ 9.38 (1H, d, *J* = 4.0 Hz, phen-*H*), 9.34 (1H, d, *J* = 8.2 Hz, phen-*H*), 9.29 (1H, d, *J* = 5.0 Hz, phen-*H*), 7.92 (1H, dd, *J* = 8.2, 5.2 Hz, Ar-*H*), 7.67 (1H, d, *J* = 8.5 Hz, Ar-H), 7.54 (1H, m, Ar-*H*), 7.19 (1H, s, Ar-*H*), 7.09 – 6.90 (5H, m, Ar-*H*), 3.85 (3H, s, Ar-O-C*H*$_3$), 3.81 (3H, s, Ar-O-C*H*$_3$), 2.35 (6H, s, Ar-C*H*$_3$) ppm. ^{13}C{^{1}H} NMR (101 MHz, CDCl$_3$) δ 197.3, 197.3, 189.3, 153.1, 153.0, 152.0, 151.3, 148.6, 145.8, 145.4, 140.8, 140.7, 136.1, 133.3, 132.8, 130.8, 127.1, 126.5, 125.8, 125.6, 125.3, 124.4, 123.4, 122.4, 115.3, 62.0, 56.4, 21.7. HRMS (ES)(%): found *m/z* = 809.0546 [M + H]$^+$; {$C_{32}H_{25}O_5N_4Br^{185}Re$} requires 809.5032. IR (KBr plates): 2020 (s), 1892 (bs), 1709 (w), 1594 (w), 1478 (m), 1399 (w), 1345 (w), 1267 (m), 1234 (w), 1078 (w), 1059 (w), 999 (w), 808 (w), 725 (w) cm^{-1}. UV-vis λ_{max} (ε / M^{-1} cm $^{-1}$) (CHCl$_3$): 261 (77 700), 287 (sh) (46,800), 414 (6500) nm.

Synthesis of [ReBr(CO)$_3$(47)]

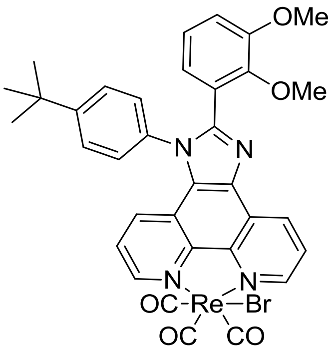

The title compound was prepared in a similar manner to [ReBr(CO)$_3$**(44)**] using lophine (**47**) (0.060 g, 0.123 mmol) and pentacarbonylbromorhenium (0.05 g, 0.123 mmol) to give the product [ReBr(CO)$_3$(**47**)] as a yellow solid (0.085 g). ^{1}H NMR (400 MHz, CDCl$_3$) δ 9.39 (1H, dd, *J* = 5.1, 1.2 Hz, phen-*H*), 9.32 (1H, dd, *J* = 8.3, 1.1 Hz, phen-*H*), 9.27 (1H, dd, *J* = 5.1, 0.9 Hz, phen-*H*), 7.93 (1H, dd, *J* = 8.2, 5.2 Hz, Ar-*H*), 7.65 (1H, dd, *J* = 8.6, 0.9 Hz, Ar-*H*), 7.55 – 7.48 (3H, m, Ar-H), 7.36 (2H, m, Ar-*H*), 7.11 – 7.03 (1H, m, Ar-*H*), 7.03 – 6.93 (2H, m, Ar-*H*), 3.85 (3H, s, Ar-O-C*H*$_3$), 3.76 (3H, s, Ar-O-C*H*$_3$), 1.37 (9H, s, Ar-H) ppm. ^{13}C{^{1}H} NMR (101 MHz, CDCl$_3$) δ 197.6, 197.6, 189.7, 154.6, 153.7, 153.3, 152.1, 151.3, 148.7, 146.0, 145.5, 137.1, 134.0, 133.4, 130.9, 128.2, 127.9, 127.8, 127.7, 127.5, 127.1, 126.6, 125.5, 125.0, 124.8, 123.7, 122.8, 115.3, 62.2, 56.6, 35.7, 31.9 ppm. HRMS (ES)(%): found *m/z* = 837.0848 [M + H]$^+$; {$C_{34}H_{29}BrN_4O_5{}^{185}Re$}$^+$ requires 837.0845. IR (KBr plates): 2020 (s), 1891 (bs), 1709 (w), 1600 (w), 1512 (w), 1478 (m), 1459 (m), 1266 (m), 1085 (w), 1061 (w), 993 (w), 808 (w), 725 (w) cm^{-1}. UV-vis λ_{max} (ε / M^{-1} cm $^{-1}$) (CHCl$_3$): 262 (115 800), 418 (1800) nm.

Synthesis of [ReBr(CO)$_3$(48)]

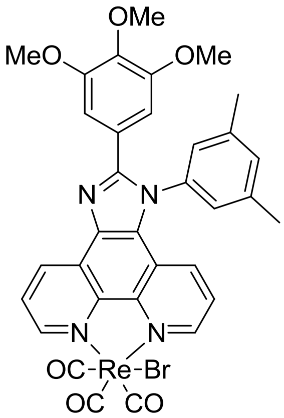

The title compound was prepared in a similar manner to [ReBr(CO)$_3$**(44)**] using lophine (**48**) (0.060 g, 0.123 mmol) and pentacarbonylbromorhenium (0.05 g, 0.123 mmol) to give product [ReBr(CO)$_3$(**48**)] as a green powder (0.080 g). ^{1}H NMR (400 MHz, CDCl$_3$) δ 9.41 – 9.33 (2H, m, phen-*H*), 9.27 (1H, dd, *J* = 5.1, 1.2 Hz, phen-*H*), 7.95 (1H, dd, *J* = 8.2, 5.2 Hz, Ar-*H*), 7.66 (1H, dd, *J* = 8.6, 1.2 Hz, Ar-*H*), 7.53 (1H dd, *J* = 8.6, 5.1 Hz, Ar-*H*), 7.38 (1H, s, Ar-*H*), 7.20 (1H, bs, Ar-*H*), 6.96 (2H, s, Ar-*H*), 3.88 (3H, s, Ar-O-C*H*$_3$), 3.73 (6H, s, Ar-O-C*H*$_3$), 2.46 (6H, d, *J* = 4.8 Hz, Ar-C*H*$_3$) ppm. ^{13}C{^{1}H} NMR (101 MHz, CDCl$_3$) δ 153.6, 153.2, 153.2, 151.7, 150.8, 145.4, 145.1, 141.8, 141.5, 139.70, 137.4, 136.5, 133.1, 132.7, 130.4, 127.5, 126.3, 126.1, 125.8, 125.1, 124.1, 122.2, 106.6, 63.66, 61.1, 56.0, 21.5, ppm. HRMS (ES)(%): found *m/z* = 863.0467 [M + Na]$^+$; {$C_{33}H_{26}BrN_4O_6{}^{187}ReNa$}$^+$ requires 863.0469. IR (KBr plates): 2020 (s), 1869 (bs), 1589 (m), 1479 (m), 1235 (w), 1126 (m), 999 (w), 808 (w), 725 (w) cm^{-1}. UV-vis λ_{max} (ε / M^{-1} cm $^{-1}$) (CHCl$_3$): 278 (30 200), 347(sh) (8600), 425 (3700) nm.

Synthesis of [ReBr(CO)$_3$(49)]

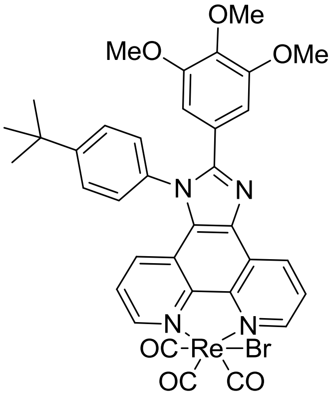

The title compound was prepared in a similar manner to [ReBr(CO)$_3$**(44)**] using lophine (**49**) (0.063 g, 0.123 mmol) and pentacarbonylbromorhenium (0.05 g, 0.123 mmol) to give product [ReBr(CO)$_3$(**49**)] as a yellow powder (0.086 g). ^{1}H NMR (400 MHz, CDCl$_3$) δ 9.41 – 9.34 (2H, m, phen-*H*), 9.26 (1H, dd, *J* = 5.1, 1.2 Hz, phen-*H*), 7.95 (1H, dd, *J* = 8.2, 5.2 Hz, Ar-*H*), 7.76 (2H, d, *J* = 8.6 Hz, Ar-*H*), 7.69 (1H, dd, *J* = 8.6, 1.2 Hz, Ar-*H*), 7.54 – 7.48 (3H, m, Ar-*H*), 6.86 (2H, s, Ar-*H*), 3.87 (3H, s, Ar-O-C*H*$_3$), 3.68 (6H, s, Ar-O-C*H*$_3$), 1.47 (9H, s, Ar-C(CH$_3$)$_3$) ppm. ^{13}C{^{1}H} NMR (101 MHz, CDCl$_3$) δ 197.2, 197.1, 189.2, 155.3, 153.9, 153.4, 152.0, 151.0, 145.7, 145.3, 140.0, 134.8, 133.2, 130.3, 128.5, 128.4, 128.2, 127.6, 126.3, 126.3, 125.2, 123.9, 122.3, 106.9, 61.3, 56.3, 35.6, 31.7 ppm. HRMS (ES)(%): found *m/z* = 869.0962 [M + H]$^+$; {$C_{35}H_{31}BrN_4O_6{}^{187}Re$}$^+$ requires 869.0963. IR (KBr plates): 2960 (m), 2020 (s), 1894 (s), 1585 (w), 1512 (w), 1477 (m), 1414 (m), 1383 (w), 1345 (w), 1301 (w), 1235 (m), 1127 (s), 1056 (w), 846 (w), 807 (w), 725 (m) cm^{-1}. UV-vis λ_{max} (ε / M^{-1} cm^{-1}) (CHCl$_3$): 278 (46 700), 341 (sh) (14 700), 426 (6000) nm.

Synthesis of [ReBr(CO)$_3$(50)]

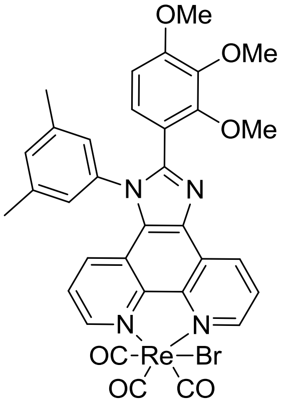

The title compound was prepared in a similar manner to [ReBr(CO)$_3$**(44)**] using lophine (**50**) (0.060 g, 0.123 mmol) and pentacarbonylbromorhenium (0.05 g, 0.123 mmol) to give product [ReBr(CO)$_3$(**50**)] as a yellow solid (0.075 g). ^{1}H NMR (400 MHz, CDCl$_3$) δ 9.38 (1H, s, phen-*H*), 9.34 – 9.25 (2H, m, phen-*H*), 7.97 – 7.89 (1H, m, Ar-*H*), 7.72 (1H, d, *J* = 7.9 Hz, Ar-*H*), 7.57 – 7.50 (1H, m, Ar-*H*), 7.18

(1H, s, Ar-*H*), 7.11 – 7.02 (3H, m, Ar-*H*), 6.67 (1H, d, *J* = 8.4 Hz, Ar-*H*), 3.88 (3H, s, Ar-O-CH_3), 3.78 (6H, s, Ar-O-$\mathrm{CH_3}$), 2.35 (6H, s, Ar-$\mathrm{CH_3}$) ppm. ^{13}C NMR (101 MHz, $\mathrm{CDCl_3}$) δ 155.8, 153.3, 152.6, 151.5, 150.8, 145.4, 145.0, 141.9, 140.3, 140.1, 136.5, 136.3, 132.9, 132.1, 130.5, 126.8, 126.6, 126.4, 126.1, 125.7, 125.3, 124.9, 122.2, 116.5, 107.1, 61.6, 61.0, 56.2, 21.4, 21.4 ppm. HRMS (EI)(%): found *m/z* = 841.0642; {$\mathrm{C_{33}H_{27}BrN_4O_6Re}$} requires 841.0653. IR (KBr plates): 2935 (w), 2020 (s), 1891 (s), 1599 (m), 1508 (w), 1474 (m), 1427(w), 1412 (w), 1293 (m), 1233 (w), 1215 (w), 1096 (m), 1055 (w), 1011 (w), 807 (w), 725 (w) cm^{-1}. UV-vis λ_{max} (ε / M^{-1} cm $^{-1}$) ($\mathrm{CHCl_3}$): 239 (55 800), 261 (85 700), 295 (sh) (38 400), 417 (6300) nm.

Synthesis of [ReBr(CO)$_3$(51)]

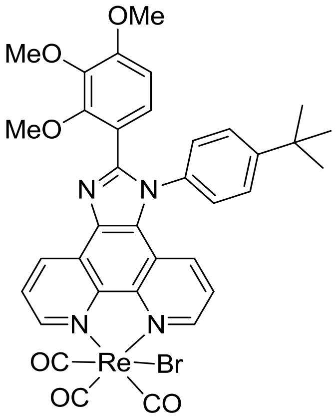

The title compound was prepared in a similar manner to [ReBr(CO)$_3$**(44)**] using lophine (**51**) (0.064 g, 0.123 mmol) and pentacarbonylbromorhenium (0.05 g, 0.123 mmol) to give product [ReBr(CO)$_3$(**51**)] as a yellow solid (0.065 g). ^{1}H NMR (400 MHz, $\mathrm{CDCl_3}$) δ 9.33 – 9.30 (1H, m, phen-*H*), 9.25 (1H, dd, *J* = 8.2, 1.2 Hz, phen-*H*), 9.21 (1H, d, *J* = 4.1 Hz, phen-*H*), 7.86 (1H, dd, *J* = 8.2, 5.1 Hz, Ar-*H*), 7.73 – 7.69 (1H, m, Ar-*H*), 7.49 – 7.42 (3H, m, *J* = 8.7, 5.1 Hz, Ar-*H*), 7.30 – 7.22 (2H, m, Ar-*H*), 7.09 (1H, d, *J* = 8.6 Hz, Ar-*H*), 6.63 (1H, d, *J* = 8.6 Hz, Ar-*H*), 3.81 (3H, s, Ar-O-CH_3), 3.62 (6H, d, *J* = 9.6 Hz, Ar-O-CH_3), 1.31 (9H, s, Ar-C($\mathrm{CH_3}$)$_3$) ppm. ^{13}C NMR (101 MHz, $\mathrm{CDCl_3}$) δ 155.8, 153.9, 153.6, 152.3, 151.6, 150.8, 145.4, 145.0, 141.9, 136.6, 133.6, 132.9, 130.4, 127.8, 127.6, 127.0, 126.8, 126.6, 126.5, 126.1, 124.9, 122.2, 116.5, 107.2, 61.4, 61.0, 56.2, 35.2, 31.4 ppm. LRMS (ES+): found *m/z* 830.12. {C37H33N5O6Re}$^+$ requires 830.20. IR (KBr plates): 2962 (w), 2020 (s), 1893 (bs), 1709 (m), 1600 (m), 1512 (m), 1463 (m), 1412 (w), 1342 (w), 1292 (m), 1221 (m), 1096 (m), 1081 (m), 808 (m) cm^{-1}. UV-vis λ_{max} (ε / M^{-1} cm $^{-1}$) ($\mathrm{CHCl_3}$): 274 (260 000), 408 (3800) nm.

Synthesis of [ReBr(CO)$_3$(52)]

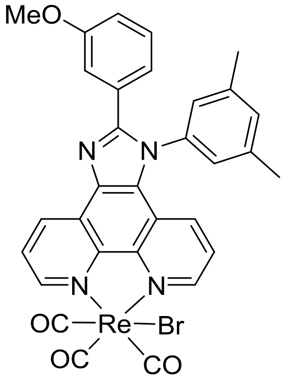

The title compound was prepared in a similar manner to [ReBr(CO)$_3$**(44)**] using lophine (**52**) (0.052 g, 0.123 mmol) and pentacarbonylbromorhenium (0.05 g, 0.123 mmol) to give product [ReBr(CO)$_3$(**52**)] as a green solid (0.090 g). ^{1}H NMR (400 MHz, CDCl$_3$) δ 9.39 (1H,dd, *J* = 5.1, 1.4 Hz, phen-*H*), 9.35 (1H, dd, *J* = 8.3, 1.4 Hz, phen-*H*), 9.27 (1H, dd, *J* = 5.0, 1.3 Hz, phen-*H*), 7.95 (1H, dd, *J* = 8.2, 5.1 Hz, Ar-*H*), 7.62 (1H, d, *J* = 1.2 Hz, Ar-*H*), 7.60 (1H, d, *J* = 1.3 Hz, Ar-*H*), 7.52 (1H, dd, *J* = 8.6, 5.1 Hz, Ar-*H*), 7.37 (1H, s, Ar-*H*), 7.29 – 7.19 (3H, m, Ar-*H*), 7.16 (2H, d, *J* = 8.1 Hz, Ar-*H*), 6.96 (1H, dd, *J* = 8.1, 1.5 Hz, Ar-*H*), 3.75 (3H, s, Ar-O-C*H*$_3$), 2.45 (6H, d, *J* = 7.2 Hz, Ar-C*H*$_3$) ppm. ^{13}C NMR (101 MHz, CDCl$_3$) δ 197.4, 189.5, 159.9, 154.2, 152.0, 151.0, 145.8, 145.4, 141.8, 141.6, 137.3, 136.9, 133.3, 133.1, 130.7, 130.6, 130.1, 127.9, 126.7, 126.4, 126.3, 126.1, 125.3, 122.6, 122.0, 117.0, 114.6, 55.7, 21.8 ppm. HRMS (EI)(%): found *m/z* = 779.0450; {$C_{31}H_{23}BrN_4O_4{}^{185}Re$} requires 779.0432. IR (KBr plates): 2017 (s), 1890 (bs), 1458 (w), 1381 (w), 1242 (w), 1149 (w), 1093 (w), 1051 (w), 987 (w), 808 (w) cm^{-1}. UV-vis λ_{max} (ε / M^{-1} cm $^{-1}$) (CHCl$_3$): 274 (49 300), 292 (sh) (33 600), 421 (4800) nm.

3.12 References

(1) E. Gaidamauskas; D. C. Crans; H. Parker; K. Saejueng; B. A. Kashemirov; C. E. McKenna *New. J. Chem.* **2011**, *35*, 2877.

(2) Nuñez, C.; Fernandez-Lodeiro, J.; Dinis, M.; Larguinho, M.; Capelo, J. L.; Lodeiro, C. *Inorg. Chem. Commun.* **2011**, *14*, 831.

(3) C. Queirós; A. M. G. Silva; S. C. Lopes; G. Ivanova; P. Gameiro; M. Rangel *Dyes Pigments* **2012**, *93*, 1447.

(4) Bartusek, M.; Sommer, L. *J. Inorg. Nucl. Chem.* **1965**, *27*, 2397.

(5) C. Aronica; J. Guerin; J. Chauvin; V. Robert; G. Lemercier *J. Photoch. Photbio. A.* **2010**, *211*, 147.

(6) Riedel, F.; Spange, S. *J. Phys. Org, Chem.* **2012**, *25*, 1261.

(7) Evangelio, E.; Hernando, J.; Imaz, I.; Bardaj, G. G.; Alibes, R.; Busque, F.; Ruiz-Molina, D. *Chem. Eur. J.* **2008**, *14*, 9754

(8) G-Y Bai; K-Z Wang; Z-M Duan; L-H Goa *J. Inorg. Biochem.* **2004**, *98*, 1017.

(9) Stevens, B. *Spectrochim. Acta* **1961**, *18*, 439.

(10) Azumi, T.; McGlynn, S. P. *J. Chem. Phys.* **1962**, *37*, 2413.

(11) Zweig, A.; Maricle, D. L.; Brinen, J. S.; Maurer, A. H. *J. Am. Chem. Soc.* **1967**, *89*, 473.

(12) Langelaar, J.; Rettschnick, R. P. H.; Hoijtink, G. J. *J. Chem. Phys.* **1971**, *54*, 1.

(13) Almgren, M.; Grieser, F.; Thomas, J. K. *J. Am. Chem. Soc.* **1979**, *101*, 2021.

(14) Suh, H.; Jin, Y.; Park, S. H.; Kim, D.; Kim, J.; Kim, C.; Kim, J. Y.; Lee, K. *Macromolecules* **2005**, *38*, 6285.

(15) Jin, Y.; Kim, Y.; Kim, S. H.; Song, S.; Woo, H. Y.; Lee, K.; Suh, H. *Macromolecules* **2008**, *41*, 5548.

(16) Jin, Y.; Yoo, C.; Kim, K.; Song, S.; Kim, J.; Kim, J.; Suh, H. *Synth. Met.* **2008**, *158*, 417.

(17) Osawa, M.; Hoshino, M.; Akita, M.; T., W. *Inorg. Chem.* **2005**, *44*, 1157.

(18) Wu, D.; Descalzo, A. B.; Weik, F.; Emmerling, F.; Shen, Z.; You, X.-Z.; Rurack, K. *Angew. Chem. Int. Ed.* **2008**, *47*, 193.

(19) Walther, M. E.; Wenger, O. S. *Dalton Trans.* **2008**, 6311.

(20) Zhang, P.; Wang, J.; Huang, H.; Qiao, L.; Ji, L.; H., C. *Dalton Trans.* **2013**, *42*, 8907.

(21) Miao, T.-F.; Liao, S.-Y.; Qian, L.; Zheng, K.-C.; Ji, L.-N. *Biophys. Chem.* **2009**, *140*, 1.

(22) Q-L Zhang; J-H Liu; X-Z Ren; Xu., H.; Y. Huang; J-Z Liu; L-N Ji *J. Inorg. Biochem.* **2003**, *95*, 194.

(23) McOmie, J. F. W.; West, D. E. *Org. Synth.* **1969**, *49*, 50.

(24) Albrecht, M.; Janser, I.; Fröhlich, R. *Synthesis-Stuttgart* **2004**, *12*, 1977.

(25) Matsuo, Y.; Muramatsu, A.; Kamikawa, Y.; Kato, T.; Nakamura, E. *J. Am. Chem. Soc.* **2006**, *128*, 9586.

(26) Nguyen, N. H.; Cougnon, C.; Gohier, F. *J. Org. Chem.* **2009**, *74*, 3955.

(27) Bandyopadhyay, B. N.; Harriman, A. *Chem. Soc. Farday. Trans. 1.* **1977**, *73*, 663.

(28) M. Homocianu; A. Airinei; D. O. Dorohoi *J. Adv. Res. Phys.* **2011**, *2*, 1.

(29) Veroni, I.; Mitsopoulou, C. A.; Lahoz, F. J. *J. Organomet. Chem.* **2008**, *693*, 2451.

(30) Thorp-Greenwood, F. L.; Coogan, M. P.; Hallett, A. J.; Laye, R. H.; Pope, S. J. A. *J. Organomet. Chem.* **2009**, *694* 1400.

(31) Lees, A. J. *Chem. Rev.* **1987**, *87*, 711.

(32) Bonello, R. O.; Morgan, I. R.; Yeo, B. R.; Jones, L. E. J.; Kariuki, B. M.; Fallis, I. A.; Pope, S. J. A. *J. Organomet. Chem.* **2014**, *749*, 150.

Chapter 4 : Synthesis and characterisation of fluorescent R′-substituted imidazole[4,5-*f*]-1,10-phenanthroline derivatives and their Re(I) carbonyl complexes

4.1 Introduction

Chapters 2 and 3 investigated the effects of differing R groups on the fused imidazole [4,5-*f*]-1,10-phenanthroline system, exploring the effects of altering the apical R group and pendant side-arm R′ group on the system. In terms of the R′ group, both chapters only exploited the use of two substituents, the 3,5-dimethylphenyl and 4-^{t}butylphenyl groups. This chapter includes the incorporation of a selection of bulkier R′ groups that alter solubility, sterics and electronics, as well as introducing additional binding sites. For the ligand systems in this chapter the substituents of choice were 2,2′:6′,2″-terpyridine, triphenylmethane, and azobenzene. Additionally, a bulky apical ligand, formylphenylbenzoate was also investigated. The introduction will briefly highlight the chemistry of these substituents.

4.2 2,2′:6′,2″-terpyridine (terpy)

2,2′:6′,2″-terpyridine (terpy), **53** (Figure) is a very well-known ligand system that has also been investigated for many sensing, binding and detection studies, including DNA binding,[1] biosensing,[2] anion recognition[3] and lanthanide and actinide detection.[4,5]

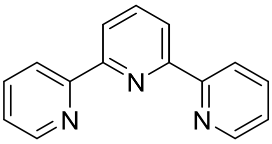

53

Figure 87: Molecular structure of 2,2′:6′,2″-terpyridine, **53**

In the context of coordination chemistry, terpy has shown preferential binding in some instances, for example showing higher selectivity for An(III) over Ln(III) than 2,2′-bipyridine in competition and liquid-liquid extraction studies.[6] Terpyridine-uranyl complexes show distinctive photophysical properties, including displaying luminescence upon excitation as a result of LMCT. For example, a recent paper described the crystal structures of three terpyridine uranyl complexes ($UO_2Cl_4.H_2$(terpy).H_2O,(**54a**) $UO_2Cl_4.H_2$(terpy).2Cl (**54b**) and UO_2Cl_2(terpy))(**54c**) and examined their luminescence properties.[5]

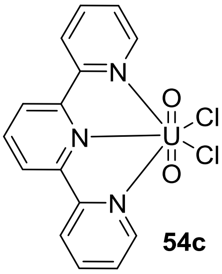

54c

Figure 88: Structure of [UO_2Cl_2(terpy)], **54c**

All complexes were found to be emissive when excited at 365 nm, characterised by a series of broad bands in the region of 500-575 nm attributed to a uranyl-centred LMCT emission.

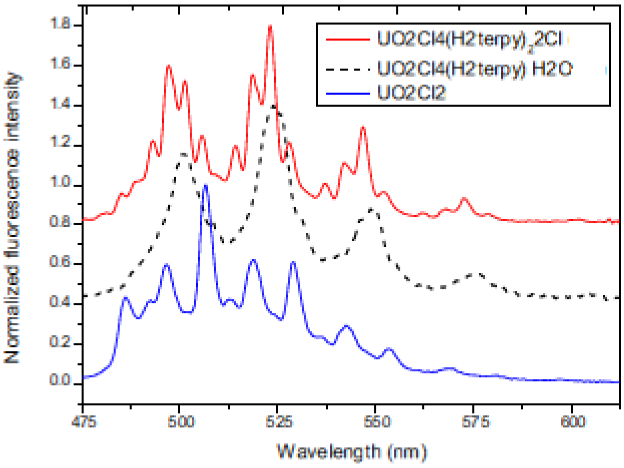

Figure 89: Emission spectra of **54a-c**.[5]

4.3 2,2′:6′,2″-terpyridine-rhenium coordination chemistry

While studies of the Re(I) tricarbonyl diimine system has grown extensively in recent years, investigations into meridionally-coordinated tridentate triimine Re(I) dicarbonyl complexes are rare.[7] The incorporation of 2,2′:6′,2″-terpyridine ligand should provide enhanced stability due to the chelate effect.[8] Hightower and co-workers synthesised a series of meridionally-coordinated tridentate 2,2′:6′,2′-terpyridine Re(I) dicarbonyl complexes of the type *mer*,*cis*-[Re(terpy)$(CO)_2$(L)], **55** (Figure 90).

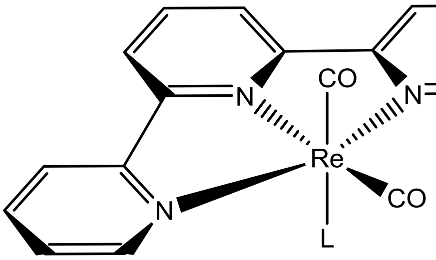

55

Where L = Cl^-, $OSO_2CF_3^-$, $NCCH_3$ CN^-, NC_5H_5, PMe_3, PEt_3, PPh_3, $P(OMe)_3$ and $P(OEt)_3$

Figure 90: Structure of *mer,cis*-[Re(terpy)$(CO)_2$(L)], **55**

Under relatively mild conditions, (toluene, reflux, 4 hrs), the rhenium did not coordinate to all three nitrogen atoms of the terpyridine. Instead it coordinated to two of the nitrogen atoms and formed a tricarbonyl complex similar to those discussed in chapters 2 and 3. In order to form the dicarbonyl complex with all three coordinated terpyridine nitrogens harsher temperature conditions were required (275°C for a further 4-6 hrs.). IR spectroscopy studies of the complexes displayed two stretching modes observed in the region of 1795-1865 and 1890-1940 cm^{-1} which was expected of a Re(I) dicarbonyl species, and which were also consistent for a *cis*-CO geometry for all the complexes. The electronic absorption spectra in MeCN showed high energy $\pi \rightarrow \pi^*$ transitions in the region of 200-300 nm and also absorptions between 300-350 nm which were attributed to an admixture of ligands centred $\pi \rightarrow \pi^*$ and MLCT transitions. Luminescence studies of these complexes showed that the complexes were not emissive at room temperature in MeCN, however phosphorescence emission was observed at 77 K in 4:1 methanol-ethanol glass with emissions observed at the low energy end of the spectrum. For example *mer,cis*- [Re(terpy)$(CO)_2$Cl] showed an emission centred at 522 nm at 77 K, which increased to 548 nm when the temperature was raised to 125 K (with loss of signal intensity). This signal was attributed as a ^{3}MLCT.

The observation that Re(I)-carbonyl complexes favour coordination to bidentate diimine ligands instead of tridentate terpyridine ligands has been well established.[9] Studies into the fluxional behaviour of the bidentate rhenium tricarbonyl complexes have been undertaken, and mechanisms into the Re-N linkage fluxion have been proposed (Figure 91).[10]

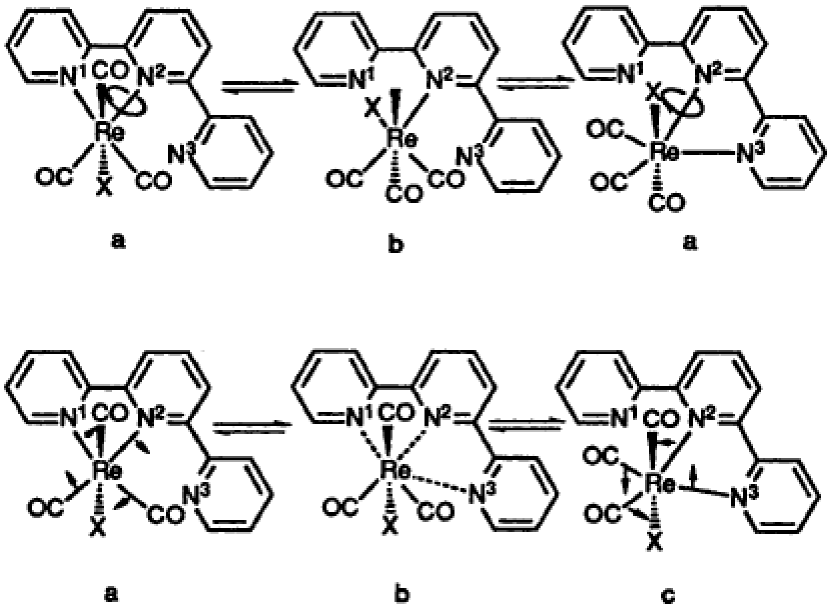

Figure 91: Two proposed mechanisms for fluxional behaviour of Re complex.[10]

4.4 Triphenylmethane “Trityl” as a bulky substituent

An essential requirement of commercial applications of light-emitting diodes is high efficiency of the system. Processes such as self-quenching reduce the efficiency of light emitting diodes and as such make them less suitable for commercial applications. Self-quenching can be reduced with the incorporation of bulky substituents which reduce aggregation of compounds such as polymer chains. For example, the efficiency of a PPV derivative (**56b**, Figure 92) was found to increase 9-fold compared to its parent polymer (**56a**) as a result of the incorporation of a triphenylmethane (“trityl”-phenyl) group.[11]

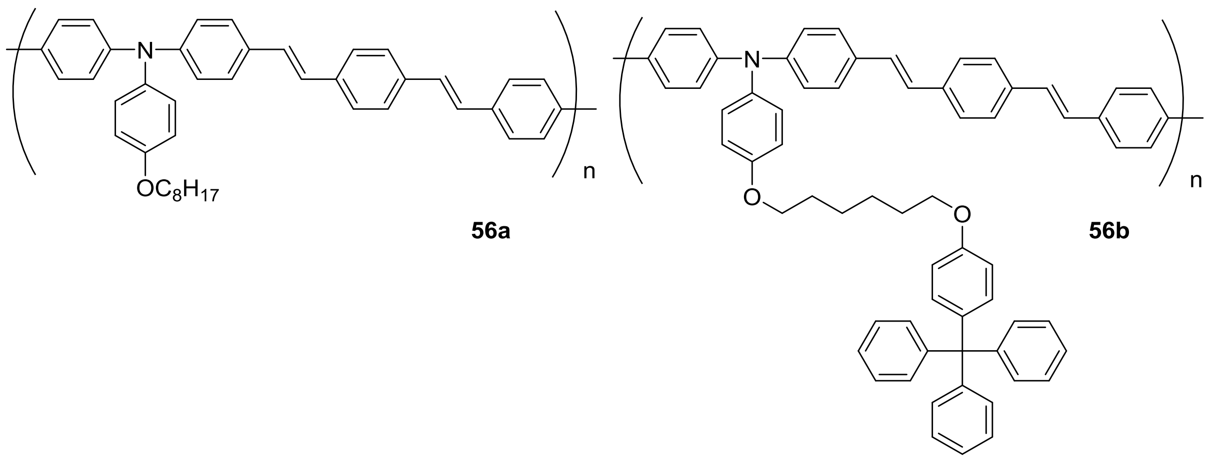

56a

56b

Figure 92: Parent polymer (**56a,** left) and tetraphenylmethyl derivative (**56b**, right)

Additionally, tetraphenylmethyl derivative showed much less concentration quenching effect. These observations were attributed to reduced interactions of the polymer chains as a result of the incorporation of a tetraphenyl methyl moiety.

4.5 Conformational differences of Azobenzene

Azobenzene exists at equilibrium in the dark as the more stable *trans* isomer (Figure 93). Irradiation with UV light results in the formation of the *cis* isomer which may then be converted back to the *trans* conformation either thermally or through irradiation with blue light.[12] The *cis* (**57a)** and *trans* (**57b**) isomers have different photophysical properties, and these characteristics have led to azobenzene being employed as a photoswitch for the determination of the structure and function of biological targets.

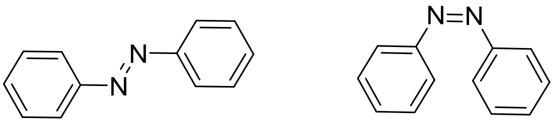

57a **57b**

Figure 93: Isomers of azobenzene

This photoisomerisation of azobenzene chromophores can also be exploited in metal complexes for potential use in photochemical molecular devices. For example, a series of rhenium tricarbonyl complexes have been isolated of the type $[Re(CO_3)(N^\wedge N)L]ClO_4$ where N^N = 2,2′-bipyridine and 1,10-phenanthroline, and L = a range of pyridyl azo ligands (Figure 94).[13]

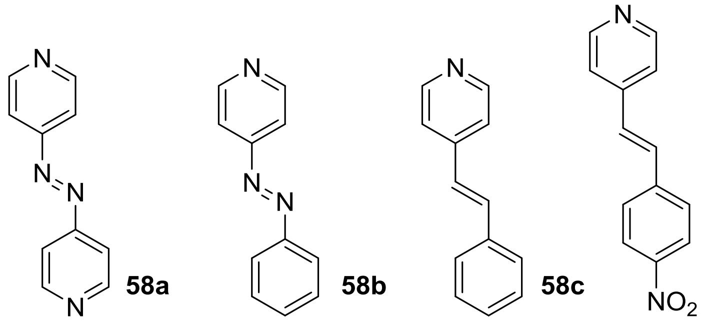

58a **58b** **58c** **58d**

Figure 94: Selected pyridyl azo ligands (from left to right) AZO (**58a**), PHAZO (**58b**), STYPY (**58c**) and NSP (**58d**)

Complexes containing these molecules exhibited bands in the electronic absorbance spectrum at 320-400 nm assigned to a $d\pi \rightarrow \pi^*$(bpy/phen) transition. However, the intensity of this band was larger than expected for an MLCT transition, and it was found that the free ligands of **58a**, **58b**, **58c** and **58d** also absorbed in a similar region of the spectra. Therefore the band was assigned as an admixture of intra-ligand(IL) $\pi \rightarrow \pi^*$(L) and MLCT character. The complexes displayed a yellow-green emission between 510-580 nm when excited at 350 nm, and a large Stokes' shift combined with a relatively lengthy lifetime suggested an emission from a triplet origin derived from the ^{3}MLCT $d\pi \rightarrow \pi^*$(bpy/phen) state. Photoisomerisation studies of the complexes showed a change in the emission spectra upon a *trans/cis* isomerisation of the azo unit. The complex $[Re(CO)_3(bpy)($**58b**$)]ClO_4$ displayed an emission band at 550 nm, but upon steady-state photolysis for 12h using a 200 W xenon lamp, there was a drastic increase (40-fold) in quantum yield and a shift in the emission maxima to 570 nm (Figure 95). As has been previously described, for the free azo chromophore the triplet-state energy of the *trans* isomer is generally lower than that of the *cis* counterpart as a result of the steric constraints in the latter. It was possible that some energy from the excited triplet state was intramolecularly transferred to the *trans*-azo moiety (pre-photolysis) which resulted in a non-radiative deactivation pathway. However, due to the relatively high energy of the unfavoured *cis* conformation the intra-molecular energy transfer was blocked, resulting in a higher percentage radiative deactivation of the triplet excited state.

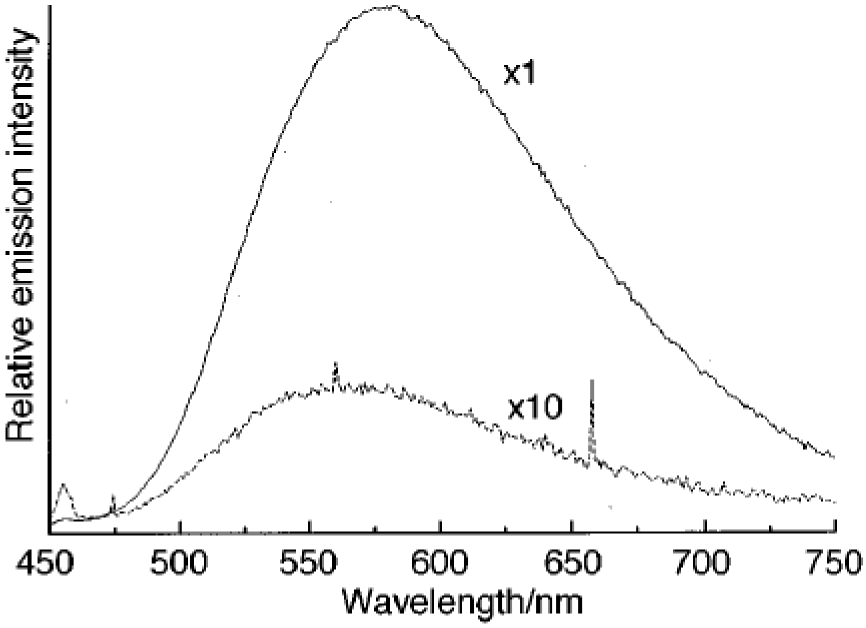

Figure 95: Emission spectra of $[Re(CO)_3(bpy)($**58b**$)]ClO_4$ before (top) and after (bottom) photolysis. [13]

4.6 Aims

The aims of this chapter will be developed through these key areas:

- Synthesis and characterisation of novel heterocyclic chromophoric “lophine” ligands with tuneable optical properties.
- Investigation of the effects of bulky R′ substituents on the optical properties, solubility and sterics of the systems.
- Investigation of the effects of a bulky apical R substituent on the optical properties, solubility and sterics of the system.
- Incorporation of an additional binding site located on the R′ substituent.
- Synthesis and characterisation of novel Re(I) complexes allowing for investigation of photophysical aspects.
- An investigation of the preferred binding site of Re(I) upon coordination to a ligand with two potential binding sites.
- Analysis of the crystal structures of these systems, allowing insight into the structure of the complexes and how it may affect phosphorescence emission.

4.7 Results and Discussion

Listed in Figure 96 **Error! Reference source not found.**are the compounds which were isolated in this chapter, along with their designated number for reference.

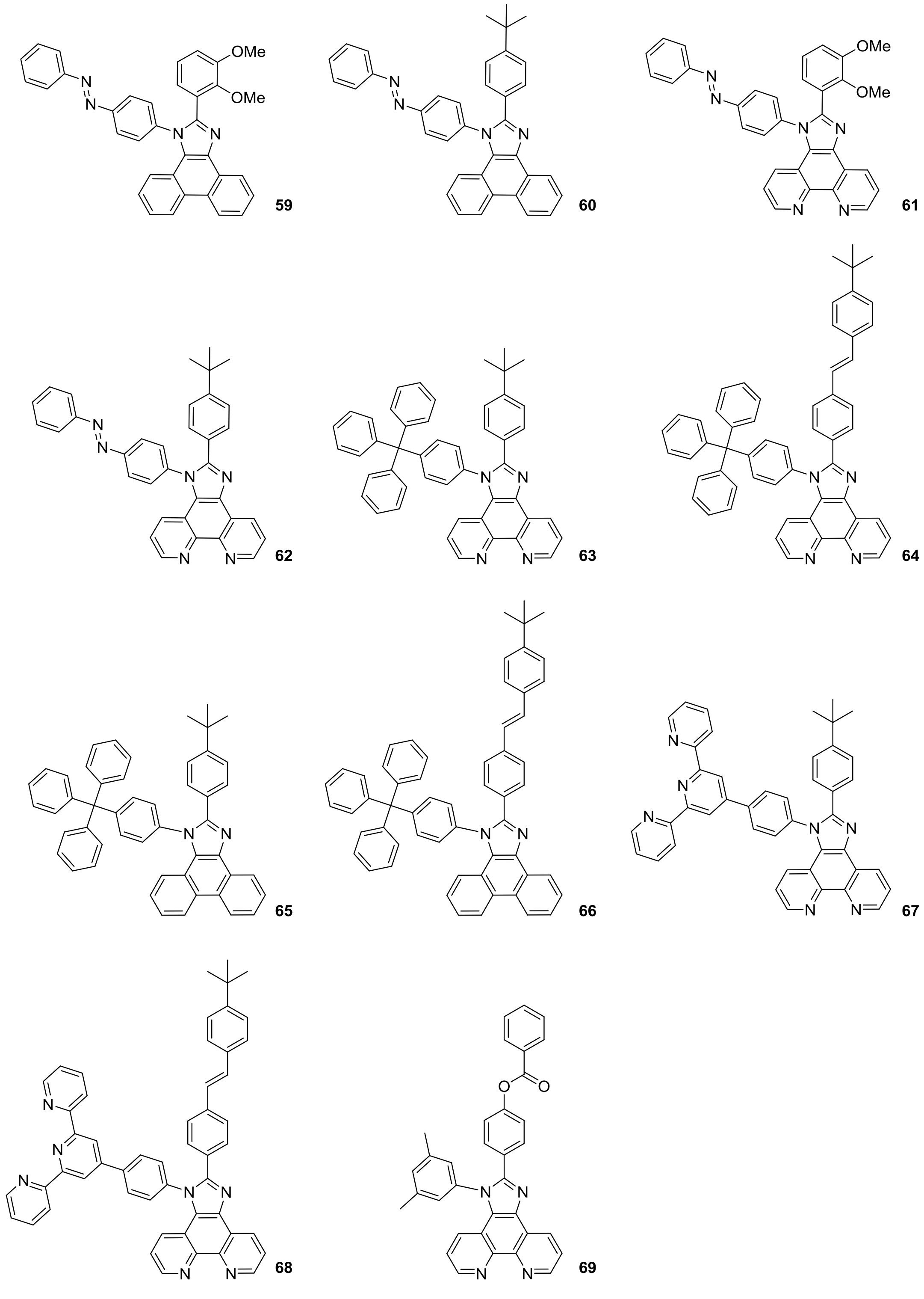

Figure 96: List of isolated ligands

This chapter presents a study of fused imidazo[4,5-*f*]-1,10-phenanthroline ligands and their subsequent reactions to form Re(I) complexes. The ligands have been designed with differing functional groups in order to explore changes in solubility, and also to investigate the effect of functional groups on the electronics and optical properties of the systems. In particular changes to the R′ group have been investigated. All ligands have been fully characterised using a variety of spectroscopic and analytical techniques, confirming the proposed structures in each case. All relevant supporting data is presented in the experimental section (4.10).

4.7.1 Synthesis of the ligands

The ligands were obtained using the same general synthetic methods as described in chapters 2 and 3. All ligands were isolated in poor-to-moderate yields (Table 22). The molecules which displayed the lowest yield were those containing a “terpy” or “trityl” phenyl R′ group. This is potentially a result of the differences in reactivity of the aniline starting materials, as the more electron withdrawing substituents on the aniline can alter the C-N bond length and the pKa of the aniline, and potentially its reactivity.[14] The ligands were typically isolated as off-white powders, with the exception of the ligands containing the azobenzene substituent, which were obtained as light orange powders. The ligands generally displayed good solubility in a range of common organic solvents, including $CHCl_3$, MeOH and MeCN.

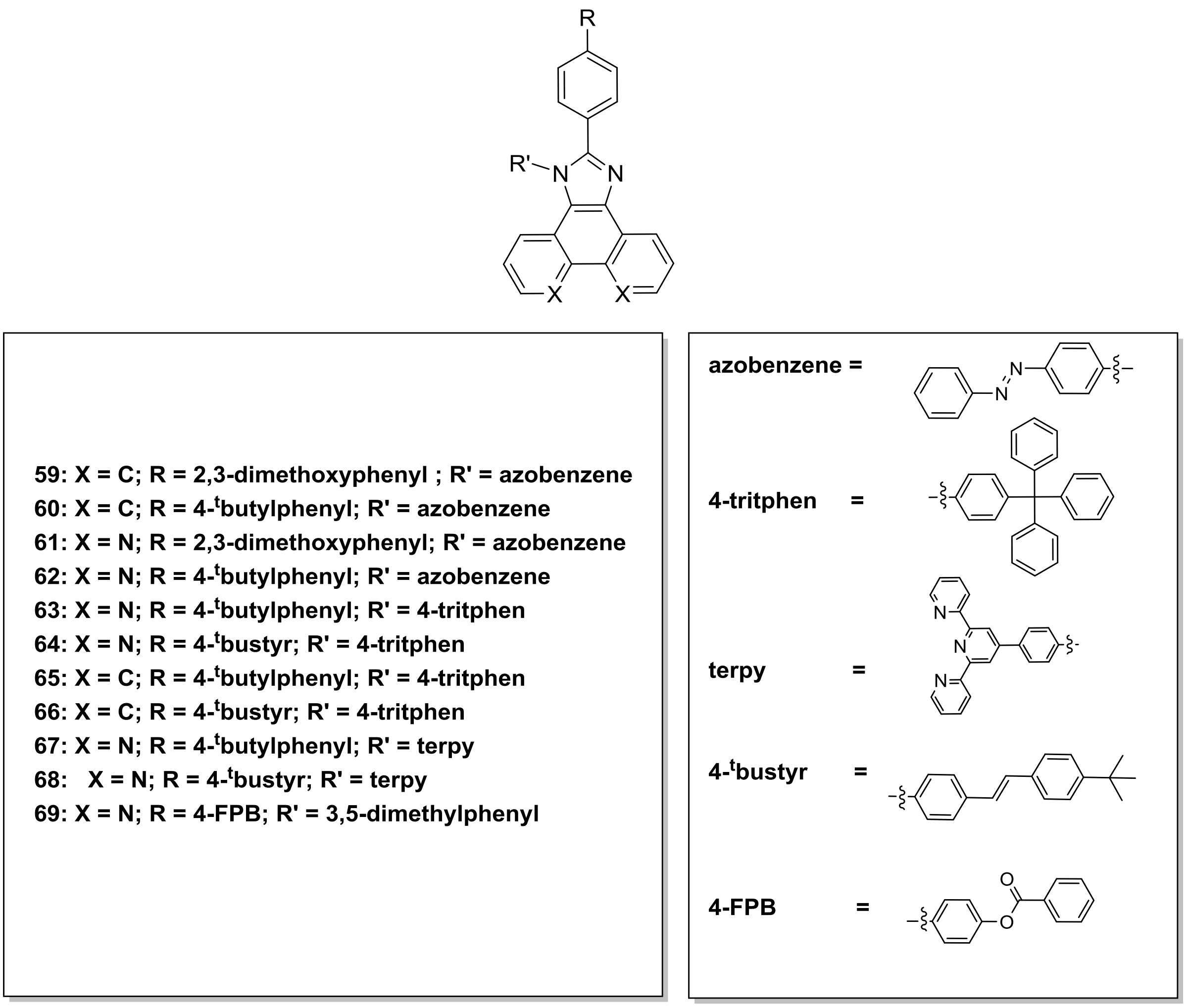

59: X = C; R = 2,3-dimethoxyphenyl ; R' = azobenzene
60: X = C; R = 4-^{t}butylphenyl; R' = azobenzene
61: X = N; R = 2,3-dimethoxyphenyl; R' = azobenzene
62: X = N; R = 4-^{t}butylphenyl; R' = azobenzene
63: X = N; R = 4-^{t}butylphenyl; R' = 4-tritphen
64: X = N; R = 4-^{t}bustyr; R' = 4-tritphen
65: X = C; R = 4-^{t}butylphenyl; R' = 4-tritphen
66: X = C; R = 4-^{t}bustyr; R' = 4-tritphen
67: X = N; R = 4-^{t}butylphenyl; R' = terpy
68: X = N; R = 4-^{t}bustyr; R' = terpy
69: X = N; R = 4-FPB; R' = 3,5-dimethylphenyl

Scheme 7: Formation of ligands **59-69**

Compound Number	Core	R	R′	Yield (%)
59	phenanthrene	2,3-dimethoxy	azo	65
60	phenanthrene	4-^{t}Bu	azo	75
61	1,10-phenanthroline	2,3-dimethoxy	azo	64
62	1,10-phenanthroline	4-^{t}Bu	azo	47
63	1,10-phenanthroline	4-^{t}Bu	4-tritphen	21
64	1,10-phenanthroline	4-^{t}Bustyr	4-tritphen	24
65	phenanthrene	4-^{t}Bu	4-tritphen	42
66	phenanthrene	4-^{t}Bustyr	4-tritphen	40
67	1,10-phenanthroline	4-^{t}Bu	terpy	19
68	1,10-phenanthroline	4-^{t}Bustyr	terpy	29
69	1,10-phenanthroline	4-FPB	3,5-diMe	54

Table 22: Isolated ligands and their respective yields

4.7.2 Characterisation of the ligands

All isolated compounds were investigated via ^{1}H and ^{13}C{^{1}H} NMR spectroscopy. The characteristics of the ^{1}H NMR spectra are similar to those described in chapter 2 and 3, with the loss of a benzaldehyde peak at ca. 10 ppm, and the observation of signals at ca. 8.5-9.5 ppm assigned to phenanthroline/phenanthrene aromatic protons. The incorporation of highly aromatic chromophores into these ligands have led to complicated ^{1}H NMR spectra, particularly in the aromatic region. Shown in Figure 97 is an example of a ^{1}H NMR spectrum of an azo-benzene containing lophine, **60**, which displayed signals between 8.70 and 8.95 ppm corresponding to the significantly deshielded protons of the phenanthrene moiety. Other aromatic protons associated with the molecule such as those of the azobenzene and ^{t}butylphenyl substituents are much less downfield shifted than the phenanthrene protons with signals observed between 7.25 and 8.20 ppm. A singlet is observed at 1.30 ppm which corresponds to the ^{t}butylphenyl aliphatic protons.

In comparison, the analogous 1,10-phenanthroline based compound **62** shows a more dramatic downfield shift of the 1,10-phenathroline protons, in the range of 9.05-9.25 ppm. This observation is true for all analogous phenanthrene/1,10-phenanthroline pairs, and is attributed to the increased electron withdrawing abilities of the diimines leading to greater deshielding of the protons and therefore a more pronounced downfield shift.

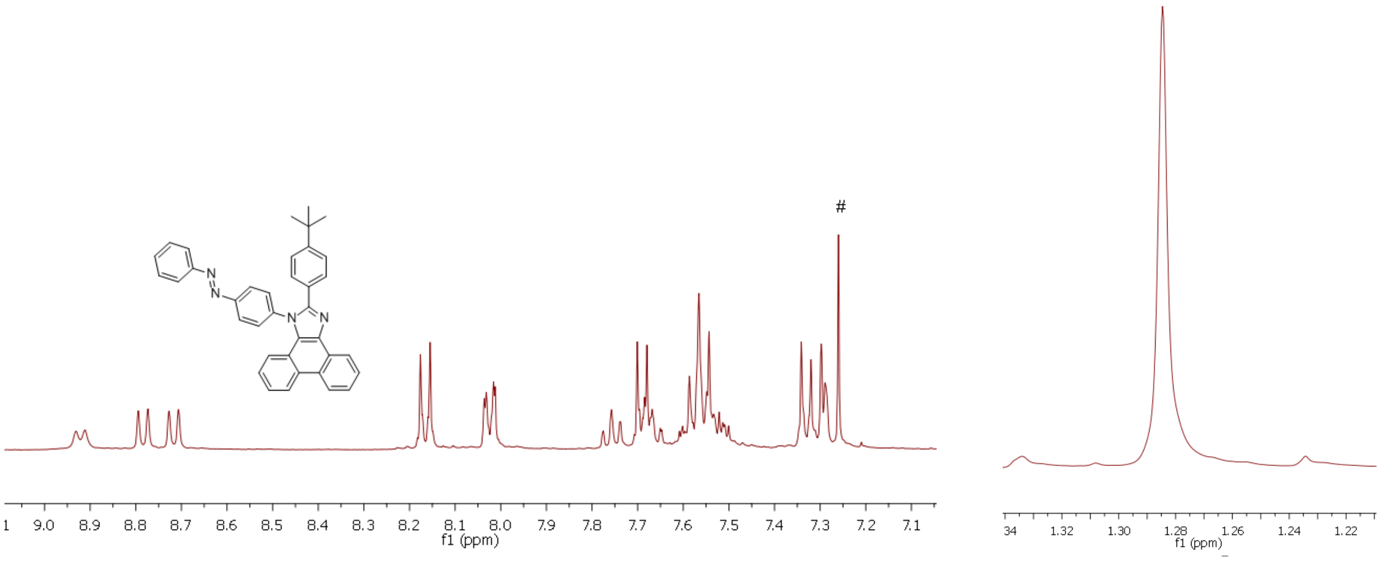

60 (aromatic region) # = $CDCl_3$

60 (aliphatic region)

Figure 97: ^{1}H NMR spectrum of **60**

Similarly, the ^{13}C{^{1}H} NMR spectra were very complicated in the aromatic region (for example compound **69** contains 32 aromatic carbon environments). Some of these environments were not observed in the spectrum (Figure 98), possibly due to weak signals of the quaternary carbons, or alternatively as a result of accidental degeneracy of the signals. For example, the carbonyl carbon of the ester group is usually observed in the region of 170-185 ppm however this is not observed in the spectrum. A strong signal was observed in the aliphatic region of the spectrum, corresponding to the dimethyl groups associated with the R′ substituent.

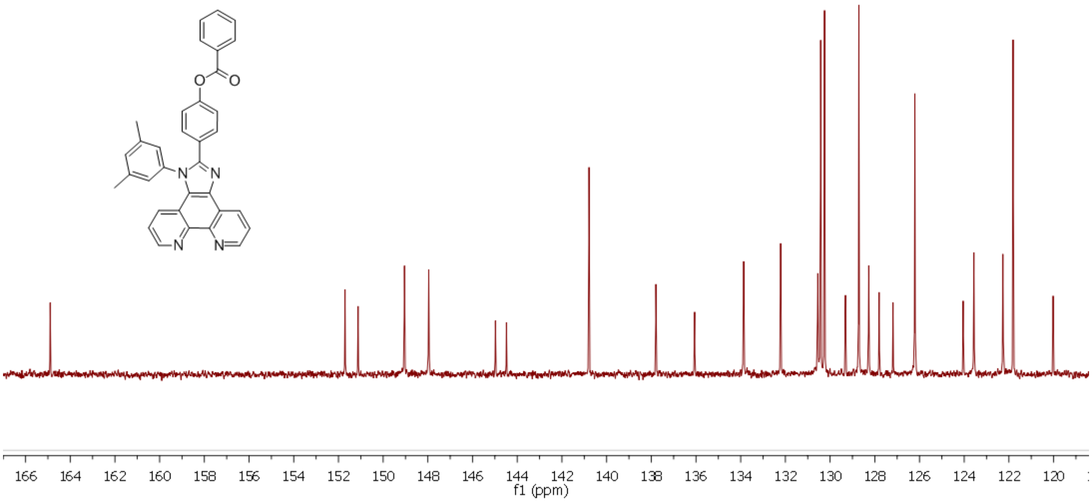

Figure 98: $^{13}C\{^{1}H\}$ NMR spectrum (aromatic region) of **69**

All other obtained chromophores also displayed similar complicated aromatic regions in the $^{13}C\{^{1}H\}$ NMR spectrum, with strong signals observed for carbons in the aliphatic region corresponding to alkyl groups associated with the apical R substituents in each case.

Additional data from high resolution electrospray mass spectrometry confirmed the presence of the protonated molecular ion in each case (Figure 99).

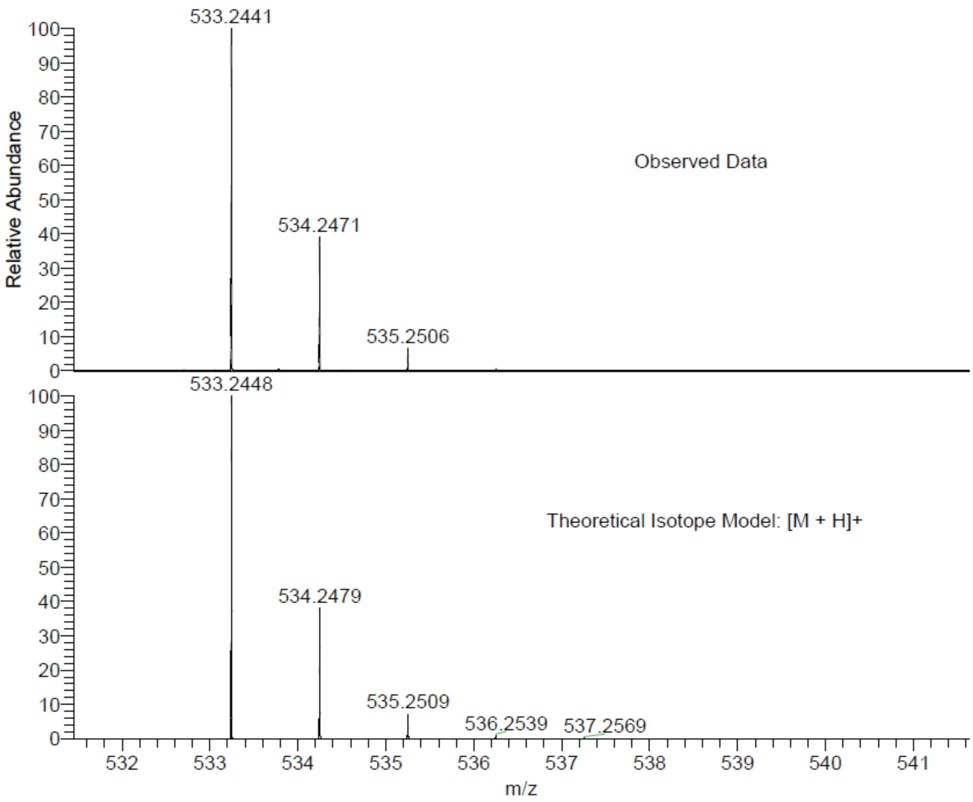

Figure 99: Observed mass spectrometry and theoretical isotope model for **62**

Infrared spectroscopic studies were also undertaken, using KBr plates for each chromophore, for which numerous peaks were observed. Each compound had a band at ≈ 2900 cm^{-1}, corresponding to an alkyl C-H stretch and numerous bands in the "fingerprint" region of the spectra. Compound **69** which contains an ester group revealed a C=O stretch at 1734 cm^{-1}, and C-O stretches at 1263 and 1060 cm^{-1}.

4.7.3 Electronic Absorption Spectroscopy of the ligands

Table 23 collects the electronic absorption data of compounds **59-69**.

Ligand	Core	R	R′	Absorption λ_{max}/nm (ε/M^{-1}cm^{-1})
59	phenanthrene	2,3-dimethoxy	azo	259 (90,700), 285 (39,500), 307 (36,700), 328 (sh)(31,800), 347 (sh)(23,600)
60	phenanthrene	4-^{t}Bu	azo	263 (137,800), 320 (sh) (45,300), 354(sh)(18,500)
61	1,10-phenanthroline	2,3-dimethoxy	azo	255 (54,000), 284 (48,000), 314 (sh) 33,200, 450 (3500)
62	1,10-phenanthroline	4-^{t}Bu	azo	276 (44,300), 299 (sh) (38,600), 433 (sh) (1100)
63	1,10-phenanthroline	4-^{t}Bu	4-tritphen	274 (54,600), 300 (sh)(30,400), 313 (sh)(23,600), 362 (2700)
64	1,10-phenathroline	4-^{t}Bustyr	4-tritphen	276 (101,100), 349 (38,700)
65	phenanthrene	4-^{t}Bu	4-tritphen	262 (69,500), 314 (20,200), 329 (19,100), 361 (8600)
66	phenanthrene	4-^{t}Bustyr	4-tritphen	260 (52,600), 306 (26,500), 350 (47,900), 365 (48,300)
67	1,10-phenanthroline	4-^{t}Bu	terpy	277 (97, 800), 315 (sh) (31,300)
68	1,10-phenanthroline	4-^{t}Bustyr	terpy	283 (61,500), 326 (sh)(37,800), 405 (sh) (6410)
69	1,10-phenanthroline	4-FPB	3,5-diMe	274 (117,400)

Table 23: Electronic Absorption data for **59-69**, obtained in $CHCl_3$

A large molar absorption coefficient was observed for the π→π* transition in each chromophore, with the largest absorption of each molecule ranging from 52,600 to 137,800 M^{-1}cm^{-1}. In general, it was observed that the phenanthrene containing molecules had slightly larger molar absorption coefficients than the 1,10-phenanthroline analogues.

59-62 showed that the incorporation of an azo moiety affected the electronic absorption spectra of the chromophores through observations of new peaks. For example, the azo-containing phenanthrene/phenanthroline pair of **59** and **61** showed significant vibronic structure for the broad peak between 275-375 nm, as both spectra show numerous peaks and shoulders. In comparison, other methoxy-containing ligands (detailed in section 3.8.1 in chapter 3) only show one significant peak (e.g. 260 nm for **46**) which indicates that the other absorptions may result from π→π* transitions involving the azobenzene moiety. Both **59** and **61** also show a broad shoulder at ≈ 425 nm, with a relatively low molar absorption coefficient, likely attributed to an n→π* transition.

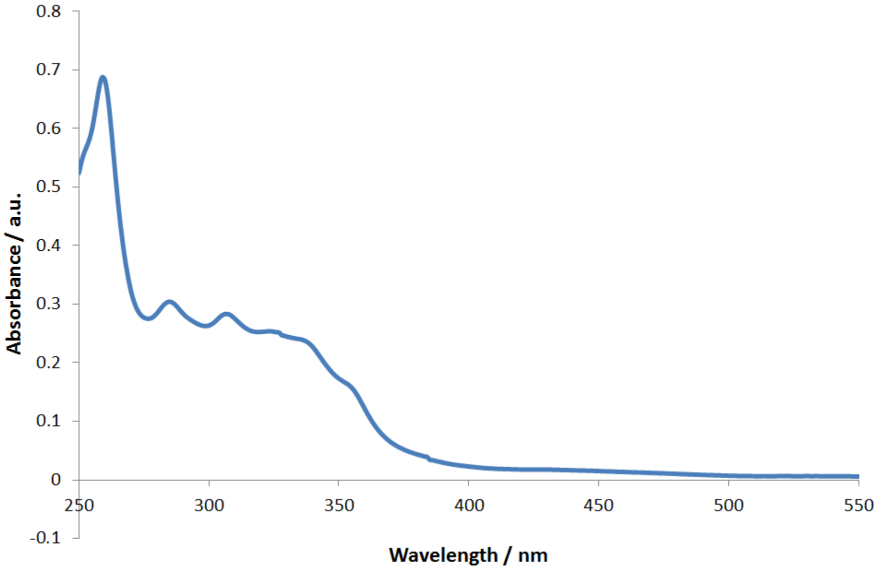

Figure 100: Absorption spectrum of **59** in $CHCl_3$ at 298K

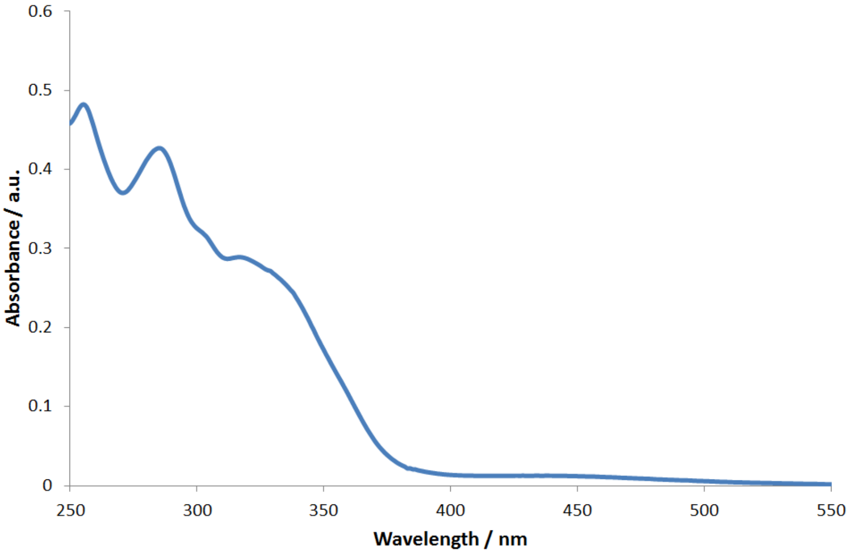

Figure 101: Absorption spectrum of **61** in $CHCl_3$ at 298K

Comparing the electronic absorption spectra of the chromophores according to their different R′ ("trityl", azo and "terpy") groups revealed differences in band positions and intensity. The azo-containing chromophores showed numerous bands, often at lower energy wavelengths, assigned to the localised π→π* transition of the azobenzene moiety. Contrastingly, the "trityl"-containing chromophores often displayed a single high-energy peak, and the "terpy"-containing chromophores displayed a single high energy and high intensity peak with lower intensity shoulders.

4.7.4 Luminescence properties of the ligands

All ligands were found to be emissive in solution, with small to moderate Stokes' shifts and relatively short lifetimes, attributed to fluorescence. Table 24 shows the λ_{ex} and λ_{em} of the ligands (**59-69**), along with their lifetimes, τ.

Ligand	Core	R	R′	λ_{ex} (nm)	λ_{em} (nm)	τ (ns)
59	phenanthrene	2,3-dimethoxy	azo	276	404	3.6
60	phenanthrene	4-^{t}Bu	azo	367	395	1.5
61	1,10-phenanthroline	2,3-dimethoxy	azo	273	414	3.6
62	1,10-phenanthroline	4-^{t}Bu	azo	391	415	3.7
63	1,10-phenanthroline	4-^{t}Bu	4-tritphen	346	414	3.7
64	1,10-phenathroline	4-^{t}Bustyr	4-tritphen	269	422	1.2
65	phenanthrene	4-^{t}Bu	4-tritphen	262	393	3.2
66	phenanthrene	4-^{t}Bustyr	4-tritphen	250	438	1.3
67	1,10-phenanthroline	4-^{t}Bu	terpy	350	415	3.6
68	1,10-phenanthroline	4-^{t}Bustyr	terpy	247	427	1.2
69	1,10-phenanthroline	4-FPB	3,5-diMe	367	410	2.6

Table 24: λ_{ex} (nm), λ_{em} (nm) and τ (ns) of ligands **59-69**

As observed in chapter 3, there was a significant difference in the emission spectra between phenanthrene and 1,10-phenanthroline-based chromophores. A higher energy emission was observed for the phenanthrene analogue in the compound couples **62/60** and **63/65**.

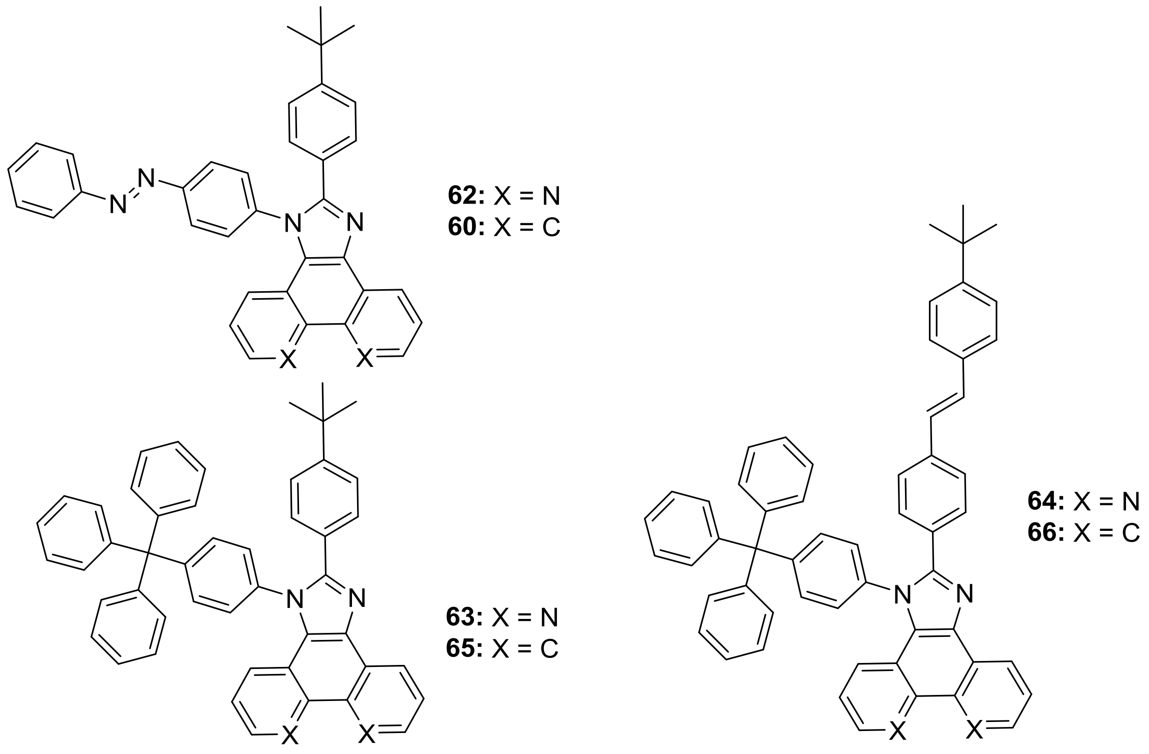

62: X = N
60: X = C

63: X = N
65: X = C

64: X = N
66: X = C

Figure 102: Molecular structures of isolated ligands

Contrastingly, the phenanthrene/1,10-phenanthroline analogues of **66**/**64** did not display the same tendencies. Of the two, the 1,10-phenanthroline-containing **64** displayed the highest energy emission (422 nm compared to 438 nm). This is likely a result of the inclusion of the 4-^{t}Bustyr moiety, which as was discussed in chapter 2, caused a red-shift in the emission spectrum compared to a chromophore containing a ^{t}butylphenyl apical R group. A red shift of the emission is observed for both **66** and **64** (Figure 103), however, chromophore **66** displayed the most pronounced red-shift and thus a lower energy emission.

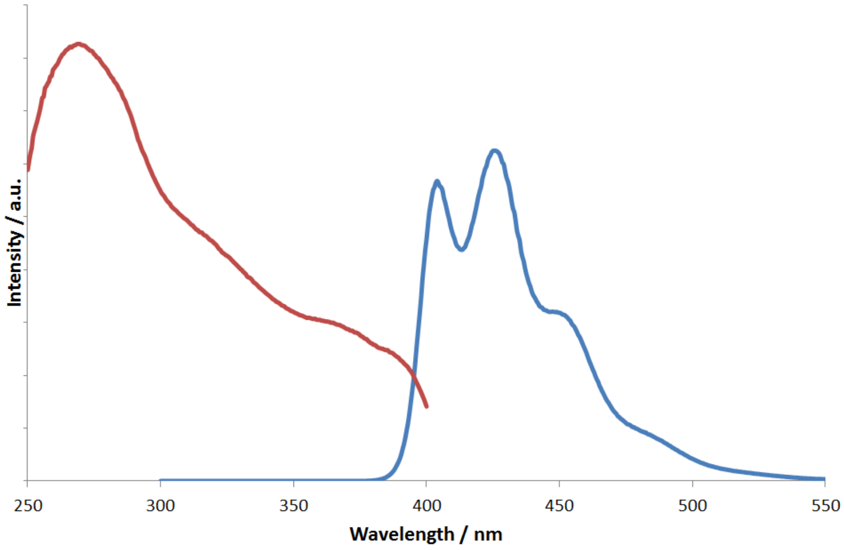

Figure 103: Excitation (red) and emission (blue) spectra of **64** in $CHCl_3$ at 298K

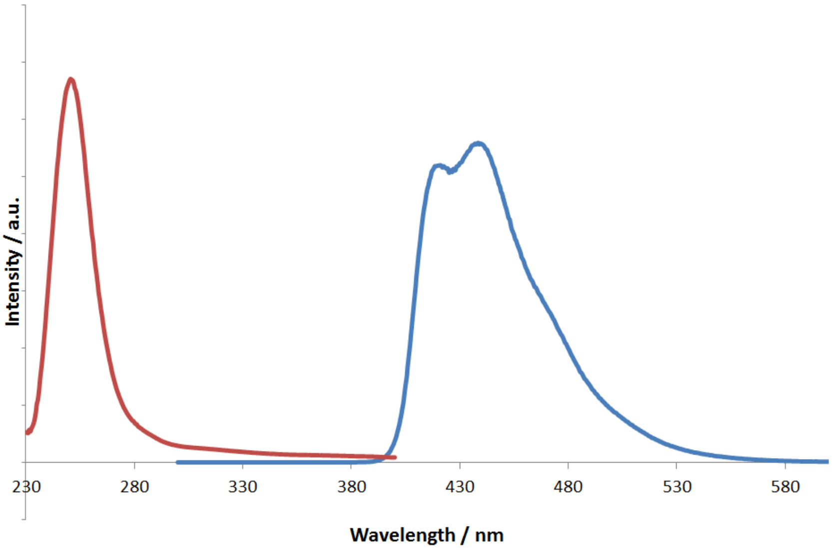

Figure 104: Excitation (red) and emission (blue) spectra of **66** in $CHCl_3$ at 298K

The three pairs of **65/66**, **67/68** and **63/64** are structurally similar with the only difference the apical R group is different where **65, 67** and **63** contain a 4-^{t}butylphenyl substituent while **66, 68** and **64** incorporate the 4-^{t}Bustyr substituent (Figure 105).

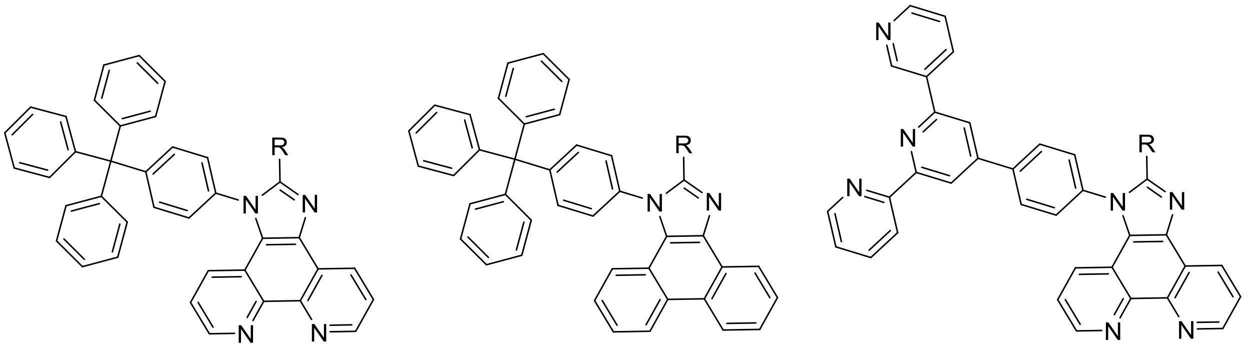

63: R = ^{t}butylphenyl
64: R = ^{t}bustyr

65: R = ^{t}butylphenyl
66: R = ^{t}bustyr

67: R = ^{t}butylphenyl
68:   R = ^{t}bustyr

Figure 105: Molecular structures of **63-68**

The effect on the emission was similar to that reported in chapter 2 (compounds **27** and **28**), with the inclusion of a 4-^{t}Bustyr substituent resulting in a red shift of between 10-40 nm, depending on the chromophore. Additionally, there was significant vibronic structure observed as a result of a rigid structural framework. Figure 106 shows the emission profiles of the trityl-containing **63** and its ^{t}Bustyr containing analogue **64,** the latter displaying pronounced vibronic structure and a moderate red shift in emission maximum.

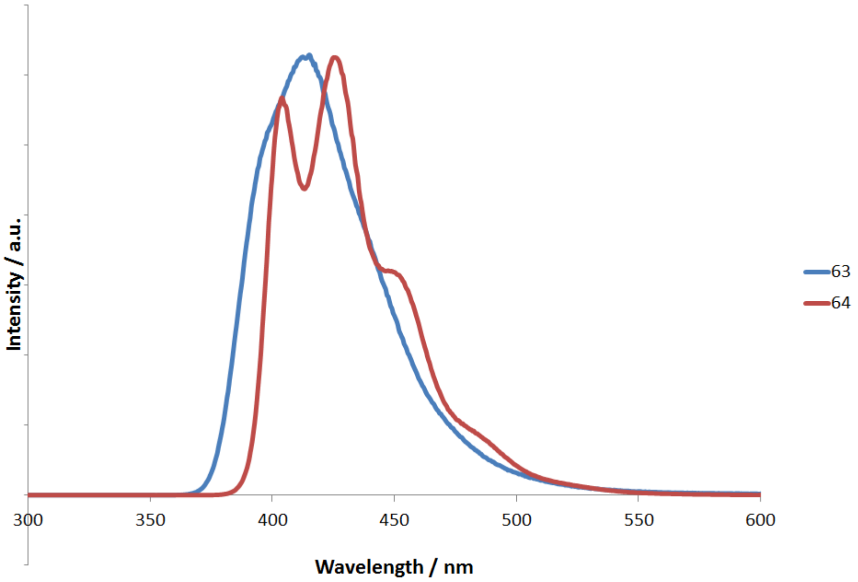

Figure 106: Normalised emission profiles of **63** (blue line) and **64** (red line) in $CHCl_3$ at 298K

As has been discussed previously, trityl groups have been used to prevent aggregation and self-quenching. This has led to a lophine species which is highly emissive in both solution and in the solid state. When the emission profile of **66** was obtained in $CHCl_3$, it displayed an emission wavelength at 438 nm (λ_{ex} = 250 nm), and when run in the solid state there was a slight red shift of emission to

448 nm (λ_{ex} = 281)(Figure 107). The slight variances in these values are likely a result of solute-solvent interactions between the sample and $CHCl_3$.

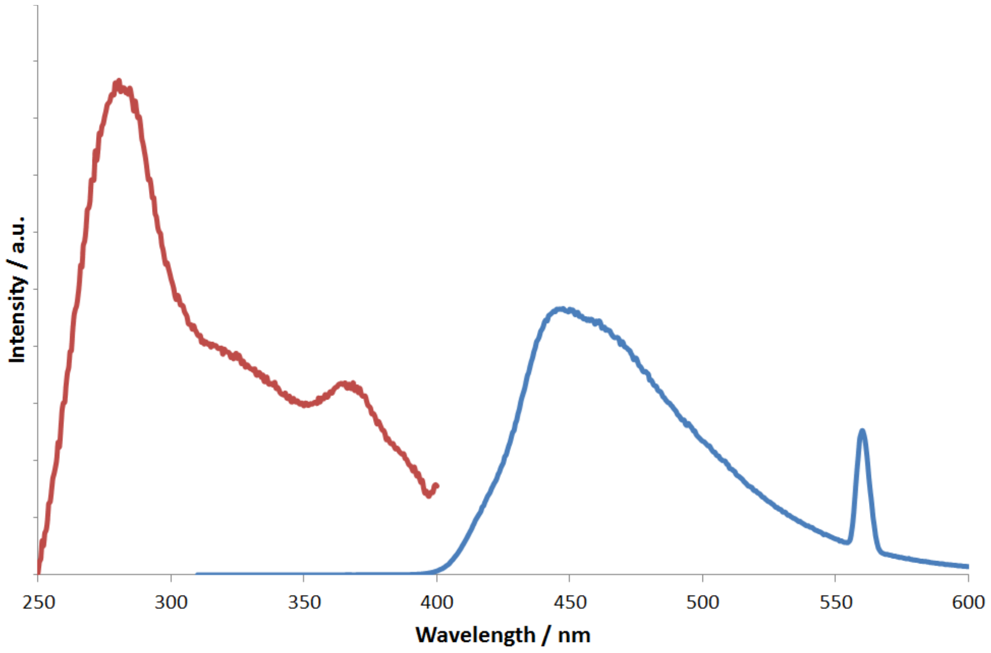

Figure 107: Solid state excitation (red) and emission (blue) profiles of **66**

4.8 Coordination chemistry of the ligands with Re(I)

The coordination chemistry of some of the 1,10-phenanthroline-containing ligands (**61**, **62**, **63**, **67** and **69**) was explored with Re(I), wherein heating stoichiometric equivalents of ligand and $[ReBr(CO)_5]$ in toluene for 24 hr produced the desired complexes, of the general formulation *fac*-$[ReBr(CO)_3(N^\wedge N)]$ (where N^N = **61**, **62**, **63**, **67** and **69**), as powdered solids in moderate to good yields (Figure 108).

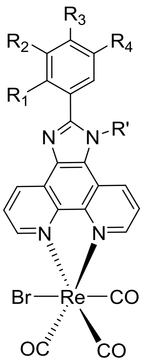

$[ReBr(CO)_3$(61)] R_1= R_2= OMe.R_3=R_4 = H. R' = azo

$[ReBr(CO)_3$(62)] R_1= R_2=R_4=H. R_3 = ^{t}Bu. R' = azo

$[ReBr(CO)_3$(63)] R_1=R_2=R_4 =H. R_3=^{t}Bu. R' = tritylphenyl

$[ReBr(CO)_3$(67)] R_1=R_2=R_4 =H. R_3=^{t}Bu. R' = terpy

$[ReBr(CO)_3$(69)] R_1=R_2=R_4=H. R_3=Benzoate R' = 3,5-diMe-Ph

Figure 108: Formation of complexes of the type $[Re(CO)_3Br(N^\wedge N)]$

The complexes often showed slightly diminished solubility in $CHCl_3$ and methanol compared to the free ligands, with the terpy functionalised complex $[ReBr(CO)_3$(**67**)] being poorly soluble in most organic solvents.

4.8.1 Characterisation of the complexes

All isolated compounds were investigated via ^{1}H and $^{13}C\{^{1}H\}$ NMR spectroscopy where solubility permitted. In each instance successful coordination of the ligand was evident by significant downfield shifted resonances of the phenanthroline protons, similar to that observed in other diimine complexes of rhenium tricarbonyl.[15] Comparison of **69** and [ReBr(CO)$_3$(**69**)] (Figure 109), showed the most significant shift was observed for the phenanthroline protons (from 9.0-9.2 to 9.25-9.4 ppm) with smaller shifts observed for other aromatic protons. The $^{13}C\{^{1}H\}$ NMR spectra often showed three small peaks at ≈ 190 ppm corresponding to the carbonyl carbons. Slight changes were observed for the resonances in the $^{13}C\{^{1}H\}$ NMR spectra of the Re complexes compared to the corresponding free ligand.

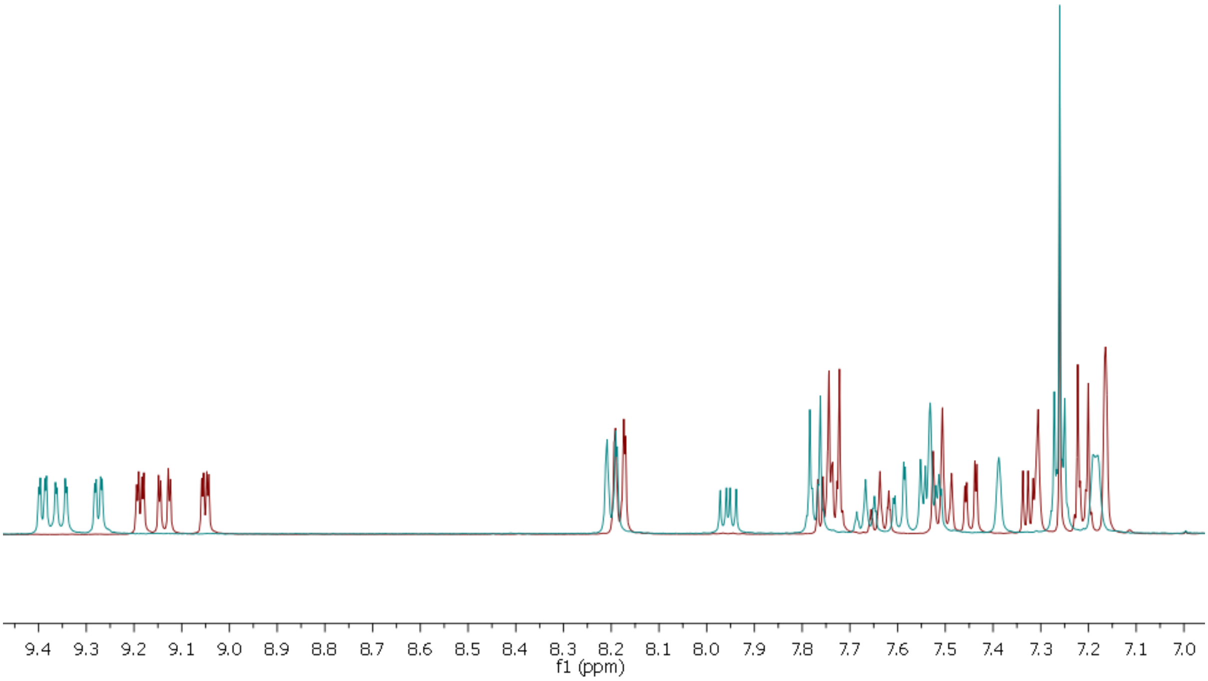

Figure 109: ^{1}H NMR spectra of the aromatic region of **69** (red) and [ReBr(CO)$_3$(**69**)] (blue) in $CDCl_3$ at 298K

Ligand **67** (Figure 110) contained two potential coordination sites for the rhenium metal, the phenanthroline moiety and the terpyridine moiety. As was described in the introduction, reaction temperatures must be kept at a very high temperature for a long period of time to form the tridentate terpyridine complex, therefore the most likely coordination about the rhenium metal was either a bidentate coordination of the terpyridine substituent or bidentate coordination of the phenanthroline moiety.

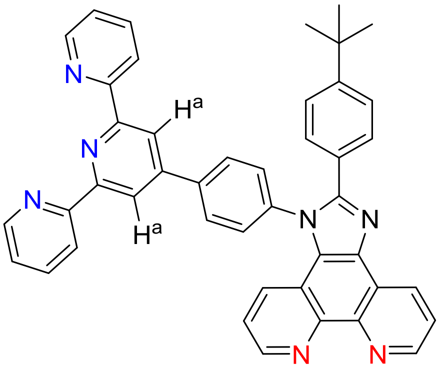

Figure 110: Molecular structure of **67**

The ^{1}H NMR spectrum of the rhenium coordinated complex [ReBr(CO)$_3$(**67**)] was obtained in DMSO due to lack of solubility in other solvents. Comparing the ^{1}H NMR spectra of both the free ligand and the coordinated complex showed significant shifts in some of the peaks which indicated coordination of the rhenium metal. The peaks that showed the furthest downfield shift were those associated with the phenanthroline protons of the ligand. This suggested that the highly deshielding rhenium atom was in close proximity to these hydrogens. The most easily identifiable signal corresponding to the terpyridine substituent was a singlet that arises in the free ligand at 8.87 ppm in DMSO (denoted by H^a in Figure 110). This signal was not shifted at all upon coordination to rhenium, indicating that the protons were not influenced by the deshielding effects of a nearby rhenium metal. The presence of only one signal for the terpyridine and for the aliphatic ^{t}butyl group of the apical R group indicated a single species was isolated which was coordinated in one site to the ligand.

All complexes were examined via solid state IR spectroscopy and commonly showed either three distinct bands or two, one of which was significantly broadened. Complex [ReBr(CO)$_3$(**69**)] **,** which contains the benzoate group displayed the characteristic peaks that were observed in the free ligand, with the C=O group visible at around 1700 cm^{-1} and the C-O stretches visible as strong peaks at 1200 and 1057 cm^{-1}.

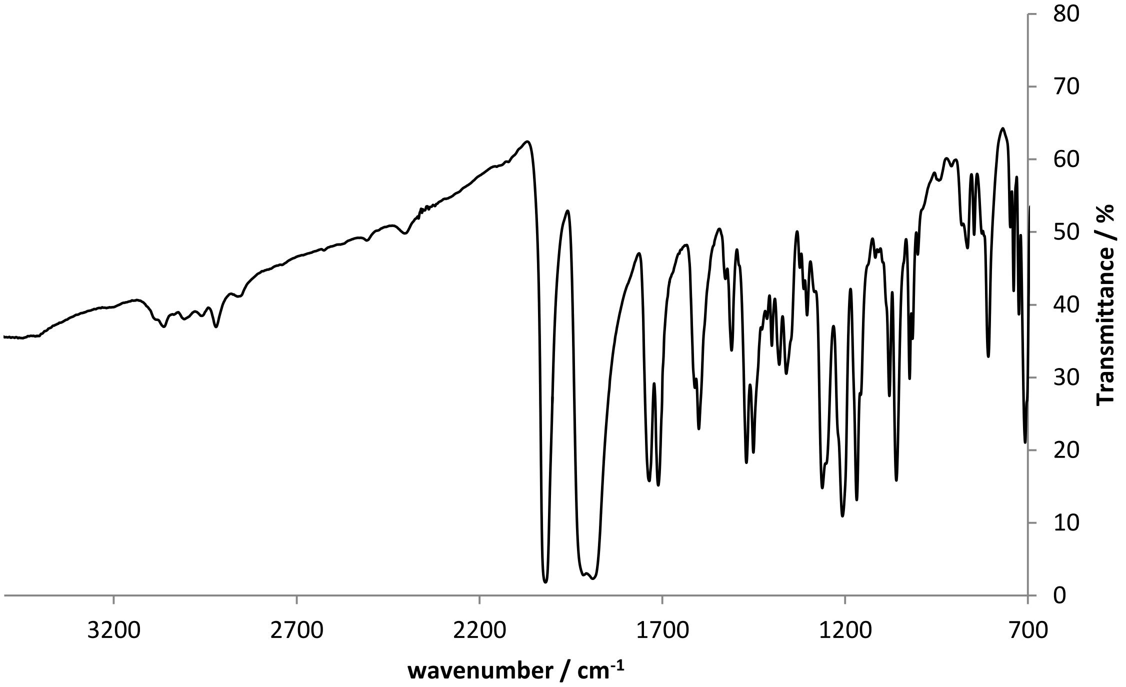

Figure 111: IR spectrum of [ReBr(CO_3)(**69**)]

The IR spectrum of the rhenium coordinated [ReBr$(CO)_3$(**67**)] showed two bands at 2020 cm^{-1} and 1900 cm^{-1} (the latter of which was split in two), which indicated that there was only one coordinated rhenium tricarbonyl core, otherwise other peaks would have become visible. Only two bands would have been apparent if the terpyridine ligand was acting as a tridentate ligand. All the evidence collected together indicates that a rhenium tricarbonyl core was present, and that it was coordinated to the phenanthroline moiety.

Additional data from high resolution electrospray mass spectrometry confirmed the presence of the protonated molecular ion in each case (Figure 112). The isotope pattern is consistent with that of a rhenium containing molecule.

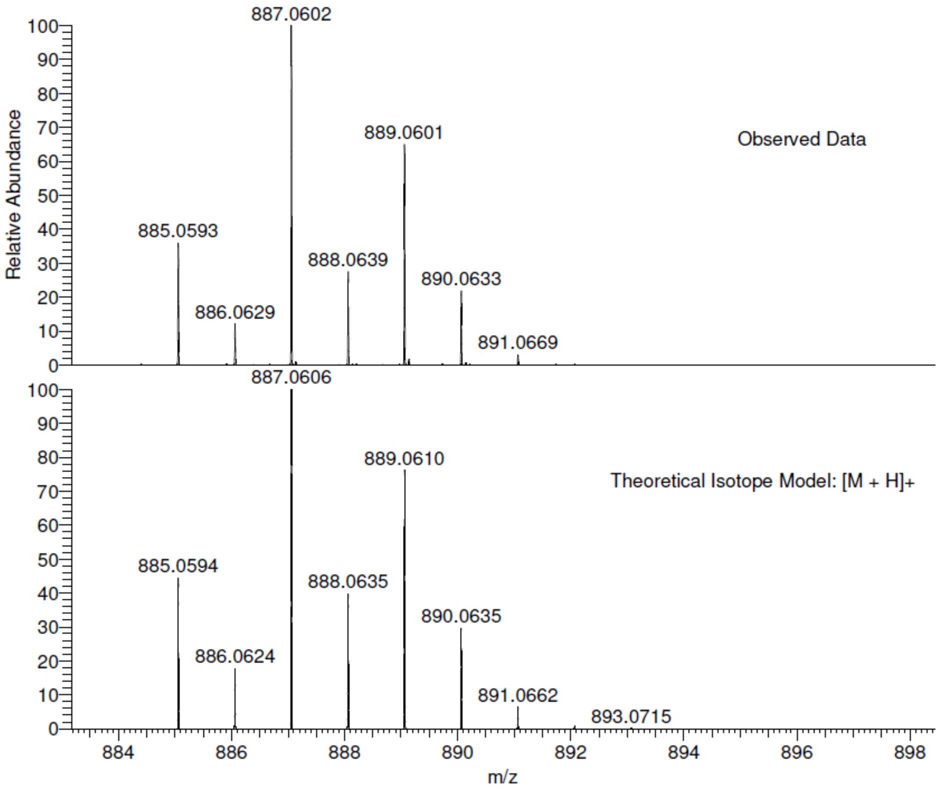

Figure 112: Observed and theoretical mass spectrometry for [ReBr(CO)$_3$(**61**)]

4.8.2 Structural Studies

Single crystal X-ray diffraction studies were undertaken on two complexes, ***fac*-[ReBr(CO)$_3$(62)]**, and ***fac*-[ReBr(CO)$_3$(69)]**. Suitable crystals were obtained by slow diffusion of hexane into toluene over the course of 72hrs. ***fac*-[ReBr(CO)$_3$(62)]** crystallised as a toluene solvate in P-1 symmetry, while ***fac*-[ReBr(CO)$_3$(69)]** crystallised as a toluene disolvate in P-1 symmetry. The parameters associated with the data collection for ***fac*-[ReBr(CO)$_3$(62)]** are shown in Table 25, and Figure 113 illustrates the structure of ***fac*-[ReBr(CO)$_3$(62)]** in the solid-state with selected bond length and angle data. The structure of ***fac*-[ReBr(CO)$_3$(62)]** displayed octahedral coordination geometry as expected for a d^6 Re(I) complex, with **62** chelating *trans* to two carbonyl ligands, with the third CO ligand and bromide donors occupying axial positions. Bond lengths and angles were typical for a {ReBr(CO)$_3$} complex of a chelating diimine.[16,17] As with the structures described in chapters 2 and 3, the imidazo[4,5-*f*]-1,10-phenanthroline core of the ligand framework is essentially co-planar with the 'Re(CO)$_2$' fragment of the complex. The apical *p*-^{t}butylphenyl substituent deviates from planarity by a torsion angle of 36.02°. The azobenzene sidearm is observed in its *trans*-conformation and is effectively orthogonal to the plane of the rest of the molecule with a torsion angle of 77.26°.

Table 25**:** Crystal data and structure refinement details of $ReBrCO_3$(**62**)

Empirical formula	$C_{76}H_{56}Br_2N_{12}O_6Re_2$	
Formula weight	1765.55	
Temperature	100(2) K	
Wavelength	0.71075 Å	
Crystal system	Triclinic	
Space group	P–1	
Unit cell dimensions	a = 11.5396(8) Å	α = 107.654(9)°
	b = 13.0071(9) Å	β = 110.170(6)°
	c = 14.2545(12) Å	γ = 92.687(7)°
Volume	1886.1(2) $Å^3$	
Z	1	
Density (calculated)	1.554 Mg / m^3	
Absorption coefficient	4.323 mm^{-1}	
F(000)	864	
Crystal	Chip; Yellow	
Crystal size	0.05 × 0.04 × 0.01 mm^3	
θ range for data collection	2.93 – 27.48°	
Index ranges	$-14 \leq h \leq 14$, $-16 \leq k \leq 16$, $-18 \leq l \leq 18$	
Reflections collected	24100	
Independent reflections	8559 [R_{int} = 0.0596]	
Completeness to θ = 27.48°	99.1 %	
Absorption correction	Semi–empirical from equivalents	
Max. and min. transmission	0.9580 and 0.8129	
Refinement method	Full-matrix least-squares on F^2	
Data / restraints / parameters	8559 / 131 / 484	
Goodness-of-fit on F^2	1.028	
Final R indices [$F^2 > 2\sigma(F^2)$]	$R1$ = 0.0522, $wR2$ = 0.1150	
R indices (all data)	$R1$ = 0.0787, $wR2$ = 0.1270	
Largest diff. peak and hole	1.380 and –0.947 e $Å^{-3}$	

Diffractometer: *Rigaku AFC12* goniometer equipped with an enhanced sensitivity (HG) *Saturn724+* detector mounted at the window of an *FR-E+ SuperBright* molybdenum rotating anode generator with VHF *Varimax* optics (70µm focus). **Cell determination and data collection**: *CrystalClear-SM Expert 2.0 r11* (Rigaku, 2011). **Data reduction, cell refinement and absorption correction**: *CrystalClear-SM Expert 2.0 r13* (Rigaku, 2011). **Structure solution**: *SHELXS97* (Sheldrick, G.M. (2008). Acta Cryst. A64, 112-122). **Structure refinement**: *SHELXL97* (Sheldrick, G.M. (2008). Acta Cryst. A64, 112-122). **Graphics:** *OLEX2* (Dolomanov, O. V., Bourhis, L. J., Gildea, R. J., Howard, J. A. K. & Puschmann, H. (2009). J. Appl. Cryst. 42, 339-341).

Special details:

Crystal Structure contains one toluene molecule disordered over inversion centre. It has been modelled with PART -1 command in SHELXL.

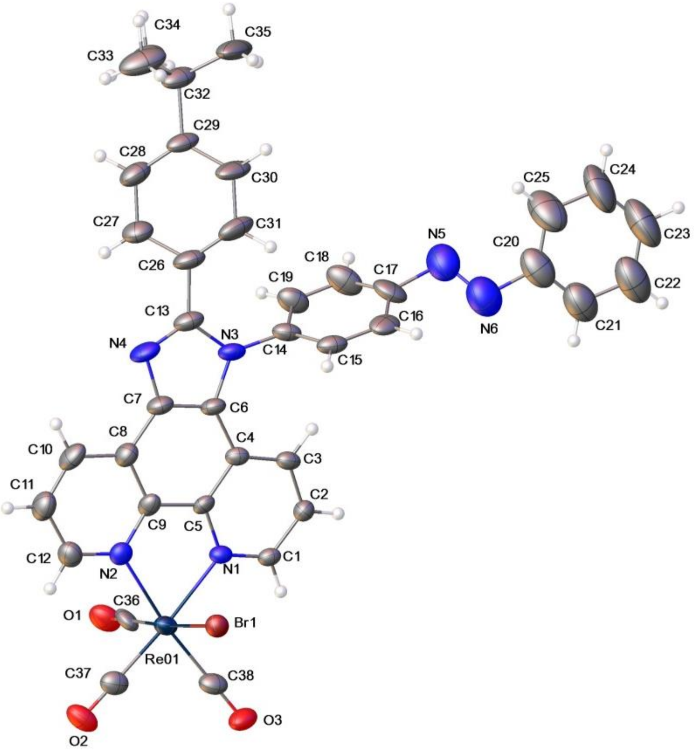

Figure 113:Ortep3 plot of complex **_fac_-[ReBr(CO)$_3$(62)]**. Ellipsoids are drawn at 50% probability. Selected data - bond lengths (Å): C36–Re01, 1.957(9); C37–Re01, 1.914(8); C38–Re01, 1.918(8); N1–Re01, 2.189(5); N2–Re01, 2.181(5); Br1–Re01, 2.6149(8). Bond angles(°): O2–C37–Re01, 178.1(7); O3–C38–Re01, 178.1(7); C1–N1–Re01, 125.5(4); C5–N1–Re01, 115.3(4); C12–N2–Re01, 125.8(5); C9–N2–Re01, 115.0(4); C37–Re01–C38, 87.2(3); C37–Re01–C36, 88.7(3); C38–Re01–C36, 91.6(3); C37–Re01–N2, 98.8(3); C38–Re01–N2, 173.0(3); C36–Re01–N2, 92.1(3); C37–Re01–N1, 173.7(3); C38–Re01–N1, 98.3(3); C36–Re01–N1, 94.2(2); N2–Re01–N1, 75.5(2); C37–Re01–Br1, 93.8(2); C38–Re01–Br1, 91.4(2); C36–Re01–Br1, 176.2(2); N2–Re01–Br1, 84.65(14); N1–Re01–Br1, 83.06(14);

The parameters associated with the data collection for **_fac_-[ReBr(CO)$_3$(69)]** are shown in Table 26, and Figure 114 illustrates the structure of **_fac_-[ReBr(CO)$_3$(69)]** in the solid-state with selected bond length and angle data. The structure showed similar structural characteristics to **_fac_-[ReBr(CO)$_3$(62)]** with the apical formyl phenyl benzoate displaying a small torsion angle (12.46°) and the R′ group 3,5-dimethylphenyl showing a larger torsion angle of 71.80°. The smaller torsion angle displayed by the R group of **_fac_-[ReBr(CO)$_3$(69)]** compared to **[ReBr(CO)$_3$(62)]** implying that there may be less steric hindrance from the R′ group resulting in less deviation from planarity.

Table 26: Crystal data and structure refinement details.$ReBr(CO)_3$(**69**)

Empirical formula	$C_{47.50}H_{36}BrN_4O_5Re$	
Formula weight	1008.91	
Temperature	100(2) K	
Wavelength	0.71075 Å	
Crystal system	Triclinic	
Space group	$P-1$	
Unit cell dimensions	a = 12.3462(9) Å	α = 73.929(5)°
	b = 13.2725(9) Å	β = 64.950(5)°
	c = 14.2352(10) Å	γ = 76.725(6)°
Volume	2013.7(2) Å^3	
Z	2	
Density (calculated)	1.664 Mg / m^3	
Absorption coefficient	4.063 mm^{-1}	
F(000)	998	
Crystal	Fragment; Yellow	
Crystal size	$0.06 \times 0.04 \times 0.01$ mm^3	
θ range for data collection	2.99 – 27.48°	
Index ranges	$-15 \le h \le 16, -17 \le k \le 17, -18 \le l \le 17$	
Reflections collected	26424	
Independent reflections	9188 [R_{int} = 0.0437]	
Completeness to θ = 27.48°	99.5 %	
Absorption correction	Semi–empirical from equivalents	
Max. and min. transmission	0.9605 and 0.7926	
Refinement method	Full-matrix least-squares on F^2	
Data / restraints / parameters	9188 / 6 / 550	
Goodness-of-fit on F^2	1.102	
Final R indices [$F^2 > 2\sigma(F^2)$]	$R1$ = 0.0422, $wR2$ = 0.1031	
R indices (all data)	$R1$ = 0.0520, $wR2$ = 0.1076	
Largest diff. peak and hole	3.729 and –1.238 e Å^{-3}	

Diffractometer: *Rigaku AFC12* goniometer equipped with an enhanced sensitivity (HG) *Saturn724+* detector mounted at the window of an *FR-E+ SuperBright* molybdenum rotating anode generator with VHF *Varimax* optics (70µm focus). **Cell determination and data collection**: *CrystalClear-SM Expert 2.0 r11* (Rigaku, 2011). **Data reduction, cell refinement and absorption correction**: *CrystalClear-SM Expert 2.0 r13* (Rigaku, 2011). **Structure solution**: *SHELXS97* (Sheldrick, G.M. (2008). Acta Cryst. A64, 112-122). **Structure refinement**: *SHELXL97* (Sheldrick, G.M. (2008). Acta Cryst. A64, 112-122). **Graphics:** *OLEX2* (Dolomanov, O. V., Bourhis, L. J., Gildea, R. J., Howard, J. A. K. & Puschmann, H. (2009). J. Appl. Cryst. 42, 339-341).

Special details:

Crystal structure contains two solvent molecules (toluene). One of these is disordered over centre of inversion and was modelled as 50% occupied over two equivalent sites with PART -1 instruction. AFIX 66 was used to maintain sensible planar geometry.

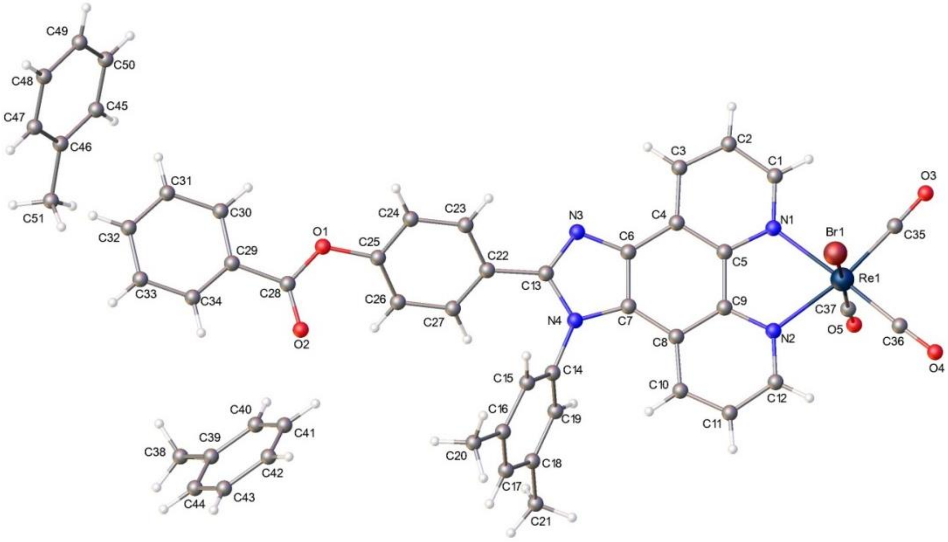

Figure 114:Ortep3 plot of complex ***fac*-[ReBr(CO)$_3$(69)]**. Ellipsoids are drawn at 50% probability. Selected data - bond lengths (Å): C35–Re1, 1.923(5); C36–Re1, 1.916(5); C37–Re1, 2.014(6); N1–Re1, 2.175(4); N2–Re1, 2.192(4); Br1–Re1, 2.6058(6); O3–C35–Re1, 177.8(5); O4–C36–Re1, 177.8(5); O5–C37–Re1, 174.3(5); C1–N1–Re1,125.6(3); C5–N1–Re1, 115.8(3); C12–N2–Re1, 125.5(3); C9–N2–Re1, 115.7(3); C36–Re1–C35, 87.9(2); C36–Re1–C37, 88.1(2); C35–Re1–C37, 90.4(2); C36–Re1–N1, 172.38(19); C35–Re1–N1, 96.04(18); C37–Re1–N1, 98.35(17); C36–Re1–N2, 100.93(18); C35–Re1–N2, 171.20(18); C37–Re1–N2, 90.30(17); N1–Re1–N2, 75.17(14); C36–Re1–Br1, 86.99(17); C35–Re1–Br1, 94.50(17); C37–Re1–Br1, 172.93(14); N1–Re1–Br1, 86.19(10); N2–Re1–Br1, 85.61(11);

4.8.3 Electronic Absorption Spectroscopy of the complexes

The electronic absorption spectra were obtained for each of the isolated [ReBr(CO)$_3$(N^N)] complexes and the results are displayed in Table 27, along with the excitation and emission wavelengths, and lifetimes.

Complex	R	R′	λ_{max}(nm)	λ_{ex} (nm)	λ_{em} (nm)	τ (ns)
ReBr(CO)$_3$(**61**)	2,3-dimethoxy	azo	260 (70,900), 301 (47,700), 330 (sh)(35,000), 420 (6600)	284	583	197
ReBr(CO)$_3$(**62**)	4-^{t}Bu	azo	282 (62,300), 306 (54,000), 425 (7123)	380	558	269
ReBr(CO)$_3$(**63**)	4-^{t}Bu	4-tritphen	276 (208,200), 346(sh)(12,400), 421 (7500)	371	585	164
ReBr(CO)$_3$(**67**)	4-^{t}Bu	terpy	278 (94,000), 338 (sh)(16,900), 420 (8500)	271	585	169
ReBr(CO)$_3$(**69**)	4-FPB	3,5-diMe	277 (67,000), 299 (sh) (43,800), 336 (sh) (14,400), 422 (6300)	380	583	162

Table 27: Electronic absorption and luminescence data for Re complexes

All complexes displayed high energy absorptions (≈ 270 nm) which were assigned to ligand-based π→π* transitions expected of an extended π framework. Other weaker bands were observed at lower energy for some of the complexes (≈ 350 nm) which were tentatively assigned to intra-molecular n→π* transitions. A band was also observed at >400 nm for each complex, which corresponds to a ^{1}MLCT (Re(d)→π^*) transition. It should be noted that the azobenzene-containing ligands also showed broad, weak absorption band in this region which was obscured by the new ^{1}MLCT transition. The band positions assigned to the ligand based π→π* transitions did not appear to be affected in any of the complexes. The rhenium complexes of [ReBr(CO)$_3$(**61**)] and [ReBr(CO)$_3$(**62**)] and showed a slight bathochromic shift upon coordination (shifting ≈ 5 nm), which is within error and as such cannot be reliably assigned a bathochromic shift.

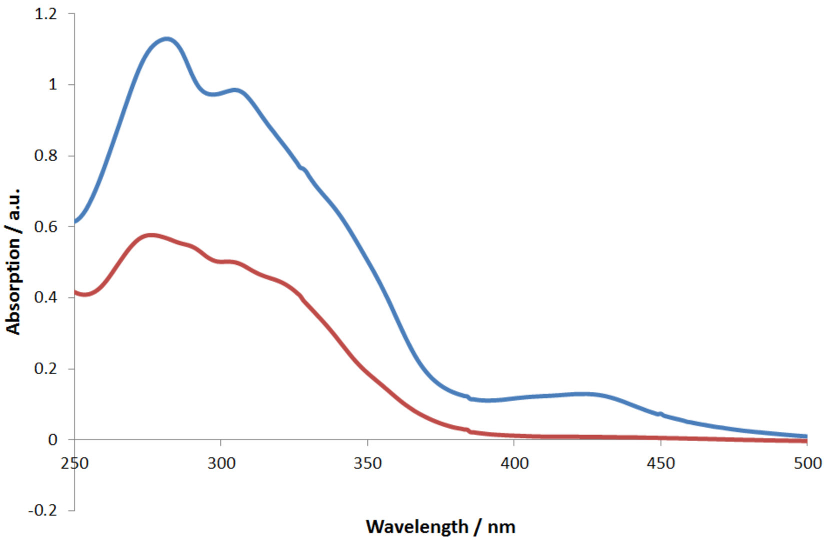

Figure 115: Electronic absorption spectra of **62** (red line) and [ReBr(CO)$_3$(**62**)] (blue line) in CHCl$_3$ at 298K

4.8.4 Luminescence studies of the complexes

All complexes were found to be emissive, with complexes [ReBr(CO)$_3$(**61**)], [ReBr(CO)$_3$(**63**)], [ReBr(CO)$_3$(**67**)], and [ReBr(CO)$_3$(**69**)] all emitting at ≈ 585 nm. Each of the complexes displayed a relatively long lifetime emission between 150-200 ns and a large Stokes' shift. Taken together these characteristics were attributed to a ^{3}MLCT. Figure 116 presents the excitation/emission spectrum of complex [ReBr(CO)$_3$(**63**)].

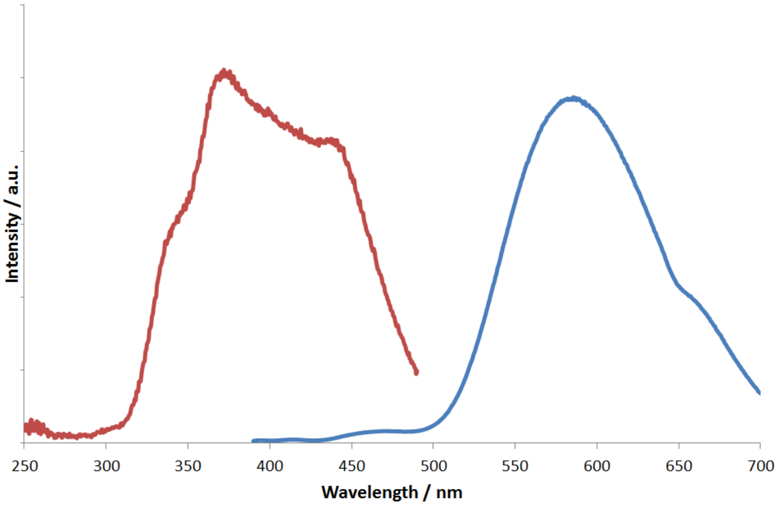

Figure 116: Excitation (red) and emission (blue) spectra of [ReBr(CO)$_3$(**63**)] in CHCl$_3$ at 298K

In comparison to the other complexes, [ReBr(CO)$_3$(**62**)] displayed anomalous emission spectra. The emission wavelength of the complex was blue-shifted compared to the complexes discussed previously (558 nm), together with the longest lifetime (269 ns) consistent with a larger energy gap.

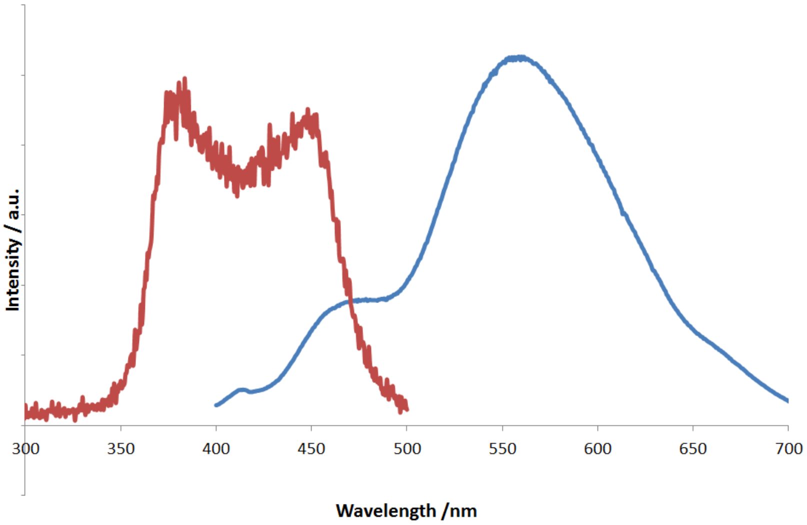

Figure 117: Excitation (red) and emission (blue) spectra of complex [ReBr(CO)$_3$(**62**)]

4.9 Conclusions

In conclusion a series of substituted imidazole[4,5-*f*]-1,10-phenanthroline derivatives and their Re(I) carbonyl complexes have been isolated and fully characterised, and their optical properties investigated. Substituents incorporated include an azo-benzene moiety, the terpyridine moiety which may potentially provide an additional binding site, and the “trityl” moiety, which due to its steric bulk leads to a decrease in aggregation in solution and therefore a reduction in self-quenching which also resulted in solid-sate luminescence. All compounds were found to be highly emissive and Re(I) complexes of the ligand showed increased Stokes’ shifts and also elongated lifetimes attributed to the relaxation of a triplet excited state. A rhenium complex of a ligand containing both a phenanthroline and terpyridine moiety showed exclusive preferential binding to the phenanthroline moiety, as evidenced by shifts in the NMR and information gained form the IR spectrum. All rhenium complexes displayed emission as a result of a MLCT, although one complex did show anomalous results of a shorter wavelength emission and longer lifetime which was consistent with a larger energy gap.

4.10 Experimental

Synthesis of 59

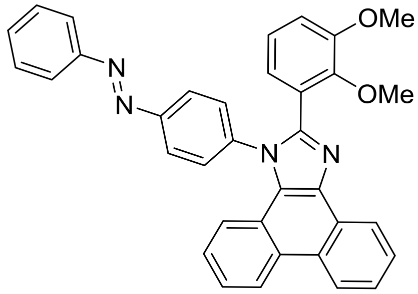

Into a round bottom flask was added NH_4OAc (1.11 g, 14.4 mmol), 2,3-dimethoxybenzaldehyde (0.239 g, 1.44 mmol), 9,10-phenanthrenedione (0.300 g, 1.44 mmol), 4-phenylazoaniline (0.284 g, 1.44 mmol) and acetic acid (30ml) and then the reaction mixture was left at reflux for 3 hours. Upon cooling, the product was precipitated from water (50 ml). The light brown precipitate was extracted with chloroform (2x 150 ml). The combined organics were washed with water (3 x 50ml) and brine (1 x 50ml), and then dried and the volatiles removed *in vacuo*. The resulting brown oil was recrystalised using chloroform and hexane to give product (**59**) as an orange powder (0.500g, 0.935 mmol). ^{1}H NMR (400 MHz, $CDCl_3$) δ 8.85 (1H, dd, *J* = 8.0, 1.1 Hz, phen-*H*), 8.80 (1H, d, *J* = 8.3 Hz, phen-*H*), 8.74 (1H, d, *J* = 8.3 Hz, phen-*H*), 7.99 (2H, d, *J* = 8.6 Hz, Ar-*H*), 7.95 (2H, dd, *J* = 8.0, 1.6 Hz, Ar-*H*), 7.77 – 7.71 (1H, m, Ar-*H*), 7.69 – 7.64 (1H, m, Ar-*H*), 7.64 – 7.59 (2H, m, Ar-*H*), 7.58 – 7.50 (4H, m, Ar-*H*), 7.39 – 7.27 (2H, m, Ar-*H*), 7.06 – 7.01 (2H, m, Ar-*H*), 6.97 – 6.90 (1H, m, Ar-*H*), 3.82 (3H, s, Ar-O-C*H*$_3$), 3.77 (3H, s, Ar-O-C*H*$_3$) ppm. Insufficient solubility to obtain $^{13}C\{^1H\}$ NMR. HRMS (EI)(%): found *m/z* = 534.2054; $\{C_{35}H_{26}N_4O_2\}$ requires 534.2050. IR (KBr plates): 3060 (bw), 2934 (w), 1709 (w), 1677 (w), 1598 (m), 1580 (m), 1530 (w), 1500 (s), 1477 (s), 1451 (s), 1427 (w), 1380 (s), 1343 (w), 1327 (w), 1299 (w), 1266 (s), 1232 (m), 1203 (w), 1126 (w), 1076 (s), 1051 (s), 1005 (m), 990 (m), 924 (w), 869 (w), 854 (w), 794 (w), 769 (s) cm^{-1}. UV-vis λ_{max} (ε / M^{-1} cm^{-1}) ($CHCl_3$): 259 (90 700), 285 (39 500), 307 (36 700), 328 (sh)(31 800), 347 (sh)(23 600) nm.

Synthesis of 60

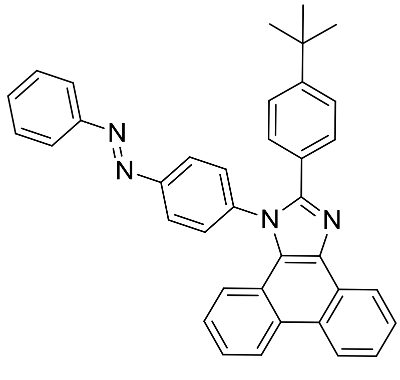

This material was prepared by a similar method to **59** using 4-tertbutylbenzaldehyde (0.24 ml, 1.44 mmol), 9,10-phenanthrenedione (0.300 g, 1.44 mmol), 4-phenylazoaniline (0.284 g, 1.44 mmol), and ammonium acetate (1.11 g, 14.4 mmol). The crude product was recrystalised from chloroform and hexane to give product (**60**) as an orange powder (0.570g, 1.074 mmol). ^{1}H NMR (400 MHz, $CDCl_3$) δ 8.92 (1H, d, *J* = 7.8 Hz, phen-*H*), 8.78 (1H, d, *J* = 8.4 Hz, phen-*H*), 8.72 (1H, d, *J* = 8.3 Hz, phen-*H*), 8.20 – 8.12 (2H, m, Ar-*H*), 8.02 (2H, dd, *J* = 8.0, 1.6 Hz, Ar-*H*), 7.76 (1H, t, *J* = 7.2 Hz, Ar-*H*), 7.71 – 7.63 (3H, m, Ar-*H*), 7.62 – 7.49 (6H, m, Ar-*H*), 7.37 – 7.27 (4H, m, Ar-*H*), 1.28 (9H, s, Ar-$C(CH_3)_3$) ppm. ^{13}C NMR (101 MHz, $CDCl_3$) δ 152.8, 152.6, 152.3, 151.2, 140.9, 137.7, 132.0, 130.2, 129.4, 129.4, 129.2, 128.4, 128.1, 127.4, 127.3, 126.5, 125.8, 125.5, 125.0, 124.6, 124.3, 123.3, 123.2, 123.1, 122.9, 121.0, 34.8, 31.3 ppm. HRMS (EI)(%): found *m/z* = 531.2534; $\{C_{37}H_{30}H_5\}^+$ requires 531.2543. IR (KBr plates): 2960 (w), 1610 (w), 1594 (w), 1575 (w), 1515 (w), 1500 (m), 1475 (m), 1450 (m), 1425 (w), 1409 (w), 1379 (m), 1364 (w), 1298 (w), 1147 (m), 1112 (w), 1070 (w), 1013 (w), 978 (w), 954 (w), 859 (m), 842 (m), 752 (s), 721 (s) cm^{-1}. UV-vis λ_{max} (ε / M^{-1} cm^{-1}) ($CHCl_3$): 263 (137 800), 320 (sh) (45 300), 354(sh)(18 500) nm.

Synthesis of 61

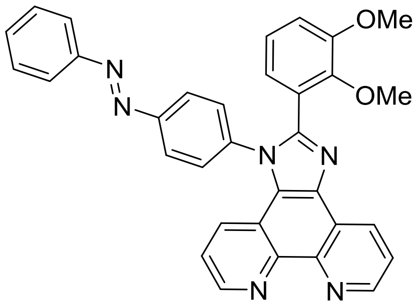

This material was prepared by a similar method to **59** using 2,3-dimethoxybenzaldehyde (0.237 g, 1.43 mmol), 1,10-phenanthroline-5,6-dione (0.300 g, 1.43 mmol), 4-phenylazoaniline (0.282 g, 1.43 mmol), and ammonium acetate (1.10 g, 14.3 mmol). The crude product was recrystalised from chloroform and hexane to give product (**61**) as an orange powder (0.490 g, 0.913 mmol). ^{1}H NMR (400 MHz, $CDCl_3$) δ 9.25 (1H, dd, *J* = 4.4, 1.5 Hz, phen-*H*), 9.17 (1H, dd, *J* = 8.1, 1.5 Hz, phen-*H*), 9.10 (1H, dd, *J* = 4.3, 1.3 Hz, phen-*H*), 8.03 (2H, d, *J* = 8.4 Hz, Ar-*H*), 7.95 (2H, dd, *J* = 7.5, 1.8 Hz, Ar-*H*), 7.79 (1H, dd, *J* = 8.1, 4.5 Hz, Ar-*H*), 7.67 (1H, dd, *J* = 8.4, 1.3 Hz, Ar-*H*), 7.62 (2H, d, *J* = 8.4 Hz, Ar-*H*), 7.58 – 7.51 (3H, m, *J* = 11.9, 3.9 Hz, Ar-*H*), 7.36 (1H, dd, *J* = 8.4, 4.4 Hz, Ar-*H*), 7.09 – 6.94 (3H, m, Ar-*H*), 3.83 (3H, s, Ar-O-CH_3), 3.78 (3H, s, Ar-O-CH_3) ppm. ^{13}C NMR (101 MHz, $CDCl_3$) δ 153.0, 153.0, 152.8, 151.1, 149.4, 148.6, 148.4, 145.2, 144.7, 139.4, 136.5, 132.2, 131.0, 129.7, 129.5, 128.7, 126.6, 125.4, 124.5, 124.5, 124.5, 124.0, 123.7, 123.5, 122.7, 120.1, 114.7, 62.0, 56.3 ppm. HRMS (EI)(%): found *m/z* = 536.1962; $\{C_{33}H_{24}N_6O_2\}$ requires 536.1955. IR (KBr plates):

2931 (w), 2828 (w), 1597 (w), 1579 (w), 1559 (m), 1505 (m), 1476 (s), 1461 (m), 1426 (m), 1381 (m), 1340 (w), 1328 (w), 1303 (w), 1263 (s), 1235 (w), 1158 (w), 1081 (s), 1074 (m), 1055 (w), 990 (s), 928 (w), 874 (w), 816 (w) cm^{-1}. UV-vis λ_{max} (ε / M^{-1} cm^{-1}) ($CHCl_3$): 255 (54 000), 284 (48 000), 314 (sh) (33 200), 450 (3500) nm.

Synthesis of 62

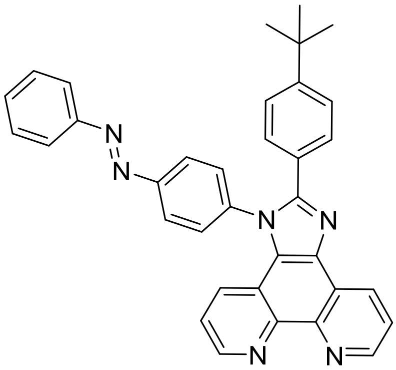

This material was prepared by a similar method to **59** using 4-tertbutylbenzaldehyde (0.24 ml, 1.43 mmol), 1,10-phenanthroline-5,6-dione (0.300 g, 1.43 mmol), 4-phenylazoaniline (0.282 g, 1.43 mmol), and ammonium acetate (1.10 g, 14.3 mmol). The crude product was recrystalised from chloroform and hexane to give product (**62**) as an orange powder (0.360 g, 0.676 mmol). ^{1}H NMR (400 MHz, $CDCl_3$) δ 9.22 (1H, d, *J* = 4.2 Hz, phen-*H*), 9.18 (1H, d, *J* = 8.1 Hz, phen-*H*), 9.06 (1H, d, *J* = 3.3 Hz, phen-*H*), 8.19 (2H, d, *J* = 8.4 Hz, Ar-*H*), 8.05 – 7.99 (2H, m, Ar-*H*), 7.82 – 7.76 (1H, m, Ar-*H*), 7.71 (2H, d, *J* = 8.4 Hz, Ar-*H*), 7.60 – 7.51 (6H, m, Ar-*H*), 7.38 – 7.29 (3H, m, Ar-*H*), 1.27 (9H, s, Ar-C(CH_3)$_3$) ppm. ^{13}C NMR (101 MHz, $CDCl_3$) δ 153.1, 152.8, 152.4, 152.4, 149.1, 148.0, 144.9, 144.4, 139.9, 136.4, 132.1, 130.7, 129.8, 129.4, 129.1, 128.0, 126.8, 125.6, 124.8, 124.0, 123.6, 123.3, 122.3, 119.8, 34.8, 31.2 ppm. HRMS (EI)(%): found *m/z* = 533.2441; {$C_{35}H_{29}N_6$} requires 533.2448. IR (KBr plates): 2963 (w), 1594 (w), 1556 (w), 1502 (m), 1471 (w), 1442 (m), 1376 (w), 1339 (w), 1300 (w), 1268 (w), 1152 (w), 1062 (w), 1018 (w), 977 (w), 867 (w), 841 (s), 809 (m), 795 (w), 769 (s) cm^{-1}. UV-vis λ_{max} (ε / M^{-1} cm^{-1}) ($CHCl_3$): 276 (44 300), 299 (sh) (38 600), 433 (sh) (1100) nm.

Synthesis of 63

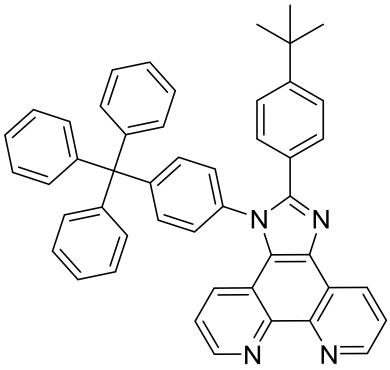

This material was prepared by a similar method to **59** using 4-tertbutylbenzaldehyde (0.24 ml, 1.43 mmol), 1,10-phenanthroline-5,6-dione (0.300 g, 1.43 mmol), 4-tritylaniline (0.480 g, 1.43 mmol), and ammonium acetate (1.10 g, 14.3 mmol). The crude product was recrystalised from acetone to give product (**63**) as an off-white powder (0.200 g, 0.298 mmol). ^{1}H NMR (400 MHz, $CDCl_3$) δ 9.18 (1H, dd, J = 4.3, 1.6 Hz, phen-*H*), 9.14 (1H, dd, J = 8.1, 1.6 Hz, phen-*H*), 9.07 (1H, dd, J = 4.3, 1.6 Hz, phen-*H*), 7.75 (1H, dd, J = 8.1, 4.4 Hz, Ar-*H*), 7.53 (5H, d, J = 5.3 Hz, Ar-*H*), 7.43 (2H, d, J = 8.6 Hz, Ar-*H*), 7.38 – 7.27 (18H, m, Ar-*H*), 1.35 (9H, s, Ar-$C(CH_3)_3$) ppm. ^{13}C {^{1}H} NMR (101 MHz, $CDCl_3$) δ 152.7, 152.4, 149.7, 149.1, 147.9, 146.2, 144.9, 144.4, 136.2, 135.9, 133.3, 131.2, 130.6, 129.0, 128.0, 128.0, 127.0, 126.9, 126.6, 125.4, 124.1, 123.6, 122.1, 119.9, 65.2, 34.9, 31.3 ppm. HRMS (EI)(%): found m/z = 671.3167; {$C_{48}H_{39}N_4$} requires 671.3169. IR (KBr plates): 3055 (w), 2957 (w), 1598 (w), 1558 (w), 1506 (m), 1492 (s), 1468 (w), 1443 (s), 1391 (w), 1340 (w), 1299 (w), 1191 (w), 1152 (w), 1035 (w), 980 (w), 841 (s), 808 (w), 767 (w), 753 (s), 741 (s), 701 (s) cm^{-1}. UV-vis λ_{max} (ε / M^{-1} cm $^{-1}$) ($CHCl_3$): 274 (54 600), 300 (sh)(30 400), 313 (sh)(23 600), 362 (2700) nm.

Synthesis of 64

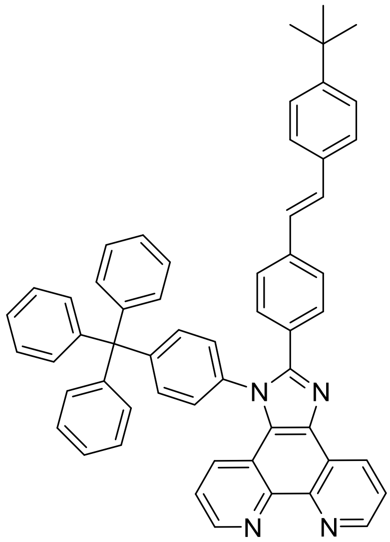

This material was prepared by a similar method to **59** using 4-*tert*-butylstyryl-benzaldehyde (0.251 g, 0.952 mmol), 1,10-phenanthroline-5,6-dione (0.200 g, 0.952 mmol), 4-tritylaniline (0.319 g, 0.952 mmol), and ammonium acetate (0.734 g, 9.52 mmol). The crude product was recrystalised from ethanol to give product (**64**) as an off-white powder (0.180g, 0.233 mmol). ^{1}H NMR (400 MHz, $CDCl_3$) δ 9.20 (1H, dd, *J* = 4.3, 1.7 Hz, phen-*H*), 9.16 (1H, dd, *J* = 8.1, 1.7 Hz, phen-*H*), 9.07 (1H, dd, *J* = 4.3, 1.6 Hz, phen-*H*), 7.77 (dd, *J* = 8.1, 4.4 Hz, 1H, Ar-*H*), 7.61 (d, *J* = 8.4 Hz, 2H, Ar-*H*), 7.55 (2H, d, *J* = 8.6 Hz, Ar-*H*), 7.52 – 7.46 (4H, m, Ar-*H*), 7.46 – 7.40 (5H, m, *J* = 8.5, 5.9 Hz, Ar-*H*), 7.38 – 7.27 (16H, m, Ar-*H*), 7.20 – 7.05 (2H, m, *J* = 39.7, 16.3 Hz, Ar-*H*), 1.34 (9H, d, *J* = 8.6 Hz, Ar-$C(CH_3)_3$) ppm. $^{13}C\{^1H\}$ NMR (101 MHz, $CDCl_3$) δ 152.0, 151.4, 149.9, 149.1, 148.0, 146.2, 144.9, 144.4, 138.6, 136.3, 135.9, 134.3, 133.4, 131.1, 130.7, 130.1, 129.6, 128.6, 128.1, 128.0, 127.1, 126.6, 126.6, 126.4, 125.9, 124.1, 123.7, 122.2, 119.9, 65.2, 34.8, 31.4 ppm. HRMS (ES)(%): found *m/z* = 771.3473; $\{C_{56}H_{45}N_4\}^+$ requires 771.3482. IR (KBr plates): 2960 (w), 1598 (w), 1559 (w), 1505 (w), 1468 (w), 1442 (w), 1378 (w), 1150 (w), 1106 (w), 1034 (w), 978 (w), 833 (w), 804 (w), 749 (w), 740 (s), 701 (w) cm^{-1}. UV-vis λ_{max} (ε / M^{-1} cm^{-1}) ($CHCl_3$): 276 (101,100), 349 (38,700) nm.

Synthesis of 65

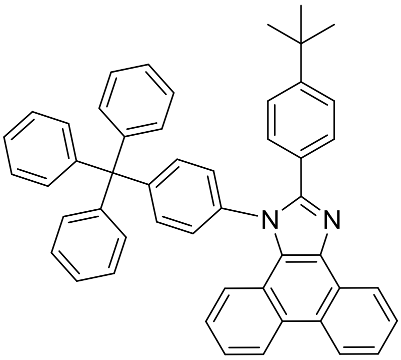

This material was prepared by a similar method to **59** using 4-*tert*-butylbenzaldehyde (0.24 ml, 1.44 mmol), 9,10-phenanthrenedione (0.300 g, 1.44 mmol), 4-tritylaniline (0.483 g, 1.44 mmol), and ammonium acetate (1.10 g, 14.4 mmol). The crude product was recrystalised from acetonitrile to give product (**65**) as an off-white powder (0.400 g, 0.598 mmol).^{1}H NMR (400 MHz, $CDCl_3$) δ 8.87 (1H, d, *J* = 7.0 Hz, phen-*H*), 8.77 (1H, d, *J* = 8.5 Hz, phen-*H*), 8.70 (1H, d, *J* = 8.3 Hz, phen-*H*), 7.73 (1H, t, *J* = 7.0 Hz, Ar-*H*), 7.68 – 7.61 (1H, m, Ar-*H*), 7.56 – 7.50 (3H, m, Ar-*H*), 7.49 – 7.40 (4H, m, Ar-*H*), 7.38 – 7.27 (15H, m, Ar-*H*), 7.24 – 7.14 (4H, m, Ar-*H*), 1.34 (9H, s, Ar-*H*) ppm. ^{13}C NMR (101 MHz, $CDCl_3$) δ 152.1, 151.1, 149.0, 146.8, 146.3, 137.5, 136.7, 133.0, 131.8, 131.2, 130.2, 129.8, 129.3, 129.1, 129.1, 128.4, 128.3, 128.1, 128.0, 127.9, 127.7, 127.6, 127.4, 126.5, 126.2, 126.0, 125.6, 125.3, 125.2, 124.9, 124.2, 123.2, 123.2, 122.8, 120.9, 119.0, 65.1, 34.8, 31.3, 14.3 ppm. HRMS (EI)(%): found *m/z* = 669.3258; $\{C_{50}H_{41}N_2\}$ requires 669.3264. IR (KBr plates): 3055 (w), 2957 (w), 1668 (w), 1596 (w), 1575 (w), 1505 (m), 1491 (m), 1450 (m), 1381 (w), 1361 (w), 1267 (w), 1187 (w), 1146 (w), 1035 (w), 839 (s), 750 (s), 723 (s), 699 (s) cm^{-1}. UV-vis λ_{max} (ε / M^{-1} cm $^{-1}$) ($CHCl_3$): 262 (69 500), 314 (20 200), 329 (19 100), 361 (8600) nm.

Synthesis of 66

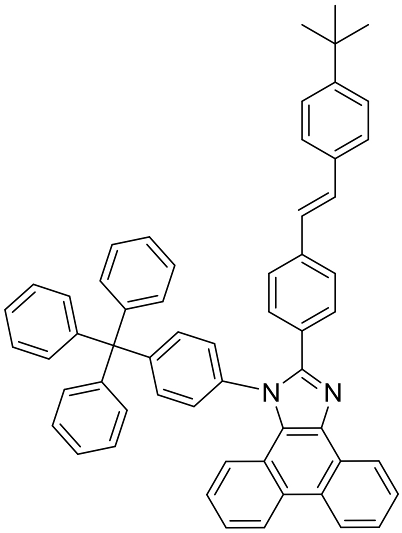

This material was prepared by a similar method to **59** using 4-*tert*-butylstyryl-benzaldehyde (0.380 g, 1.44 mmol), 9,10- phenanthrenedione (0.300 g, 1.44 mmol), 4-tritylaniline (0.483 g, 1.44 mmol), and ammonium acetate (1.11 g, 14.4 mmol). The crude product was recrystalised from acetonitrile to give product (**66**) as an off-white powder (0.440 g, 0.571 mmol). ^{1}H NMR (400 MHz, $CDCl_3$) δ 8.90 – 8.86 (1H, m, phen-*H*), 8.77 (1H, d, *J* = 8.5 Hz, phen-*H*), 8.71 (1H, d, *J* = 8.3 Hz, phen-*H*), 7.78 – 7.71 (1H, m, Ar-*H*), 7.69 – 7.63 (1H, m, Ar-*H*), 7.60 (2H, d, *J* = 8.4 Hz, Ar-*H*), 7.57 – 7.52 (1H, m, Ar-*H*), 7.52 – 7.47 (4H, m, Ar-*H*), 7.45 – 7.40 (6H, m, Ar-*H*), 7.38 – 7.27 (17H, m, Ar-*H*), 7.15 (2H, dd, *J* = 28.5, 12.2 Hz, Ar-*H*), 1.36 (9H, s, Ar-$C(CH_3)_3$). ^{13}C NMR (101 MHz, $CDCl_3$) δ 151.3, 150.7, 149.2, 146.3, 139.0, 138.0, 137.6, 136.7, 134.5, 133.1, 131.2, 130.3, 129.7, 129.4, 129.3, 128.3, 127.9, 127.3, 126.5, 126.2, 125.8, 125.7, 125.0, 124.3, 123.2, 123.1, 122.9, 121.0, 65.2, 34.8, 31.4 ppm. HRMS (EI)(%): found *m/z* = 771.3710; {$C_{58}H_{47}N_2$} requires 771.3739. IR (KBr plates): 3026 (w), 2961 (w), 1595 (w), 1573 (w), 1506 (m), 1488 (m), 1469 (m), 1446 (m), 1384 (m), 1268 (w), 1145 (w), 1107 (w), 1032 (w), 961 (s), 942 (w), 840 (s), 757 (s), 724 (m), 700 (s) cm^{-1}. UV-vis λ_{max} (ε / M^{-1} cm $^{-1}$) ($CHCl_3$): 260 (52 600), 306 (26 500), 350 (47 900), 365 (48 300) nm.

Synthesis of 67

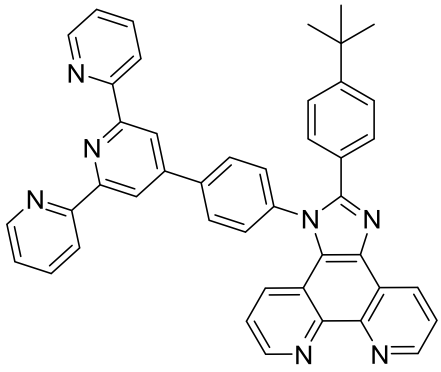

This material was prepared by a similar method to **59** using 4-tertbutylbenzaldehyde (0.15 ml, 0.892 mmol), 1,10-phenanthroline-5,6-dione (0.187 g, 0.892 mmol), 4-([2,2':6',2''-terpyridin]-4'-yl)aniline (0.230 g, 0.981 mmol), and ammonium acetate (0.688 g, 8.92 mmol). The crude product was recrystalised from chloroform/hexane and the filtered through a pad of silica in 2% methanol in chloroform to give product (**67**) as an off-white powder (0.110g, 0.166 mmol). ^{1}H NMR (400 MHz, $CDCl_3$) δ 9.21 (1H, dd, *J* = 4.4, 1.8 Hz, phen-*H*), 9.18 (1H, dd, *J* = 8.1, 1.8 Hz, phen-*H*), 9.08 (1H, dd, *J* = 4.3, 1.6 Hz, phen-*H*), 8.86 (2H, s, Ar-*H*), 8.78 – 8.75 (2H, m, Ar-*H*), 8.73 (2H, d, *J* = 7.9 Hz, Ar-*H*), 8.15 (2H, d, *J* = 8.4 Hz, Ar-*H*), 7.94 (2H, td, *J* = 7.7, 1.8 Hz, Ar-*H*), 7.78 (1H, dd, *J* = 8.1, 4.4 Hz, Ar-*H*), 7.73 – 7.69 (2H, m, Ar-*H*), 7.59 – 7.54 (3H, m, Ar-*H*), 7.45 – 7.36 (5H, m, Ar-*H*), 1.31 (9H, s, Ar-$C(CH_3)_3$) ppm. ^{13}C NMR (101 MHz, $CDCl_3$) δ 156.5, 156.0, 152.9, 152.6, 149.4, 149.1, 148.1, 140.9, 138.8, 137.4, 136.4, 130.9, 130.1, 129.7, 129.6, 129.1, 128.1, 127.0, 126.9, 125.8, 125.6, 124.4, 124.2, 123.7, 122.6, 121.7, 120.0, 119.3, 35.0, 31.3 ppm. HRMS (ES)(%): found *m/z* = 660.2868; $\{C_{42}H_{34}N_7\}^+$ requires 660.2870. IR: 2954 (w), 1608 (w), 1585 (m), 1568 (m), 1516 (m), 1467 (m), 1444 (m), 1390 (m), 1265 (w), 1114 (w), 842 (m), 790 (s) cm^{-1}. UV-vis λ_{max} (ε / M^{-1} cm^{-1}) ($CHCl_3$): 277 (97 800), 315 (sh) (31 300) nm.

Synthesis of 68

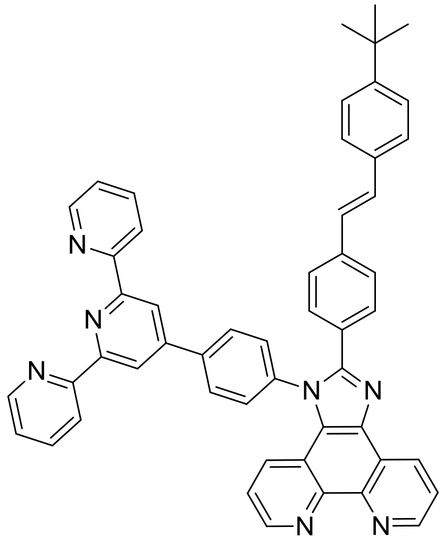

This material was prepared by a similar method to **59** using 4-*tert*-butylstyrylbenzaldehyde (0.300 g, 1.13 mmol), 1,10-phenanthroline-5,6-dione (0.283 g, 1.13 mmol), 4-([2,2':6',2"-terpyridin]-4'-yl)aniline (0.366 g, 1.13 mmol), and ammonium acetate (0.871 g, 11.3 mmol). The crude product was recrystalised from hot toluene and the filtered to give product (**68**) as an off-white powder (0.250g). ^{1}H NMR (400 MHz,) δ 9.25 – 9.14 (2H, m, phen-*H*), 9.08 (1H, dd, *J* = 4.3, 1.6 Hz, phen-*H*), 8.85 (2H, s, Ar-*H*), 8.78 – 8.70 (4H, m, Ar-*H*), 8.16 (2H, d, *J* = 8.4 Hz, Ar-*H*), 7.94 (2H, td, *J* = 7.8, 1.8 Hz, Ar-*H*), 7.78 (1H, dd, *J* = 8.1, 4.4 Hz, Ar-*H*), 7.71 (2H, d, *J* = 8.4 Hz, Ar-*H*), 7.63 – 7.58 (3H, m, Ar-*H*), 7.51 – 7.35 (9H, m, Ar-*H*), 7.18 – 7.00 (2H, m, Ar-*H*), 1.32 (9H, s, Ar-C(CH$_3$)$_3$) ppm. ^{13}C{^{1}H} NMR (101 MHz, CDCl$_3$) δ 156.4, 155.9, 152.1, 151.2, 149.2, 149.1, 148.8, 148.0, 144.9, 144.4, 140.9, 138.7, 138.6, 137.2, 136.4, 134.3, 130.7, 130.1, 129.5, 129.4, 128.9, 128.3, 128.0, 126.9, 126.5, 126.4, 125.7, 124.2, 124.0, 123.6, 122.4, 121.6, 119.8, 119.2, 34.7, 31.3 ppm. HRMS (ES)(%): found *m/z* = 778.3284; { $C_{42}H_{40}N_7O$ }$^+$ requires 778.3289. IR (KBr plates): 3028 (w), 2960 (w), 1710 (s), 1646 (w), 1601 (m), 1584 (s), 1567 (s), 1517 (s), 1466 (s), 1443 (m), 1418 (w), 1388 (s), 1265 (m), 1221 (m), 1186 (w), 1150 (w), 1108 (w), 965 (w), 856 (w), 838 (w), 791 (s), 741 (s) cm^{-1}. UV-vis λ_{max} (ε / M^{-1} cm^{-1}) (CHCl$_3$): 283 (61,500), 326 (sh)(37,800), 405 (sh) (6400) nm.

Synthesis of 69

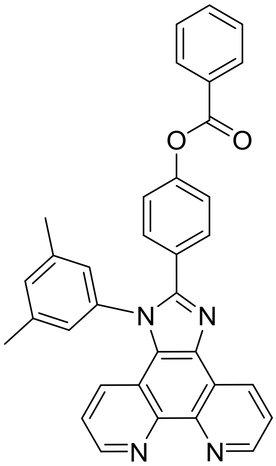

This material was prepared by a similar method to **59** using 4-formylphenylbenzoate (0.324 g, 1.43 mmol), 1,10-phenanthroline-5,6-dione (0.300 g, 1.43 mmol), 3,5-dimethylaniline (0.18 ml, 1.43 mmol), and ammonium acetate (1.10 g, 14.3 mmol). The crude product was recrystalised from chloroform and hexane to give product (**69**) as an off-white powder (0.400g, 0.768 mmol). ^{1}H NMR (400 MHz, $CDCl_3$) δ 9.19 (1H, dd, *J* = 4.4, 1.7 Hz, phen-*H*), 9.14 (1H, dd, *J* = 8.1, 1.8 Hz, phen-*H*), 9.05 (1H, dd, *J* = 4.3, 1.6 Hz, phen-*H*), 8.22 – 8.15 (2H, m, Ar-*H*), 7.79 – 7.71 (3H, m, Ar-*H*), 7.67 – 7.60 (1H, m, Ar-*H*), 7.51 (2H, t, *J* = 7.7 Hz, Ar-*H*), 7.45 (1H, dd, *J* = 8.4, 1.6 Hz, Ar-*H*), 7.35 – 7.29 (2H, m, Ar-*H*), 7.24 – 7.18 (2H, m, Ar-*H*), 7.16 (2H, s, Ar-*H*), 2.43 (6H, s, C(CH_3)) ppm. ^{13}C{^{1}H} NMR (101 MHz, $CDCl_3$) δ 164.9, 151.7, 151.1, 149.1, 148.0, 145.0, 144.5, 140.8, 137.8, 136.1, 133.9, 132.2, 130.6, 130.4, 130.3, 129.3, 128.7, 128.3, 127.8, 127.2, 126.2, 124.0, 123.6, 122.3, 121.8, 120.0, 21.5 ppm. IR (KBr plate): 2928 (m), 1734 (s), 1609(w), 1599 (w), 1565 (w), 1471 (s), 1450 (s), 1393 (w), 1342 (w), 1333 (w), 1263 (s), 1202 (s), 1166 (m), 1078 (s), 1061 (s), 880 (w) cm^{-1}. UV-vis λ_{max} (ε / M^{-1} cm $^{-1}$) ($CHCl_3$): 274 (117 400) nm.

Synthesis of [ReBr(CO)$_3$(61)]

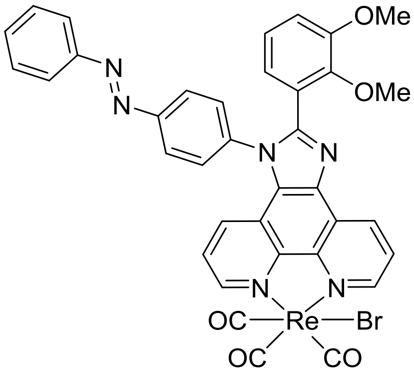

Into a round bottom flask was added lophine (**61**) (0.066 g, 0.123 mmol), pentacarbonylbromorhenium (0.05 g, 0.123 mmol) and toluene (30ml) and the reactants were left at reflux for 3 hours. The solvent was removed *in vacuo* to yield orange oil. $CHCl_3$ was added (2ml) and was precipitated from hexane to give product [ReBr(CO)$_3$(**61**)] as an orange powder (0.072g, 0.081 mmol). ^{1}H NMR (400 MHz, $CDCl_3$) δ 9.34 (1H, dd, *J* = 5.1, 1.3 Hz, phen-*H*), 9.30 (1H, dd, *J* = 8.3, 1.2 Hz, phen-*H*), 9.24 (1H, dd, *J* = 5.1, 1.2 Hz, phen-*H*), 8.04 – 7.96 (2H, m, Ar-*H*), 7.92 – 7.86 (3H, m, Ar-*H*), 7.77 (1H, dd, *J* = 8.6, 1.2 Hz, Ar-*H*), 7.61 – 7.52 (2H, m, Ar-*H*), 7.52 – 7.44 (4H, m, Ar-*H*), 7.05 – 7.00 (1H, m, Ar-*H*), 6.96 – 6.91 (2H, m, Ar-*H*), 3.77 (3H, s, Ar-O-CH_3), 3.71 (3H, s, Ar-O-CH_3) ppm. ^{13}C {^{1}H} NMR (101 MHz, $CDCl_3$) δ 197.0, 189.1, 153.2, 153.1, 152.8, 152.4, 151.8, 151.1, 148.0, 145.6, 145.1, 137.9, 136.8, 132.9, 132.2, 130.3, 129.5, 129.2, 128.9, 126.8, 126.6, 126.2, 125.1, 124.6, 124.5, 124.5, 124.1, 123.3, 123.0, 122.0, 115.0, 61.7, 56.0 ppm. HRMS (ES)(%): found *m/z* = 885.0593; $\{C_{36}H_{25}BrN_6O_5{}^{185}Re\}^+$ requires 885.0594. IR (KBr plates): 2020 (s), 1914 (s), 1891 (s),1710 (m), 1616 (w), 159 (w), 1581 (w), 1530 (w), 1501 (w), 1478 (w), 1458 (w), 1384 (w), 1362 (w), 1302 (w), 1266 (w), 1221 (w), 1086 (w), 1062 (w), 993 (w) cm^{-1}. UV-vis λ_{max} (ε / M^{-1} cm^{-1}) ($CHCl_3$): 260 (70 900), 301 (47 700), 330 (sh) (35 000), 420 (6600) nm.

Synthesis of [ReBr(CO)$_3$(62)]

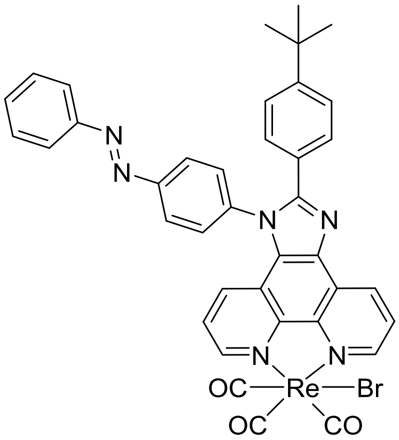

The title compound was prepared using lophine (**62**) (0.066 g, 0.123 mmol) and pentacarbonylbromorhenium (0.05 g, 0.123 mmol) to give the product [ReBr(CO)$_3$(**62**)] as a yellow/orange solid (0.085 g, 0.0963 mmol). ^{1}H NMR (400 MHz, $CDCl_3$) δ 9.62 (1H, bs, phen-*H*), 9.42 (1H, d, *J* = 4.7 Hz, phen-*H*), 9.31 (1H, d, *J* = 5.2 Hz, phen-*H*), 8.27 (2H, d, *J* = 8.1 Hz, Ar-*H*), 8.08 – 8.02 (2H, m, Ar-*H*), 8.02 – 7.95 (1H, m, Ar-*H*), 7.80 – 7.72 (2H, m, Ar-*H*), 7.69 – 7.52 (6H, m, Ar-*H*), 7.41 (2H, d, *J* = 8.2 Hz, Ar-*H*), 7.17 (1H, d, *J* = 7.9 Hz, Ar-*H*), 1.30 (9H, s, Ar-C(CH_3)$_3$) ppm. ^{13}C NMR (101 MHz, $CDCl_3$) δ 197.0, 189.1, 154.5, 153.9, 153.6, 152.4, 151.9, 150.8, 145.5, 145.1, 138.8, 137.1, 133.1, 132.5, 130.0, 129.7, 129.5, 129.2, 128.4, 127.3, 126.4, 126.2, 126.0, 125.4, 125.2, 125.0, 123.4, 122.1, 35.0, 31.2 ppm. HRMS (EI)(%): found *m/z* = 905.0829; $\{C_{38}H_{28}BrN_6O_3{}^{185}ReNa\}$ requires 905.0828. IR (KBr plate): 2960 (w), 2020 (s), 1891 (bs), 1600 (w), 1500 (w), 1473 (w), 1447 (m), 1380 (w), 1303 (w), 1267 (w), 1155 (w), 1121 (w), 1017 (w), 988 (w), 841 (w), 805 (w), 770 (w), 724 (w) cm^{-1}. UV-vis λ_{max} (ε / M^{-1} cm^{-1}) ($CHCl_3$): 282 (62 300), 306 (54 300), 425 (7100) nm.

Synthesis of [ReBr(CO)$_3$(63)]

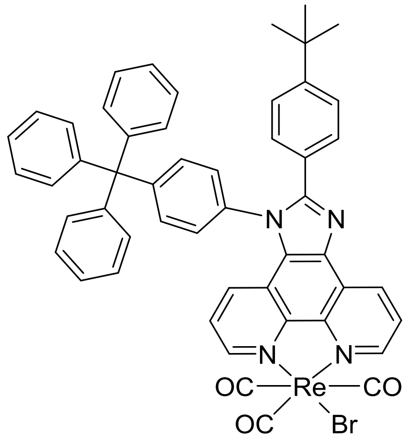

Into a round bottom flask was added lophine (**63**) (0.058 g, 0.123 mmol), pentacarbonylbromorhenium (0.05 g, 0.123 mmol) and toluene (30 ml) and the reactants were left at reflux for 3 hours. The solvent was removed *in vacuo* to yield orange oil. CHCl3 was added (2ml) and was precipitated from hexane to give product [ReBr(CO)$_3$(**63**)] as a yellow/orange powder (0.040g, 0.0398 mmol). ^{1}H NMR (400 MHz, $CDCl_3$) δ 9.40 – 9.37 (1H, m, phen-*H*), 9.34 (1H, dd, *J* = 8.3, 1.4 Hz, phen-*H*), 9.27 (1H, dd, *J* = 5.1, 1.3 Hz, phen-*H*), 7.94 (1H, dd, *J* = 8.3, 5.1 Hz, Ar-*H*), 7.66 – 7.59 (3H, m, Ar-*H*), 7.59 – 7.54 (2H, m, Ar-*H*), 7.49 – 7.41 (3H, m, Ar-*H*), 7.41 – 7.27 (17H, m, Ar-*H*), 1.36 (9H, s, Ar-C(C*H*$_3$)$_3$) ppm. ^{13}C NMR (101 MHz, $CDCl_3$) δ 151.8, 150.7, 146.0, 145.5, 142.3, 136.9, 135.0, 133.9, 133.7, 133.0, 131.1, 129.9, 129.1, 128.1, 127.9, 127.6, 126.7, 126.4, 126.1, 126.1, 125.7, 124.8, 122.1, 65.3, 35.0, 31.3 ppm. IR (KBr plates): 2955 (w), 2020 (s), 1886 (bs), 1600 (w), 1447 (w), 842 (w), 806 (w), 753 (w), 723 (w), 700 (w) cm^{-1}. UV-vis λ_{max} (ε / M^{-1} cm $^{-1}$) ($CHCl_3$): 276 (208 200), 346 (sh)(12 400), 421 (7500) nm.

Synthesis of [ReBr(CO)$_3$(67)]

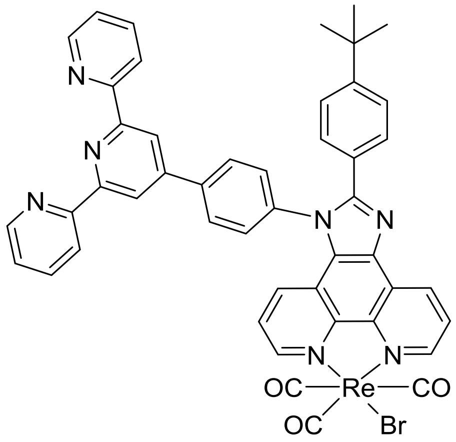

Into a round bottom flask was added lophine (**67**) (0.050 g, 0.076 mmol), pentacarbonylbromorhenium (0.030 g, 0.076 mmol) and toluene (30ml) and the reactants were left at reflux for 3 hours. The solvent was removed *in vacuo* to yield orange oil. $CHCl_3$ was added (2 ml) and was precipitated from hexane to give product [ReBr(CO)$_3$(**67**)] as orange powder (0.050 g).^{1}H NMR (400 MHz, DMSO) δ 9.46 (1H, dd, J = 5.1, 1.2 Hz, phen-*H*), 9.40 (1H, dd, J = 8.3, 1.3 Hz, phen-*H*), 9.32 (1H, d, J = 4.1 Hz, phen-*H*), 8.88 (1H, s, Ar-*H*), 8.77 (2H, d, J = 4.6 Hz, Ar-*H*), 8.71 (1H, d, J = 8.0 Hz, Ar-*H*), 8.33 (1H, d, J = 8.7 Hz, Ar-*H*), 8.22 (1H, dd, J = 8.2, 5.2 Hz, Ar-*H*), 8.11 – 7.98 (4H, m, Ar-*H*), 7.90 – 7.84 (1H, m, Ar-*H*), 7.75 (1H, d, J = 7.6 Hz, Ar-*H*), 7.68 – 7.63 (2H, m, Ar-*H*), 7.55 (2H, dd, J = 6.5, 4.8 Hz, Ar-*H*), 7.48 – 7.43 (2H, m, Ar-*H*), 1.25 (9H, s, Ar-C(CH_3)$_3$) ppm. Insufficient solubility to obtain ^{13}C{^{1}H} NMR. IR (KBr plates): 2965 (w), 2016 (s), 1891 (s), 1600 (w), 1582 (w), 1516 (w), 1466 (w), 1384 (w), 792 (w), 760 (w), 722 (w) cm^{-1}. UV-vis λ_{max} (ε / M^{-1} cm^{-1}) ($CHCl_3$): 278 (94 000), 338 (sh) (16 900), 420 (8500) nm.

Synthesis of [ReBr(CO)$_3$(69)]

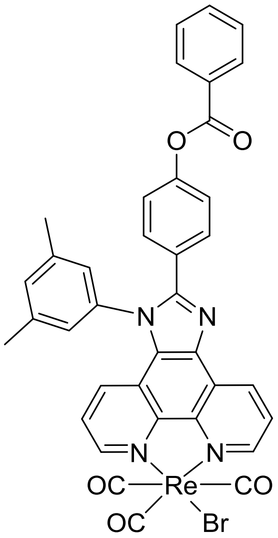

The title compound was prepared using lophine (**69**) (0.064 g, 0.123 mmol) and pentacarbonylbromorhenium (0.05 g, 0.123 mmol) to give the product [ReBr(CO)$_3$(**69**)] as a yellow/orange powder (0.085g, 0.0963 mmol). ^{1}H NMR (400 MHz, CDCl$_3$) δ 9.39 (1H, dd, *J* = 5.1, 1.4 Hz, phen-*H*), 9.35 (1H, dd, *J* = 8.3, 1.4 Hz, phen-*H*), 9.27 (1H, dd, *J* = 5.0, 1.4 Hz, phen-*H*), 8.22 – 8.18 (2H, m, Ar-*H*), 7.95 (1H, dd, *J* = 8.2, 5.1 Hz, Ar-*H*), 7.79 – 7.75 (2H, m, Ar-*H*), 7.69 – 7.64 (1H, m, Ar-*H*), 7.60 (1H, dd, *J* = 8.6, 1.4 Hz, Ar-*H*), 7.56 – 7.50 (3H, m, Ar-*H*), 7.39 (1H, s, Ar-*H*), 7.28 – 7.24 (2H, m, Ar-*H*), 7.21 – 7.17 (2H, m, Ar-*H*), 2.47 (6H, d, *J* = 5.9 Hz, Ar-C*H*$_3$) ppm. ^{13}C {^{1}H} NMR (101 MHz, CDCl$_3$) δ 197.1, 197.0, 189.1, 164.9, 153.2, 152.4, 151.8, 150.8, 145.5, 145.2, 141.7, 141.5, 136.9, 136.7, 134.1, 133.0, 133.0, 130.6, 130.4, 130.3, 129.2, 128.8, 127.6, 126.9, 126.4, 126.1, 126.0, 125.7, 125.0, 122.3, 122.2, 21.5 ppm. IR(KBr plates): 3063 (w), 2019 (s), 1890 (bs), 1735 (s), 1711 (s), 1600 (m), 1510 (w), 1469 (m), 1450 (m), 1361 (w), 1262 (s), 1207 (s), 1168 (s), 1059 (s), 1023 (m), 808 (m), 739 (w), 707 (s) cm^{-1}. UV-vis λ_{max} (ε / M^{-1} cm $^{-1}$) (CHCl$_3$): 277 (67 000), 299 (sh) (43 800), 336 (sh) (14 400), 422 (6300) nm.

4.11 References

(1) Benniston, A. C.; Harriman, A.; Lawrie, D. J.; Mehrabi, M. *Eur. J. Inorg. Chem.* **2005**, 1384.

(2) Ali, M.; Nasir, S.; Nguyen, Q. H.; Sahoo, J. K.; Tahir, M. N.; Tremel, W.; Ensinger, W. *J. Am. Chem. Soc.* **2011**, *133*, 17307.

(3) Baggi, G.; Boiocchi, M.; Ciarrocchi, C.; Fabbrizzi, L. *Inorg. Chem.* **2013**, *52*, 5273.

(4) Sessler, J. L.; Melfi, P. J.; Pantos, G. D. *Coordin. Chem Rev.* **2006**, *250*, 816.

(5) Lhoste, J.; Henry, N.; Loiseau, T.; Guyot, Y.; Abraham, F. *Polyhedron* **2013**, *50*, 321.

(6) Kolarik, Z.; Mullich, U.; Gassner, F. *Solvent Extr. Ion Exch.* **1999**, *17*, 1155.

(7) Juris, A.; Campagna, S.; Bidd, I.; Lehn, J.-M.; Ziessel, R. *Inorg. Chem.* **1988**, *27*, 4007.

(8) Frenzel, B. A.; Schumaker, J. E.; Black, D. R.; Hightower, S. E. *Dalton Trans.* **2013**, 12440.

(9) Wang, D.; Xu, Q.-L.; Zhang, S.; Li, H.-Y.; Wang, C.-C.; Li, T.-Y.; Jing, Y.-M.; Huang, W.; Zheng, Y.-X.; Accorsi, G. *Dalton Trans.* **2013**, *42*, 2716.

(10) Abel, E. W.; Dimitrov, V. S.; Long, N. J.; Orell, K. G.; Osborne, A. G.; Pain, H. M.; Sik, V.; Hursthouse, M. B.; Mazid, M. A. *J. Chem. Soc. Dalton Trans.* **1993**, 597.

(11) Li, H. C.; Liu, S. W.; Wang, L. X.; Jing, X. B.; Wang, F. S.; Wu, H. B.; Peng, J. B.; Cao, Y. *Synth. Met.* **2003**, *135*, 203.

(12) Beharry, A. A.; Sadovski, O.; Woolley, G. A. *J. Am. Chem. Soc.* **2011**, *133*, 19684.

(13) Yam, V. W.; Lau, V. C.; L-X., W. *J. Chem. Soc., Dalton Trans.* **1998**, 1461.

(14) Gross, K. C.; Seybold, P. G. *Int. J. Quantum. Chem.* **2000**, *80*, 1107.

(15) Boricha, V. P.; Patra, S.; Chouhan, Y. S.; Sanavada, P.; Suresh, E.; Paul, P. *Eur. J. Inorg. Chem.* **2009**, 1256.

(16) Thorp-Greenwood, F. L.; Coogan, M. P.; Hallett, A. J.; Laye, R. H.; Pope, S. J. A. *J. Organomet. Chem.* **2009**, *694* 1400.

(17) Veroni, I.; Mitsopoulou, C. A.; Lahoz, F. J. *J. Organomet. Chem.* **2008**, *693*, 2451.

Chapter 5 : Synthesis and characterisation of substituted imidazole [4,5-f]-1,10-phenanthroline derived uranyl complexes

5.1 Introduction

This chapter describes the synthesis and characterisation of uranyl-[4,5-*f*]-1,10-phenanthroline complexes and explores the photophysical attributes of these molecules. Studies of these complexes are important towards understanding the coordination chemistry of the 5*f* elements and provide a possible route for the detection of the uranyl species "UO_2^{2+}" in the environment.

Uranium prefers to bind two axial oxygen atoms to form the linear UO_2^{2+} in the +6 oxidation state.[1] It can then bind numerous equatorial donors (commonly from 4 to 6) depending on the nature (hard/ soft) and the steric bulk of the ligands.[2] The uranyl ion is regarded as a Lewis acid, preferring hard-donors such as O-based ligands. However the uranyl ion has also shown good ability to form complexes with S- and N- donor ligands. [3-5] As all of the complexes detailed in this chapter involved binding through the 1,10-phenanthroline moiety, an overview of this area of chemistry will also be given.

5.1.1 The actinide series

The actinide series occupies the area of the periodic table between actinium and rutherfordium. Despite the actinide series being named after actinium, it is not truly an *f*-block element and is considered a group 3 element.[6] The gradual filling of the 5*f* orbitals leads to the formation of the actinide series (also known as the actinoid series) which displays distinct chemistry compared to the transition metals and even the 4*f*-filled lanthanide series. Only three members of the actinide series are naturally occurring, Th, Pa and U. Uranium was first discovered in 1789 (to be discussed in more detail later in the chapter), followed 39 years later by the discovery of thorium by Berzelius.[7,8] It was not until 1913 that protactinium was discovered by Meitner and Hahn.[9] All other transuranium elements were prepared synthetically, via nuclear reactions, usually by bombarding heavy actinide elements with lighter elements or neutrons. Between 1940 and 1961 all eleven transuranic elements were discovered by nuclear reactions. For example, the first synthesis of plutonium involved the bombardment of ^{238}U with ^{2}H.[10]

All actinides are radioactive (only the elements with the longest decay lifetimes are naturally occurring), which is a trait that can be harnessed in processes such as nuclear energy production (to be discussed later).

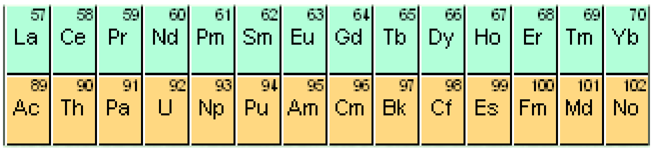

57 La	58 Ce	59 Pr	60 Nd	61 Pm	62 Sm	63 Eu	64 Gd	65 Tb	66 Dy	67 Ho	68 Er	69 Tm	70 Yb
89 Ac	90 Th	91 Pa	92 U	93 Np	94 Pu	95 Am	96 Cm	97 Bk	98 Cf	99 Es	100 Fm	101 Md	102 No

Figure 118: The lanthanides and actinides. Image taken from [11]

5.1.2 The f-orbitals

All lanthanides and actinides contain *f*-orbitals, which are commonly represented by two different sets, the cubic set (Figure 119) and the general set (Figure 120). The cubic set is more useful as a reference for molecules in which the x, y and z axes are symmetry-related (e.g. O_h or T_d point groups). The general set is used for other complexes where the x, y, and z axes are not symmetry-related.

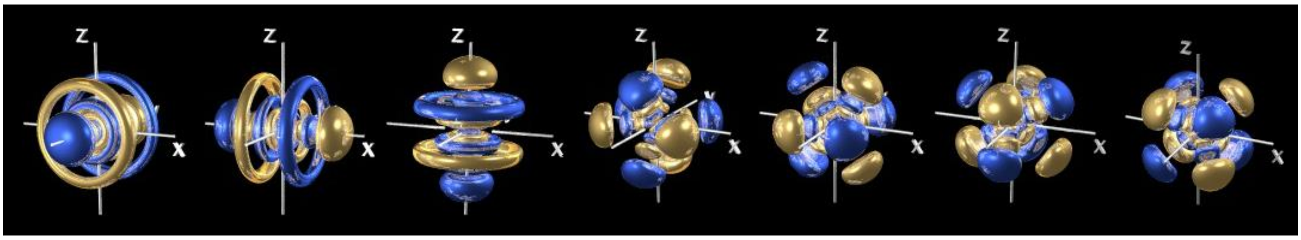

Figure 119: The cubic set for the f orbitals. From left to right: $7f_{y}^{3}$, $7f_{x}^{3}$, $7f_{z}^{3}$, $7f_{x(z^2-y^2)}$, $7f_{y(z^2-x^2)}$, $7f_{z(x^2-y^2)}$, $7f_{xyz}$. *Modified from* [12]

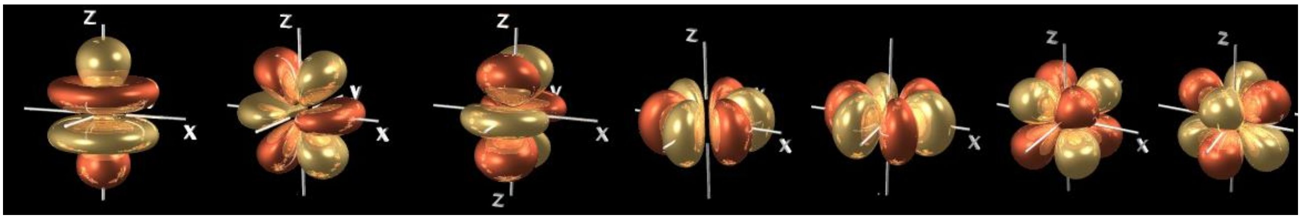

Figure 120: The general set for the f orbitals. From left to right: $4f_{z}^{3}$, $4f_{xz}^{2}$, $4f_{yz}^{2}$, $4f_{y(3x^2-y^2)}$, $4f_{x(x^2-3y^2)}$, $4f_{xyz}$, and $4f_{z(x^2-y^2)}$. [13]

The principal quantum numbers for an *f*-orbital is n = 4 (for a lanthanide) and n = 5 (for an actinide). The angular quantum number is *l* = 3, and the values for the magnetic quantum number m_l = -3, -2, -1, 0, 1, 2, 3. The m_l values give a set of seven degenerate *f* orbitals (as seen above), which are *ungerade*. The unique nature of the *f*-orbitals gives the lanthanides and actinides some unique chemical characteristics which differentiates them from the *d*-block metals.[14]

5.1.3 Electronic configuration and oxidation states of the actinides

Table 28 shows the electronic configuration of the actinide series. These are often difficult to determine given the complexity of their respective electronic spectra, but the table below presents the generally accepted ground electronic configurations of the actinide *f* elements.[6]

Element	Symbol	Atomic number	Electronic configuration
Thorium	Th	90	$[Rn]6d^27s^2$
Protactinium	Pa	91	$[Rn]5f^26d^17s^2$
Uranium	U	92	$[Rn]5f^36d^17s^2$
Neptunium	Np	93	$[Rn]5f^46d^17s^2$
Plutonium	Pu	94	$[Rn]5f^67s^2$
Americium	Am	95	$[Rn]5f^77s^2$
Curium	Cm	96	$[Rn]5f^76d^17s^2$
Berkelium	Bk	97	$[Rn]5f^97s^2$
Californium	Cf	98	$[Rn]5f^{10}7s^2$
Einsteinium	Es	99	$[Rn]5f^{11}7s^2$
Fermium	Fm	100	$[Rn]5f^{12}7s^2$
Mendelevium	Md	101	$[Rn]5f^{13}7s^2$
Nobelium	No	102	$[Rn]5f^{14}7s^2$
Lawrencium	Lr	103	$[Rn]5f^{14}6d^17s^2$

Table 28: Electronic configuration of the actinides[6]

The actinide series differs from the lanthanide series in particular in the availability of many oxidation states compared to lanthanides which commonly prefer the +3 oxidation state. Table 29 shows the oxidation states available to each actinide in their compounds, with the most stable oxidation state highlighted in bold.[6]

Element	Formal oxidation state
Thorium	+3, **+4**
Protactinium	+3, +4, **+5**
Uranium	+3, +4, +5, **+6**
Neptunium	+3, +4, **+5**, +6, +7
Plutonium	+3, **+4**, +5, +6, +7
Americium	+2, **+3**, +4, +5, +6
Curium	**+3**, +4
Berkelium	**+3**, +4
Californium	+2, **+3**, +4
Einsteinium	+2, **+3**
Fermium	+2, **+3**
Mendelevium	+2, **+3**
Nobelium	**+2**, +3
Lawrencium	**+3**

Table 29: Available oxidation states of the actinide compounds. [6]

From Table 29 we can see that there is a large range of oxidation states available to the actinides, particularly early in the series, where they have oxidation states more likened to transition metals than later on in the series. The reason for this lies in the relative energies of the *d* and *f* orbitals of the lanthanide and actinides.[15] Early in the actinide series the 6*d* orbitals are lower in energy than the 5*f* orbitals, which can be seen in the manner that Pa, U and Np are the only elements apart from Cm which contain a 6*d* electron (Table 29). The 5*f* orbitals are not shielded in the same way that lanthanides are shielded by the filled *s* and *p* subshells (in the case of actinides 6*s* and 6*p*). The 5*f* orbitals are therefore not "buried" or "core-like" like the 4*f* orbitals in lanthanides, and the near degeneracy of the 5*f*, 6*d*, and 7*s* electrons means that more electrons can be contributed towards compound formation and as such a larger number of oxidation states can be accessed.

5.1.4 Relativistic effects

Also important for consideration of oxidation states are relativistic effects on the actinides. Relativity plays an important part of the chemistry of elements with large atomic numbers. Einstein's Special Theory of Relativity tells us that the mass of a particle is linked to its velocity, which cannot exceed the speed of light, c.[6] As velocity, v, increases toward c, so does the mass of the particle increase towards ∞. The mass of a particle, *m*, at a specific velocity, *v* is related to the mass of the particle at rest m_0 by Equation 13.

$$m = \frac{m_0}{\sqrt{1 - \left(\frac{v}{c}\right)^2}}$$

Equation 13

The *v*/*c* term can be calculated for an atom of atomic number, Z, as the radial velocity of an electron is approximately Z, and the speed of light c can be expressed in atomic units of 137. Therefore for uranium, *v*/*c* is represented as

$$\frac{v_{rad}}{c} \approx \frac{92}{137} \approx 0.67$$

Equation 14

When this value is applied to Equation 14, the result of relativistic effect is that the mass of an electron in uranium, $m \approx 1.35m_e$. From these equations it is clear that relativistic effects are more pronounced in heavier atoms. The effects are also more pronounced in valence *d* and *f* orbitals which are not stabilised as the *s* and *p* orbitals are, due to the increased shielding from the outer core *s* and *p* electrons of similar radial distribution to the *d* and *f* functions. This results in the expansion and destabilisation of the *d* and *f* orbitals compared to if there were no relativistic effects. The orbital expansion affects the chemistry of the 5*f* electrons in uranium, which have a binding energy of 1665 kJmol^{-1} when calculated using non-relativistic effects and a binding energy of 869 kJmol^{-1} when calculated using relativistic effects. Using the relativistic calculations the electrons are clearly now more weakly bound and as a result are more chemically active, which could lead to a larger range of oxidation states. Relativistic effects are greater for 5*f* electrons compared to 4*f* electrons due to the larger atomic number, and as a result this could explain why 5*f* elements often show a greater number of oxidation states compared to 4*f* elements.

5.1.5 The lanthanide and actinide contractions

The lanthanide and actinide contraction describes the greater than expected decrease in ionic radii in the lanthanides and actinides when moving across a period. Elsewhere in the periodic table there is also a decrease in atomic radii across a period, however the decrease is less pronounced than for lanthanides and actinides as the increase in nuclear charge (which causes the contraction of the atom) is offset by shielding from electrons in the *s*, *p* and *d* orbitals. However for lanthanides and actinides this effect is not observed as each additional *f* electron which is added does not effectively shield the valence electrons from the increase in nuclear charge. The increased *effective* nuclear charge that is experienced by the valence electrons causes them to be attracted towards the nucleus and therefore a lanthanide or actinide contraction is observed. This has a profound effect on the periodic table, as the difference between the sizes of the third row transition metals compared to the second row metals would be expected to be similar to the difference between that of the first and second row metals.

However due to the poor shielding effects of the *f* electrons this is not the case, in fact the second and third row transition metals have very similar atomic radii.

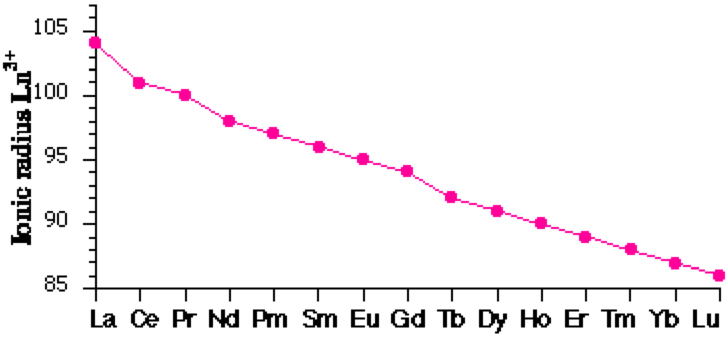

Figure 121: Ionic radius of Ln^{3+} ions.[16]

This effect is also observed for the actinide elements, although due to the low lifetimes of the transactinide elements it is difficult to ascertain what effect this would have on the 6*d* elements.

5.2 Uranium

5.2.1 Background

Uranium is the heaviest naturally occurring element found on earth. It has two main stable isotopes, ^{235}U (99.275%) and ^{238}U (0.720%), although other stable isotopes are also found in trace amounts (e.g. ^{234}U in 0.0059% abundance).[17] It was first discovered by Klaproth in 1789 from pitchblende, when he reduced the naturally occurring oxide with carbon to form a black solid which was metallic in appearance.[18] It was assumed that this was metallic uranium, and was believed to be so for another 50 years. However in 1841 Frenchman Péligot proved that the material isolated by Klaproth was the oxide UO_2, which he successfully converted to the metal.[19] After the initial discovery that uranium was a radioactive material by Becquerel,[17] work by Hahn and Strassmann discovered the ability of uranium to undergo nuclear fission, which led to uranium occupying a position of critical importance in the field of nuclear energy.[17,20]

5.3 The uranyl ion

The uranyl ion, UO_2^{2+}, is the most common and stable form of uranium, comprising a linear O=U=O with short U-O bondlengths (1.7-1.9 Å).[15] The uranium in this ion has a +6 oxidation state, and lower oxidation state uranium complexes often revert to this ion when exposed to oxygen. UO_2^{2+} complexes typically have other coordinated ligands around the equatorial plane, and the number of ligands that can coordinate in this region (usually between 4-6) is dependent on the bonding nature of the ligand

and also its steric bulk. This means that the uranyl ion can form complexes with different structures such as octahedral, pentagonal bipyramidal and hexagonal bipyramidal (Figure 122).

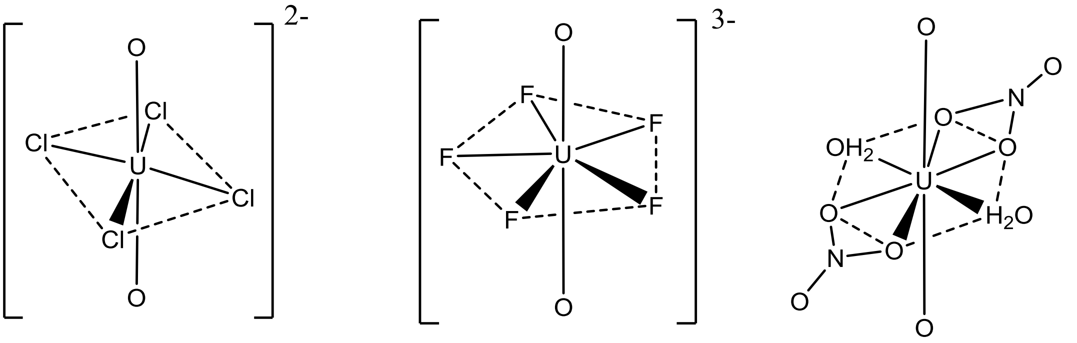

Octahedral Pentagonal bipyramidal Hexagonal bipyramidal

Figure 122: Coordination in the equatorial plane of uranyl (VI) ions[6]

5.3.1 Bonding in the uranyl ion

The molecular orbital energy diagram below (Figure 123) shows the orbitals involved with bonding of the UO_2^{2+} ion. Six linear combinations of the 2p orbitals in the oxygen atoms can bond to the 5*f* or 6*d* orbitals of the uranium atom (σ_u, σ_g, 2 x π_g, 2 x π_u) .[6] The U(VI) atom does not have any electrons in the *f*-orbital to contribute to the bonding, therefore 6 electrons are donated from each O^{2-} to fill the 6 bonding orbitals. This gives each U-O bond a formal bond order of 3 (triple bonded). The nature of this bonding creates a remarkably stable species.

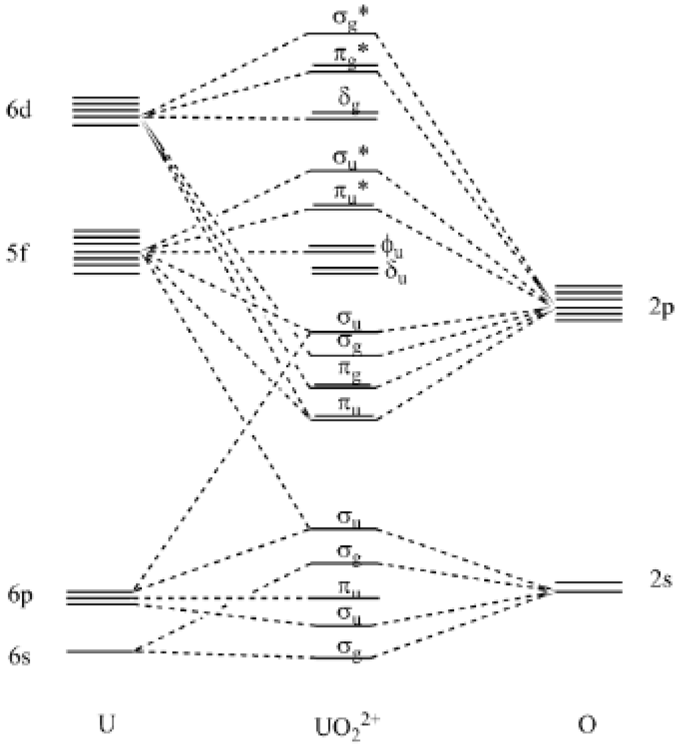

Figure 123: Molecular orbital diagram of the bonding in free uranyl ion (D_nh).[21]

5.3.2 Coordination chemistry of the uranyl ion

As this thesis will mostly investigate coordination with N-donor ligands a brief overview of some notable examples will now be given, along with some examples of O-donor ligand complexes. A review in 2006 by Sessler et al. has detailed recent uranium cation complexes with nitrogen containing ligands appearing in the literature between 2000 and 2005.[22] The review focuses on a wide range of ligands, including salicylaldehyde, pyrrole, polyamido, pyridine and pyrazine-derived ligands. The ligands reviewed also varied in the number of nitrogen donors in the ligands, and included bidentate, tridentate, tetradentate, hexadentate and macrocyclic molecules.

5.3.2.1 Uranyl complexes with N-donor ligands

Uranyl complexes that incorporate N-donor ligands have become a much studied area of chemistry, which exploits the ability of the uranyl ion to bind to soft ligand donors. A paper published in 2009 describes how multiple N-donor ligands can be incorporated into a U(V) complex containing β-diketiminate ligand (**70**).[23] The scheme for the formation of the starting material is shown in Scheme 8.

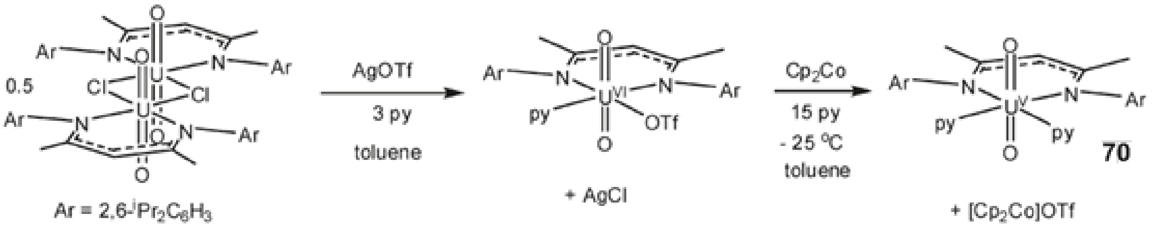

Scheme 8: Formation of starting material **70** where Cp_2Co = Bis(η^5-cyclopentadienyl)cobalt.[23]

The starting material **70** was reacted successfully with a variety of N-donor ligands, namely 2,2′-bipyridine (bipy), 1,10-phenanthroline (phen), tetramethylethylenediamine (TMEDA), or 1-methylimidazole (MeIm) to form $[UO_2(Ar_2nacnac)(bipy)]$, $[UO_2(Ar_2nacnac)(phen)$, $UO_2(Ar_2nacnac)(TMEDA)]$, and $[UO_2(Ar_2nacnac)(MeIm)_2]$ (Complexes **71a-d**,Scheme 9). Each of the complexes were characterised by X-ray crystallography.

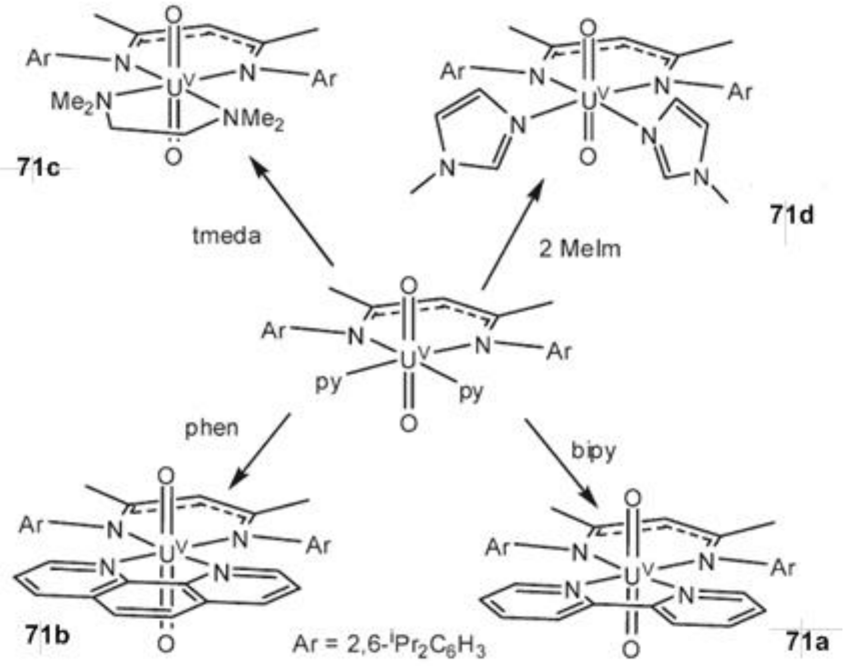

Scheme 9: Formation of uranyl complexes containing N-donor ligands.[23]

Each of the complexes exhibited *f*→*f* transitions, which despite being Laporte forbidden are allowed by heavy atom spin-orbit coupling. They manifested themselves in the electronic absorption spectrum as weak, sharp peaks at low energy 750-780 nm, and low intensity ($\varepsilon = 290\ M^{-1}cm^{-1}$ in the case of **70**). It was evident from this data that the complex formed was indeed a U(V) complex (i.e. containing a f^1 configuration). The IR spectroscopic data confirmed the presence of the O=U=O unit through asymmetric stretches (ν_{asym}) between 810-819 cm^{-1} in each instance. The isostructural U^{6+} (i.e $[UO_2(nacnac)]^+$) fragment did not accommodate any of the N-donor ligands, which was attributed to the higher polarisability of the U^{5+} ion making the coordination of N-donors more favourable relative to the U^{6+} ion. In a competition experiment between phen, bipy and TMEDA it was found that preferential coordination to the uranyl centre was in the order of phen>TMEDA>bipy. This ability of phen to displace bipy was attributed to the lower reorganizational energy required for phen to bind to a metal ion, and the ability of TMEDA to displace bipy was attributed to its higher Bronstead basicity.

A 2004 paper by Berthet et al. has highlighted how different N-donor ligands can potentially coordinate around the equatorial axis by incorporating phen, bipy and terpy (terpyridine) in differing amounts to $[UO_2(OTf)_2]$ (Figure 124).[24]

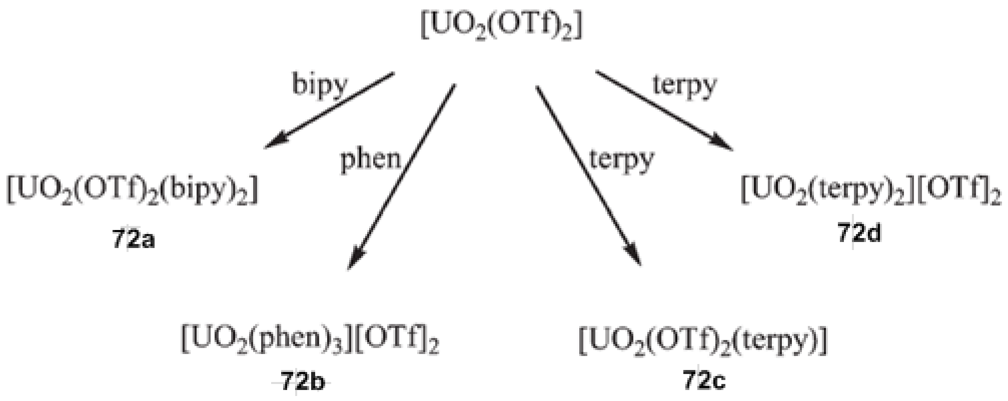

Figure 124: Reactions of polypyridine bases with $[UO_2(OTf)_2]$ to form complexes **72a-d**.[24]

The incorporation of these highly bulky N-donor ligands can lead to out-of-plane coordination, which is not commonly observed for uranyl complexes. For example **72a** and **72b** exhibited coordinating ligand atoms around the UO_2^{2+} ions which were far from co-planar which were best described as rhombohedral or bi-end-capped trigonal antiprism as opposed to the polygonal bipyramidal geometry usually employed by uranyl complexes.

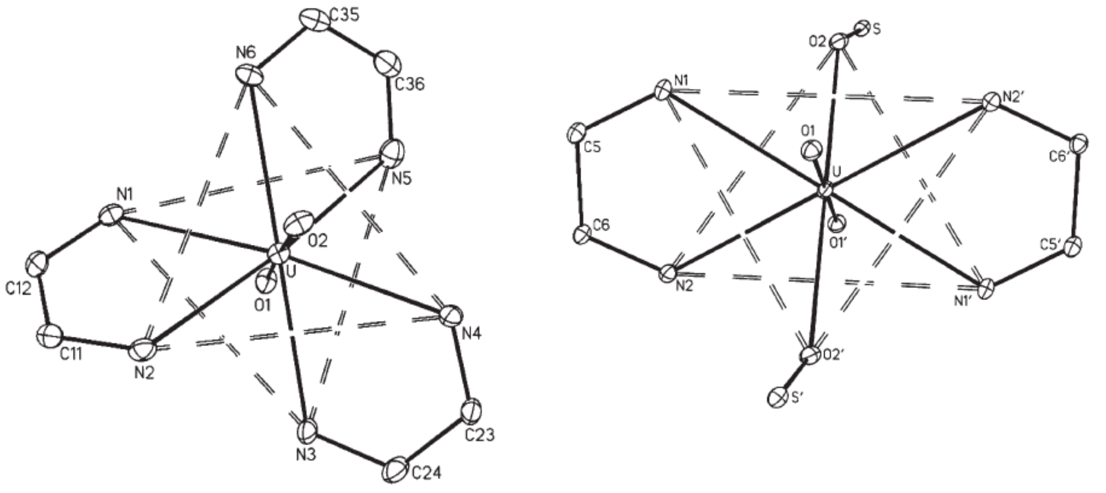

Figure 125: Crystallographic data of the immediate UO_2^{2+} environment of **72b** (left) and **72a** (right).[24]

The least-square planes UN_4O_2 in **72a** and UN_6 in **72b** are defined by a route-mean-square (rms) deviation of 0.56 and 0.60 Å, respectively, indicating the extent of which the ligands are out of plane. The results indicated that the uranyl ion successfully coordinates several neutral N-donors through the use of weakly coordinating counter ions and anhydrous solvents. The N-donors are then tilted from the equatorial plane and induce the displacement of the other coordinating ligands out of this plane.

5.3.2.2 Uranyl-diimine complexes

Although less common than O-donor ligand complexes, there is still a number of reported complexes which incorporate the 1,10-phenanthroline or 2,2′-bipyridine (bipy) motifs.[1,4,5,24-32] For example, Huang and co-workers have isolated a trinuclear uranium (VI) complex (**73**, Figure 126) which incorporates phenanthroline moieties.[1]

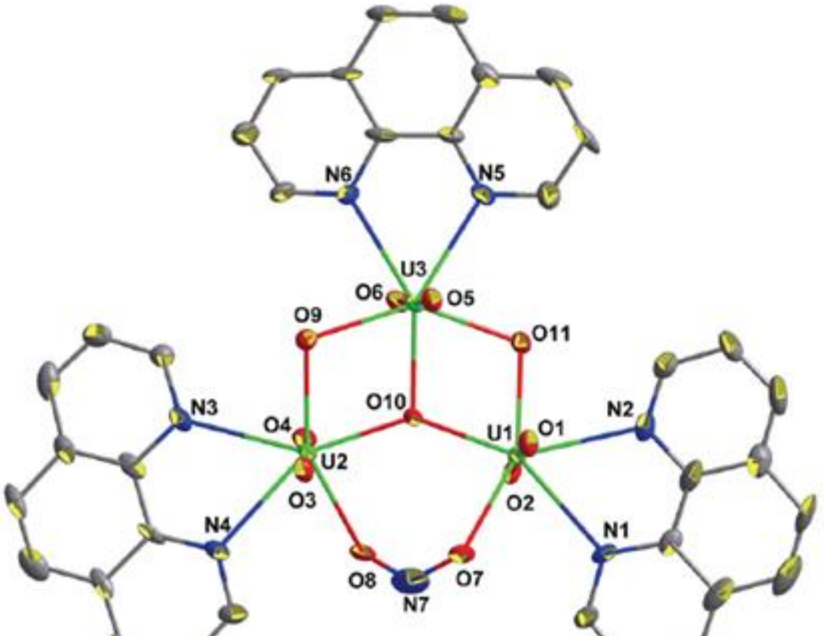

73

Figure 126: X-ray crystal structure of trinuclear uranium (VI) complex **73**.

The bond lengths of the U=O bonds of the UO_2 moiety were found to be in the range of 1.771(3)–1.790(3) Å and the bond lengths for the U-O moieties were found to be 2.250(3)–2.368(3) Å. The U-N bond lengths were slightly longer than the U-O bond lengths with a value between the ranges of 2.604(3) to 2.707(4) Å. As the uranyl ion prefers hard donors it will coordinate more strongly to the oxygen donors and more weakly to the nitrogen donors. This is reflected in the bond lengths which have shorter values for the U-O bonds. The electronic absorption spectrum of this complex showed two bands which are common for complexes of this type. The first was an absorption below 388 nm, assigned to a charge transfer centred around the U=O part of the molecule, the second is a LMCT associated with the oxygen or nitrogen donors around the equatorial plane which was centred around 388-530 nm. The luminescence spectra of the complex showed one broad band centred at about at 525 nm was observed, which was tentatively assigned a LMCT occurring between the 5*d* orbital of U(VI) and the chromophoric phenanthroline ligand (Figure 127).

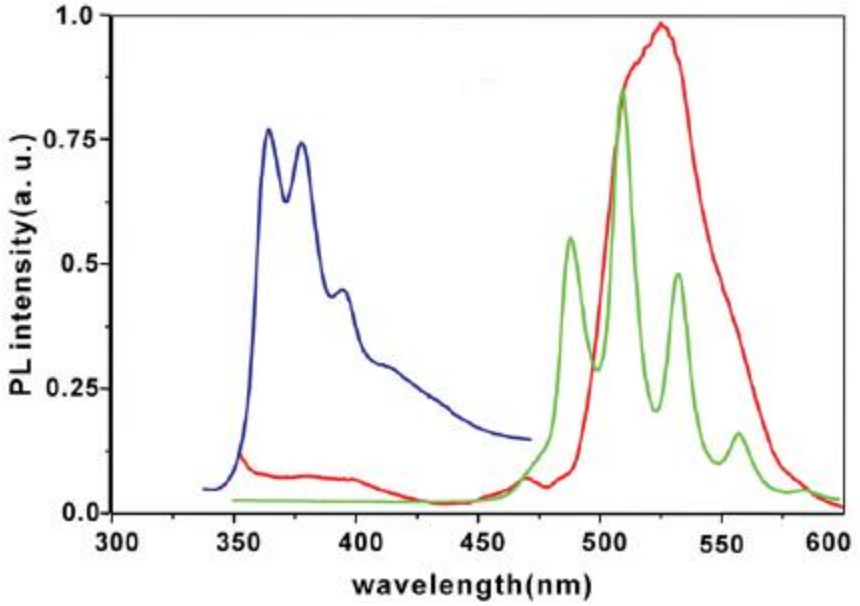

Figure 127: Luminescence spectra of 1,10-phenanthroline (blue line), [$UO_2(NO_3)_2.6H_2O$] (green line) and **73** (red line). [1]

The first crystal structure of uranyl-bipy complexes were described in 1985 by Alcock, when the crystal structures of [UO_2(bipy)$(NO_3)_2$], **74a** and [UO_2(bipy)$(CH_3COO)_2$], **74b** were reported (Figure 128).[33]

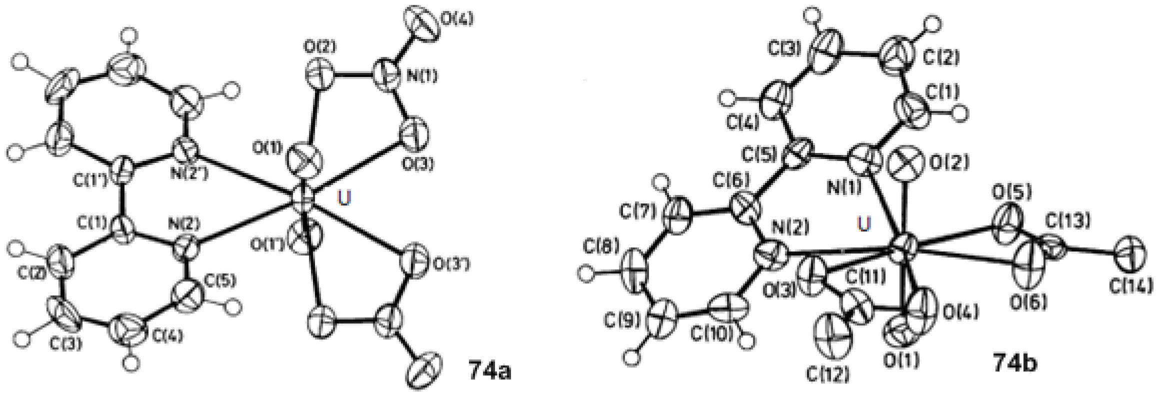

Figure 128: Molecular structures of **74a** (left) and **74b** (right).[33]

The key bond lengths reported for **74a** are described in Table 30.

Bond	Bond length (Å)
U-O (Uranyl)	1.763 (13)
U-O (Nitrate)	2.49 (13)
U-N (bipy)	2.578 (13)

Table 30: Selected bondlengths of **74a.**[33]

The bond lengths of the UO_2 moiety are very short, 1.763 Å, which is a result of the high bond order (3)of this moiety. The bond distance does not vary compared to the trinuclear phenanthroline example which was described in Figure 126 (1.771-1.790 Å). The U-N (bipy) bond lengths were much longer than the U-O (uranyl) bond lengths, and also slightly longer than the U-O (nitrate) bond lengths. This indicated that the bonding is not as strong between the U-N bonds as between the U-O bonds due to the fact that uranium preferentially binds to hard donors. A slightly shorter bond length was observed for the **74a** complex (2.578 Å) compared to the uranyl-phenanthroline complex **73** (2.604-2.707 Å), although this is statistically insignificant.

A uranyl coordination polymer, $[(UO_2)_2$ (2,2′-bipy)-$(CH_3CO_2)(O)(OH)]$,**75** was reported in 2012.[34] The crystal structure obtained consisted of two uranyl pentagonal bipyramids that were linked through cation-cation interactions (Figure 129).

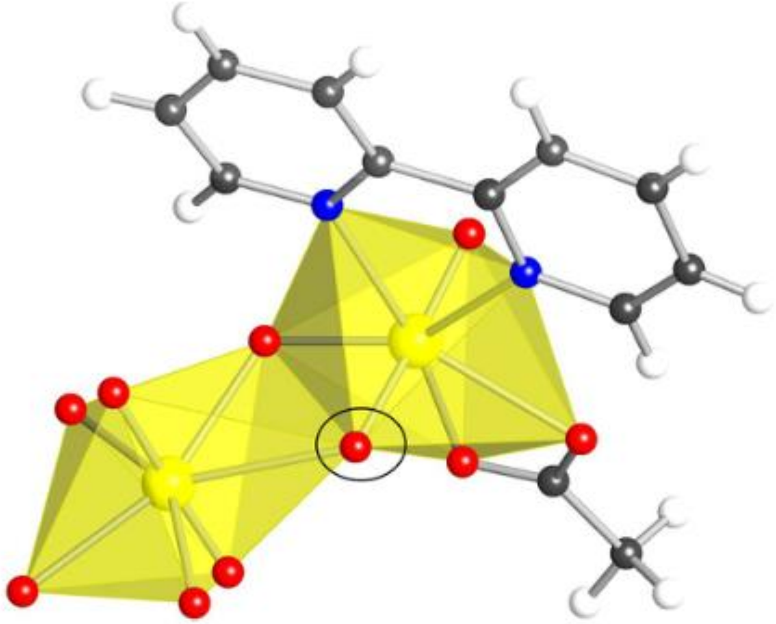

Figure 129: Illustration of the coordination environments of the two uranyl centres in **75**, black circle denotes cation-cation interaction.[34]

The electronic absorption spectrum of this complex exhibited the expected absorptions along with the fine structure associated with the charge transfer of the uranyl ion. The complex was found to be luminescent (Figure 130), emitting a green light when excited at 365 nm.

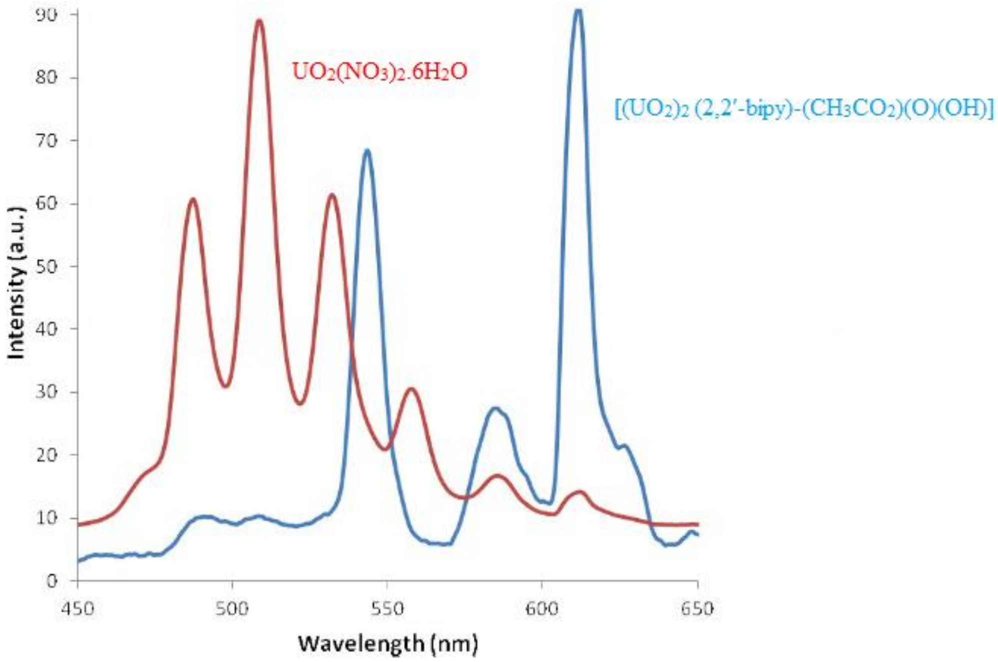

Figure 130: Emission spectra of $UO_2(NO_3)_2.6H_2O$ (red line) and **75** (blue line).[34]

The emission spectrum clearly displayed numerous shifted bands typical of uranyl compounds. The red-shift observed compared to $UO_2(NO_3)_2.6H_2O$ was attributed to the presence of the bipy in the equatorial plane.

5.3.2.3 Uranyl- imidazole[4,5-*f*]-1,10-phenanthroline complexes

There have been very few examples of an imidazole[4,5-*f*]-1,10-phenanthroline derivative being incorporated into an uranyl complex.[26,29] A complex reported by Cardinaels and co-workers, incorporated the imidazole[4,5-*f*]-1,10-phenanthroline motif in order to form metallomesogens (i.e. metal-containing liquid crystals).[26] The uranyl complex containing three imidazole[4,5-*f*]-1,10-phenanthroline coordinated molecules was isolated through reaction of uranyl triflate in ethanol (**76**, Figure 131). Typically, the design of metallomesogens involves the incorporation of a metal ion into a cavity of a flat macrocycle with peripherally attached alkyl chains. However it was discovered that complexes with a “propeller-like” molecular shape can exhibit columnar mesophases as well.[35] The uranyl ion provides a template for bringing the ligands into the correct position, giving the complex a “propeller” structure that allows it to behave as a metallomesogen. The complex did not display any luminescent properties in the solid state or solution.

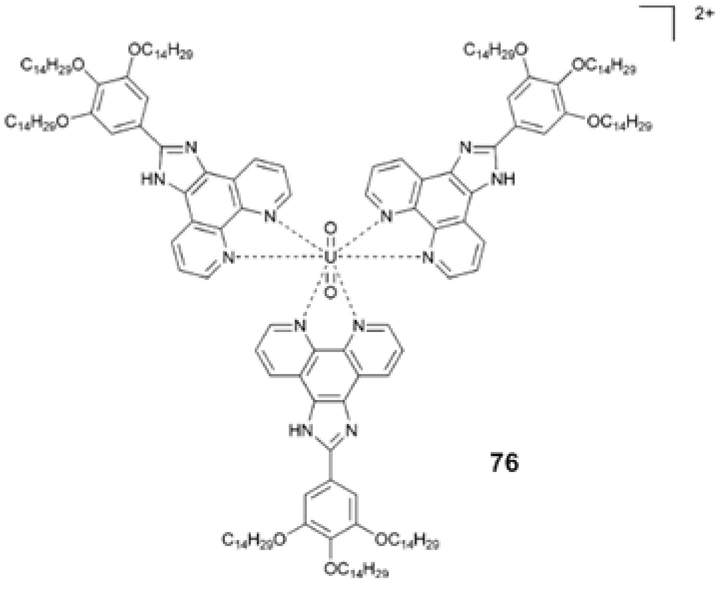

76

Figure 131: Molecular structure of metallomesogen **76**

Macrocyclic Schiff bases have been studied due to their ability to secure into their coordination moiety a specific molecule by a well-defined and specific recognition process. For example the molecule **77** (Figure 132) was reported in 2002 and contained numerous potential binding sites.[36]

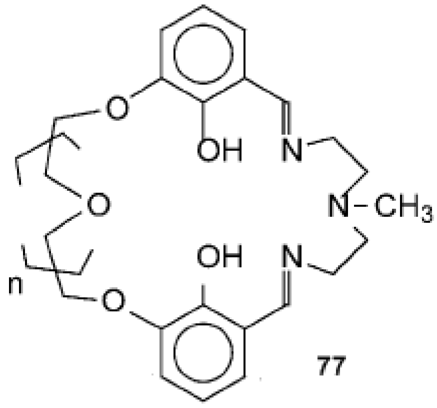

77

Figure 132: Molecular structure of **77a** (n =1) and **77b** (n=2)[36]

It was confirmed through IR, NMR and x-ray crystallography that the UO_2 moiety would successfully coordinate to the macrocycle in the N_3O_2 cavity as opposed to the O_2O_3 or O_2O_4 moiety (Figure 133).

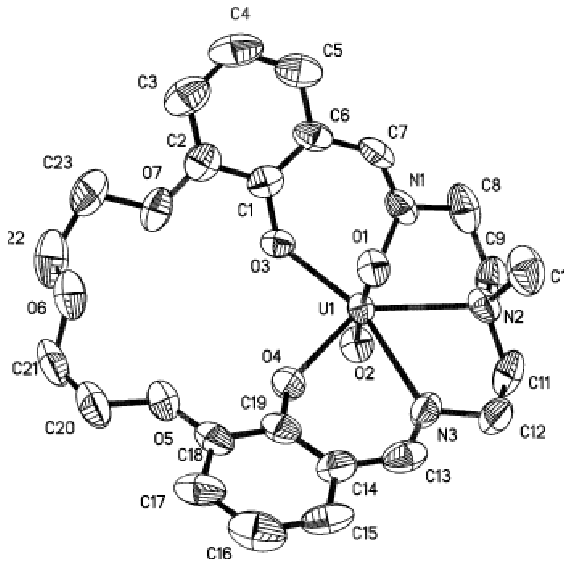

Figure 133: ORTEP view of **77a**

The U-O bond lengths in the uranyl moiety were found to be significantly shorter than the other U-O bonds (1.79Å compared to 2.26Å) which indicated a higher bond order. The U-N bond lengths were found to be 2.56 Å, slightly longer than the U-O bond lengths of the equatorial ligand. UO_2^{2+} invariably coordinated in this region of the macrocycle, which was in contrast to Ln(III) cations which would invariable coordinate in the crown-like chamber. This was taken as supramolecular evidence of the inherent preference of 5*f* cations to bind to “soft” donor ligands in comparison to 4*f* cations.

Complexation of the uranyl ion into a macrocycle is dependent on the size of the cavity, which must accommodate the axially bound oxygen atoms. For example, a macrocycle (**78**) designed for the purpose of uranyl coordination was reported in 2004 (Scheme 10).[37]

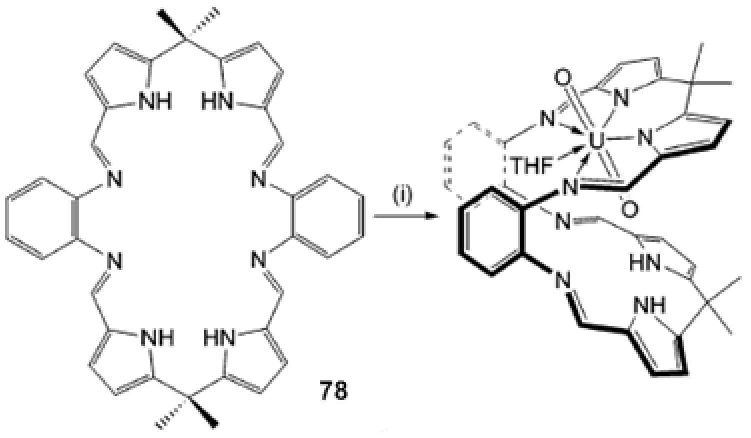

Scheme 10: Formation of [UO_2(THF)(H_2**78**)], (i)[UO_2(THF){N($SiMe_3$)$_2$}$_2$], THF.[37]

5.3.2.4 Coordination chemistry of the uranyl ion with O-donor ligands

One of the most common O-donor ligand types that have been investigated with regards to uranyl coordination is the acetylacetone (acac) ligand system. This will be described in detail in chapter 6 section 6.6 as it will relate more closely to the contents of that chapter. Therefore this section will give a brief overview of other O-donor ligands used in coordination chemistry with the uranyl ion, and comparisons to N-donor ligands. As was mentioned in section 5.3.1 the uranyl ion has access to more electrons from the *d* orbitals for bonding compared to lanthanides, and has a greater tendency to bind with soft donors as well as hard donors. A comparison of the preference of the uranyl ion to bind N-donor ligands over O-donor ligands has been explored by Sarsfield *et al.*[38] It was found that additions of R_3PNH (where R = phenyl or cyclohexyl) to solutions of $[UO_2Cl_2(R_3PO)_2]$ (**79a**) resulted in the selective displacement of the P=O ligands and the formation of phosphinimine complexes (Scheme 11). No such displacement was observed with the addition of R_3PO to $[UO_2Cl_2(R_3PNH)_2]$ (**79c**).

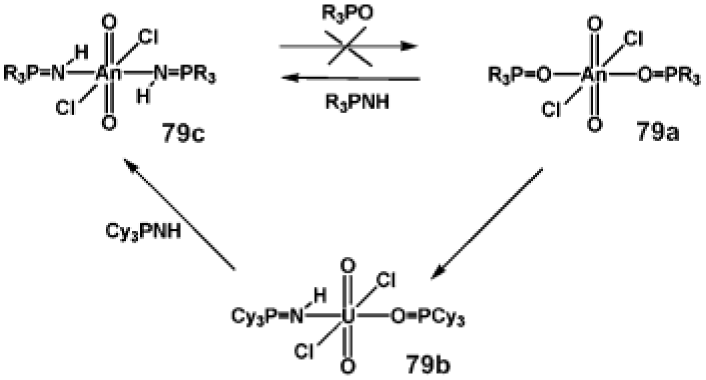

Scheme 11: Selective displacement of P=O. R =Phenyl, cyclohexyl, Cy = cyclohexyl, An = U.[38]

Addition of one equivalent of R_3PNH to **79a** resulted in the formation of an intermediate, $[UO_2Cl_2(R_3PO)(R_3PNH)]$, **79b** which would readily react with a further equivalent of R_3PNH to form **79c**.

A recent investigation by Gupta *et al* has explored the crystal structure, electrochemical behaviour and luminescence of uranyl complexes containing oxygen donor ligands.[39] The two complexes that were isolated and characterised are displayed in Figure 134.

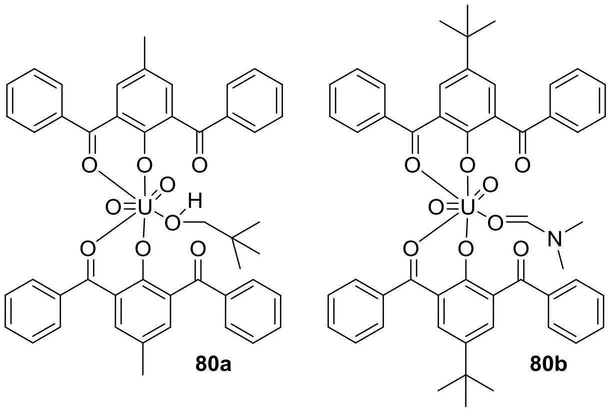

80a **80b**

Figure 134: Molecular structures of **80a** and **80b**

IR spectroscopy of the complexes confirmed the presence of a metal bound carbonyl which displayed a resonance at a lower frequency by 40-60 cm^{-1}, while the free carbonyl displayed the same resonance as the free ligand. The electronic absorption spectra of the two complexes displayed bands in the high energy region of the spectra (354–343 nm and 252–273 nm) which were attributed to intra-ligand transitions, and also weaker transitions arising from an O→U charge transfer (O 2*p*→U5*f*) which were observed at 418 and 435 nm for **80a** and **80b**, respectively. Luminescence studies of the complexes were undertaken at room temperature at various concentrations. Figure 135 shows the luminescence spectrum of **80b**. Excitation at 358 nm resulted in three weakly resolved bands, which were assigned as LMCTs occurring between the 6*d* orbital of the U and the chromophoric ligands.

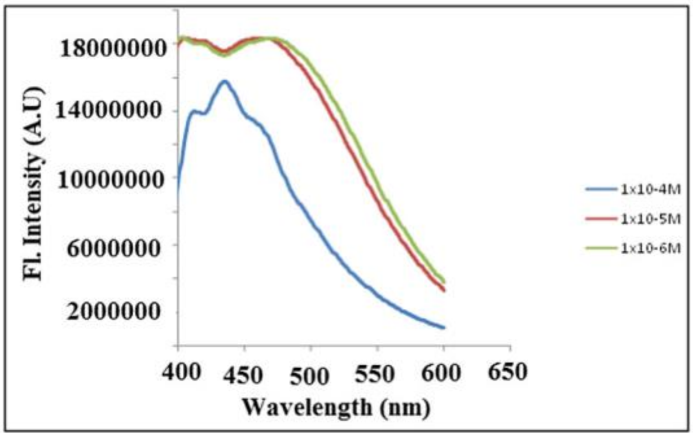

Figure 135: Luminescence spectra of **80b** at varying concentrations.[39]

5.4 Electronic absorption spectra of the uranyl ion

The photophysics and electronic absorption spectrum of the uranyl ion have been thoroughly investigated for about 50 years, and has been the subject of much debate and reviews.[2,40] Typically, uranyl based LMCT appear in the electronic absorption spectrum as a series of weak bands between ≈ 500 nm and 350 nm. The low intensity nature of the band is as a result of a triplet to singlet transition, which is spin-forbidden, however the presence of significant spin-orbit coupling means the transition is more intense than in the absence of significant spin-orbit coupling.[41] According to McGlynn and Smith, the fine structure of the absorption could be explained as the three components of the triplet state split by the local field. Further fine vibronic structure was then superimposed on these absorptions.

Recently work has been undertaken exploring the effects of ligands and counterions upon the position and nature of the LMCT band in the electronic absorption spectra. For example, the coordination of UO_2^{2+} with halides has been explored via UV in order to determine how the UO_2^{2+} favours “hardness” of the ligands. Figure 136 shows the decrease in intensity of the LMCT absorption upon addition of chloride to a DMF solution of $UO_2(DMF)_5(ClO_4)_2$, which then forms $[UO_2Cl_4]^{2-}$.[42]

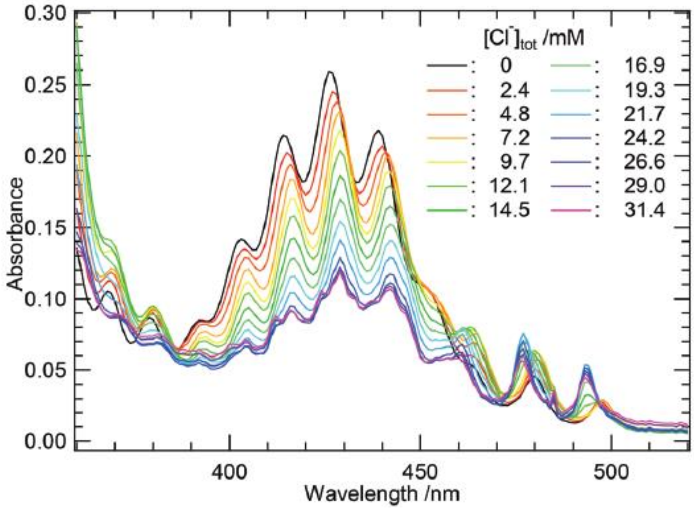

Figure 136: Electronic absorption spectra of $UO_2(DMF)_5(ClO_4)_2$ with increasing concentration of Cl^- (modified from [42])

It was concluded that chloride (the hardest halide that was explored) showed four distinct coordination steps (i.e. $[UO_2Cl_x]^{2-x}$ where x = 1,2,3 or 4), whilst the softer bromide only showed two steps. UV-vis titration experiments were undertaken in order to explore the stability constants of the halides, which proved that the harder chloride formed the most stable complex.

5.5 The uranyl emission

Uranyl exhibits a distinctive green emission (~500-550 nm), which is generally accepted to be due to a ligand to metal charge transfer (LMCT) from a bonding oxygen orbital to a vacant non-bonding 5*f* orbital of the uranium.[40] Similar to the electronic absorption spectra, fine structure is often observed for the emission spectra with 6 “hot bands” commonly observed for uranyl in solution and in the solid state.

The luminescence of uranyl has been reviewed as far back as 1974.[2] The photophysical behaviour of the uranyl ion in aqueous solution has been examined more recently by Formosinho *et* *al.* [43] Figure 137 displays the luminescence emission spectrum of uranyl nitrate in an aqueous acidic solution, the luminescence decay is shown inset.

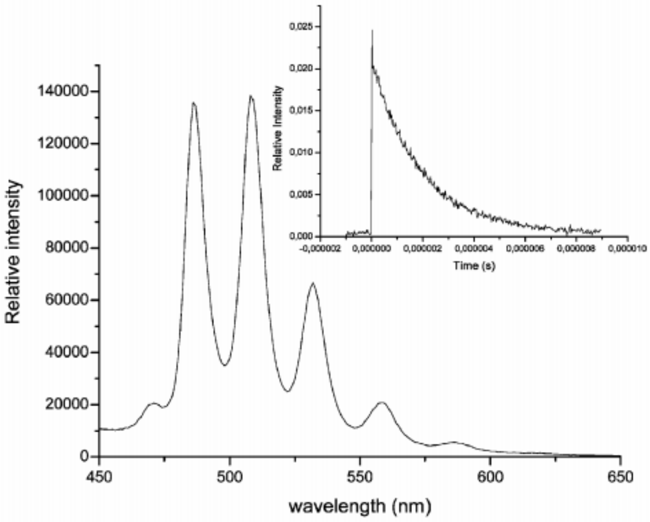

Figure 137: Emission spectrum of uranyl nitrate in aqueous acid. Inset: Decay curve of emission.[43]

The luminescence spectra of uranyl nitrate and perchlorate displayed typical structured uranyl ion emission. The decay of the emission was examined, and identical decays were observed at all wavelengths in the emission spectrum, and a luminescence lifetime of $\tau = 1.9$ μs was determined. The radiative decay constant (k_{rad}) of $[UO_2(H_2O)_5]^{2+}$ in aqueous solution was determined from the quantum yield and lifetime values to be 2.0×10^3 s^{-1}. This value strongly suggested that the transition involves a ground state which is essentially a spin singlet and an excited state with considerable triplet character.

5.5.1 Uranyl-centred emission

A phenanthroline-containing uranyl complex has been reported to display luminescence as a result of uranyl-based emission. $(UO_2)_2(phen)(BTEC)_2$ (BTEC = 1,2,4,5-benzenetetracarboxylic acid, **82**, Figure 138) has shown emission as a result of electronic transitions occurring solely within the UO_2 moiety.[27]

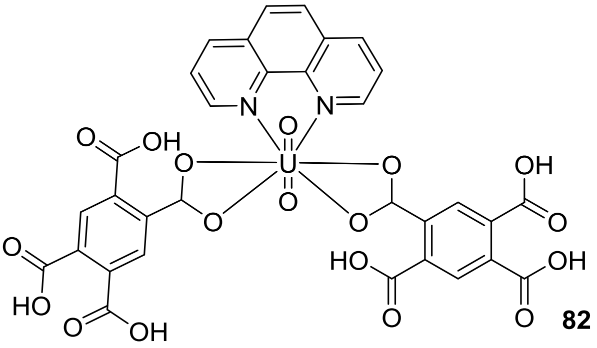

Figure 138: Structure of $(UO_2)_2$(phen)(BTEC)$_2$, **82**

The solid-state emission spectrum showed peaks at 491, 511 and 534 nm when excited at 341 nm which were attributed to uranyl ion emission from a ^{3}LMCT (O 2*p*→U5*f*). Smaller peaks were also observed at 560 and 586 nm, attributed to transitions from the first excited electronic level to the symmetric and antisymmetric vibrational levels of the uranyl ion. The excitation spectrum of this complex was sufficiently different from the ligands to rule out intra-molecular energy transfer from the ligand to the uranyl and that the uranyl ion was excited directly (Complex λ_{ex} = 341 nm, phen λ_{ex} = 322 nm and BTEC λ_{ex} = 300 nm). The observed fine structure of the emission is typical of uranyl-centred emission.

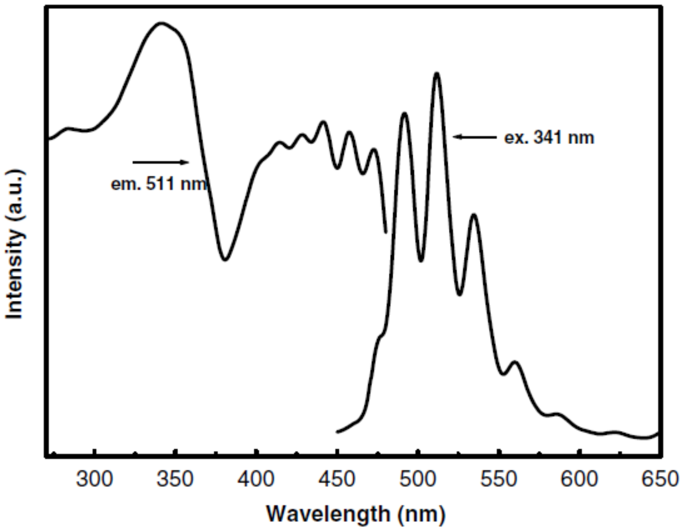

Figure 139: Excitation (left) and emission spectra of **82**. [27]

5.5.2 Ligand centred emission

Uranyl complexes have also exhibited emission centred solely on the equatorial ligands as opposed to the uranyl unit. For example, in 2008, a uranyl complex was reported (**83**) which incorporated 1,10-phenanthroline-2,9-dicarboxylic acid (PDA). [28] The free ligand was found to emit at 450 nm and was characterised by a broad, featureless band. UO_2(PDA) was found to be weakly emissive when excited at 365 nm.

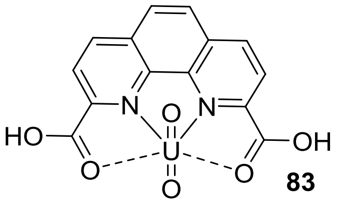
83

Figure 140: Molecular structure of complex **83**

Exploration of ligand-sensitized emission at 270 nm resulted in a similar spectrum. This led to the conclusion that the emission observed in this case is the fine structure of the PDA itself, and that the excitation at 365 nm gave rise to a uranyl emission being reabsorbed as a suggested MLCT. No lifetimes were reported for this complex.

5.6 Effects of substituents on uranyl infrared and raman spectra

It is known that the linear uranyl species has three vibrational modes, including the Raman active symmetric O=U=O stretch and O=U=O bending modes ($\nu_1 \approx 880$ and $\nu_2 \approx 210$ cm^{-1} respectively) and an infrared active asymmetric O=U=O stretch ($\nu_3 \approx 960$ cm^{-1}) as reported in 1953 by Jones and Penneman.[44] It has been discovered that the values of ν_1 and ν_3 can vary depending on the number and nature of ligands that are bound to the central uranium atom. Generally modestly complexing solution environments are found to display ν_3 frequencies in the region of 960 cm^{-1} such as $[UO_2(NO_3)_2]$(961 cm^{-1}) and $[UO_2(ClO_4)_2]$ (962.5 cm^{-1}).[45] It has been observed that ligands which donate more electron density to the uranium centre reduce the ν_3 frequency, although this has also been disputed.[46,47] Similarly, uranyl complexes which leave the uranium metal electron deficient such as anion complexes show an increase in value of the ν_3 antisymmetric stretch.[48]

5.7 Aims

- Isolate a series of uranyl-“lophine” complexes containing differing functional groups and confirm successful coordination through ^{1}H NMR spectroscopy.
- Exploit infrared spectroscopy to investigate the effects of differing lophine “ligands” on the uranyl and nitrate vibrational frequencies of the complex.
- Investigate the photophysical properties of the complexes, including the electronic absorption spectra and luminescence data.

5.8 Results and discussion

5.8.1 Synthesis of the complexes

Five substituted imidazole [4,5-*f*]-1,10-phenanthroline derived uranyl complexes have been isolated and characterised using ^{1}H NMR, infrared, electronic absorption and luminescence spectroscopy. Due to the radioactive nature of the complexes some characterisation techniques were not available for use such as $^{13}C\{^{1}H\}$ NMR spectroscopy and mass spectrometry. The isolated complexes incorporated a variety of differing functional groups, including extended chromophores, methoxy groups and azobenzene groups. The ligands incorporated into the complexes were **25**, **27** and **29** from chapter 2, ligand **50** from chapter 3 and ligand **62** from chapter 4.

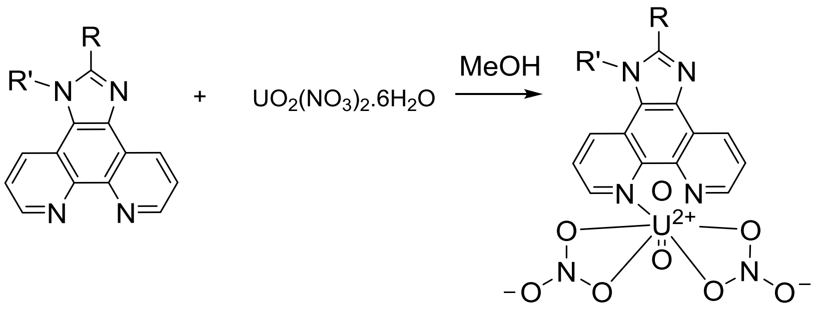

[$UO_2(NO_3)_2$(25)]: R = 4-^{t}Bu ; R' = 3,5-diMe

[$UO_2(NO_3)_2$(27)]: R = 4-^{t}Bustyr ; R' = 3,5-diMe

[$UO_2(NO_3)_2$(28)]: R = 4-^{t}Bustyr ; R' = 4-^{t}Bu

[$UO_2(NO_3)_2$(50)]: R = 2,3,4-trimethoxy ; R' = 3,5-diMe

[$UO_2(NO_3)_2$(62)]: R = 4^{t}Bu ; R' = azo

Scheme 12: Synthesis of the complexes

The complexes were obtained by reaction of equivalent amounts of ligand and uranyl nitrate hexahydrate in methanol at room temperature. Solid were obtained by the vapour diffusion of hexane into $CHCl_3$ to give the complexes in moderate to good yields as light orange, yellow or green powders. The table below shows the isolated complexes and their yields. The complexes displayed good solubility in a range of organic solvents, including $CHCl_3$, MeOH and DMSO.

Compound Number	R	R′	Yield (%)
$UO_2(NO_3)_2$**(25)**	4-^{t}Bu	3,5-diMe	67
$UO_2(NO_3)_2$**(27)**	4-^{t}Bustyr	3,5-diMe	91
$UO_2(NO_3)_2$**(28)**	4-^{t}Bustyr	4-^{t}Bu	77
$UO_2(NO_3)_2$**(50)**	2,3,4-trimethoxy	3,5-diMe	50
$UO_2(NO_3)_2$**(62)**	4-^{t}Bu	azo	88

Table 31: Isolated complexes

5.8.2 Characterisation of the complexes through ^{1}H NMR spectroscopy

Each of the complexes were characterised through ^{1}H NMR spectroscopy. In each instance a significant shift was observed for many of the proton signals, in particular those closest in proximity to the uranyl moiety. This is likely due to the fact that U(VI) is extremely electron withdrawing and as such the protons located on the phenanthroline moiety were significantly deshielded and shifted downfield. The shift of the furthest downfield signal to about +10.5 ppm is particularly pronounced compared to previously isolated uranyl-(phen) complexes which show chemical shifts to about 9.1 ppm.[25,26] It was assumed that each of the isolated complexes contained one coordinated lophine molecule, due to the stoichiometry applied. This could not be verified through the spectroscopic techniques available for compound containing radioactive materials (i.e. without ^{13}C{^{1}H} NMR and mass spectroscopy). This differs from some previous complexes which incorporate two or even three phenanthroline ligands into the complex. This may provide a possible explanation for the discrepancy in the chemical shift observed for the phenanthroline protons in the ^{1}H NMR. The highly electron deficient uranyl species does remove electron density away from the phenanthroline moiety; however the effect on each individual phenanthroline moiety will be lessened if the loss of electron density is spread over three substituents. As a result deshielding over the three phenanthroline moieties may be decreased and there will be less of a chemical shift. Other factors may also affect the chemical shift, although at present it is not known what else could result in such a large chemical shift in the ^{1}H NMR spectrum compared to the other phenanthroline-containing complexes mentioned previously. Attempts were made to isolate a complex containing two coordinating “lophine” ligands, however when the reaction was undertaken at room temperature in methanol there was a significant amount of starting material in evidence in the ^{1}H NMR spectrum. When this was repeated in ethanol with heating there was still a significant amount of uncoordinated lophine present. The steric bulk of the lophine was considered as a potential reason for the reluctance of a second lohpine moiety to coordinate to the uranyl centre, however as was observed previously, typically as many as three lophine moieties can coordinate to an uranyl centre.[26] Figure 142 displays the ^{1}H NMR of complex [$UO_2(NO_3)_2$**(27)**] which shows successful coordination of ligand **27** to the uranyl ion.

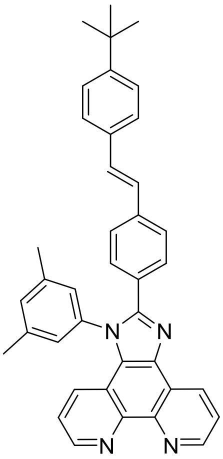

Figure 141: Molecular structure of ligand incorporated into complex [$UO_2(NO_3)_2$**(27)**]

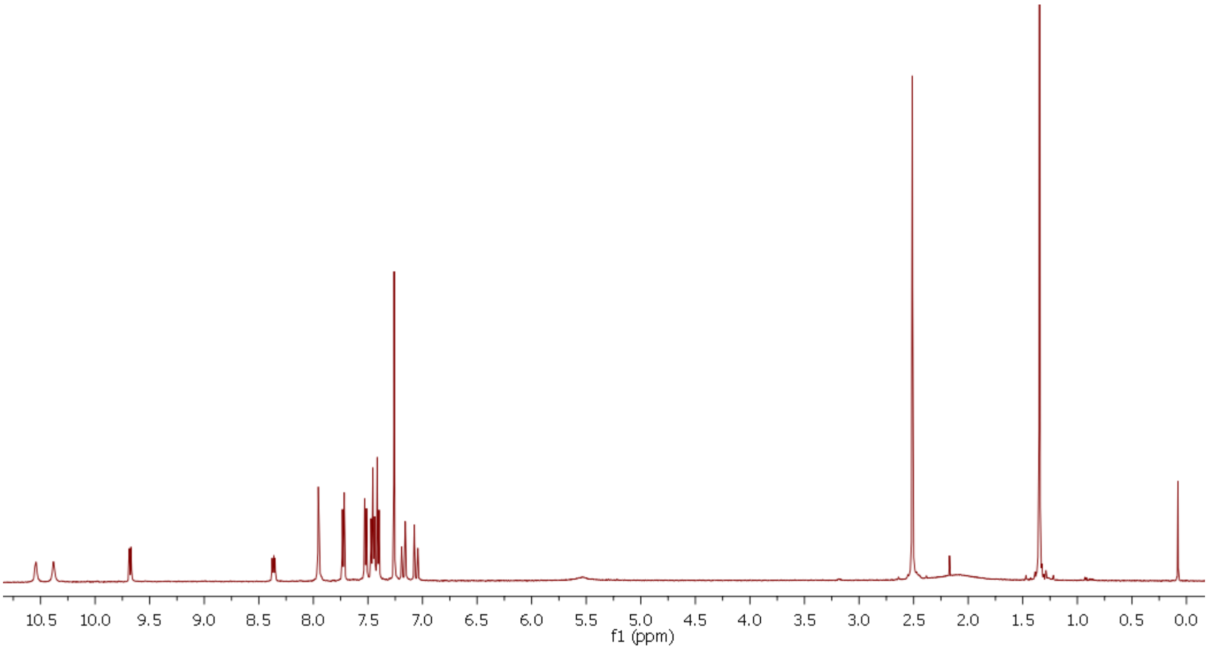

Figure 142: ^1H NMR spectrum of complex [$UO_2(NO_3)_2$**(27)**] in $CDCl_3$ at 298K

Three phenanthroline proton signals observed for the starting material between 9.0 and 9.2 ppm shifted downfield to between 9.6 and 10.6 ppm. A slight broadening of the signals was observed for the two furthest downfield shifted protons. Figure 143 shows the superimposed spectra of the aromatic region of both the uranyl complex and the free ligand **27**.

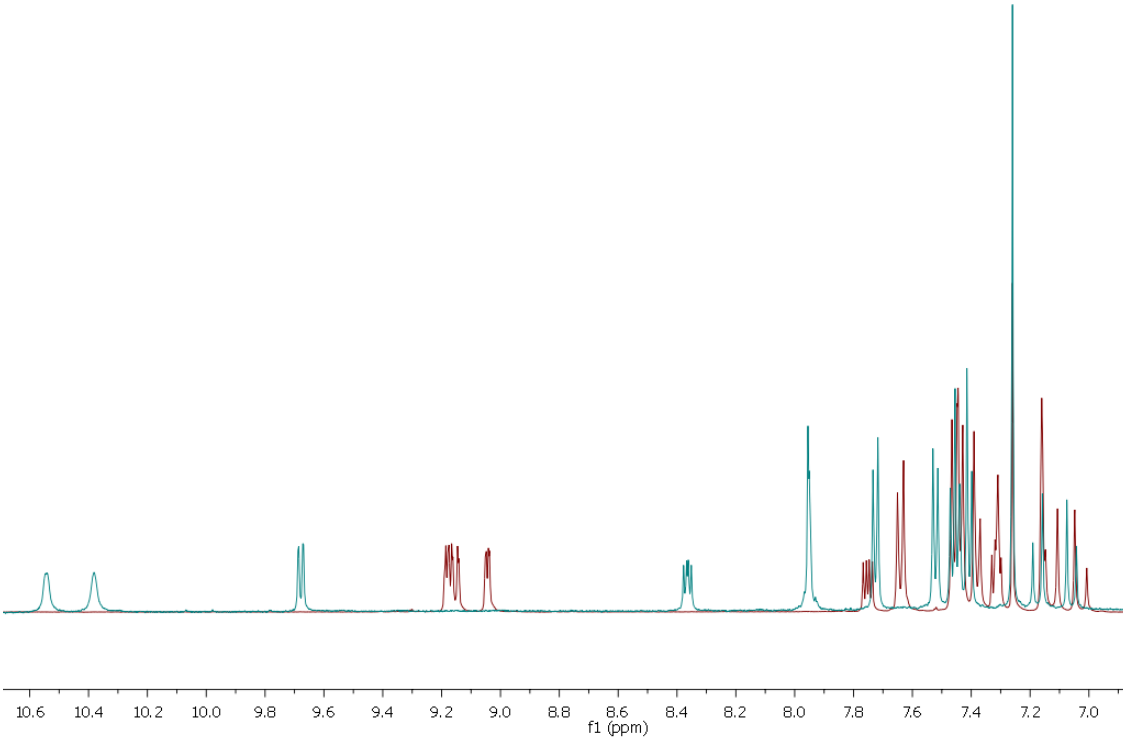

Figure 143: ^{1}H NMR aromatic region spectrum of $UO_2(NO_3)_2$**(27)** (blue line) and **27** (red line) in $CDCl_3$ at 298K

Clearly the protons most affected by the immediate presence of the uranyl ion were those associated with the phenanthroline centre, whilst a minimal shift of the signal is observed for aromatic protons located further upfield. For example the protons associated with the double bond of the styryl R group showed very little shifting of the signal. The aliphatic protons associated with the R and R′ group were also directly superimposable and do not show any shifts upon coordination. Each complex displayed similar characteristics in the ^{1}H NMR spectrum as those discussed for [$UO_2(NO_3)_2$**(27)**], including a significant shifting of the phenanthroline proton signals, and broadening of the two furthest downfield shifted signals. This data suggests the successful coordination of the ligand to the uranyl ion at the phenanthroline centre, with most likely one coordinating ligand for each uranyl moiety. The observation that a second "lophine" ligand cannot be coordinated to the uranyl centre suggests two things. The first is that there is not enough room in the coordination sphere of the uranium to accommodate a ligand as bulky as the lophine without the loss of another ligand. This is not surprising as typically uranyl will only accommodate 4-6 coordination environments around its equatorial axis. The second assumption that can be made about the system is that since there does not appear to be coordination of a second lophine ligand we can assume that the nitrate ions are too strongly bound to the uranium centre to be displaced. From this a structure may be proposed which would include both nitrate ions and the lophine ligand which would make the uranyl ion 6-coordinate around the equatorial plane (Figure 144).

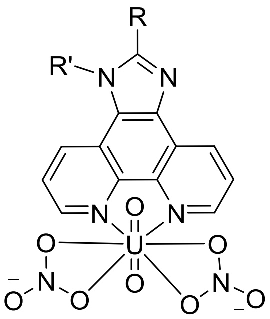

Figure 144: Proposed molecular structure for isolated complexes

The proposed structure does not account for any H_2O molecules which could be coordinated either in the inner coordination sphere or the outer coordination sphere, although no signals were observed for H_2O in the ^1H NMR spectrum. All molecular weight calculations and values obtained as a result of those calculations (i.e. yield percentage, molar absorption coefficient) have been obtained with the assumption that the complexes were isolated in their non-hydrated forms.

5.8.3 Infrared studies of the complexes

The infrared spectrum of $[UO_2(NO_3)_2.6H_2O]$ has been investigated and fully assigned.[47] It was reported that there were potentially six infrared active modes of vibration. Some of the bands are very weak and not clearly visible in the spectrum (Figure 145).

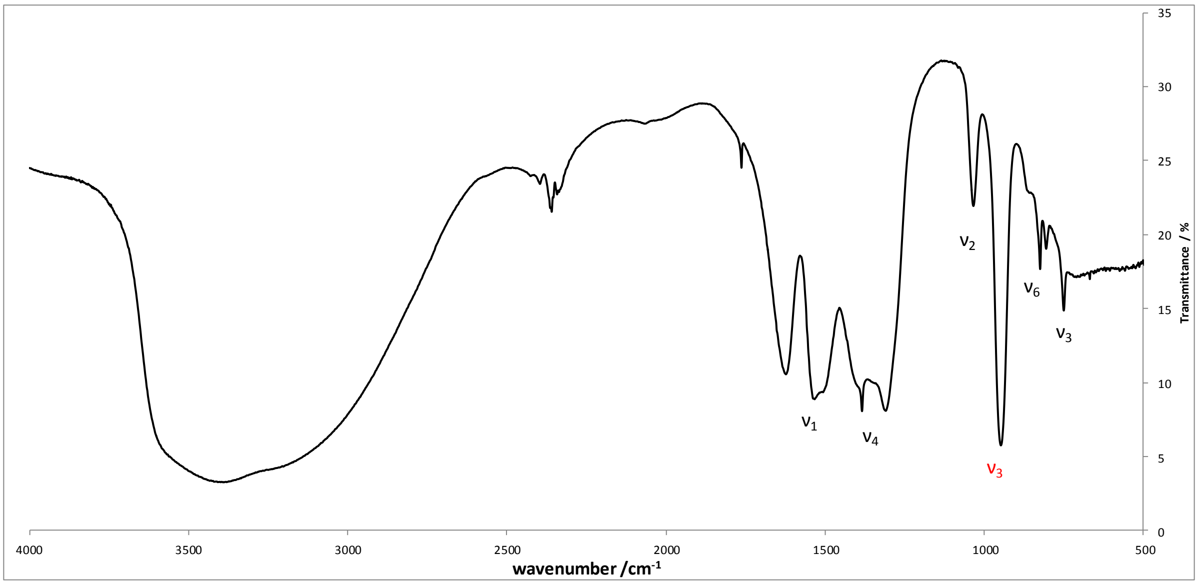

Figure 145: Infrared spectrum of $[UO_2(NO_3)_2.6H_2O]$: nitrate (black) and uranyl (red) frequencies are labelled

The symmetry of the nitrates in the complex can be approximated to a C_{2v} point group with six modes of vibration assigned to the nitrates (labelled in black $\nu_{1\text{-}6}$). ν_3, ν_5 and ν_6 produce weak signals associated with symmetrical bending, asymmetric bending and an out of plane rocking mode respectively, while a weak signal is also observed for the ν_2 mode of vibration which is assigned to a symmetric stretch of the oxygen atoms. The two strongest bands appear as a result of the ν_1 and ν_4 vibrational modes which occur as a result of an asymmetric stretch of the third oxygen atom (the furthest away from the metal centre) and asymmetric stretch of the N-O bonds closest to the metal atom respectively. As it is likely that bands will appear in the spectrum of the isolated complexes due to ligand stretching and bending modes which may cover the weaker bands, the ν_1 and ν_4 bands will be the only assigned bands in the isolated complexes. The infrared active asymmetric stretch, ν_3, of the O=U=O centre is observed in the spectrum of $UO_2(NO_3)_2.6H_2O$ at 946 cm^{-1}. The linear uranyl centre is assigned a $D_{\infty}h$ point group.

Infrared spectra were obtained by forming KBr plates of the complexes. All collected data is displayed in Table 32 below.

Compound Number	**R**	**R′**	**Nitrate ν_1, ν_4 stretch / cm^{-1}**	**Uranyl ν_3 stretch / cm^{-1}**
$[UO_2(NO_3)_2.6H_2O]$	-	-	1539, 1308	946
$[UO_2(NO_3)_2$**(25)**]	4-^{t}Bu	3,5-diMe	1536, 1268	940
$[UO_2(NO_3)_2$**(27)**]	4-^{t}Bustyr	3,5-diMe	1527. 1266	939
$[UO_2(NO_3)_2$**(28)**]	4-^{t}Bustyr	4-^{t}Bu	1538, 1267	939
$[UO_2(NO_3)_2$**(50)**]	2,3,4-trimethoxy	3,5-diMe	1532, 1276	938
$[UO_2(NO_3)_2$**(62)**]	4-^{t}Bu	azo	1533, 1268	939

Table 32: Infrared spectroscopic data of uranyl complexes (KBr plates).

Each of the complexes showed bands associated with both the nitrate and uranyl region of the molecule. The only band that showed any significant change from the starting material $[UO_2(NO_3)_2.6H_2O]$ was associated with the ν_4 stretch which lowered from 1308 cm^{-1} to ≈ 1268 cm^{-1} in each case. There was minimal change observed in the asymmetric O=U=O ν_3 stretch, which lowered by about 6 cm^{-1} for each of the complexes. This shows that the ligand had minimal effect on the electronics of the uranyl centre, for which the asymmetric ν_3 stretch can vary between 850 – 1000 cm^{-1} when different ligands are coordinated. The observed values are close to those reported for (1,10-phenathroline)$UO_2(NO_3)_2$.[47]

None of the isolated complexes differentiated greatly from each other in the infrared spectrum with regards to bands associated with either the nitrate or uranyl moieties. However, they did each contain distinctive bands associated with the lophine used in each instance. Shown below is the infrared spectrum of complex [$UO_2(NO_3)_2$**(25)**] which shows the expected bands due to nitrate and uranyl, and also other bands due to the lophine moiety in the fingerprint region.

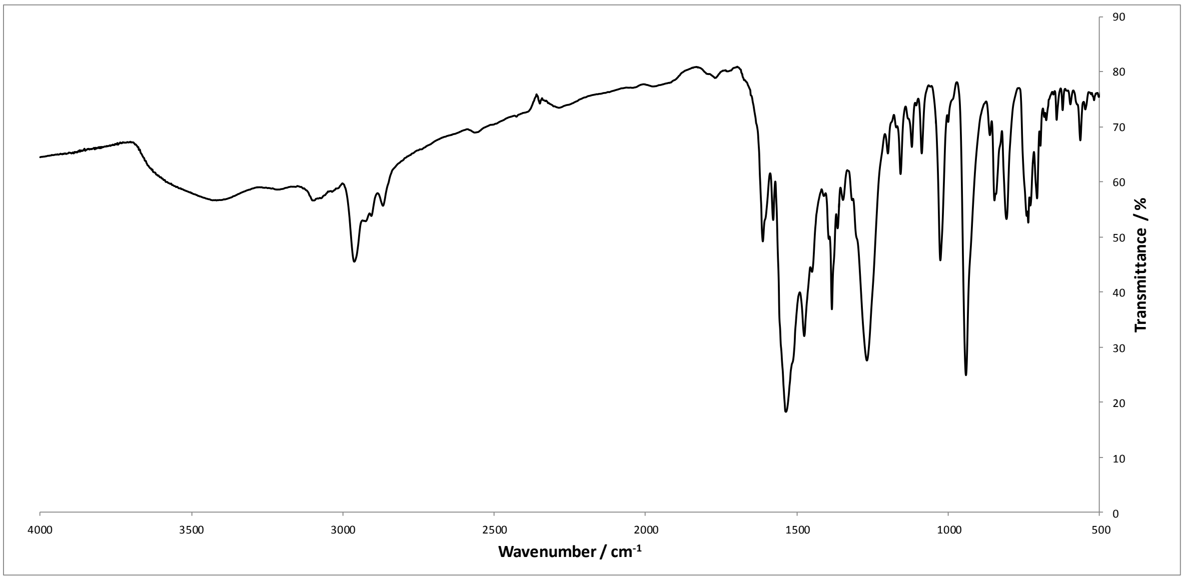

Figure 146: Infrared spectrum of [$UO_2(NO_3)_2$**(25)**]

All of the IR spectroscopic evidence collected together suggests the presence of nitrate, uranyl and lophine ligand. The slight shifts observed for the ligands suggest successful coordination of the “lophine” ligand.

5.8.4 Electronic absorption spectroscopy of the complexes

Electronic absorption spectroscopy of the complexes showed distinct bands in the high energy region of the spectrum in each case. The precise number of observed bands was dependent on the ligand itself. In some instances the electronic absorption spectra were significantly different for the starting material and the complex, and conversely some were almost identical. Data is shown in Table 33.

Compound Number	R	R′	Absorption λ_{max}/nm (ε/M^{-1}cm^{-1})
[$UO_2(NO_3)_2$**(25)**]	4-^{t}Bu	3,5-diMe	279 (27,700), 305(sh) (21,900)
[$UO_2(NO_3)_2$**(27)**]	4-^{t}Bustyr	3,5-diMe	271 (23,700), 306(sh) (27,000), 355 (42,800)
[$UO_2(NO_3)_2$**(28)**]	4-^{t}Bustyr	4-^{t}Bu	274 (42,400), 351 (37,900)
[$UO_2(NO_3)_2$**(50)**]	2,3,4-trimethoxy	3,5-diMe	260 (61,500)
[$UO_2(NO_3)_2$**(62)**]	4-^{t}Bu	azo	279 (44, 032), 298 (sh), 38,500)

Table 33: Electronic absorption data of the isolated complexes

[$UO_2(NO_3)_2$**(25)**] is an example of a complex which had a distinct electronic absorption spectrum in comparison to that of the free ligand. The complex showed two distinct bands at 279 nm and 305 nm, which considering their respective energies and their high associated molar absorption coefficient are most likely π→π* transitions. A weak absorption band was observed in the low energy region of the spectrum (360-390 nm) which could be either an absorption associated with a LMCT, or an n→π* transition. In comparison to the free ligand the main change arises in the high-energy region of the spectrum, with a new band appearing at 305 nm (Figure 147).

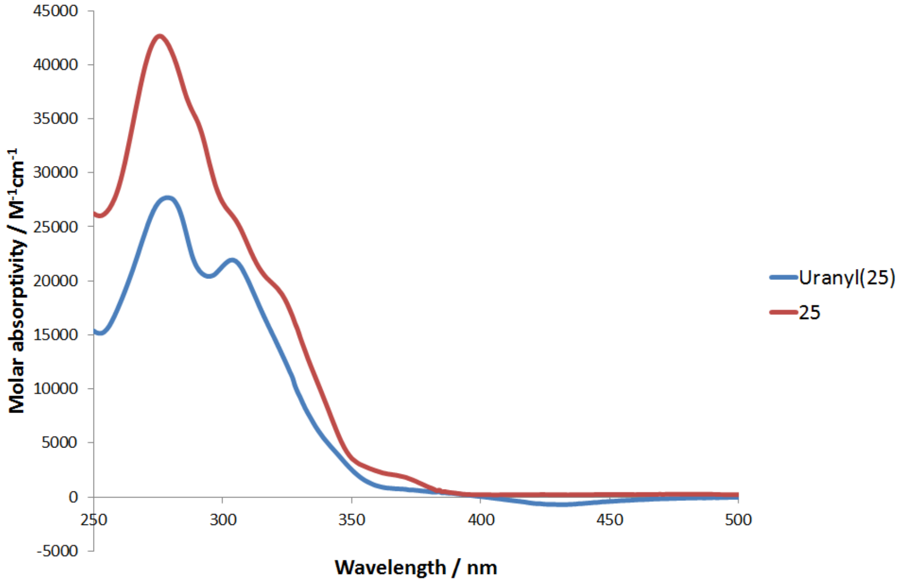

Figure 147: Electronic absorption spectra of **25** (red line) and [$UO_2(NO_3)_2$**(25)**] (blue line) in $CHCl_3$ at 298K

The absorption at 279 nm appeared in exactly the same region as with the free ligand, with no shifting of the signal upon coordination. A low energy and low intensity absorption was observed at about 360-390 nm for both the free ligand and the complex which indicates that both can be attributed to the same transition, most likely an n→π* transition. No weaker bands were observed in the 350-500 nm range when the spectra were obtained at higher concentration. The molar absorption coefficient (ε) values of the ligand are higher than that of the complex, possibly as a result of metal perturbation reducing the effective conjugation in the complex.

Contrastingly, some of the electronic absorption spectra of the free ligands and complexes were almost identical, potentially displaying dissociated free ligand. For example complex [$UO_2(NO_3)_2$**(62)]** and free ligand **62** (Figure 148) have nearly identical electronic absorption spectra, showing a broad peak centred at 279 nm with some vibronic structure. The absorption is assigned a π→π* transition, and no absorptions are observed at lower energy for [$UO_2(NO_3)_2$**(62)**] that would suggest a LMCT. This information is in contrast to the information obtained from the ^{1}H NMR spectrum of this complex which displayed clear chemical shifts indicative of successful coordination to the uranyl centre.

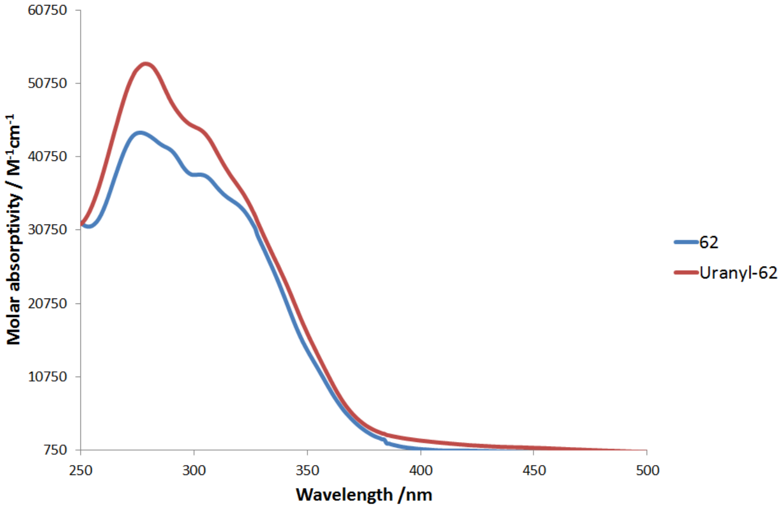

Figure 148: Electronic absorption spectra of **62** (blue line) and [$UO_2(NO_3)_2$**(62)**] (red line) in $CHCl_3$ at 298 K

All the evidence collected together suggests that the observed spectra display ligand-based π→π* transitions of either free ligand or coordinated ligand, and that there is no evidence of LMCT from the lophine ligand to the U or from the oxygen atoms of the uranyl to the U. It is possible that some bands are obscured by overlapping π→π* bands, particularly in the higher energy region of the spectrum (~350 nm). However, LMCT bands in uranyl complexes tend to appear in the 420-500 nm range in which there does not appear to be any bands that could potentially obscure the lower energy absorptions. LMCT in either case would involve the deactivation from a triplet to a singlet state which is a disallowed process, therefore it is possible that these transitions are simply too weak to be observed in the UV.

In addition to [$UO_2(NO_3)_2$**(62)**], [$UO_2(NO_3)_2$**(50)**] also displays a similar electronic absorption spectrum to the free ligand, while [$UO_2(NO_3)_2$**(27)**] and [$UO_2(NO_3)_2$**(28)**] show significant bathochromic shifts from their respective free ligands.

5.8.5 Luminescence studies of the complexes

Luminescence spectra of the complexes were initially obtained at low concentrations (≈ 1 x 10^{-5}M) in order to understand the electronics of the systems in the absence of inter-ligand interactions. The results were not as expected as although there was clear evidence of successful coordination of the uranyl ion to the ligands in the ^{1}H NMR spectra, the emission spectra of the ligands showed either free ligand emission or in the case of complexes [$UO_2(NO_3)_2$**(28)**] and [$UO_2(NO_3)_2$**(62)**] slightly shifted ligand-based emission (Table 34).

Compound Number	**R**	**R′**	**λ_{ex} (nm)**	**λ_{em} (nm)**	**Free ligand λ_{em} (nm)**
$UO_2(NO_3)_2$**(25)**	4-^{t}Bu	3,5-diMe	263	417	415
$UO_2(NO_3)_2$**(27)**	4-^{t}Bustyr	3,5-diMe	351	425	425
$UO_2(NO_3)_2$**(28)**	4-^{t}Bustyr	4-^{t}Bu	353	487	456
$UO_2(NO_3)_2$**(50)**	2,3,4-trimethoxy	3,5-diMe	286	421	415
$UO_2(NO_3)_2$**(62)**	4-^{t}Bu	azo	368	453	415

Table 34: Luminescence data for the isolated complexes at low concentration (≈1x10^{-5} M) in $CHCl_3$ at 298 K

For example, shown below (Figure 149) is the emission spectrum of complex [$UO_2(NO_3)_2$**(25)**] and free ligand **25.** Clearly there is no difference between the free ligand emission and that of the complex at low concentration.

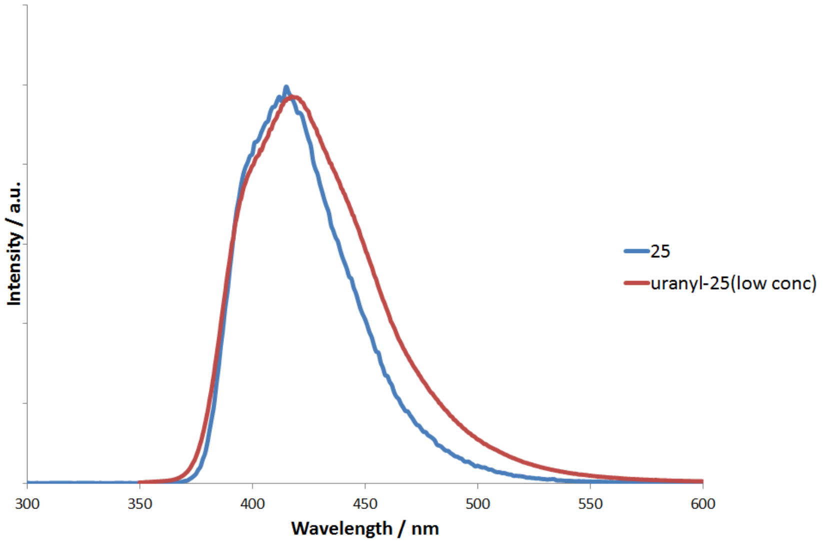

Figure 149: Emission spectra of **25** (blue) and [$UO_2(NO_3)_2$**(25)**] (red) at low concentration (≈1x10^{-5}) in $CHCl_3$ at 298 K

In order to understand the apparent lack of coordination of the uranyl ion in these complexes it was decided that the luminescence data of the complexes would be obtained at higher concentration regimes in order to replicate the condition in which the ^{1}H NMR spectra were obtained. The resulting spectra showed in each case significant shifts of the ligand-based emission as a new emission peak centred between 500-600 nm. Table 35 shows the luminescence data for the five complexes [$UO_2(NO_3)_2$**(L)**] at high concentrations and in the solid state at varying excitation wavelengths.

Compound Number	R	R′	Solution / Solid	λ_{ex} (nm)	λ_{em} (nm)	τ (ns) (solid)
[$UO_2(NO_3)_2$**(25)**]	4-^{t}Bu	3,5-diMe	Solution	300	477	2.56
			Solution	450	530	
			Solid	300	525	
			Solid	450	530	
[$UO_2(NO_3)_2$**(27)**]	4-^{t}Bustyr	3,5-diMe	Solution	300	501	-
			Solution	470	550	
			Solid	300	534	
			Solid	450	534	
[$UO_2(NO_3)_2$**(28)**]	4-^{t}Bustyr	4-^{t}Bu	Solution	300	520	-
			Solution	459	532	
			Solid	300	506	
			Solid	450	506	
[$UO_2(NO_3)_2$**(50)**]	2,3,4-trimethoxy	3,5-diMe	Solution	300	473	-
			Solution	458	522	
			Solution	500	583	
			Solid	300	519	
			Solid	400	519	
			Solid	500	567	
[$UO_2(NO_3)_2$**(62)**]	4-^{t}Bu	azo	Solution	300	588	-
			Solution	441	588	
			Solution	510	607	
			Solid	300	516	
			Solid	450	516	

Table 35: Luminescence data for the isolated complexes at high concentration (≈$1x10^{-2}$ M) and as solids

All the evidence collected together seems to suggest that there is a direct effect of increasing the concentration of the complex in solution on the emission wavelength. This is evidenced by the lower energy emissions observed at high concentration and in the solid state. This potentialy indicates that the "lophine" molecule may be weakly bound to the uranyl centre, and at low concentrations this binding is sufficiently weak to promote dissociation in solution, resulting in the observation of free ligand in the luminescence spectra. However, at higher concentrations this was not observed and a lower energy emission was observed indicating a successfully coordinated species. This however is unlikely to be the case as dissociation in $CHCl_3$ is rarely observed and therefore it is possible that the luminescence spectra that are observed are a result of the concentrated species leading to aggregation in solution.

In some instances ([$UO_2(NO_3)_2$**(25)**], [$UO_2(NO_3)_2$**(27)**] and [$UO_2(NO_3)_2$**(50)**]) the observed emission energies for the concentrated and solid state luminescence spectra were very similar or identical, suggesting that the most concentrated solutions were more representative of the uranyl complex than the less concentrated solutions. Figure 150 shows the luminescence spectra of **5**, [$UO_2(NO_3)_2$**(25)**] (concentrated) and [$UO_2(NO_3)_2$**(25)**] (solid).

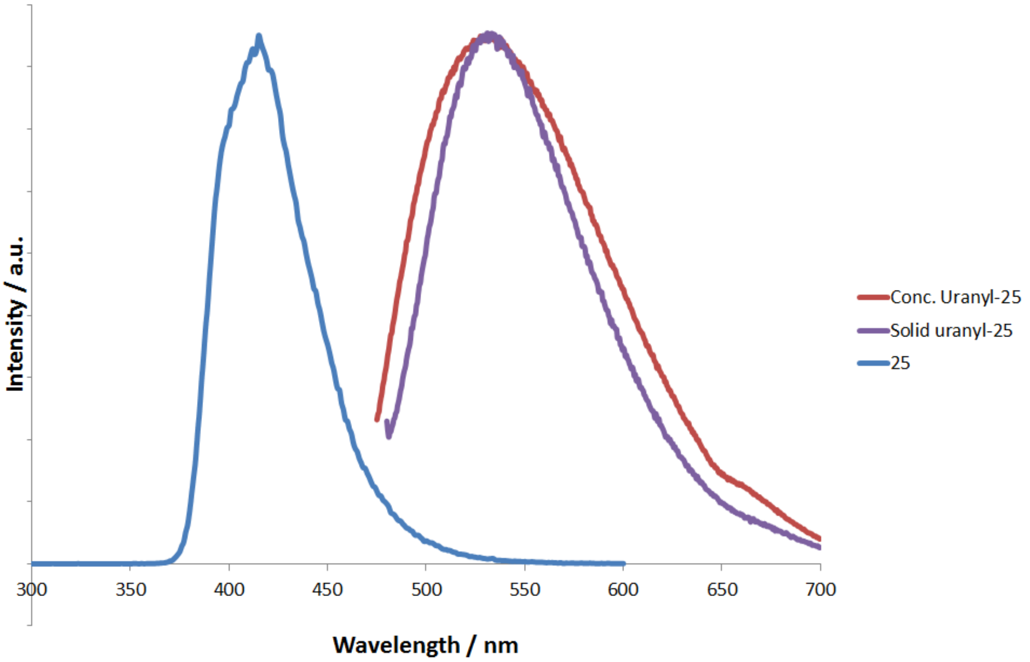

Figure 150: Emission spectra of **25**, [$UO_2(NO_3)_2$**(25)**] (~$1x10^{-2}$ M) and $UO_2(NO_3)_2$**(25)** solid

However, it was not always the case that the emission energy is identical for the concentrated solutions and the solid complex, as complexes [$UO_2(NO_3)_2$**(28)**] and [$UO_2(NO_3)_2$**(62)**] emitted at a slightly higher energy as a solid than as a high concentration solution. However, these are still significantly shifted from the emission at low concentration.

The emission wavelength of the complexes in solution can also be dependent on excitation wavelength. It was observed that the difference in emission between an excitation wavelength of ≈ 300 nm and ≈ 450 nm could vary between 0-60 nm.

There were three potential assignments for the observed emission in each of the complexes, including a ligand-based emission, an LMCT from the 1,10-phenanthroline moiety to the uranyl or an entirely uranyl-centred LMCT. Uranyl based LMCT has been extensively reported and is relatively well understood.[40] Contrastingly, there is significantly less information in the literature regarding phenanthroline-based LMCT.[1,30] This is likely a result of the redox properties of 1,10-phenanthroline. In order to take part in a LMCT, a ligand must be easily oxidised and the metal easily reduced. The more suitable the ligand and metal are to undergo these changes the more likely a LMCT will proceed. 1,10-phenanthroline however has already displayed an ability to take part in a MLCT in Re(I) complexes (as described in chapters 2,3 and 4) which would indicate that it is easily reduced. LMCT may still occur due to the nature of the uranium centre which is easily reduced, however it appears less likely to occur than an entirely uranyl-centred LMCT. In order to determine which of these is responsible for the observed emission, three attributes of the emission spectra were considered: peak position, emission profile and lifetime of the emission.

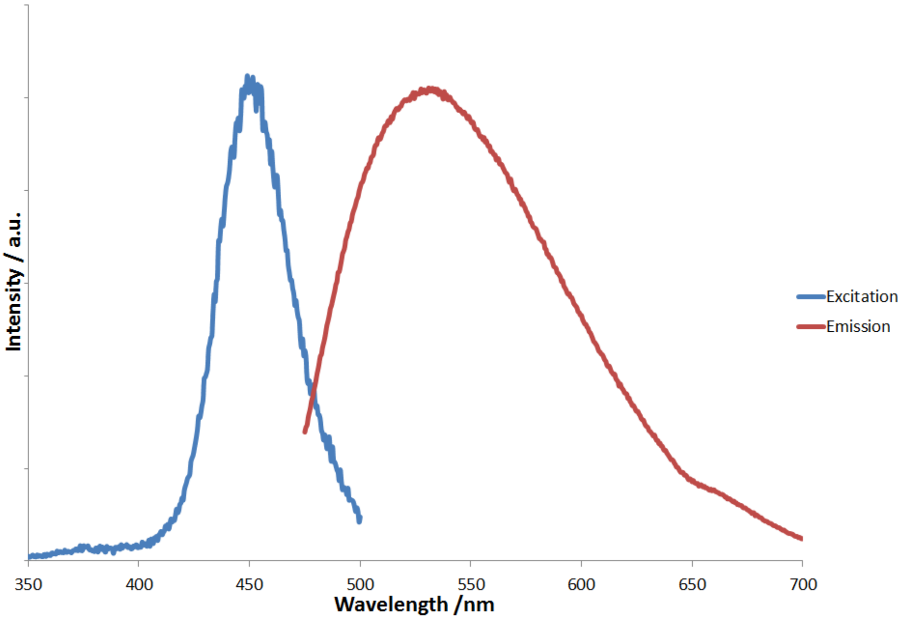

Figure 151: Excitation (blue) and emission (red) spectra for [$UO_2(NO_3)_2$**(25)**] (~$1x10^{-2}$ M)

Firstly, the peak position of, for example, [$UO_2(NO_3)_2$**(25)**] in the solid state was centred at 530 nm. This does not necessarily indicate which of the processes are responsible for the emission as it is feasible that the energy gaps between the ground state of both the phenanthroline and oxygen to the excited state of the uranium orbitals are relatively similar. It is also possible that the emission is a highly bathochromically shifted ligand-based emission, although a shift as large as this is rare. Entirely uranyl-centred emission is usually observed around 500-550 nm, although smaller peaks are sometimes visible ~ 600 nm. Although the position of the band can be altered by incorporating different ligands, it was not expected that altering the lophine ligand would change any uranyl-centred emission by a significant amount. However, what is observed in both the luminescence spectra of the concentrated solutions (Figure 152) and the solid-state spectra is a large range of emission wavelengths.

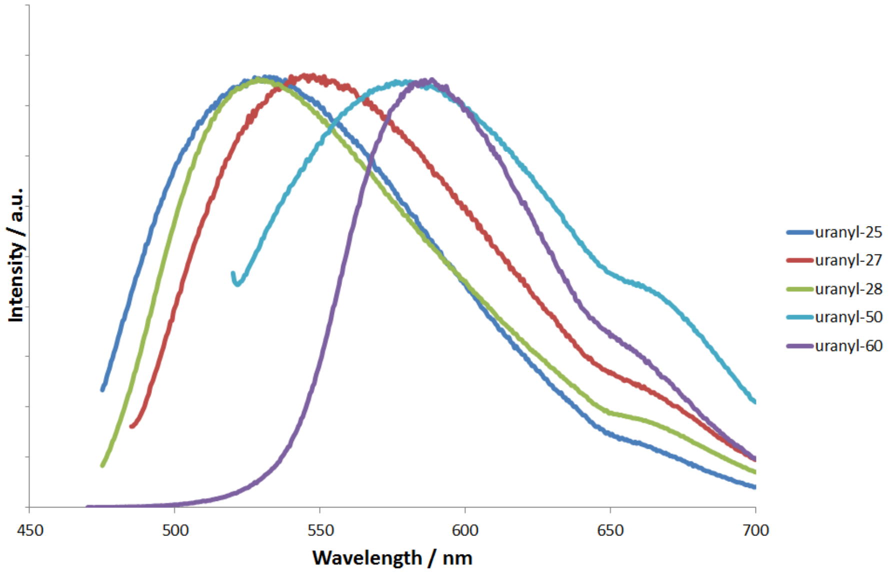

Figure 152: Emission spectra of the isolated complexes (~1x10^{-2} M) in $CHCl_3$ at 298 K

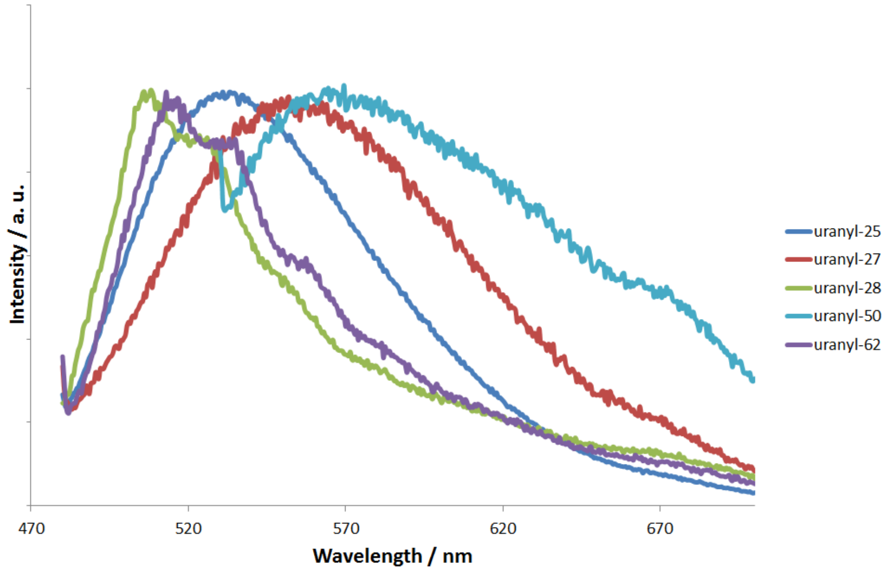

Figure 153: Emission spectra of the isolated complexes (solid) in $CHCl_3$ at 298 K

Secondly, the peak profiles of the complexes were investigated. The profiles of complexes [$UO_2(NO_3)_2$**(25)**], [$UO_2(NO_3)_2$**(27)**], and [$UO_2(NO_3)_2$**(50)**] were that of a broad, featureless band. Typically, uranyl-based emission shows multiple peaks and shoulders as part of the emission. As described in section 5.5, this was attributed to transitions from the first excited electronic level to the symmetric and antisymmetric vibrational levels of the uranyl ion. Contrastingly, emission attributed to phen-based charge transfer displays a single, broad featureless peak as was described in the introduction.[1] In contrast to the other complexes, the emission profiles of [$UO_2(NO_3)_2$**(28)**] and [$UO_2(NO_3)_2$**(62)**] did display some vibronic structure. It is difficult to predict if this is due to uranyl-centred LMCT or otherwise, however the potential assignment is further strengthened by the fact that the two emissions are also at a very similar wavelengths and are almost superimposable. This is despite the fact that [$UO_2(NO_3)_2$**(28)**] and [$UO_2(NO_3)_2$**(62)**] incorporate completely different “lophine” molecules (i.e. they do not share an R or R′ group). This may suggest that the emission does not originate from the “lophine” moiety but is centred entirely on the uranyl ion. The broad, featureless peaks that were observed for the remaining complexes could be as a result of shifted ligand-based emission. This is true even for ligands which showed vibronic structure (Figure 154) as free ligands due to the fact that this rigid structure may be lost upon coordination.

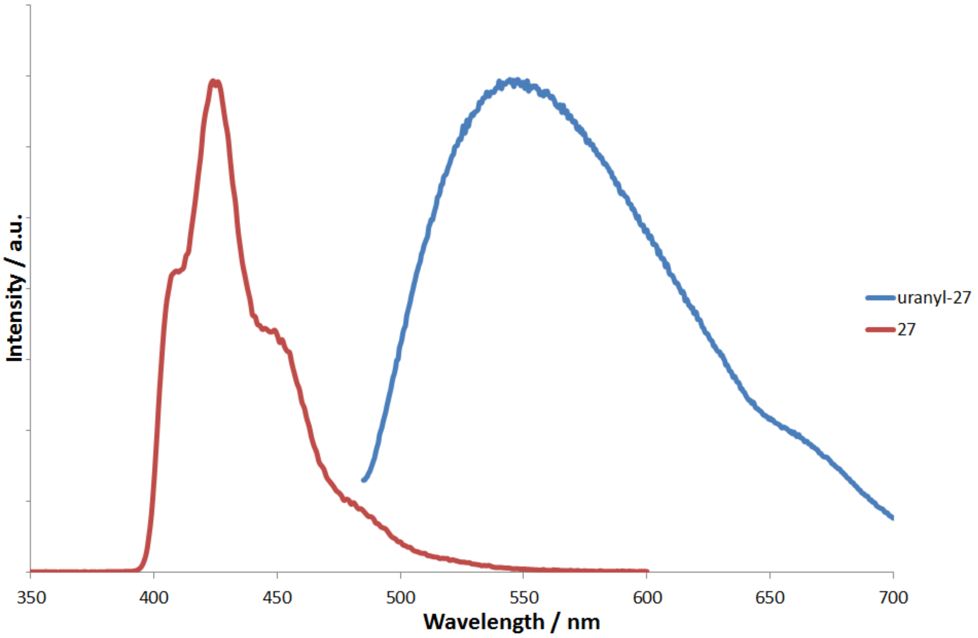

Figure 154: Emission spectra of [$UO_2(NO_3)_2$**(27)**] (blue line) and **27** (red line) (~$1x10^{-2}$M)

Finally, the lifetime emission of the isolated complexes were investigated. Unfortunately the samples were usually not emissive enough to obtain an accurate lifetime measurement within a reasonable timescale. Despite this the lifetime of one complex ([$UO_2(NO_3)_2$**(25)**]) was investigated and was found to have a short emission lifetime of 2.56 ns) which indicated that the emission is due to fluorescence and not phosphorescence. Uranyl-based emission generally involves the relaxation of an excited triplet state to the singlet ground state. This spin-forbidden process results in a long lifetime of the emission, measured sometimes in the micro- to millisecond range. This value is somewhat dependent on the other ligands which are involved, but generally they are long-lived. The lifetime of phenanthroline-centred LMCT is also expected to be long as it would undergo the same processes as a uranyl-centred LMCT, including a spin-forbidden triplet-to-singlet relaxation. Of the three options only a ligand-based emission would result in a short emission lifetime as it does not undergo ISC to form an excited triplet state.

All of the evidence collected together suggests that a tentative assignment of a highly shifted ligand centred emission could be applied to the observed emissions in each case. LMCT has been ruled out as a possible origin of the emission as the lifetimes associated with the emission are very short. Additionally, uranyl-based LMCT had been ruled out as a possibility due to the nature of the shape of the bands which display no vibronic structure in contrast to other reported uranyl-centred emissions.

5.9 Conclusion

In conclusion, five uranyl complexes have been isolated which incorporate a substituted imidazole [4,5-*f*]-1,10-phenanthroline moiety as a ligand. These complexes have been characterised and structures have been proposed through evidence collected by ^{1}H NMR and IR spectroscopy. ^{1}H NMR confirmed the successful coordination of the ligands through significant downfield shift of the signals of the phenanthroline protons, while the IR spectra confirmed in each case the presence of both nitrates and uranyl in the complexes.

The electronics of these systems were explored, first by electronic absorption spectroscopy, and then by luminescence studies. The electronic absorption spectra showed in each case high energy absorptions ($\pi \rightarrow \pi^*$), which showed either free ligand absorption, or bathochromically shifted ligand-based absorption. No lower energy absorptions were observed which indicated any LMCT absorption bands. The luminescence of the complexes is concentration dependent, as was evidenced by the fact that at low concentrations (~1×10^{-5} M) the only observed emission corresponded to free ligand in solution (or slightly bathochromically shifted emission), and at higher concentrations (~1×10^{-2} M) a drastically bathochromically shifted emission was observed. This emission was assigned as a ligand-based emission due to its low luminescence lifetime.

5.10 Experimental

[$UO_2(NO_3)_2$(25)]

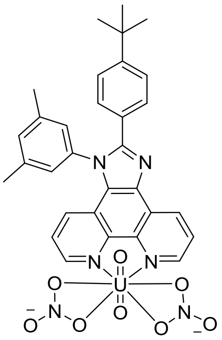

Into a round bottom flask was added lophine (**25**) (0.073 g, 0.159 mmol), uranylnitratehexahydrate (0.08 g, 0.159 mmol) and methanol (20ml) and the reactants were left to stir at room temperature for 12 hrs. The solvent was removed *in vacuo* to yield yellow oil. $CHCl_3$ was added (2ml) and was precipitated from hexane to give product [$UO_2(NO_3)_2$(**25**)] as yellow powder (0.090g). ^{1}H NMR (500 MHz, $CDCl_3$) δ 10.55 (s, 1H, phen-*H*), 10.39 (s, 1H, phen-*H*), 9.68 (dd, *J* = 8.1, 1.4 Hz, 1H, Ar-*H*), 8.37 (dd, *J* = 8.0, 5.3 Hz, 1H, Ar-*H*), 8.02 – 7.87 (m, 2H, Ar-*H*), 7.69 (d, *J* = 8.6 Hz, 2H, Ar-*H*), 7.52 – 7.37 (m, 3H, Ar-*H*), 7.31 – 7.20 (m, 2H, Ar-*H*), 2.51 (s, *J* = 15.7 Hz, 6H, Ar-CH_3), 1.35 (s, 9H, Ar-C(CH_3)$_3$) ppm. IR (KBr plates): 2962 (w), 1612 (w), 1577 (w), 1536 (s), 1475 (s), 1384 (w), 1268 (s), 1199 (w), 1157 (w), 1119 (w), 1087 (w), 1025 (m), 941 (s), 846 (w), 807 (w), 735 (w) cm^{-1}. UV-vis λ_{max} (ε / M^{-1} cm $^{-1}$) ($CHCl_3$): 279 (27,700), 305(sh) (21,900) nm.

[$UO_2(NO_3)_2$(27)]

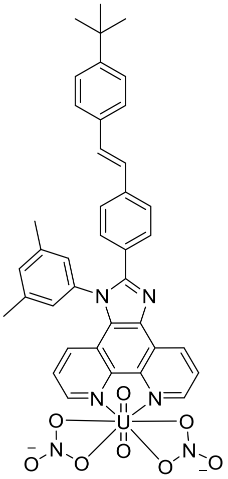

Into a round bottom flask was added lophine (**27**) (0.073 g, 0.159 mmol), uranylnitratehexahydrate (0.08 g, 0.159 mmol) and methanol (20ml) and the reactants were left to stir at room temperature for 12 hrs. The solvent was removed *in vacuo* to yield yellow oil. $CHCl_3$ was added (2ml) and was precipitated from hexane to give product [$UO_2(NO_3)_2$(**27**)] as yellow powder (0.138g). ^{1}H NMR (500

MHz, $CDCl_3$) δ 10.54 (s, 1H, phen-*H*), 10.38 (s, 1H, phen-*H*), 9.68 (dd, *J* = 8.1, 1.2 Hz, 1H, Ar-*H*), 8.36 (dd, *J* = 8.0, 5.2 Hz, 1H, Ar-*H*), 7.98 – 7.93 (m, 2H, Ar-*H*), 7.73 (d, *J* = 8.3 Hz, 2H, Ar-*H*), 7.52 (d, *J* = 8.4 Hz, 2H, Ar-*H*), 7.49 – 7.38 (m, 5H, Ar-*H*), 7.26 (s, 2H, Ar-*H*), 7.12 (dd, *J* = 57.8, 16.3 Hz, 2H), 2.51 (s, 6H), 1.35 (s, 9H) ppm. IR (KBr plates): 2960 (w), 1610 (w), 1577 (w), 1527 (s), 1474 (w), 1377 (s), 1266 (s), 1187 (w), 1109 (w), 1086 (w), 1020 (m), 940 (s), 840 (m), 807 (m), 733 (m) cm^{-1}. UV-vis λ_{max} (ε / M^{-1} cm^{-1}) ($CHCl_3$): 271 (23,700), 306(sh) (27,000), 355 (42,800) nm.

$[UO_2(NO_3)_2(28)]$

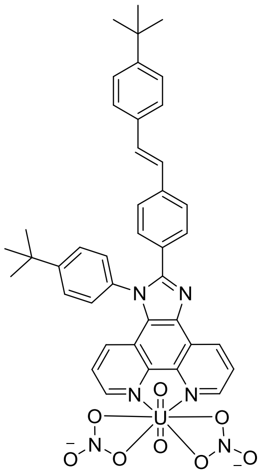

Into a round bottom flask was added lophine (**28**) (0.093 g, 0.159 mmol), uranylnitratehexahydrate (0.08 g, 0.159 mmol) and methanol (20 ml) and the reactants were left to stir at room temperature for 12 hrs. The solvent was removed *in vacuo* to yield yellow oil. $CHCl_3$ was added (2 ml) and was precipitated from hexane to give product $[UO_2(NO_3)_2($**28**$)]$ as a yellow powder (0.120 g). ^1H NMR (500 MHz, $CDCl_3$) δ 10.43 (s, 1H, phen-*H*), 10.29 (s, 1H, phen-*H*), 9.62 (s, 1H, Ar-*H*), 8.35 – 8.23 (m, 1H, Ar-*H*), 7.97 – 7.83 (m, 2H, Ar-*H*), 7.77 (d, *J* = 7.6 Hz, 2H, Ar-*H*), 7.64 (d, *J* = 7.5 Hz, 2H, Ar-*H*), 7.56 (d, *J* = 7.5 Hz, 2H, Ar-*H*), 7.50 – 7.35 (m, 6H, Ar-*H*), 7.06 (dd, *J* = 61.0, 16.1 Hz, 2H, Ar-*H*), 1.51 (s, 9H, Ar-C(CH_3)$_3$), 1.34 (s, 9H, Ar-C(CH_3)$_3$) ppm. IR (KBr plates): 2963 (w), 1603 (m), 1538 (s), 1384 (w), 1364 (w), 1267 (s), 1187 (w), 1155 (w), 1106 (w), 1076 (w), 1019 (s), 941 (s), 838 (m), 805 (m), 740 (m) cm^{-1}. UV-vis λ_{max} (ε / M^{-1} cm^{-1}) ($CHCl_3$): UV-vis λ_{max} (ε / M^{-1} cm^{-1}) ($CHCl_3$): 274 (42,400), 351 (37,900) nm.

[$UO_2(NO_3)_2$(50)]

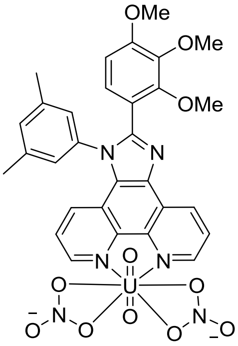

Into a round bottom flask was added lophine (**50**) (0.078 g, 0.159 mmol), uranylnitratehexahydrate (0.08 g, 0.159 mmol) and methanol (20 ml) and the reactants were left to stir at room temperature for 12 hrs. The solvent was removed *in vacuo* to yield green oil. $CHCl_3$ was added (2 ml) and was precipitated from hexane to give product [$UO_2(NO_3)_2$**(50)]** as green powder (0.070g). ^{1}H NMR (500 MHz, $CDCl_3$) δ 10.56 (s, 1H, phen-*H*), 10.42 (s, 1H, phen-*H*), 9.64 (d, *J* = 7.3 Hz, 1H, Ar-*H*), 8.36 (s, 1H, Ar-*H*), 8.06 (s, 1H, Ar-*H*), 7.97 (s, 1H, Ar-*H*), 7.23 (s, 1H, Ar-*H*), 7.18 – 7.09 (m, 3H, Ar-*H*), 6.70 (d, *J* = 8.6 Hz, 1H, Ar-*H*), 3.90 (s, 3H, Ar-O-C*H*$_3$), 3.81 (d, *J* = 9.4 Hz, 6H, Ar-O-C*H*$_3$), 2.39 (s, 6H, Ar-CH_3) ppm. IR (KBr plates): 2938 (w), 1604 (m), 1532 (s), 1476 (s), 1384 (w), 1276 (s), 1096 (s), 1050 (m), 1014 (m), 940 (s), 807 (w), 742 (w) cm^{-1}. UV-vis λ_{max} (ε / M^{-1} cm $^{-1}$) ($CHCl_3$): 260 (61,500) nm.

[$UO_2(NO_3)_2$(62)]

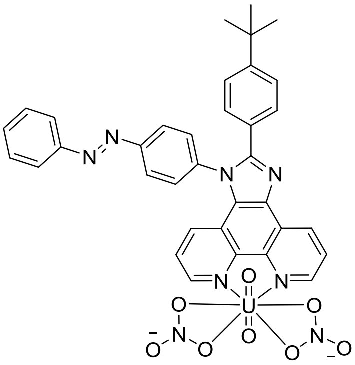

Into a round bottom flask was added lophine (**62**) (0.084 g, 0.159 mmol), uranylnitratehexahydrate (0.08 g, 0.159 mmol) and methanol (20 ml) and the reactants were left to stir at room temperature for 12 hrs. The solvent was removed *in vacuo* to yield orange oil. $CHCl_3$ was added (2 ml) and was precipitated from hexane to give product [$UO_2(NO_3)_2$**(62)**] as a light orange powder (0.130 g). ^{1}H NMR (500 MHz, $CDCl_3$) δ 10.55 (s, 1H, phen-*H*), 10.40 (s, 1H, phen-*H*), 9.69 (d, *J* = 8.2 Hz, 1H, Ar-*H*), 8.44 – 8.34 (m, 1H, Ar-*H*), 8.31 (d, *J* = 8.3 Hz, 2H, Ar-*H*), 8.12 – 8.03 (m, 3H, Ar-*H*), 7.99 – 7.93 (m, 1H, Ar-*H*), 7.82 (d, *J* = 8.4 Hz, 2H, Ar-*H*), 7.69 – 7.59 (m, 5H, Ar-*H*), 7.44 (d, *J* = 8.2 Hz, 2H, Ar-*H*), 1.33 (s, 9H, Ar-C(CH_3)$_3$) ppm. IR (KBr plates): 2962 (w), 1604 (w), 1578 (w), 1533 (s), 1447 (w), 1383 (m), 1268 (s), 1156 (w), 1074 (w), 1018 (m), 982 (w), 941 (s), 861 (w), 805 (w), 770 (w) cm^{-1}. UV-vis λ_{max} (ε / M^{-1} cm $^{-1}$) ($CHCl_3$): 279 (44, 032), 298 (sh), (38,500) nm.

5.11 References

(1) Sun, D.; Zhang, N.; Xu, Q.-J.; Huang, R.-B.; Zheng, L.-S. *Inorg. Chem. Commun.* **2010**, *13*, 859.

(2) Burrows, H. D.; Kemp, T. J. *Chem. Soc. Rev.* **1974**, *3*, 139.

(3) Ward, M. D.; Klingsporn, J. M.; Ibers, J. A. *Inorg. Chem.* **2013**, *52*, 1020.

(4) Alcock, N. W.; Flanders, D. J.; Pennington, M. *Acta. Cryst.* **1988**, *44*, 247.

(5) Gandhi, J. B.; Kulkarni, N. D. *Transit. Metal Chem.* **2001**, *26*, 96.

(6) Kaltsoyannis, N.; Scott, P. *"The f elements"* **1999**, Oxford university press.

(7) Klaproth, M. H. *Chemische Annalen* **1789**, *2*, 387.

(8) Waggoner, W. H. *J. Chem. Educ.* **1975**, *52*, 53.

(9) Sime, R. L. *J. Chem. Educ.* **1986**, *63*, 653.

(10) Seaborg, G. T. *J. Chem. Educ.* **1989**, *66*, 379.

(11) http://labspace.open.ac.uk/course/view.php?id=6653 (accessed 15/11/2013).

(12) http://winter.group.shef.ac.uk/orbitron/AOs/7f/ (accessed 6/2/2014).

(13) http://winter.group.shef.ac.uk/orbitron/AOs/4f/index.

(14) Housecroft, C. E.; Sharpe, A. G. *Inorganic Chemistry, 1st Edition, Pearson Education Ltd.* **2001**.

(15) Cotton, S. *Lanthanide and actinide chemistry* **2007**, John Wiley and sons ltd.

(16) www.wikis.lawrence.edu/display/CHEM/30+Mir+.

(17) Katz, J. J.; Seaborg, G. T.; Morss, L. R. *Chemistry of the actinide elements second edition* **1986**, J. W. Arrowsmith Ltd.

(18) Klaproth, M. H. *Chem. Ann. (Crell) II* **1789**, 387.

(19) Peligot, E. *J. Prakt. Chem.* **1841**, *1*, 442.

(20) Hahn, O.; Strassmann, F. *Naturwissenschaften* **1939**, *27*, 11.

(21) Baker, R. J. *Chem. Eur. J.* **2012**, *18*, 16258

(22) Sessler, J. L.; Melfi, P. J.; Pantos, G. D. *Coordin. Chem Rev.* **2006**, *250*, 816.

(23) Schettini, M. F.; Wu, G.; Hayton, T. W. *Inorg. Chem.* **2009**, *48*, 11799.

(24) Berthet, J.-C.; Nierlich, M.; Ephritikhine, M. *Dalton Trans.* **2004**, 2814.

(25) Berthet, J.-C.; Nierlich, M.; Ephritikhine, M. *Chem. Commun.* **2003**, 1660.

(26) Cardinaels, T.; Ramaekers, J.; Guillon, D.; Donnio, B.; Binnemans, K. *J. Am. Chem. Soc.* **2005**, *127*, 17602.

(27) Jiang, Y.-S.; Yu, Z.-T.; Liao, Z.-L.; Li, G.-H.; Chen, J.-S. *Polyhedron* **2006**, *25*, 1359.

(28) Dean, N. E.; Hancock, R. D.; Cahill, C. L.; Frisch, M. *Inorg. Chem.* **2008**, *47*, 2000.

(29) Cardinaels, T.; Ramaekers, J.; Nockemann, P.; Driesen, K.; Van Hecke, K.; Van Meervelt, L.; Shengbin, L.; De Feyter, S.; Guillon, D.; Donnio, B.; Binnemans, K. *Chem. Mater.* **2008**, *20*, 1278.

(30) Das, S.; Madhavaiah, C.; Verma, S.; Bharadwaj, P. K. *Inorg. Chim. Acta.* **2006**, *359*, 548.

(31) Thuery, P. *Eur. J. Inorg. Chem.* **2013**, 4563.

(32) Hnatejko, Z.; Lis, S.; Starynowicz, P.; Stryla, Z. *Polyhedron* **2011**, *30*, 880.

(33) Alcock, N. W.; Flanders, D. J.; Brown, D. *J. Chem. Soc. Dalton Trans.* **1985**, *5*, 1001.

(34) Adelani, P. O.; Burns, P. C. *Inorg. Chem.* **2012**, *51*, 11177.

(35) Zheng, H.; Swager, T. M. *J. Am. Chem. Soc.* **1994**, *116*, 761.

(36) Casellato, U.; Tamburini, S.; Tomasin, P.; Vigato, P. A. *Inorg. Chim. Acta.* **2002**, *341*, 118.

(37) Arnold, P. L.; J. Blake, A.; Wilson, C.; Love, J. B. *Inorg. Chem.* **2004**, *43*, 8206.

(38) Sarsfield, M. J.; May, I.; Cornet, S. M.; Helliwell, M. *Inorg. Chem.* **2005**, *44*, 7310.

(39) Guptaa, S. K.; Sena, N.; Butcher, R. J. *Polyhedron* **2014**, *71*, 34.

(40) Natrajan, L. S. *Coordin. Chem Rev.* **2012**, *256*, 1583.

(41) McGlynn, S. P.; Smith, J. K. *J. Mol. Spectrosc.* **1961**, *6*, 164.

(42) Takao, K.; Takao, S.; Ikeda, Y.; Bernhard, G.; Hennig, C. *Dalton Trans.* **2013**, *42*, 13101.

(43) Formosinho, S. J.; Burrows, H. D.; da Graca Miguel, M.; Azenha, M. E. D. G.; Saraiva, I. M.; Ribeiro, A. C. D. N.; Khudyakov, I. V.; Gasanov, R. G.; Bolte, M. *Photoch. Photobio. sci.* **2003**, *2*, 569.

(44) Jones, L. H.; Penneman, R. A. *J. Chem. Phys.* **1953** *21*, 542.

(45) Gal, M.; Goggin, P. L.; Mink, J. *J. Mol. Struct.* **1984**, *114*, 459.

(46) McGlynn, S. P.; Smith, J. K.; Neely, W. C. *J. Chem. Phys.* **1961**, *35*, 105.

(47) Bullock, J. I. *J. Inorg. Nucl. Chem.* **1967**, *29*, 2257.

(48) Van Stipdonk, M. J.; Kullman, M.; Moore, D. T.; Polfer, N.; Oomens, J.; Siboulet, B.; de Jong, W. A. *J. Phys. Chem. A.* **2008** *112*, 508.

Chapter 6: Determining the partitioning of uranyl and trivalent lanthanide complexes in a microemulsion

6.1 Introduction

This chapter describes SANS (small angle neutron scattering) experiments performed to determine the partitioning of uranyl and trivalent lanthanide complexes in an SDS 4.5T microemulsion system (to be described in detail in section 6.2). Addition of various O and N-donor ligands to uranyl nitrate in the microemulsion resulted in the formation of complexes, which partitioned to specific areas of the microemulsion as a result of their differing solubilities. Competition experiments involving trivalent lanthanides were also performed and the SANS data analysed.

The luminescence spectra of the microemulsions were investigated in an attempt to correlate the position of the complex within the microemulsion and the nature of the observed emission. The combination of these structural and spectroscopic techniques provided information regarding the partitioning of the metal complexes in the microemulsion system. The longer term goal of this work, which is beyond the scope of this thesis, is the consideration of this approach in providing a method for preconcentration and detection of radioactive metals in solution.

6.2 Microemulsions

A microemulsion is defined as a thermodynamically stable, isotropic liquid, usually containing "droplets" of oil-in-water or water-in-oil. Their thermodynamical stability is the main difference between microemulsions and emulsions, as the latter tend to phase separate over a period of time. The typical model of a microemulsion is a hydrophobic "core" and an outer "shell" of the surface active material, typically consisting of a surfactant (surface active agents) and co-surfactant dispersed in a liquid colloid.

Conventional surfactants are molecules that include two distinct parts. The first is a hydrophobic moiety, commonly an alkyl chain or fluorinated alkyl chain, and the second is hydrophilic headgroup, which is a highly polar water soluble moiety which may or may not bear a charge. The differences in these two parts of the molecule results in interesting properties, such as the ability to self-assemble at certain concentrations to form intricate structures often termed as "micelles".[1] The threshold at which the concentration of surfactant is sufficient enough to form micelles is known as the "critical micelle concentration" (CMC).

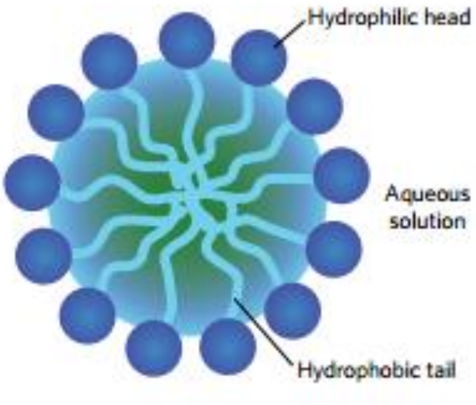

Figure 155: Schematic of a spherical micelle.[2]

The addition of other components, such as a co-surfactant and a hydrophobic molecule to a micelle can provide access to more intricate systems. These systems include a surfactant rich region and a hydrophobic molecule rich "core", which are often described as "swollen" micelles, but for the purpose of this thesis they will be termed "droplets".

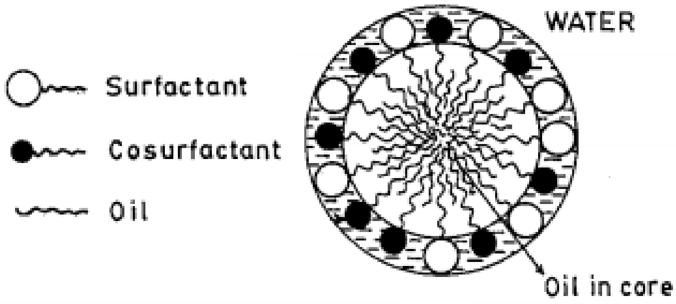

Figure 156: Schematic of an "oil in water" droplet.[3]

Although schematics of droplets and microemulsions often depict defined regions of a hydrophobic core, a surfactant shell and an aqueous continuous phase, this is in fact an over-simplification. Microemulsions are dynamic entities and are constantly changing, meaning for example that H_2O molecules may still be found in a hydrophobic core. For the purposes of the thesis, however, the microemulsion structure as portrayed in Figure 156 is accurate enough for discussion of the SANS results.

6.3 Metallosurfactants

Metallosurfactants contain the same aspects as surfactants but as the name suggests incorporates a metal in the polar headgroup as an integral structural component. This can be beneficial as regular surfactants are generally chemically inert, however metallosurfactants include variability in magnetic properties, charge, catalytic activity and luminescence and provide a means of concentrating these features at interfaces.

Recent developments in metallosurfactants have been highlighted by Fallis and Griffiths,[4] including an investigation of a Tb(III) containing metallosurfactant [Tb(**84**)(H_2O)$_2$$Cl_3$] (**84** is shown in Figure 157).

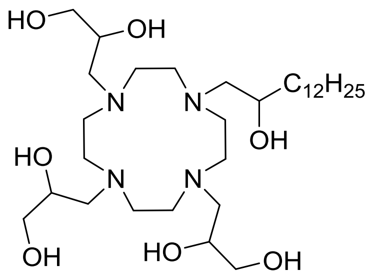

Figure 157: Molecular structure of **84**

Sensitised emission from the Tb(III) headgroups, situated on the outer shell, were found to be significant when bound to naphthalene acetic acid (NAA). However when the NAA was not bound and was located either in the oil-rich core or the aqueous phase, the sensitization of the Tb(III) was minimal. This illustrated the intimate co-localisation of emitter and sensitiser. This proved useful for determining the CMC of the microemulsion in question because the emission would only be observed if the metallosurfactant self-assembled to form a micelle. Figure 158 displays the emission spectra below and above the CMC.

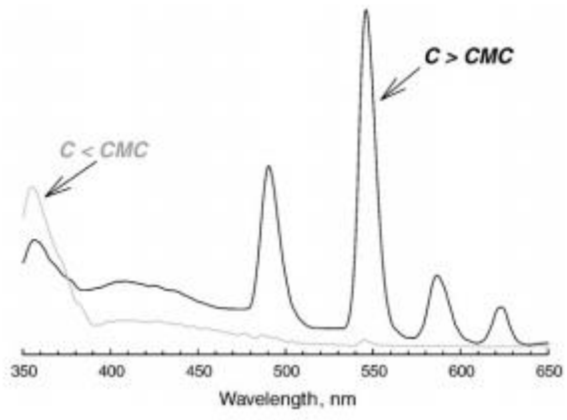

Figure 158: NAA sensitised emission from Tb(**84**)(H_2O)$_2$$Cl_3$ – gray line indicates C<CMC and black line indicates C>CMC.[4]

Figure 159 displays the processes leading to NAA sensitised emission from Tb(III). It shows the polar Tb(III) heads on the outer corona of the micelle, with the hydrophobic tail imparted by a long alkyl chain extending to the centre of the micelle. When the NAA was directly attached to the Tb(III) complex there was an efficient energy transfer to the Tb(III) headgroup which resulted in emission.

This process was found to be inefficient when the NAA was in a different location in the micelle (i.e. in the hydrophobic core) and in that instance emission was not observed.

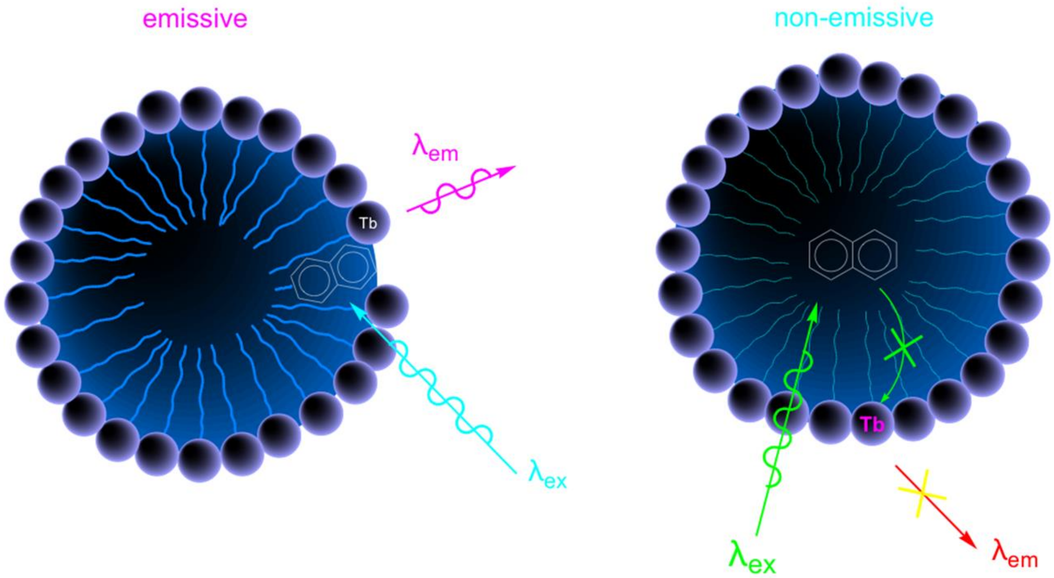

Figure 159: Representation of a metallosurfactant micelle resulting in sensitised emission. Image used with permission form the author.

6.4 The SDS 4.5T microemulsion system

The SDS 4.5T microemulsion system is composed of water, toluene, butanol-1-ol and sodium dodecylsulfate (SDS) and the exact structure of an almost identical microemulsion-SDS 5T- has been described by Fallis and Griffiths. [5] The composition by wt.% of the microemulsion was 10% sodium dodecyl sulphate, 5.0% toluene, 9% butanol and 76% H_2O (Figure 160). By contrast the SDS 4.5T microemulsion system contains only 4.5% toluene; however the structural studies undertaken on the SDS 5T system will provide a good approximation of the structure of SDS 4.5T.

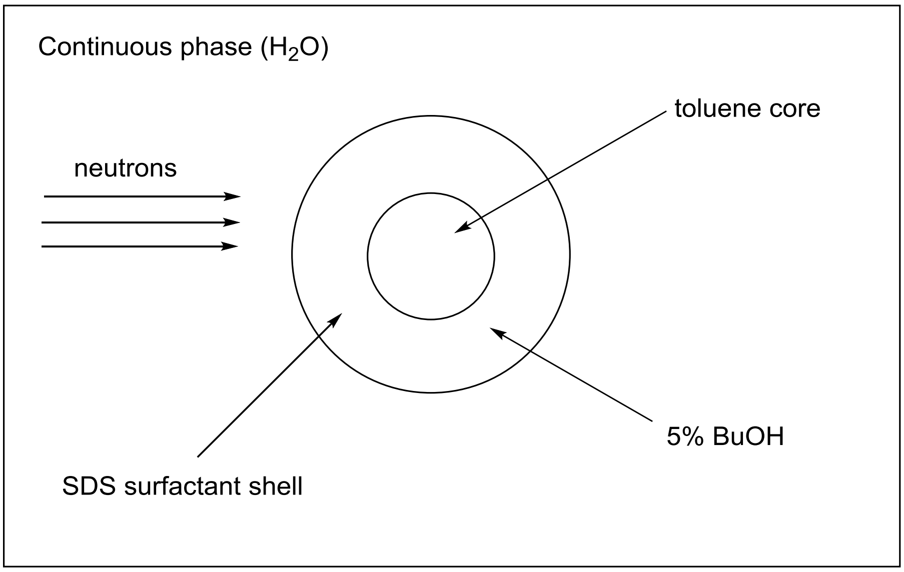

Figure 160: Schematic of SDS4.5T microemulsion

A contrast experiment, as was described in chapter 1 involves a series of experiments involving small alterations to a microemulsion in order to determine its structure. This is achieved by exploiting the fact that deuterium scatters neutrons strongly and positively, while protons scatter neutrons negatively, which makes them easy to distinguish. By running a series of neutron scattering experiments in which the components of the microemulsion (i.e. the core , shell and continuous phase) are substituted from their protic form into a deuterated form, it is possible to view each component of the microemulsion independently of the other components.

Through contrast experiments it was found that the exact size of the core, the thickness of the shell and the size of the whole "droplet" (i.e. core + shell) could be obtained for SDS 5T.[5] This was possible through the substitution of each component with deuterated analogues. If, for example, the dimensions of the toluene core were to be obtained, a system compromising D_2O, h-toluene, d-butanol and d-SDS would be employed. Similarly, if the thickness of the core were to be determined, a system compromising D_2O, h-SDS, h-butanol and d-toluene would be employed. Fully hydrogenous materials in D_2O would give the dimensions of the whole "droplet".

Through appropriate design, microemulsion systems can be applied to the detection of chemical species. Investigation into the suitability of the SDS 5T microemulsion as a detection method for the chemical warfare agent (CWA) sulfur mustard (**HD, 85a**, Figure 161) was undertaken. Simulants were also investigated, including **PhSim** (**85b**) and **EtSim (85c)** (Figure 161) due to the hazardous nature of **85a**.

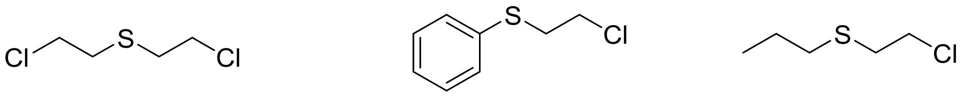

85a **85b** **85c**

Figure 161: Molecular structures of **85a-c**

There are numerous ways of detoxifying **85a**, including oxidation to the non-vesicant sulfoxide (**86a**), making sure not to over oxidise to the vesicant sulfone (**86b**) (Figure 162). There are numerous obstacles however to overcome in the selection of a suitable solvent and oxidant. Firstly most suitable oxidants are water soluble, which is problematic due to the immiscibility of **85a** in water. This obstacle can be overcome by employing an oil-in-water microemulsion (such as SDS 5T), which allows for intimate contact of dispersed **85a** with the water based oxidant. Secondly, the oxidant employed is crucial. One of the most effective **85a** oxidising systems incorporates hypochlorite (bleach) based microemulsions.[6,7] The use of bleach however has been deemed too corrosive and environmentally unacceptable for wide-scale use. Therefore Griffiths and Fallis employed peroxides as the oxidants. Peroxides however react slowly with organic sulfides, therefore a catalyst had to be incorporated into the system. An oil-soluble manganese catalyst (MnCl**(87)**) was decided upon which was isolated from its parent molecule from adapting the method of Jacobsen et al (Figure 162).[8]

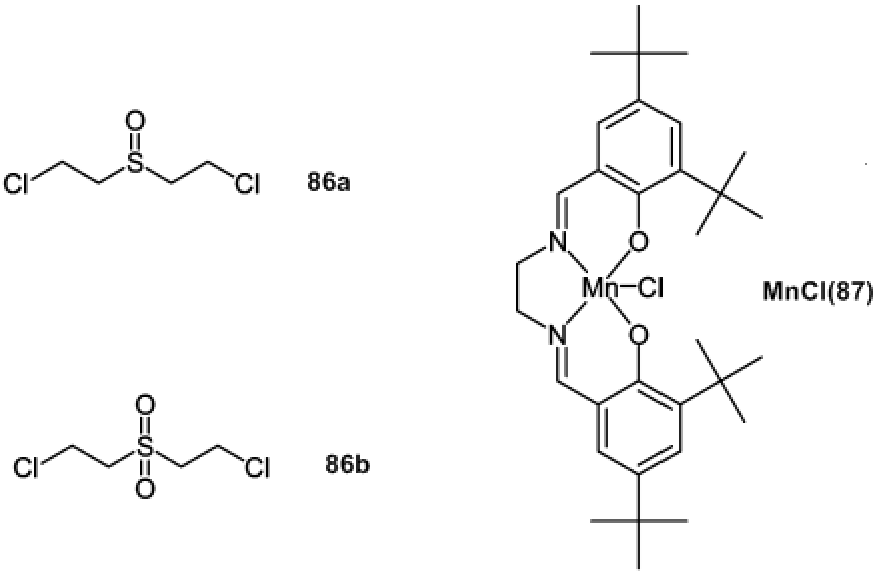

Figure 162: Molecular structures of **86a, 86b** and MnCl**(87**)

SANS experiments were undertaken on various components in order to determine how they partition in SDS 5T (Figure 163).

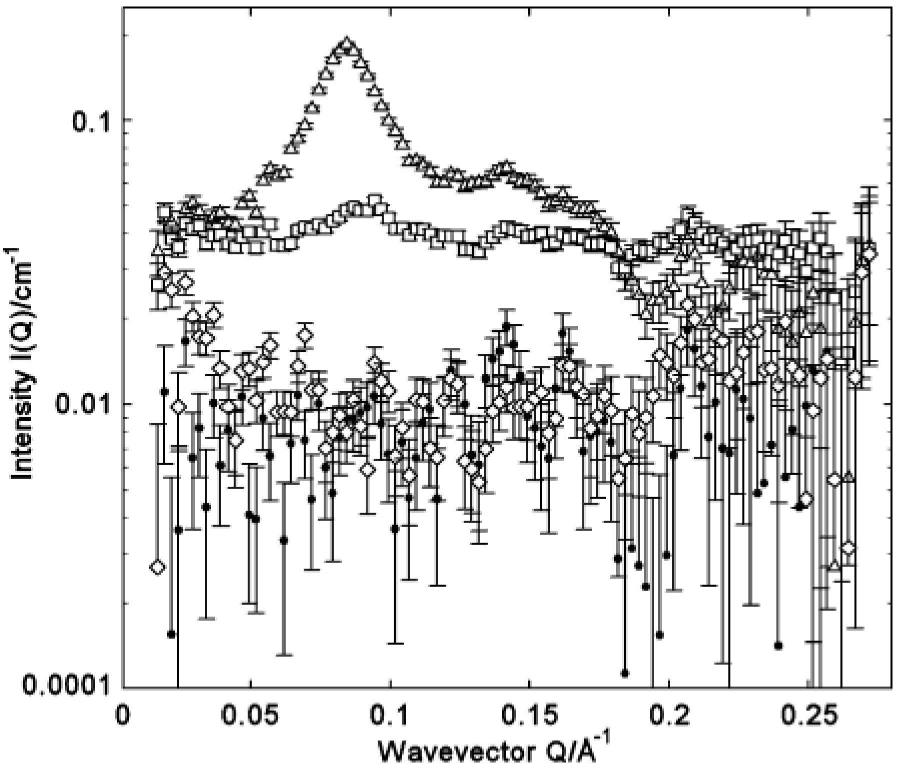

Figure 163: Small-angle neutron scattering from an undiluted perdeuterated SDS 5T microemulsion control (●); containing 1 wt. % **85c** (◊); 1wt. % **85b** (□), and catalyst (1 wt.% [MnCl(**87**)] (△). [5]

The lipophilic simulant **85b** and the catalyst [MnCl(**87**)] were found to partition into the oil phase of droplet. This was observable in the SANS as the partitioning manifested a peak in the SANS pattern. The weaker intensity observed for the **85b** was attributed to the hydrolysis of the molecule to form $PhSCH_2CH_2OH$ which was soluble in the water phase. No scattering pattern was observed for the SDS 5T control or the alternate simulant **85c**. The half-life of the formation of a sulfoxide was measured using peroxide, [MnCl(**87**)] and the simulant PhSim was measured at 90 s.

6.5 Triarylimidazoles in microemulsions

The electronic behaviour of triarylimidazoles in microemulsions is an area of interest which is investigated in this chapter. Understanding the luminescent behaviour of triarylimidazoles in microemulsions will provide valuable information regarding its potential use as a luminescent “tag” for uranyl detection. The luminescence of coordinated and uncoordinated triarylimidazoles in specific locations in the microemulsion could potentially vary according to its immediate solvent environment. The reorganisation of solvent molecules around a dipole created by an excited triplet state may alter the observed emission through stabilisation of the LUMO.

The spectroscopic and chemiluminescent behaviour of two lophine species (Figure 164), have been previously explored in micellar environments.[9]

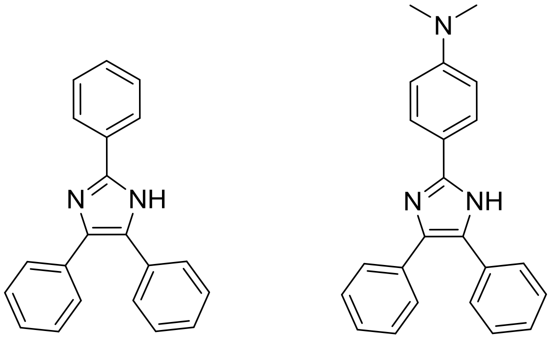

88a **88b**

Figure 164: Molecular structure of compound **88a**and **88b**

Two micelle systems were employed, the cationic cetyltrimethylammonium bromide (CTAB) and the anionic sodium dodecyl sulphate (SDS) and were compared to homogenous solutions (hexane, ethanol or methanol). These systems were employed in order to detect a “micellar effect” on the light reaction yields and rates of **88a** and **88b**. The fluorescence emission spectra of **88b** in CTAB showed a significant broadening and red-shift in comparison to homogeneous solutions of hexane and ethanol. Additionally, the increase in solvent polarity reduced the fluorescence quantum yield of the system (Φ_F). No similar observations were made for lophine **88a,** and it was therefore suggested that molecule **88b** could have a potential use as a fluorescent probe.

Solubilisation of **88b** in anionic SDS resulted in a light-insensitive solution. Its electronic absorption spectrum showed an unexpected red shift to 350 nm (Figure 165), with a shoulder at 310 nm associated with the original absorption of this molecule. This shifted band could be removed with the addition of a base to form the anion, which would then absorb at 310 nm. A dependence of wavelength and molar absorptivity was also found to be surfactant concentration dependent. The shift in wavelength was attributed to an electron donor-acceptor (EDA) complex between the *p*-dimethylamino group of the lophine and the sulphate of the SDS which is highly favoured within the orientation of the molecule inside the micelle. No bands were observed in this region in a methanolic solution of Na_2SO_4 therefore it was assumed that a specific orientation of the molecule within the micelle was responsible for this behaviour.

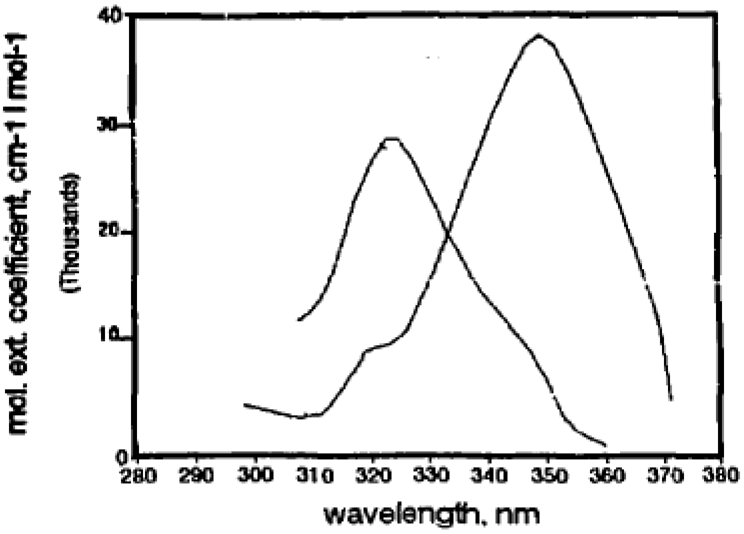

Figure 165: Electronic absorption spectrum of **88a** (left) and **88b** (right) modified from[9]

The chemiluminescence of lophines **88a** and **88b** with atmospheric oxygen were also investigated in CTAB (no chemiluminescence was observed in SDS). A reaction scheme was proposed in which any small amount of anionic (deprotonated) lophine would react with atmospheric oxygen to form a triphenyl-imidazolyl radical giving rise to peroxide (Scheme). The degradation of this is the source of the chemiluminescence. Both **88a** and **88b** were chemiluminescent in the presence of atmospheric oxygen as well as singlet oxygen.

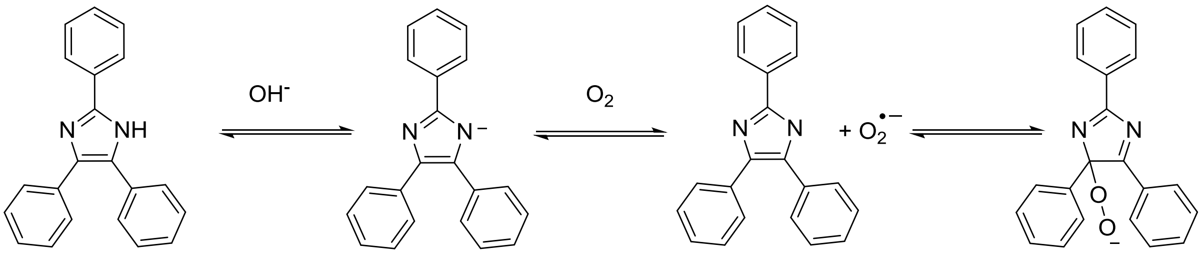

Scheme 13: Formation of peroxide anion as source of chemiluminescence

6.6 Uranyl acetylacetone complexes

For our own studies on the partitioning of both trivalent lanthanide complexes and uranyl species, among the ligands investigated were acetylacetone derivatives (acac, or β-diketonate), N-donor diimine ligands such as 1,10-phenanthroline and a fused [4,5-*f*]-1,10-phenanthroline derivative (described earlier in Chapter 2). A brief overview of the uranyl complexes formed with these ligands will now be given.

Uranyl acetylacetone monohydrate was first isolated by Blitz and Clinch in the early 1900s, [10] but it was not until the early 1950s that the chemistry of this complex was fully explored. [11-14]

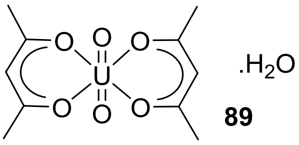
89

Figure 166: Uranyl acetylacetone monohydrate

In 1958 Comyns and co-workers reported the crystal structures of uranyl acetylacetonate monohydrate, discovering that it could crystallise in three forms (two of which were stable), which was dependent on seeding. IR spectroscopic studies of the complex found bands associated with the asymmetric stretching frequencies of the uranyl ion in the region of 900-950 cm^{-1}. The electronic absorption spectra of the complex were found to include numerous bands, including absorptions in the high-energy region of the spectrum (272, 353 nm), which were assigned to ligand-based $\pi \rightarrow \pi^*$ transitions and lower energy bands (448, 510 nm) with small molar absorption coefficients which were assigned to ligand-modified uranyl-centred LMCT absorption. The crystals of the uranyl acetylacetonate monohydrate complex showed varying emission upon excitation with ultraviolet light dependent on the type of crystal that had formed. For example, an orthorhombic structure displayed a strong yellow fluorescence at low (-196°C) and room temperatures, while a crystalline form of a prismatic structure was found to be weakly emissive at low temperature and non-emissive at room temperature.

The first isolated uranyl hexafluoroacetylacetonate complex and its properties were first described in 1960 by Belford and co-workers.[13]

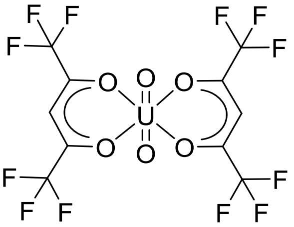
90

Figure 167: Molecular structure of uranyl hexafluoroacetylacetone, **90**

Differences were noted in the electronic absorption spectra of bis(acetylacetone)-UO_2, bis(trifluoroacetylacetonate)-UO_2 and bis(hexafluoroacetylacetonate)-UO_2. Firstly, the introduction of a trifluoro methylated ligand appeared to increase the intensity of bands centred at ≈ 360 nm, which increased again with the introduction of hexafluoroacetylacetone ligands. The absorption band at 360 nm was assigned to a ligand based $\pi \rightarrow \pi^*$ transition. A charge transfer assignment was ruled out for this absorption due to the insensitivity of the position of this band with changing ligand basicity. The IR spectra of the complexes showed stretches in the hydroxyl region, identifying the complexes as hydrates. The successful coordination of the ligands was also confirmed by the lack of carbonyl stretches associated with the unreacted ligand. Bands were also observed in the region of 950-1000 cm^{-1} which was assigned to stretches of the linear UO_2 unit.

Research into uranyl-acetylacetonate complexes in the last 15 years have included wide ranging investigations into electrochemical properties,[15] thermal and vibrational studies,[16] the coordination of N-donor ligands to U(V) β-diketiminate complexes,[17] and also a theoretical study of the increased extraction of uranyl into supercritical CO_2 upon the introduction of fluorine to the acetylacetone.[18]

Interpreting SANS data

SANS data is usually displayed in graphical form with the intensity of the scattering on the *y*-axis and the wavevector on the *x*-axis. The wavevector relates to the distance in between the two scattering locations in a microemulsion, for example if there was scattering material in the core of a “droplet” the wavevector would give information about the distance in between two cores. Put simply, any peaks observed in the graph is indicative of neutrons scattering at a specific location in the droplet. The intensity of the scattering is directly related to the amount of scattering material in that location.

This information is useful for the purpose of this experiment as conclusions can be drawn by observations of peaks, their intensities and their wavevectors. For example, any material that does not partition into the droplet will be evenly dispersed throughout the continuous phase and as a result a peak will not manifest itself in the SANS data. Conversely if scattering material partitions into a specific location such as the shell or core of the droplet, a peak will manifest itself in the data at a wavevector dependent on the exact location of the scattering material. Comparing the SANS data of two materials that partition into the droplet may provide information on whether they are in the same location.

When obtaining SANS data it is usually prudent to perform a series of “control” experiments, in addition to the main experiment that is being investigated. Control experiments involve collecting data on specific components of a system in order to have the ability to prove that any data collected for the complete system is not a result of any one component. For example if the main experiment involves a system containing a metal and a coordinating ligand, a “control” experiment will be performed which will collect SANS data of the coordinating ligand in the absence of metal. This data can then be directly compared to the main experiment.

6.7 Aims

- Investigate the SANS data for ten microemulsion systems, each of which contain uranyl nitrate and a series of ligands.
- Investigate the differences in scattering induced by differing ligands, including acetylacetonates, 1,10-phenanthroline and a fused [4,5-*f*]-1,10-phenanthroline derivative.
- Investigate the emission spectra of each of the microemulsions, and suggest correlations between the luminescence data and the scattering data (i.e. solvent effects)

6.8 Results and discussion

It is worth noting that all data obtained will be discussed qualitatively rather than quantitatively. This is due to the concentrations at which the samples were run. There are two factors that affect SANS data, the "form" factor and the "structure" factor. In order for SANS data to be considered quantitative, both form and structure factors must be deconvoluted. At high concentrations the structure factor is dominant and the form factor cannot be observed, therefore the data cannot be accurately fitted. However it was necessary to use highly concentrated samples (0.05M) in order to obtain enough data within a rigid timescale.

6.9 Microemulsion formulation

The SDS 4.5T microemulsion comprised dispersed hydrophobic droplets (toluene) surrounded by a corona of surface active species (SDS and butanol), which are referred to as a "core" and a "shell" respectively. Between each droplet is a continuous phase of H_2O (or D_2O). The formulation of the microemulsion is shown in Table 36. SANS data was obtained from ≈ 660 µl of each sample.

Component	wt. %
D_2O	76.5
d-toluene	4.5
d-BuOH	9
d-SDS	10

Table 36: Wt.% of each component of SDS 4.5T

The table below lists the ten samples which were investigated. Each of the samples contained 1 equivalent of uranyl nitrate hexahydrate ($UO_2(NO_3)_2.6H_2O$) in comparison to their respective ligands.

Sample Code	Ligand(s)	Additives	Comments
U 1	HAcac (3 equiv)	NaOH (3 equiv)	
U 2	HFA (3 equiv)	NaOH (3 equiv)	
U 3	HMe_6A (3 equiv)	NaOH (3 equiv)	
U 4	Phen (1 equiv)	None	
U 5	Lophine(1 equiv)	None	
U 6	Phen + HFA (3 equiv)	NaOH (3 equiv)	
U 7	Phen + HFA (3 equiv)	Yb (1 equiv)	
U 8	Phen + HFA (3 equiv)	Eu(1 equiv)	Some precipitation noted
U 9	Phen + HFA (3 equiv)	Nd(1 equiv)	Extensive crystallisation noted
U 10	Phen + HFA (3 equiv)	Eu, Nd(1 equiv each)	

Table 37: Samples used for SANS

6.10 Microemulsions containing only aceteylacetonate ligands (U1-U3)

Samples **U1**, **U2** and **U3** each contain uranyl nitrate, an acetylacetonate, and base (NaOH). Each sample was investigated with regards to their neutron scattering and also their electronic properties via electronic absorption and luminescence spectroscopy.

6.10.1 SANS data for U1-U3

Figure 169 shows the scattering data for **U1**, **U2**, and **U3**. The ligands used in each instance were acetylacetone (acac) for **U1**, hexafluoroacetylacetone (HFA) for **U2** and hexamethylacetylacetone (Me_6acac) for **U3** (Figure 168).

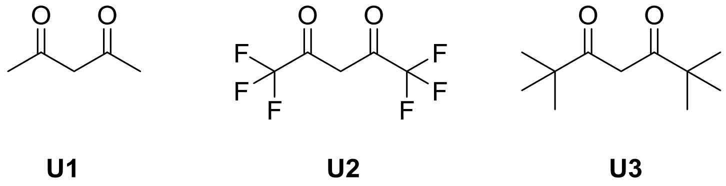

Figure 168: Molecular structures of acetylacetonates used

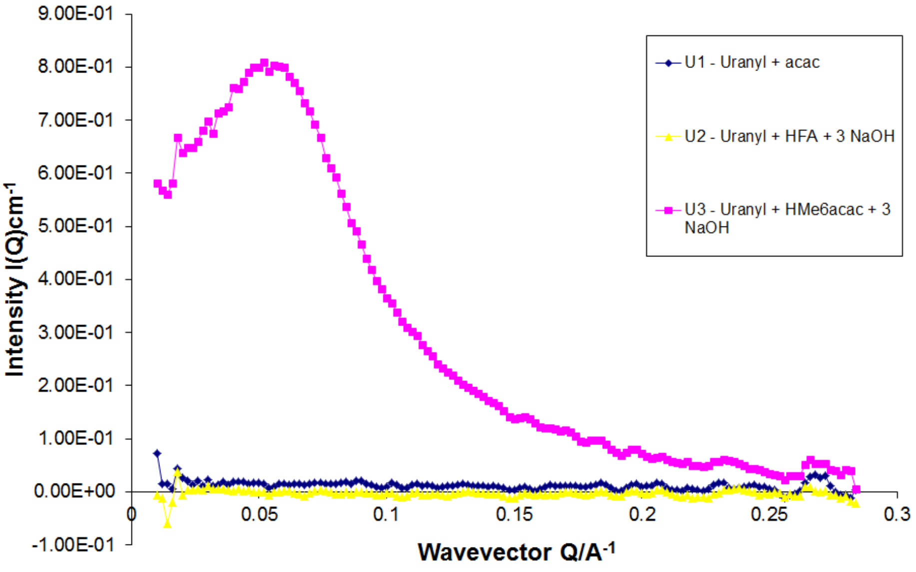

Figure 169: SANS neutron scattering data of **U1-U3**

The lack of scattering observed for samples **U1** and **U2** indicated that there was no scattering material in the SDS shell or the toluene core of the microemulsion and therefore that the the uranyl-acac complex did not partition into the SDS/toluene droplet. Contrastingly, sample **U3** displayed the most scattering for any of the ten samples run. It is worth noting that it is difficult to determine exactly how much of the scattering material has partitioned into the SDS/toluene droplet as each molecule will scatter according to the amount of protons that are present in the molecule. **U3** has numerous protons (19 for each coordinating Me_6acac) and as a result will scatter strongly. Due to the fact that Me_6acac is a hydrophobic molecule, it is also not surprising that it may partition into the toluene core, or the SDS/BuOH shell, instead of the H_2O continuous phase (Scheme 14).

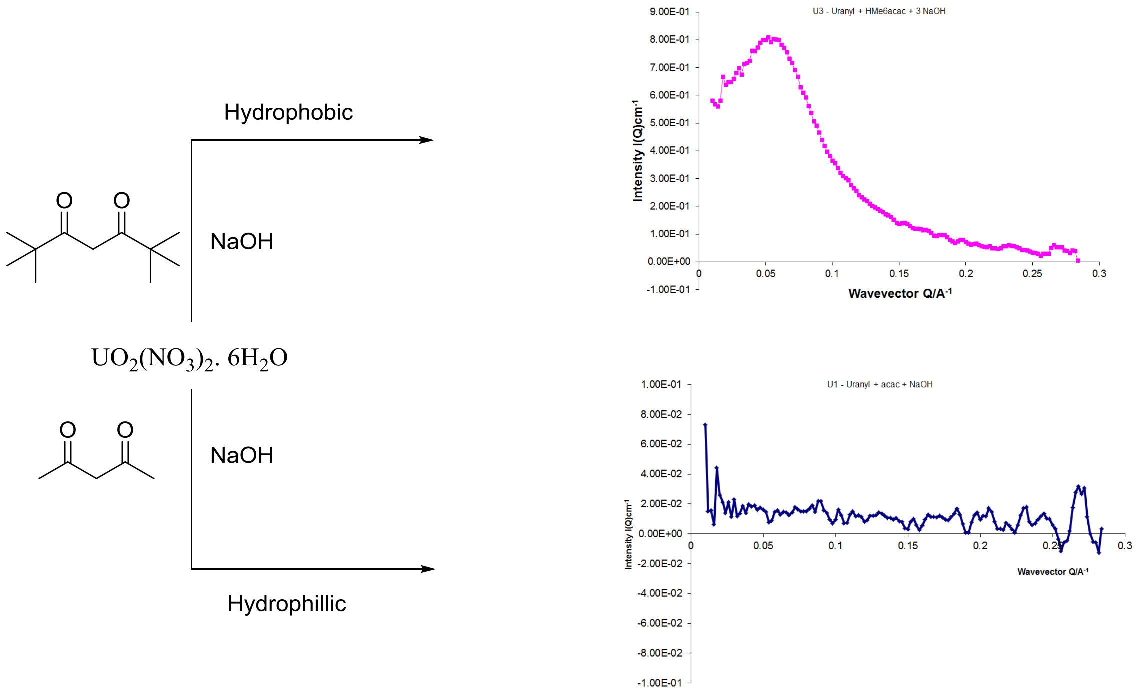

Scheme 14: SANS data for **U1** and **U3**

Figure 170 shows the complete scattering data for **U3**, including the "control" experiments. Sample **U3** contains three components- uranyl, HMe$_6$acac, and NaOH. In order to confirm that observed data for the system is not a result of partitioning of HMe$_6$acac independent of uranyl, control experiments were run whereby SANS data was collected for HMe$_6$acac on its own, and in the presence of base (without uranyl in each case).

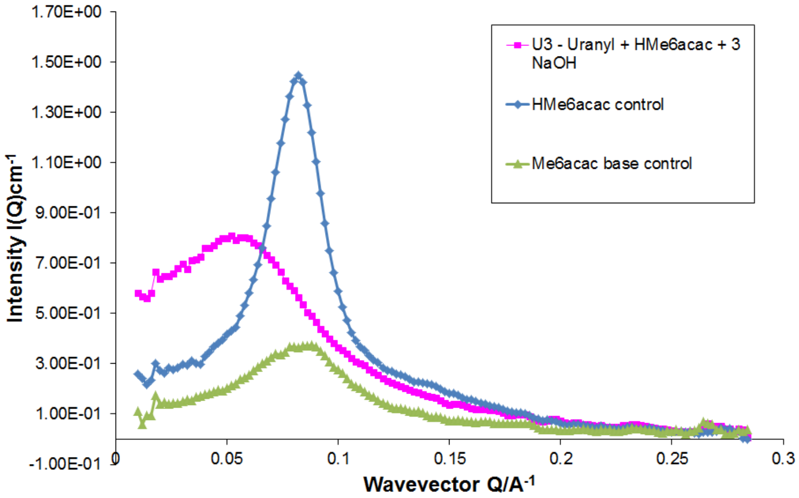

Figure 170: Scattering data including controls for **U3**

Figure 170 reveals that the strongest scattering was observed for uncoordinated HMe_6acac, indicating the greatest amount of scattering material in the droplet. The Me_6acac base control also displayed scattering although significantly less than the non-basified equivalent. This possibly indicated the tendency of the basified ligand to dissolve in H_2O due to the fact that the enolate anionic form is dominant in the presence of base (Figure 171).

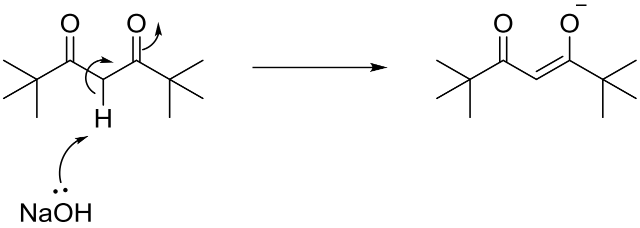

Figure 171: Formation of an enolate

The uranyl-containing sample **U3** showed scattering intensity between that of the basified and non-basified controls. Also notable is its wavevector, Q, which defines the position of the scattering material in the droplet. Although it would be difficult to discern the exact position of the scattering material based on this data, it is immediately obvious that the scattering material present in the controls are in a different location to the scattering materials of the complex. The potential locations for these molecules are in the toluene core, the SDS/BuOH shell or on the surface in between phases. The determination of the exact location is beyond the scope of this thesis.

6.10.2 Electronic Absorption Spectra of U1-U3

The concentration of **U1-U3** as they were prepared for SANS was far too high to obtain reliable electronic absorption spectra, and therefore they were diluted by half. In the case of **U3**, the addition of diluting H_2O caused the microemulsion to become unstable, resulting in phase separation. Therefore, it was diluted with further SDS 4.5T. Samples were not diluted by any more than half in order to best represent the formulation that was used to obtain the SANS data. The electronic absorption spectrum for **U1** is shown in Figure 172. The SDS component of the microemulsion absorbs strongly in the region < 385 nm, masking any potential bands, therefore only data obtained above this wavelength will be discussed.

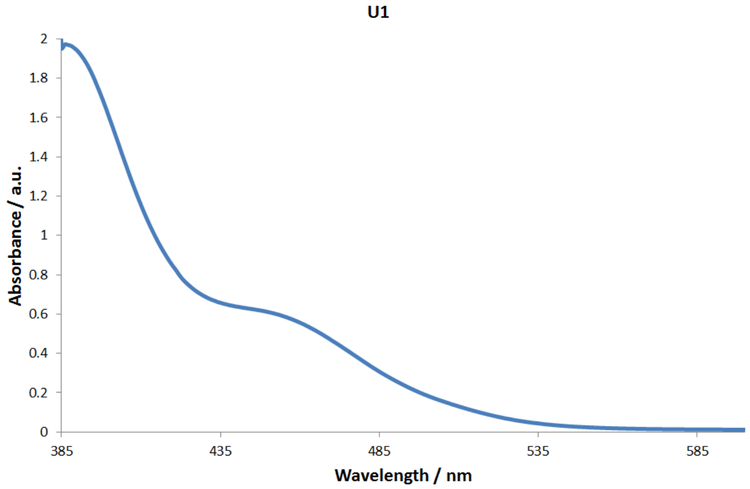

Figure 172: Electronic absorption spectrum of **U1**

The electronic absorption spectrum of **U1** displayed absorptions in the region > 400 nm including a broad shoulder observed at ≈ 435 nm. The low energy absorptions observed, particularly the one at 435 nm could be a result of uranyl-centred LMCT transition. Typically, uranyl-centred absorptions display more vibronic structure, however the wavelength observed in this instance is consistent with the wavelengths observed in the literature for an uranyl-centred LMCT. An absorption centred solely on the ligand in this case is unlikely as it would be expected to be of a higher energy.

The electronic absorption spectrum of **U2** is displayed in Figure 173.

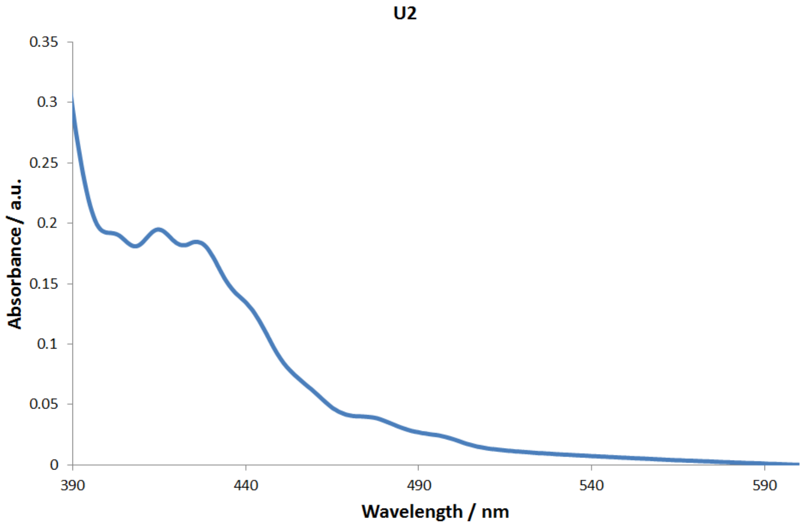

Figure 173: Electronic absorption spectrum of **U2**

The observed spectrum displayed a profile which is expected for a uranyl-containing complex. There are numerous bands observed in the region between 390 and 490 nm which were likely a result of the numerous absorption energies that promote an electron from an oxygen bonding orbital to a non-bonding 5*f* orbital. In some instances, a maximum of 12 transitions can be resolved for an uranyl centred LMCT.[19]

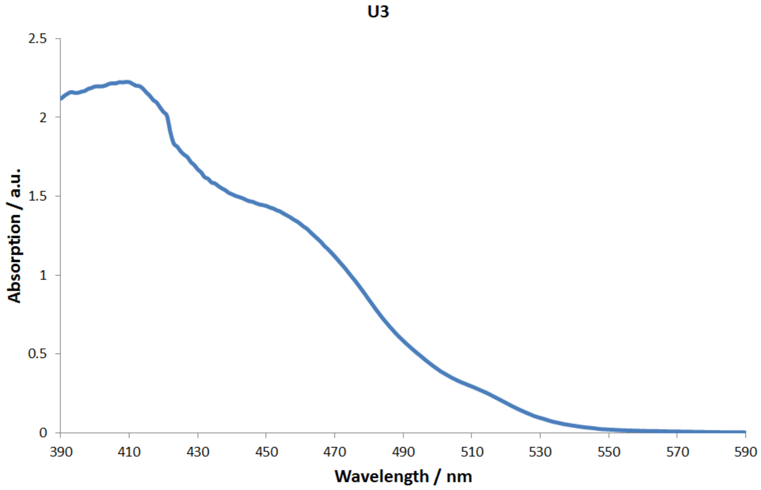

Figure 174: Electronic absorption spectrum of **U3**

The electronic absorption spectrum of **U3** (Figure 174) showed comparable characteristics to that of **U1**, i.e. it had broad absorption bands at low energies. It was concluded that this absorption is also related to a LMCT involving the uranyl unit. Each of the samples displayed bands in comparable regions to those previously reported in the literature.[11,13]

6.10.3 Luminescence Spectra of U1-U3

The corresponding emission spectra were obtained for the samples **U1-U3**. In each instance an emission was observed in the region of 500 -550 nm. The luminescence spectra may provide an insight into the immediate solvent environment, as CT bands are sensitive to the solvent environment. **U2** and **U3** have similar emission wavelengths however **U1** has a slightly lower energy emission, possibly as a result of the solvent environment.

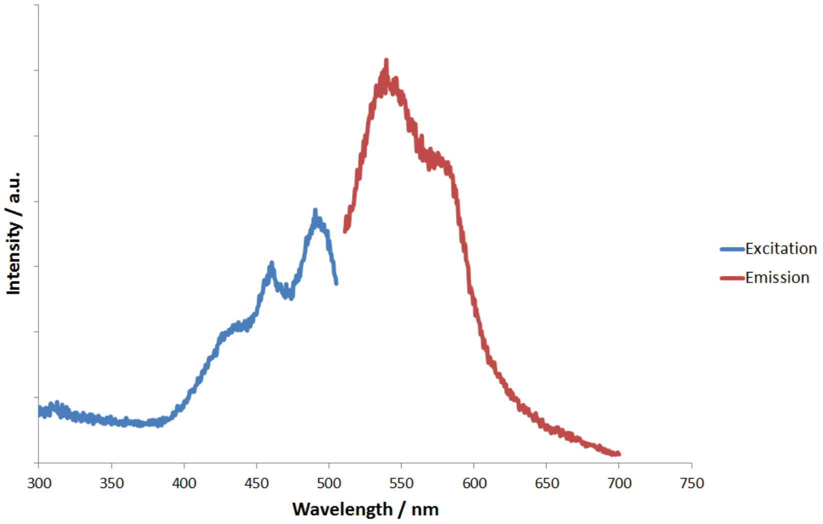

Figure 175: Excitation (blue)/Emission (red) spectra of **U1**

The emission spectrum of **U1** (Figure 175) showed an emission centred at 539 nm, with a relatively small Stokes' shift. The excitation wavelength was in the region of the electronic absorption spectra which was associated with the uranyl-centred LMCT. Although the emission profile does not share similar bands to other uranyl species, there did appear to be some vibronic structure associated with the emission peak. This emission has therefore been tentatively assigned to a LMCT excited state localised on the uranyl centre. Figure 176 shows the resultant emission spectra for uranyl nitrate + acac in each of the components that make up the SDS 4.5T microemulsion system.

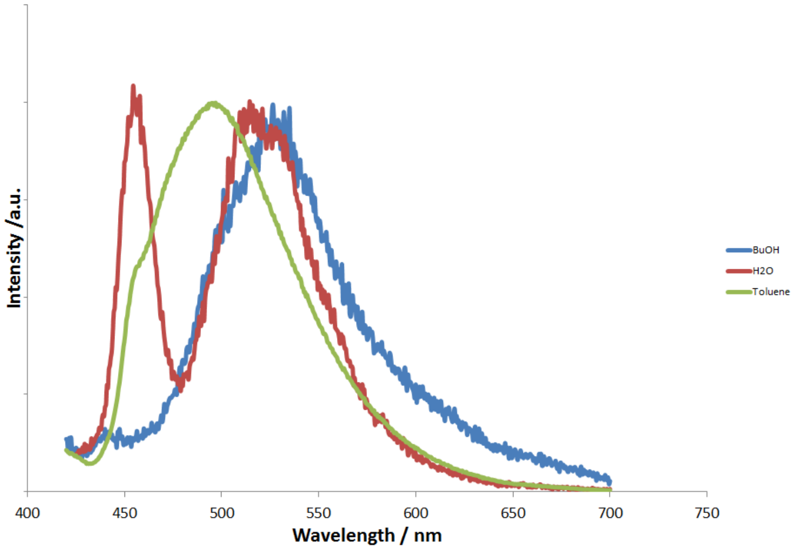

Figure 176: Normalised emission Spectra of the components of **U1**

The strongest emission for **U1** was observed in toluene, which had an emission wavelength of 496 nm. This is in contrast to when the sample was dissolved in H_2O or BuOH, which both displayed lower intensity and lower energy emission (517 and 532 nm respectively). In comparison, the emission wavelength of the SDS 4.5T system containing **U1** (which emits at 539 nm) implies that the uranyl-acac complex has partitioned into the BuOH/SDS phase. However from the scattering data it was known that the sample did not partition into the BuOH or toluene phases. Therefore the observed emission was most likely a result of the molecule existing in a unique environment within the micelle which cannot be replicated with individual solvents. For example the molecule could exist on the partition between the continuous/SDS phases or on the partition between SDS/toluene phases, although it would be difficult to prove which environment, if any, the molecule is in. The peak observed at ~ 450 nm was most likely a water Raman band.

Figure 177 shows the excitation and emission spectra of **U2**. The intensity of the emission was much greater than that observed for **U1**. The sample emitted at 506 nm and the profile was characterised by a shoulder at 529 nm which was also assigned as a uranyl-centred LMCT. It was decided that the emission could not be a result of ligand centred π-π* transition, which would involve higher energy emissions, and that the wavelength was more indicative of those typically seen in complexes displaying uranyl-centred LMCT emission

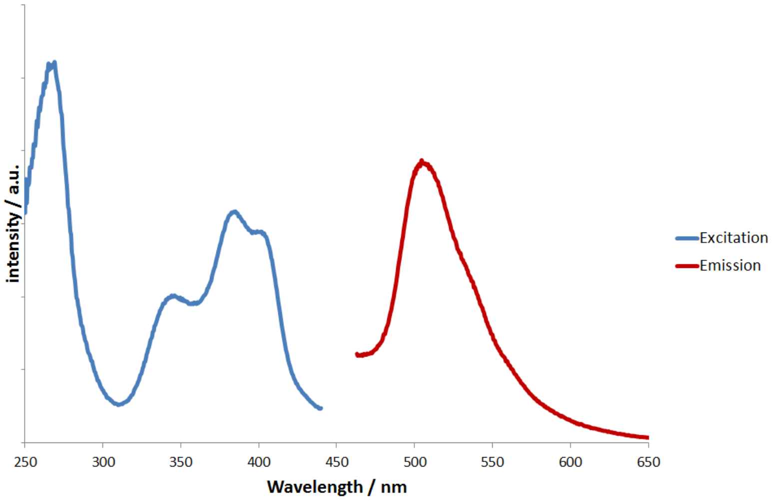

Figure 177: Excitation (blue) and Emission (red) spectra of **U2**

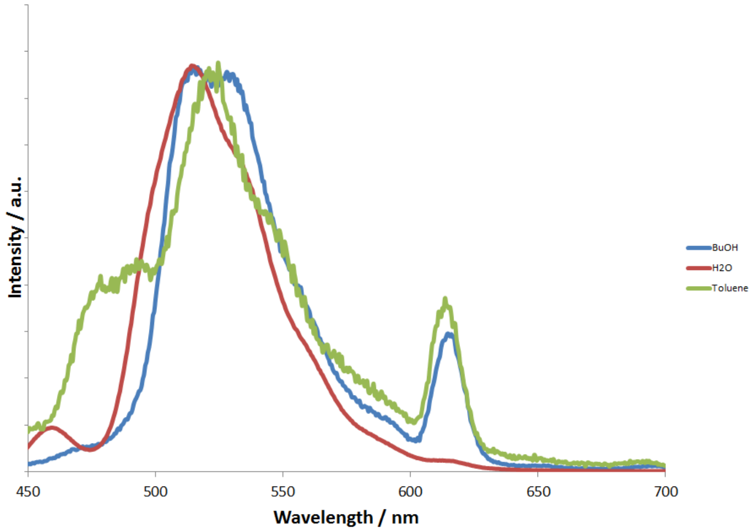

Figure 178: Emission spectra of components of **U2**

The emission spectra of **U2** in the different solvent components of the microemulsion (Figure 178) showed that the LMCT emission maximum showed a subtle solvent dependence. The main observed differences arose in the emission profile, which showed more pronounced vibronic structure for the toluene and BuOH samples than in the more polar H_2O solvent. The peaks at 625 nm observed in BuOH and toluene are harmonic wavelengths.

Sample **U3** displays a broad featureless emission centred at 506 nm. This is a similar wavelength to that observed for sample **U2** and the same assignment (uranyl-centred LMCT) was made for this sample based on its emission wavelength. Uranyl emission can in some instances vary, although not significantly (usually from ≈ 500 - 540 nm) as the electronics of the system are slightly sensitive to changes of the ligands in the equatorial plane. Alterations to these ligands in the past literature have shown to change the emission wavelengths by small amounts.[20]

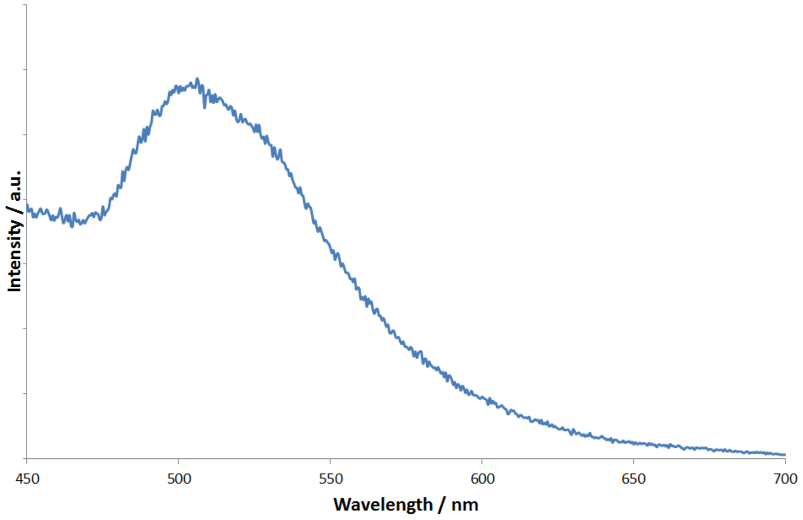

Figure 179: Emission spectrum of **U3**

Figure 180 shows the emission spectra of **U3** in H_2O and BuOH. No data was available for **U3** in toluene due to insufficient solubility.

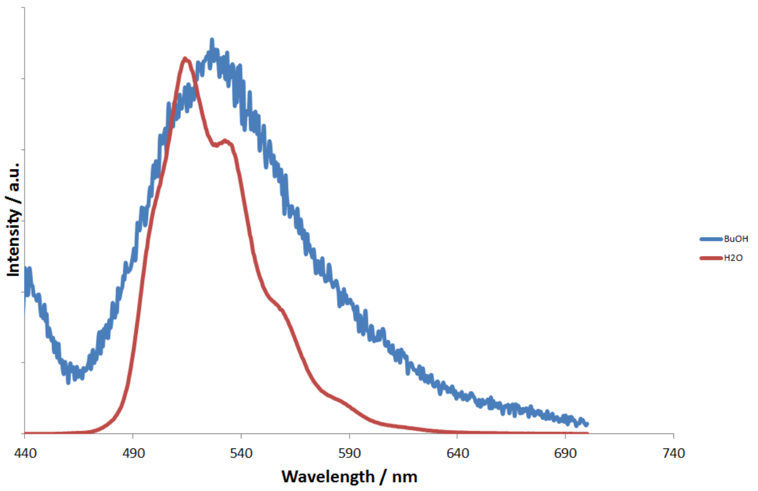

Figure 180: Emission spectra of components of **U3** (note complex was completely insoluble in toluene)

When the spectrum of **U3** was obtained in H_2O, the sample displayed a significant amount of vibronic structure, which is typical of a uranyl-centred LMCT emission. This was not true however for the emission profile when the sample was run in BuOH, which exhibited a broad featureless peak of weak intensity. The emission maximum was slightly shifted from 515 (H_2O) to 525 (BuOH) nm, meaning that the emission wavelength of **U3** in SDS 4.5T was closer to **U3** in H_2O than BuOH. However, there were far more similarities between the profiles of the sample run in SDS 4.5T and BuOH than in H_2O. This was also in agreement with the SANS data which showed that **U3** potentially partitioned into the SDS/BuOH shell. Due to the insolubility of **U3** into toluene it is unlikely that it would partition to this area of the micelle, which was considered a possibility based on the SANS data.

6.11 Microemulsions containing N-donor ligands (U4-U6)

The samples of **U4**, **U5** and **U6** contain 1,10-phenanthroline, a fused triaryl imidazole (compound **25** from chapter 2), and a mixture of 1,10-phenanthroline and HFA respectively.

6.11.1 SANS data for U4-U6

The SANS results are shown below (Figure 181). **U4** did not scatter at all, indicating that if the complex was indeed formed (it did not give an indicative intense yellow solution observed for the other samples) then it did not partition into the microemulsion droplet. **U6** scattered relatively strongly in comparison to the other two samples, which was perhaps surprising considering that neither **U2** nor

U4 exhibited any scattering pattern. This could be due to the presence of base resulting in an increased likelihood of successful coordination of the 1,10-phenanthroline. This is because in acidic solutions and increased amount of H^+ will compete with the UO_2^{2+} for binding to the N-donors resulting in less successful coordination to the phen ligand. It has been reported that 1,10-phenanthroline has a pKa of 4.27 (i.e. at pH = 4.7 there is an equal amount of protonated and deprotonated 1,10-phenanthroline).[21] This supports the assumption that a uranyl-phenanthroline complex will be more favourable at higher pH, which could then partition into the microemulsion droplet.

U5 showed a weak scattering pattern characterised by a low intensity peak with a similar Q value to **U6**. The ability of **U5** to partition into the microemulsion droplet while the 1,10-phenanthroline containing **U4** does not is probably due to two factors. Firstly, compound **25** may coordinate with uranyl nitrate at a lower pH than 1,10-phenanthroline, or, the presence of the alkyl groups on ligand **25** may increase the solubility of the complex in toluene or BuOH and therefore promote partitioning into the hydrophobic core of the microemulsion.

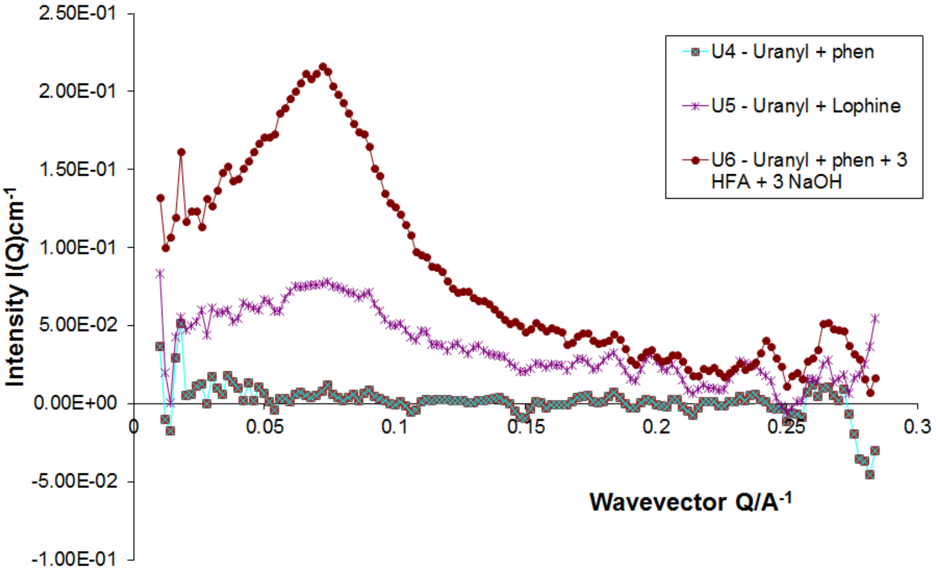

Figure 181:SANS scattering results for **U4**, **U5** and **U6**

Figure 182 displays the control experiments carried out on 1,10-phenanthroline and HFA with and without the presence of base. Also displayed in the figure is the experimental data for **U6**.

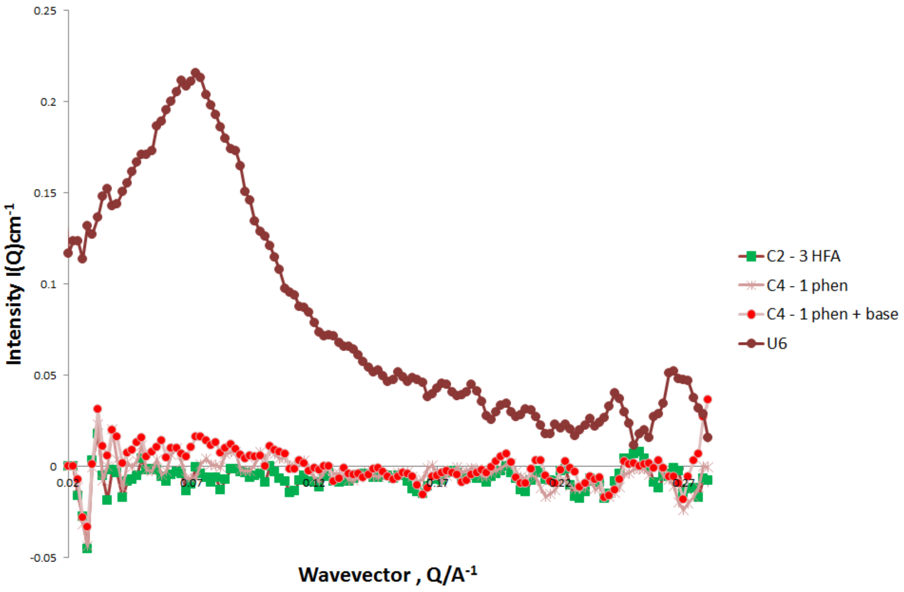

Figure 182: SANS data of **U6** and control experiments

The scattering data shown in Figure 182 showed that the ligands HFA, 1,10-phenanthroline and 1,10-phenanthroline in the presence of base did not scatter neutrons, indicating non-partitioning of the free ligands into the droplet. The complex in **U6**, however did show a significant scattering pattern, suggesting successful coordination of the uranyl ion to the ligands resulted in partitioning into the toluene core or the shell of the droplet.

6.11.2 Electronic Absorption Spectra of U4-U6

Samples **U5** and **U6** in SDS 4.5T displayed an intense yellow colour while **U4** was a very pale green. The electronic absorption spectra for **U4-U6** are shown in Figure 183-Figure 185. Low energy absorptions were observed for each sample (≈ 400 nm), which is in the region associated with uranyl-centred LMCT. A series of weak shoulders were observed for **U4** from 400 -500 nm which can be tentatively assigned to the series of bands that are generally observed for uranyl complexes. Any phen-based π→π* transition could not be observed due to the SDS component of the SDS 4.5T masking any absorptions in the high energy region of the spectrum. **U5** did not possess any vibronic structure, with only a single broad band from 380-440 nm. This low energy absorption was significantly different from the lowest energy absorption observed for the free ligand of 318nm. This suggested that the new absorption band was a result of either a metal perturbed shifted π→π* absorption, or a uranyl-centred LMCT transition.

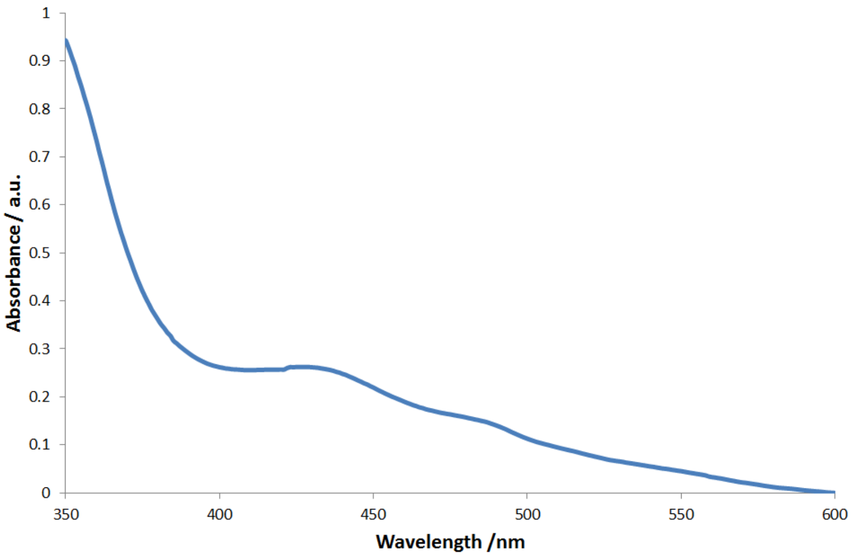

Figure 183: Electronic Absorption Spectrum of **U4**

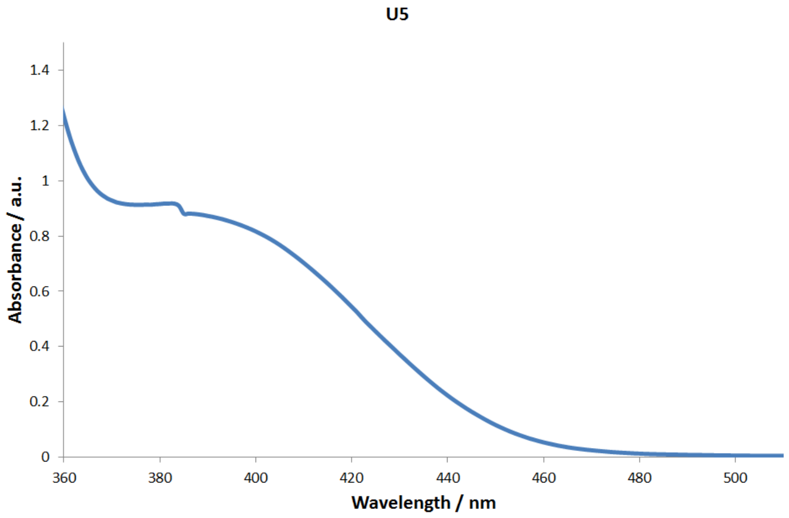

Figure 184: Electronic Absorption Spectrum of **U5**

U6 showed the most characteristic absorption as a result of uranyl-centred LMCT as there are at least six defined bands visible between 400-530 nm. The profile of the absorption was similar to that observed for **U2,** which also contained the HFA ligand. This suggested that there was successful coordination of the HFA ligand to the uranyl ion.

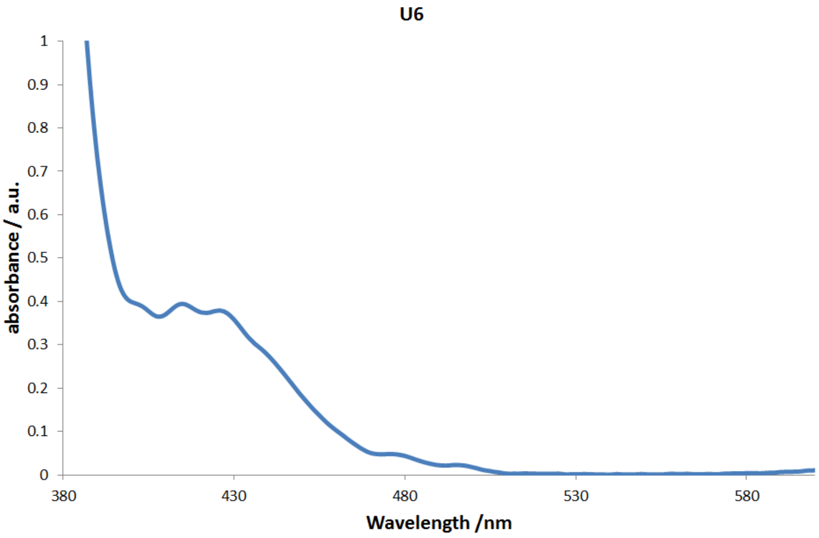

Figure 185: Electronic Absorption Spectrum of **U6**

6.11.3 Luminescence Spectra of U4-U6

The luminescence spectra of **U4-U6** are displayed in Figure 186-Figure 189. Each sample was emissive at room temperature and in each example a broad emission band was observed.

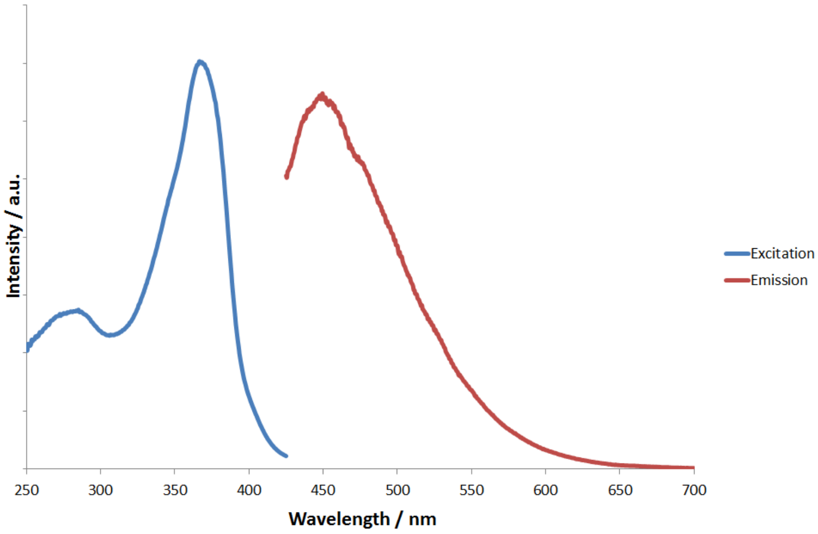

Figure 186: Excitation (blue) and emission (red) spectra of **U4**

The emission wavelength for **U4** (Figure 186) was considerably higher energy than that observed for all other samples (450 nm). The excitation spectra displayed bands similar in wavelength (350-420 nm) to others in this chapter, and also in the literature, for example those shown in .[20] This suggests that the uranyl centre was being sensitised directly and the resultant observed emission was completely uranyl-centred emission. Alternatively the emission could be a result of ligand centred π→π* transition, which has resulted in a red shift of the emission wavelength.

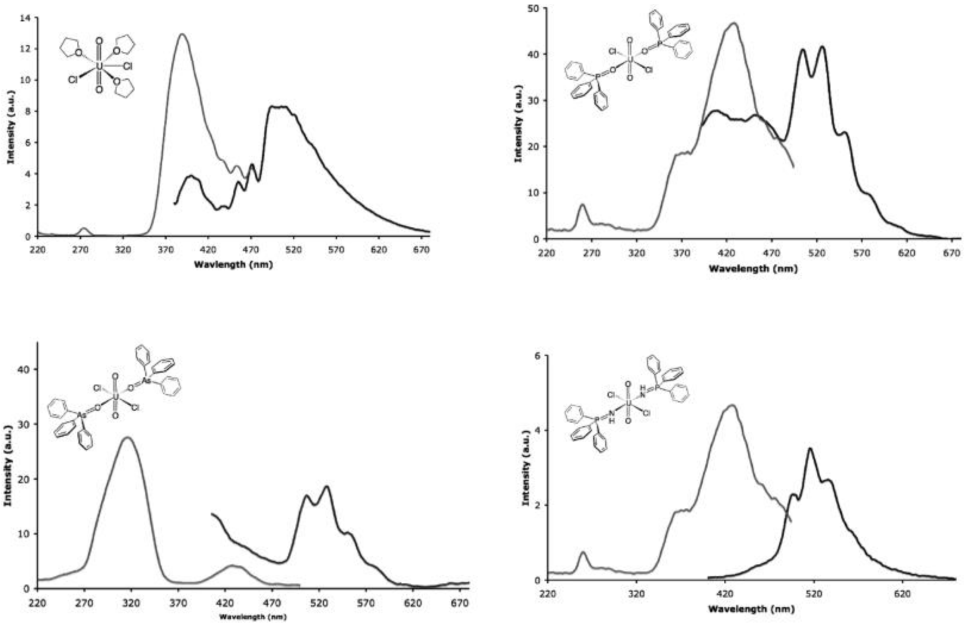

Figure 187: Excitation (grey) and emission (black) spectra of uranyl complexes. [20]

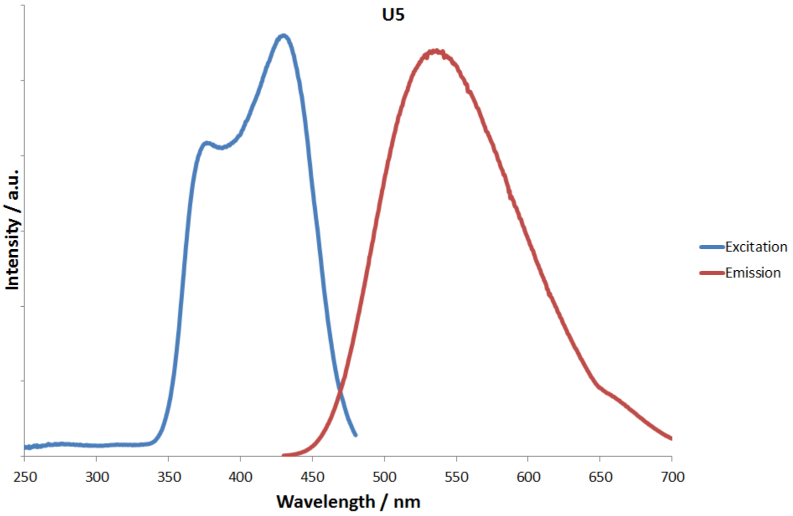

Figure 188: Excitation (blue) and emission (red) spectra of **U5**

The luminescence spectra of **U5** and **U6** both showed broad bands at low energy, with the fused triarylimidazole-containing **U5** displaying the lowest observed wavelength of 535 nm, with **U6** emitting at a higher energy wavelength of 490 nm. Assuming that both emissions are assigned as uranyl-centred LMCT, the difference in emission must be due to the ligand variation in the equatorial plane, or the solvent environment in which the molecules are present. According to the scattering data, both **U5** and **U6** partitioned into the droplet of the SDS 5T microemulsion, although it appears that **U6** does this more efficiently. It is therefore possible that the difference in emission was a result of different solvent environments.

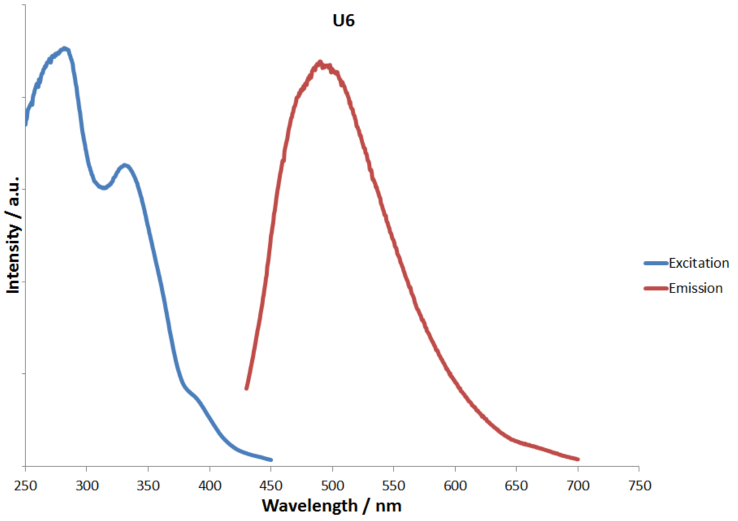

Figure 189: Excitation (blue) and emission (red) spectra **U6**

6.12 Microemulsions containing trivalent lanthanides (U7-U10)

The ultimate goal of these experiments is to determine the feasibility of using microemulsions as a preconcentration method for the detection of uranyl in solution. The source of the analyte could potentially be from numerous locations, with varying levels of uranyl concentration. Therefore the sensitivity of these microemulsion systems towards uranyl must be high compared to other ions which will also be present. For instance if a sample is taken from storage/cooling ponds or contaminated land then uranyl will only be one of numerous ions in the solution, among them lanthanides formed as a result of fission. In order to determine the effect of competing ions in solution upon microemulsion systems, SANS experiments were performed. Each of the samples **U7-U10** contained one equivalent of uranyl nitrate, one equivalent of 1,10-phenanthroline and three equivalents of HFA. In addition, at least one equivalent of trivalent lanthanides Nd(III), Eu(III) and Yb(III) were added (and in the case of **U10** one equivalent each of Nd(III) and Eu(III) were added).

6.12.1 SANS data for U7-U10

Each of the samples showed some degree of scattering, although both the intensity and the wavevector values did vary slightly.

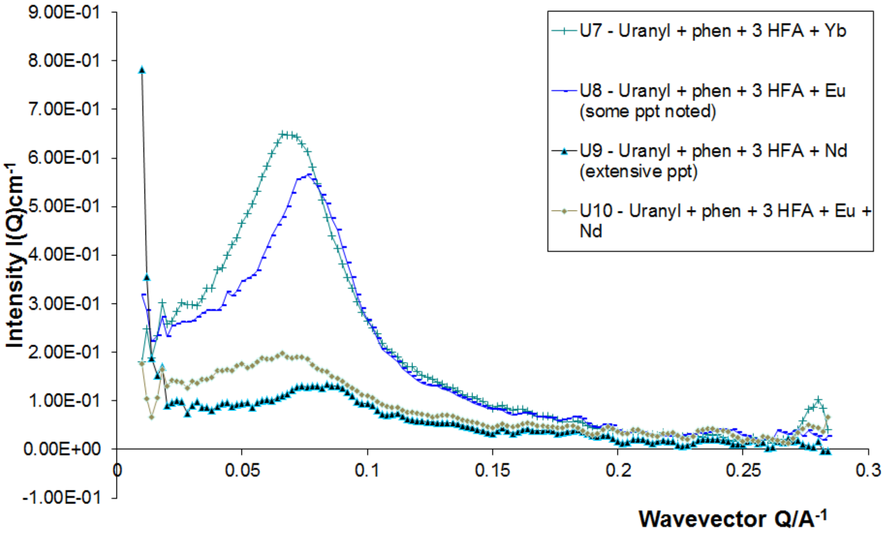

Figure 190: SANS data for samples **U7-U10**

At this point it is worth noting that some precipitation was noted for samples **U8** and **U9**. It is unclear at this stage what the precipitation may be or how it would affect the scattering. It is reasonable to assume however that the precipitate could diminish the amount of scattering material in the droplet. **U9**, which had the most precipitate, also revealed the least amount of scattering material within the droplet. Since the ligands used are the same it was assumed the amount of scattering material should remain the same for each complex, and so the difference in intensity is due to the amount of scattering material within the droplet.

The two samples which showed the strongest scattering were **U7** and **U8**, which contained one equivalent of Yb(III) and Eu(III) respectively. **U7** had the highest intensity of the two, with also a slightly lower wavevector value. This suggests that the two samples may partition to different locations within the droplet. Some precipitate was noted for **U8**, however this was not extensive and may not have a large contribution to the observed scattering intensity. The competition experiment of **U10**, which contained both Eu(III) and Nd(III) also showed a weak scattering pattern, however it was still slightly stronger than the Nd(III)-containing **U9**.

The control experiments exhibited in Figure 182 show no partitioning of the HFA and 1,10-phenanthroline ligands, but a significant scattering pattern for **U6** which contains uranyl, HFA and 1,10-phenanthroline. Samples **U7-U10** also displayed scattering patterns, although they are distinct from that observed for **U6**. This proves that the presence of other metals may affect the partitioning of any uranyl complexes in solution, or displace coordinated ligands from the uranyl centre.

The samples of **U7-U10** were far more sensitive to changes in the solvent system compared to any of the non-lanthanide containing samples. As a result, any attempt to dilute the samples with water or SDS 4.5T would result in the phase separation of the sample. Due to this fact no electronic absorption or luminescence spectra were obtained for these samples.

6.13 Conclusions

In conclusion a series of ten samples containing uranyl nitrate, and various ligands and additives were investigated with regard to their ability to partition into a micelle in an SDS 4.5T system. The results are displayed in Table 38:

Sample Code	Ligand(s)	Additives	Partitions?	Luminescence wavelength (nm)
U 1	HAcac (3 equiv)	NaOH (3 equiv)	No	539
U 2	HFA (3 equiv)	NaOH (3 equiv)	No	506
U 3	HMe_6A (3 equiv)	NaOH (3 equiv)	Yes	506
U 4	Phen (1 equiv)	None	No	450
U 5	Lophine(1 equiv)	None	Yes (Weak)	537
U 6	Phen + HFA (3 equiv)	NaOH (3 equiv)	Yes	490
U 7	Phen + HFA (3 equiv)	Yb (1 equiv)	Yes	-
U 8	Phen + HFA (3 equiv)	Eu(1 equiv)	Yes	-
U 9	Phen + HFA (3 equiv)	Nd(1 equiv)	Yes (Weak)	-
U 10	Phen + HFA (3 equiv)	Eu, Nd(1 equiv each)	Yes (Weak)	-

Table 38: Summary of data

The SANS patterns observed for each sample indicated that the choice of ligand influenced the partitioning of the complex within the micelle. This was evident in samples **U2** and **U3,** with the HFA containing **U2** not showing any scattering pattern (indicating no partitioning into the droplet) while the Me_6acac containing **U3** showed the most partitioning for any of the samples investigated.

The luminescence of the complexes in SDS 4.5T were also investigated, and the samples showed a range of emission wavelengths from 450 nm to 539 nm. All of the emission bands were tentatively assigned as uranyl-centred LMCT due to the low energy nature of the bands. The exact value of the wavelength appeared to be affected somewhat by the nature of the ligand which was bound in the equatorial plane and also the solvent environment the complex was found in. The electronic absorption spectra of the samples showed in each case distinct band in the region of 380 nm- 425 nm. This region is typical of an absorption relating to a uranyl-centred LMCT and this was further proven by the fact that some of the samples (particularly those containing HFA) showed significant vibronic structure which is typical of an absorption relating to a uranyl-centred LMCT.

6.14 References

(1) Griffiths, P. C.; Fallis, I. A.; Chuenpratoom, T.; Watanesk, R. *Adv. Colloid Interfac.* **2006**, *122*, 107.

(2) Pasquali, M. *Nat. Mater.* **2010**, *9*, 381.

(3) Moulik, S. P.; Paul, B. K. *Adv. Colloid Interfac.* **1998**, *77*, 99.

(4) Griffiths, P. C.; Fallis, I. A.; Tatchell, T.; Bushby, L.; Beeby, A. *Adv. Colloid Interfac.* **2008**, *144*, 13.

(5) Fallis, I. A.; Griffiths, P. C.; Cosgrove, T.; Dreiss, C. A.; Govan, N.; Heenan, R. K.; Holden, I.; Jenkins, R. L.; Mitchell, S. J.; Notman, S.; Platts, J. A.; Riches, J.; Tatchell, T. *J. Am. Chem. Soc.* **2009**.

(6) Menger, F. M.; Elington, A. R. *J. Am. Chem. Soc.* **1991**, *113*, 9621.

(7) Menger, F. M.; Elington, A. R. *J. Am. Chem. Soc.* **1990**, *112*, 8201.

(8) Larrow, J. F.; Jacobsen, E. N.; Gao, Y.; Hong, Y.; Nie, X.; Zepp, C. M. *J. Org. Chem.* **1994**, *59*, 1939.

(9) Boyatzis, S.; Nikokavouras, J. *J. Photochem. Photobiol. A: Chem.* **1993**, *74*, 65.

(10) Blitz; Clinch *Z. Anorg. Chem.* **1904**, *40*, 218.

(11) Comyns, A. E.; Gatehouse, B. M.; Wait, E. *J. Chem. Soc.* **1958**, *938*, 4655.

(12) Sacconi, L.; Giannoni, G. *J. Chem. Soc.* **1954**, 2368.

(13) Belford, R. L.; Martell , A. E.; Calvin, M. *J. Inorg. Nucl. Chem.* **1960**, *14*, 169.

(14) Sacconi, L.; Giannoni, G. *J. Chem. Soc.* **1954**, 2751.

(15) Yamamura, T.; Shiokawa, Y.; Yamana, H.; Moriyama, H. *Electrochim. Acta.* **2002**, *48*, 43.

(16) Sadeek, S. A.; Teleb, S. M.; Refat, M. S.; Elmosallamy, M. A. F. *J. Coord. Chem.* **2005**, *58*, 1077.

(17) Schettini, M. F.; Wu, G.; Hayton, T. W. *Inorg. Chem.* **2009**, *48*, 11799.

(18) Galand, N.; Wipff, G. *J. Phys. Chem. B.* **2005**, *109*, 277.

(19) Natrajan, L. S. *Coordin. Chem Rev.* **2012**, *256*, 1583.

(20) Redmond, M. P.; Cornet, S. M.; Woodall, S. D.; Whittaker, D.; Collison, D.; Helliwell, M.; Natrajan, L. S. *Dalton Trans.* **2011**.

(21) Albert, A.; Goldacre, R.; Phillips, J. *J. Chem. Soc.* **1948**, 2240.

6.15 Final conclusions and future work

The aim of this thesis was to investigate the luminescent and photophysical properties of imidazole[4,5-*f*]-1,10-phenanthroline derivatives and determine any potential applications. The ability to “tune” the solubility and luminescent properties of this class of ligand-also known as “lophine”-through alterations to functional groups made this a suitable ligand as a molecular “tag”. Chapters 2-4 explored the nature of the free ligands, specifically investigating how changes to the functional groups on the lophine can impact the luminescent nature and solubility of the compounds.

Chapter 2 examined the structural and luminescent properties of lophine ligands incorporating halide-containing functional groups, varying alkyl groups and extended chromophores. All ligands were found to be luminescent with short-lived lifetimes (1-5 ns) and were able to coordinate to rhenium to form complexes of the type $[ReBr(CO)_3\mathbf{L}]$- where **L** represents the imidazole[4,5-*f*]-1,10-phenanthroline ligands. All ligands and complexes were characterised through ^{1}H and ^{13}C NMR spectroscopy, IR and UV spectroscopy, mass spectrometry and additionally the luminesce emission and lifetime profiles were obtained. Crystal structures were also obtained for certain rhenium complexes. The luminescence profiles of the varying ligands often displayed maxima at different wavelengths, confirming the ability to “tune” this class of ligand through changes to functional groups. Most of the rhenium complexes in this chapter displayed long-lived luminescence (>100 ns), which occurs as a result of relaxation from and excited ^{3}MLCT state. One exception, however was the complex $[ReBr(CO)_3(\mathbf{28})]$ which was found to be a dual emissive species. The reasons behind this are unclear, however it again demonstrated how seemingly small changes to molecular structure of the lophine could significantly alter photophysical properties.

Chapter 3 examined the possibility of incorporating an additional coordination site in the form of a catechol moiety in the apical position of the ligand. These were accessed either by direct reaction with the catechol benzaldehydes or through the deprotection of methoxy groups. The solubility of these ligands often differed from those examined in chapter 2, specifically showing a tendency to dissolve in polar solvents such as MeOH and DMSO. One of the ligands was investigated for its solvatochromism, as it displayed a subtle increase in emission wavelength with an increase in solvent polarity; indicating an element of charge transfer to the emission. Chapter 4 investigated the incorporation of various functional groups on the side arm of the chromophore, including another potential binding site in the form of a terpyridine moiety. Rhenium complexes of the type $[ReBr(CO_3)\mathbf{L}]$ were again isolated and fully characterised in chapters 3 and 4.

One of the aims of this thesis was to develop and evaluate ligands as potential detector molecules for uranium via fluorescence. With this in mind Chapter 5 examined the luminescent properties of substituted imidazole[4,5-*f*]-1,10-phenanthroline derivatives isolated in chapter 2-4 when coordinated to an uranyl centre (UO_2^+). Five complexes were synthesised in total, with the general formula [$UO_2(NO_3)_2$(**L**)] which was confirmed via ^{1}H NMR, IR and UV spectroscopies. The luminescence properties of these complexes were examined, and were found to luminesce in the region of 500 nm with short lifetimes (< 5 ns) with broad emission profiles. This was attributed to shifted ligand-centred emissions rather than luminescence involving the uranyl centre itself. This may provide a method of detection of uranyl in solution, where the observed emission is specific to the uranyl-ligand combination. Further work related to chapter 5 would be to establish the preference of the imidazole[4,5-*f*]-1,10-phenanthroline derivatives over other ions in solution, namely those that may be found as a result of the fission process in nuclear reactors. This would establish whether other ions would affect, mask, or quench the observed emissions of the [$UO_2(NO_3)_2$(**L**)] complexes discussed in chapter 5.

Chapter 6 discussed the concept of using micelles as a method of preconcentration of uranyl for detection via luminescence. By altering the functional groups on the ligand, it was possible to change the amount of uranyl complex that would partition into a droplet containing a toluene core and an SDS/BuOH outer shell. This was established through the use of SANS (Small Angle Neutron Scattering), which could prove whether uranyl was present in the droplet or remained in the continuous phase. This method has provided a way of sequestering uranyl in solution, whilst analysis of the luminescence spectra of the droplets provide a speedy method of detection for U(VI). Further work in this area could include the investigation of further ligands, in particular chromophores could be employed which could give unique luminescent profiles. Similar to chapter 5, evaluation of ligands with other ions in solution would be necessary in order to establish which ligands would selectively bind to uranyl in solution and thus create an efficient, cheap method of detection for this ion.